IMAGING FLUORESCENCE CORRELATION SPECTROSCOPY: THEORY, SIMULATIONS AND APPLICATIONS TO PROBE LIPID-MEMBRANE DYNAMICS

JAGADISH SANKARAN

(B.Tech. Anna University)

A THESIS SUBMITTED

FOR THE DEGREE OF DOCTOR OF PHILOSOPHY

IN COMPUTATION AND SYSTEMS BIOLOGY (CSB)

SINGAPORE-MIT ALLIANCE

NATIONAL UNIVERSITY OF SINGAPORE

2012

Declaration

I hereby declare that this thesis is my original work and it has been written by me in its entirety. I have duly acknowledged all the sources of information which have been used in the thesis.

This thesis has also not been submitted for any degree in any university previously.

Jagadish Sankaran

27 June 2012

Acknowledgements

First and foremost, I would like to acknowledge my NUS supervisor Assoc. Prof. Dr. Thorsten Wohland for offering me a challenging project that kindled my interest in Biophysics. Having had training in Biotechnology, this project had the right mix of wet and dry lab experiments that provided me a strong foundation for a career in Biophysics. I learnt a variety of things from him during the project; the need for being meticulous, rigorous, passionate, open-minded, systematic and focused in research.

I would like to thank my MIT supervisor Prof. Dr. Forbes. C. Dewey for all the thought provoking discussions with him during the course of this project and for hosting me in his lab during my MIT trip.

I would like to thank Assoc. Prof. Dr. Rachel. S. Kraut (NTU) for very useful discussions about the field of lipid rafts during my project and for the financial support towards the end of my candidature.

An inter-disciplinary project at the culmination of Spectroscopy, Statistics and Computing would not have been possible, if not, for discussions with experts from respective fields. My thanks are due to Dr. Lee Hwee Kuan (Bioinformatics Institute, Singapore), Dr. Sun Defeng (Mathematics, NUS), Dr. Jacob White (EECS, MIT), Dr. Roy Welsch (ESD, MIT) and Dr. Imura Masataka (Bioimaging, Osaka) for their time.

Thanks to internet and online forums, these are people who I never got to meet, but who helped in debugging my programs. John Weeks, Larry Hutchinson and Howard Rodstein (Wavemetrics) and Joachim Wuttke (Forschungszentrum Juelich GmbH)

This project had a quantum leap with the availability of computing facilities from the Center for BioImaging Sciences. I would like to thank Al Davis for all the help.

A very special thank you to my predecessor and successor in the project, Guo Lin and Nirmalya respectively from the lab, for all the useful discussions and the aaha moments we had during the project. The undergraduates who worked with me during the project, Soh Xin Yi, Thomas Ellinghaus and Goh Jun Lee! Thanks to you guys for the joint venture! I would also like to thank Priscilla for being a wonderful collaborator for the graphene and nanodiamond project and for introducing me to material sciences. Many thanks are due to Xianke, Manoj, Xiaoxiao and Anand for the samples and/or image stacks and for all the ensuing discussions about the same and to all my labmates for the food and fun during the stay in lab.

Thanks to Hamamatsu Photonics, Keybond technology and Photometrics for providing sCMOS and EMCCD cameras for evaluation.

Thanks to the administrative personnel in SMA, for all the help during the 5 years.

I would like to thank my thesis proof-readers, Nirmalya, Priscilla and my dearest grandfather for reading through my thesis. I know, it should have been tough!

On a personal front, thanks to all my friends in Singapore for a pleasant time! It was a great decision for me to even take up a Ph. D. Thanks to Balasubramaniam uncle, thathas, mama, chithi, periamma, athais and all my cousins and friends for all the support. To wind up using my dad's favorite signature phrases, I am really, really short of words and tan π/2 sin Q/cos Q to my mom! If not for you, I would not be writing this thesis. I would like to dedicate this thesis to my dearest dad.

Table of contents

Declaration ..... **i**

Acknowledgements ..... **ii**

Table of contents ..... **iv**

Summary ..... **vii**

List of tables ..... **ix**

List of figures ..... **x**

List of symbols ..... **xii**

1 Introduction **1**

2 Fluorescence Correlation Spectroscopy: Theory, Instrumentation and Data Analysis **14**

2.1 Fluorescence correlation spectroscopy **15**

2.1.1 Introduction to autocorrelation 17

2.1.2 Theory of FCS 18

2.1.2.1 Derivation of diffusion propagator 20

2.1.2.2 Derivation of observation volume 23

2.2 Image Correlation Spectroscopy (ICS) **24**

2.3 Imaging FCS-Illumination schemes **25**

2.3.1 Total Internal Reflection 25

2.3.1.1 Theory 26

2.3.2 Variable angle FCS 29

2.3.3 Single Plane Illumination Microscopy 31

2.4 Imaging FCS-experimental set up **31**

2.5 Imaging FCS-detection **33**

2.5.1 CCD 33

2.5.2 ICCD 33

2.5.3 EMCCD 34

2.5.4 sCMOS 35

2.5.5 Characterization of noise in EMCCD and sCMOS 36

2.5.5.1 Multiplicative noise in EMCCD 37

2.5.6 Signal to Noise Ratio in imaging systems 38

2.6 Imaging FCS-calculation of correlation functions **42**

2.6.1 Correlation: Types and architecture 43

2.6.1.1 Linear correlation 43

2.6.1.2 Semi-logarithmic correlation 44

2.7 Imaging FCS-data analysis by ImFCS 46

3 Estimation of mobility, number of particles, PSF and heterogeneity by Imaging FCS 49

3.1 Materials and Methods 49

3.1.1 Reagents 49

3.1.2 Preparation of clean cover slides 50

3.1.3 Preparation of Supported Lipid Bilayers (SLB) 50

3.1.4 Preparation and Immobilization of GUVs 50

3.1.5 Preparation of supported mixed lipid bilayers 51

3.1.6 Diffusion and simulated flow measurements 51

3.2 Theory 52

3.2.1 Derivation of a General Fitting Model for cross-correlation 52

3.2.2 Effective Volume in Camera-FCS 57

3.2.3 Fitting models in TIRF-FCS 59

3.2.4 Fitting models in SPIM-FCS 60

3.3 Results and Discussion 62

3.3.1 Mobility and Number density from Imaging FCS 62

3.3.1.1 Calibration of mechanical microscope stage 63

3.3.1.2 Autocorrelation analysis of flow and diffusion processes 63

3.3.1.3 Cross-correlation functions (CCF) for diffusion and flow 66

Pseudo-autocorrelations in flow measurements 68

Split integration 68

Fitting cross-correlation data 70

3.3.1.4 Comparison of CCF versus ACF 84

3.3.2 Methods to characterize the heterogeneity from Imaging FCS 85

3.3.2.1 Diffusion law 85

3.3.2.2 *ΔCCF* distribution 87

ΔCCF images on supported mixed lipid bilayers 90

Characterization of cell membrane organization by *ΔCCF* 90

3.4 Conclusion 94

4 Accuracy and precision of estimates of mobility, number and heterogeneity from Imaging FCS 95

4.1 Methods 96

4.1.1 Free diffusion simulations 96

4.1.2 Domain simulations 98

4.2 Results and discussion 99

4.2.1 Effect of instrumental factors on mobility and number density 100
4.2.1.1 Effect of $\Delta\tau$, T and PSF 100
4.2.1.2 Effect of spatial sampling and total measurement time on PSF determination 104
4.2.1.3 Effect of τ_{max} and N 106
4.2.1.4 Guidelines in Performing an Imaging FCS experiment 107
4.2.2 Effect of instrumental factors on heterogeneity 109
4.2.2.1 Effect of experimental parameters on diffusion laws 109
4.2.2.2 Effect of experimental parameters on ΔCCF distributions 110
4.2.2.3 Effect of total measurement time, PSF and pixel size on intercepts in the FCS diffusion law 114
4.2.3 Heterogeneity estimates from simulations with domains 115
4.3 Conclusion 119
5 Applications of mobility, number density and heterogeneity estimates obtained from Imaging FCS 120
5.1 Materials and methods 120
5.1.1 Transfection and Imaging of cell-membrane proteins 120
5.1.2 Preparation of lipid bilayers on nanodiamond and graphene 120
5.2 Results and discussion 121
5.2.1 Live-cell imaging of membrane dynamics 121
5.2.1.1 EGFR 122
5.2.1.2 PMT 122
5.2.1.3 Experimental details 122
5.2.1.4 Mobility of membrane proteins on live-cells 123
5.2.1.5 Number density of membrane proteins on live-cells 124
5.2.1.6 Heterogeneity of membrane proteins on live-cells 125
5.2.2 Imaging FCS-a tool to study membrane formation and disruption 125
5.2.2.1 Action of antimicrobials probed by Imaging FCS 129
5.2.3 Combined electrical and optical detection 131
5.2.3.1 Principle of electrical detection of membrane dynamics 134
5.2.3.2 Demonstration of simultaneous optical and electrical detection 134
5.3 Conclusion 137
6 Conclusion 138
Bibliography 143
Appendix 172

Summary

The cell membrane is a complex structure made up of a diverse array of lipids, proteins and carbohydrates. These molecules organize themselves into different structures and it has been difficult to visualize these structures since they are believed to possess sizes below the optical resolution limit. Hence the development of new tools which probe the biophysical properties of cell membranes are necessary. Imaging FCS performed using EMCCD cameras and TIRF illumination is one such tool which allows the measurement of mobility at a large number of contiguous locations on cell membranes of live-cells with millisecond time resolution. In this technique, autocorrelation of time traces are performed; fitted to pre-determined models and mobility parameters (for instance-diffusion coefficients and velocities) are extracted.

The first chapter is an introduction to the various techniques available for studying dynamics of biomolecules in cell-membranes. This is followed by a detailed description of spatiotemporal correlation spectroscopy. In the temporal domain, it is referred to as fluorescence correlation spectroscopy (FCS) and in the spatial domain; it is referred to as image correlation spectroscopy (ICS). The needs for techniques which bridge between the aforementioned two techniques are described. Imaging FCS is one such technique. The last part is a review on the evolution of Imaging FCS.

The second chapter is a theoretical introduction to spatiotemporal correlation spectroscopy. The fitting models in FCS and ICS are derived. After the theoretical description, a detailed description of the instrumentation in imaging FCS is provided. The last part of the chapter describes the open-source software which has been written to analyze imaging FCS data.

The third chapter is a theoretical study to derive a suitable data analysis model to extract accurate and precise mobility parameters from Imaging FCS. The fitting models were later tested on experimental data. The fitting models yielded

reliable estimates of mobility parameters. The second part of this chapter provides methods to characterize the heterogeneity of the cell-membrane from Imaging FCS. Two different approaches allow us to infer the heterogeneity of membranes from Imaging FCS; *ΔCCF* distributions and diffusion laws.

The fourth chapter describes the simulations to study the effects of experimental parameters on the accuracy and precision of the estimates of mobility and heterogeneity from imaging FCS. Simulations demonstrate that the heterogeneity caused due to domains as small as 100 nm (below the resolution limit) can be resolved by Imaging FCS.

The fifth chapter describes the applications of imaging FCS which were carried out. The technique was used to check whether lipid bilayers can form on different surfaces. Mobility and organization of membrane proteins were probed by imaging FCS. The last part describes the coupling of Imaging FCS with impedance spectroscopy.

Thus, it is demonstrated that unlike single point FCS which yields only mobility, imaging FCS provides not only mobility but also other metrics to characterize the heterogeneity of membranes and will prove to be a valuable biophysical tool to characterize the dynamics and organization of lipids and proteins in a living cell-membrane.

List of tables

Table 2-1: Characteristics of TIRF instruments used in the thesis 30

Table 2-2: Characteristics of EMCCD and sCMOS cameras plotted in Fig. 2.8 A.... 38

Table 3-1: Parameters retrieved from autocorrelation functions 61

Table 3-2: ACF Covariance matrix..... 63

Table 3-3: Decomposition of a CCF with into its constituent ACF and CCFs..... 66

Table 3-4: Influence of w_0 on fitting of CCF 67

Table 3-5: Covariance matrix of cross-correlation function..... 69

Table 3-6: Parameters retrieved from cross-correlation functions..... 71

Table 3-7: Uncertainty propagation in *PSF* 73

Table 3-8: Error in *PSF* from CCF at different binning sizes..... 74

Table 3-9: Summary of various methods to determine PSF 78

Table 4-1: Parameters used in the simulations..... 95

Table 4-2: Comparison of methods to quantitate heterogeneity. ……106

List of figures

Fig. 1.1: Schematic of techniques to probe lipid rafts..... 6

Fig. 2.1: Processes probed by FCS. 16

Fig. 2.2: Determination of mobility and number of particles by FCS. 17

Fig. 2.3: Autocorrelation is a measure of self-similarity. 18

Fig. 2.4: Total Internal Reflection: Principles and Instrumentation..... 26

Fig. 2.5: Illumination schemes in camera based FCS. 30

Fig. 2.6: Schematic of EMCCD and sCMOS architecture..... 35

Fig. 2.7: Representative autocorrelation curves from different cameras. 41

Fig. 2.8: Comparison of EMCCD and sCMOS cameras. 41

Fig. 2.9: Representative ACFs from different correlator architectures..... 46

Fig. 2.10: Readouts in Imaging FCS..... 47

Fig. 2.11: Screen shot of ImFCS..... 48

Fig. 3.1: Schematic representation of the regions on a CCD chip. 53

Fig. 3.2: Change in observation volume due to the PSF..... 60

Fig. 3.3: Schematic representation of Observation volume. 62

Fig. 3.4: Calibration of microscope stage. 63

Fig. 3.5: Autocorrelations of systems exhibiting diffusion and/or flow. 65

Fig. 3.6: An error in *PSF* leads to an error in *D* and *N*. 67

Fig. 3.7: Forward and backward cross-correlations of diffusion and flow. 67

Fig. 3.8: Decomposition of correlation into auto-and cross-correlations..... 69

Fig. 3.9: Influence of w_0 on fitting of CCF..... 71

Fig. 3.10: CCF converges to a single minimum in χ^2. 73

Fig. 3.11: Auto- and cross-correlations of diffusion and/or flow. 74

Fig. 3.12: Contour plots of χ^2 value of CCFs..... 77

Fig. 3.13: PSF determination by autocorrelation and ICS methods..... 81

Fig. 3.14: Cross-validation of PSF measurements:..... 82

Fig. 3.15: Fit free determination of PSF. 82

Fig. 3.16: Heterogeneity metrics from Imaging FCS. 86

Fig. 3.17: Detection of borders by *ΔCCF*. 89

Fig. 3.18: Detection of borders between phase separated regions by ΔCCF. 91

Fig. 3.19: Effect of MβCD on *D* and *ΔCCF* of SBD labeled cells. 93

Fig. 4.1: Schematic of the simulations. 98

Fig. 4.2: Dynamic range of time resolution in Imaging FCS. 102

Fig. 4.3: Effect of spatial sampling and *T* on PSF determination. 105

Fig. 4.4: Dependence of accuracy and precision of estimates on *N* and *Δτ*. 107

Fig. 4.5: Heterogeneity estimates from Imaging FCS. 111

Fig. 4.6: Dependence of heterogeneity estimates on T. 113

Fig. 4.7: Dependence of heterogeneity estimates on detection area. 113

Fig. 4.8: ΔCCF distributions for flow. 114

Fig. 4.9: ΔCCF distributions for diffusion. 115

Fig. 4.10: ΔCCF distributions for anisotropic diffusion. 115

Fig. 4.11: Demonstration of Kolmogrov-Smirnov test. 116

Fig. 4.12: Estimation of heterogeneity for simulations with domains. 118

Fig. 5.1: Membrane dynamics probed by Imaging FCS. 126

Fig. 5.2: Supported lipid bilayers on graphene. 127

Fig. 5.3: Mimics of bacterial membrane grown on graphene. 129

Fig. 5.4: Action of melittin and magainin probed by Imaging FCS. 132

Fig. 5.5: Simultaneous electrical and optical detection. 136

List of symbols

2f-FCS	Two focus-fluorescence correlation spectroscopy
ACF	Autocorrelation function
AFM	Atomic force microscopy
APD	Avalanche photodiodes
CCF	Cross-correlation function
CDS	Correlated double sampling
CHO	Chinese hamster ovary
CIC	Clock induced charge
CMOS	Complementary metal oxide semiconductor
cps	counts per second per molecule
CVD	Chemical vapor deposition
DC-FCCS	Dual color-fluorescence cross-correlation spectroscopy
DI	Deionized
DLPC	1,2-dilauroyl-*sn*-glycero-3-phosphocholine
DLS	Dynamic light scattering
DSPC	1,2-distearoyl-sn-glycero-3-phosphocholine
EGFP	Enhanced green fluorescent protein
EGFR	Epidermal growth factor receptor
EMCCD	Electron multiplying charge coupled device
FCCS	Fluorescence cross-correlation spectroscopy
FCS	Fluorescence correlation spectroscopy
FET	Field effect transistor
FLIM	Fluorescence life time imaging microscopy
FLIP	Fluorescence loss in photobleaching
FRAP	Fluorescence recovery after photobleaching
FRET	Fluorescence resonance energy transfer
GPI	Glycophosphatidyl inositol

GUV	Giant unilamellar vesicle
ICCD	Intensified charge coupled device
ICS	Image correlation spectroscopy
ITIR-FCS	Imaging total internal reflection-fluorescence correlation spectroscopy
IVA-FCS	Imaging variable angle-fluorescence correlation spectroscopy
kICS	k space image correlation spectroscopy
kstat	Kolmogrov-Smirnov statistic
L_d	Liquid disordered phase
L_o	Liquid ordered phase
MβCD	Methyl beta cyclodextrin
NA	Numerical aperture
NFCS	Numerical fluorescence correlation spectroscopy
NK cells	Natural killer cells
PALM	Photoactivation localization microscopy
PBS	Phosphate buffer saline
pCF	Pair correlation function
PIP3	Phosphatidyl inositol (3,4,5) triphosphate
PMT	Photomultiplier tubes
PMT	Plasma membrane targeting sequence
POPC	Palmitoyl-2-oleoyl-sn-glycero-3-phosphocholine
POPG	1-Palmitoyl-2-Oleoyl-*sn*-Glycero-3-[Phospho-*rac*-(1-glycerol)]
PSF	Point spread function
QD	Quantum dot
QE	Quantum efficiency
Rho-PE	1,2-dipalmitoyl-sn-glycerol-3-phosphoethanolamine-N-(lissamine rhodamine B sulfonyl) ammonium salt
RICS	Raster image correlation spectroscopy
S/N	Signal to noise ratio
SBD	Sphingolipid binding domain

sCMOS	Scientific complementary metal oxide semiconductor
SEM	Scanning electron microscopy
SLB	Supported lipid bilayer
SPIM	Single plane illumination microscopy
SPM	Scanning probe microscopy
SPT	Single particle tracking
STED	Stimulated emission depletion
STED	Stimulated emission depletion
STICS	Spatio-temporal image correlation spectroscopy
STORM	Stochastic optical reconstruction microscopy
sv-FCS	Spot variation fluorescence correlation spectroscopy
SW-FCCS	Single wavelength fluorescence cross-correlation spectroscopy
TIRF	Total internal reflection fluorescence
TMR	Tetra methyl rhodamine
ΔCCF	Differences in cross-correlation function
μ_1	Refractive index of optically denser medium
μ_2	Refractive index of optically rarer medium
a	Pixel side length of the EMCCD
A_{eff}	Effective area
C	Concentration of fluorophore
D	Diffusion coefficient of the molecule
d_p	Penetration depth
F	Excess noise factor
$G(\tau)$	Autocorrelation function
G_∞	Convergence at longer lagtime
η	Viscosity of medium
J	Mass per unit area per unit time
k	Ellipticity of confocal volume
k_B	Boltzmann constant
M	Gain in an EMCCD

N	Number of particles in the effective observation volume
n	Number of frames
N	Number of particles diffusing in the effective area
N_t	Number of particles diffusing in the entire simulation region
P_{cic}	Current observed due to the clock induced charge
P_d	Dark current
q	Efficiency of detection
R	Radius of the diffusing molecule
R_s	Radius of the simulation region
T	Temperature
T	Total measurement time $T = n\,\Delta\tau$
t_{acq}	Acquisition time of the stack in Imaging FCS
T_{min}	Minimum total measurement time for a particular error level
v	Velocity of flow
V_c	Confocal volume
V_{eff}	Effective volume
w_0	e^{-2} radius of PSF
w_{xy}	Radial width of confocal volume
w_z	Axial length of confocal volume
ξ	Lagspace
$\Delta\tau$	Time resolution of the EMCCD
θ_c	Critical angle of illumination
λ	Wavelength of light in vacuum
λ_2	Wavelength of light in optically rarer medium
λ_{em}	Emission wavelength
τ	Lagtime
τ_D	Diffusion time
τ_{max}	Last point in the lagtime till which the correlation is calculated
χ^2	Chi-squared value obtained during fitting

1 Introduction

The cell membrane is one of the most important organelles in a cell. It is a complex structure made up of a diverse array of lipids, proteins and carbohydrates. It is known that there are at least 500 different lipid species in the cell membrane. One third of the genome codes for membrane proteins[1]. It is made up of two lipid leaflets referred to as the outer leaflet and the inner leaflet. Both leaflets differ in their composition. Certain lipids (e.g. phosphatidyl serine) are enriched only in the inner membrane[2]. The cell actively maintains the composition of the lipids in the outer and inner layers. The appearance of certain lipids in the outer leaflet which are enriched only in the inner leaflet is an assay for cell-death[3]. The cell membrane has a wide variety of functions attributed to it. The proteins in the cell membrane serve as receptors for ligands which play a role in proliferation, cell-death and infection.

The most common perception of a cell membrane has been that of a "fluid mosaic" model[4]. In this model, the cell membrane is assumed to be a homogenous fluid made up of lipids in which are interspersed the various peripheral and integral membrane proteins. The integral membrane proteins span both layers of the membrane while the peripheral membrane proteins span only one layer of the membrane. The plasma membrane is made up of different lipid classes namely sphingolipids, cholesterol and glycerophospholipids. Over the last decade, it has become known that the cell membrane of cells, far from being uniform, is highly organized yet dynamic, consisting of a multitude of interacting sub domains within the lipid membrane. The length scales of these associations on the membrane span a wide range of magnitudes ranging from small, nanometer sized cholesterol rich rafts to large, micron sized ceramide rich platforms[5-7]. These highly heterogeneous structures exhibit dynamics in the millisecond time scale[8]. The membrane exhibits a range of diffusion coefficients due to the presence of regions of lower mobility called "lipid rafts" embedded in a fluid phase of higher mobility. Lipid rafts have been reviewed in recent literature[6, 9]. A definition[5] coined at the 2006 keystone symposium

on lipid rafts and cell function states, “lipid rafts are small (10-200 nm), heterogeneous, highly dynamic, sterol- and sphingolipid-enriched domains that compartmentalize cellular processes.” Reconstituted lipid rafts in model membranes have proven to be very useful in understanding the dynamics of these heterogeneous structures[10].

The enrichment of sterols and sphingolipids in the cell membrane is facilitated by lipid sorting in the trans-golgi network[9]. This suggests that there is lateral segregation of lipids in the transport vesicles as well. Another class of microdomains found in the cell are called caveolae which are membrane invaginations enriched in a protein called caveolin[11-12]. The proteins targeted to caveolae and lipid rafts were hypothesized to be surrounded by lipid shells[12]. The lipid droplets found in the cell are lipid storage organelles[13]. They are made up of a monolayer covering a core rich in esterified neutral lipids. The structure of lipid droplets enables them to localize near the caveolae and hence the lipid droplets play a crucial role in the transport of biomolecules to and from the caveolae.

Different organelles in the cell have different lipid compositions[14]. For instance, when compared to the plasma membrane, the mitochondrial membranes are more abundant in phosphatidyl ethanolamine (PE). In addition to that, mitochondrial membranes are enriched in cardiolipin (CL). The conical shape of PE and CL lead to a different packing when compared with the bulk of membrane made up of cylindrically shaped domains. This leads to lateral segration of PE and CL into distinct domains[15].

The improvements in lipidomics over the last decade enables one to quantitate the amount of various lipids from a small amount of sample[16-17]. The lipidomic analysis of raft clusters in activated T cell receptor clusters yielded quantitative measures of the abundances of various lipids inside and outside the rafts[18]. Visualization in biomolecules is performed by fusing them to fluorescent reporters. However, it has been difficult to visualize these structures since they are

believed to possess sizes below the optical resolution limit. The resolution of optical images is governed by fundamental laws of diffraction. Two point sources which are separated by distances less than the point spread function (PSF ~ half the wavelength of light ~ 200 nm) cannot be differentiated and hence there arose a need to overcome this fundamental limit. Recent advances in microscopy allow imaging beyond this limit. Some examples of these so-called super-resolution techniques include photoactivation localization microscopy (PALM), stochastic optical reconstruction microscopy (STORM), stimulated emission depletion (STED), and structured illumination[19]. Near field scanning optical microscopy (NSOM) has been used to image clusters below the resolution limit in the T cell membranes before and after stimulation with ligands[20].

Although fluorescence is considered a standard in biology, it also suffers from the disadvantage that in order to observe any biomolecule, it has to be fused with a reporter protein. This fusion might lead to a loss in function or the fusion might hinder its movement. Hence label free methods are becoming increasingly popular to observe biomolecules. One popular approach is based on Raman spectroscopy. Certain biomolecules like lipids have a characteristic Raman signal which is used to monitor its fate over time[21].

Cells are fixed in order to observe organization of and localization of biomolecules. Fixing cells leads to many artifacts. Recently Schnell *et al* have highlighted the disadvantages of immunostaining[22]. The permeabilization, fixing and staining protocols in immunostaining lead to redistribution of various proteins. Hence there is a need to perform live-cell imaging of the cell membrane in order to observe the molecular dynamics of the lipids and proteins embedded in it. In conventional live-cell fluorescence imaging approaches, contrast is given by time-averaged intensities. Instead, methods those utilize fluorescence lifetimes, anisotropy, mobility, energy transfer, etc., give information about the physical state of molecules in living cells and thus promise to provide new insights to biologists. Ideally measurements are

performed at a physiological concentration. Experiments conducted using over-expression of proteins may not represent the real picture of the biomolecules. Hence the development of new tools which probe the biophysical properties in live-cell-membranes at physiological concentrations is necessary. The various fluorescence techniques to probe lipid rafts can be grouped into certain categories namely photobleaching, energy transfer, tracking and correlation. The different biophysical methods to characterize lipid domains have been comprehensively reviewed[23-24].

The two techniques which fall in the photobleaching category include fluorescence recovery after photobleaching (FRAP) and fluorescence loss in photobleaching (FLIP). These techniques have been successfully employed to monitor the dynamics of raft associated molecules[25]. In the case of FRAP, a high power laser is used to selectively photobleach a certain area. The recovery of fluorescence in this area by the diffusion of fluorophores from the vicinity is monitored over time. The recovery curve is fitted with theoretical models to extract diffusion coefficients and get insights into the mobility of the fluorescent molecule. The initial studies on raft association of molecules using FRAP led to the notion of dynamic partitioning of molecules in and out of raft regions and ruled out the possibilities of stable mobile/immobile rafts[26]. In the case of FLIP, photobleaching is performed at a certain area and the fluorescence is monitored at a different area in order to probe the trafficking of certain proteins into the bleached area. FLIP is useful for monitoring the continuity of organelles in a cell. This technique was used to monitor the association of caveolin with microdomains on the cell-membrane[11].

The next set of techniques based on energy-transfer includes FRET[27], FRET-FLIM[28] and homo-FRET[29]. Fluorescence resonance energy transfer (FRET) is based on energy transfer between two different fluorescent molecules (referred to as donor and acceptor) which are within a distance of 10 nm of each other. FRET is quantified by the efficiency of non-radiative energy transfer between the two molecules. The efficiency decreases with the 6^{th} power of the distance between the molecules since

the transfer is due to dipole-dipole interactions[30]. FRET efficiency is an indirect measure of the association between two proteins. It was shown using FRET that neurokinin-1 receptor exhibited cholesterol sensitive clustering into microdomains[31]. FRET measurements are performed by monitoring the loss in fluorescence of the acceptor and the gain in fluorescence of the acceptor upon the excitation of the donor. The FRET interaction can be confirmed by photobleaching the acceptor upon which there will be a gain in donor fluorescence.

The combination of FRET with fluorescence life time imaging microscopy (FLIM) led to the development of FRET-FLIM[32]. There is a reduction in the lifetime of the donor upon FRET interactions with the acceptors. FRET-FLIM has been successfully used to characterize the lipid raft localization of tetanus neurotoxin[33]. FRET measurements are performed using two different molecules, one serving as the donor and the other as acceptor. The energy transfer between the same molecules can be quantified by monitoring the fluorescence anisotropy referred to as homo-FRET. Homo-FRET measurements yield insight about number of molecules in a cluster and the size distribution of clusters[34]. GPI-AP was shown to be arranged into microdomains of sizes of 70 nm by cross linking experiments[35] and homo-FRET measurements[36]. Later the microdomain hypothesis was revised and homo-FRET measurements showed that there are cholesterol dependent nano-clusters of GPI and of sizes less than 5 nm[37] and hedgehog forms nanometer sized oligomers and colocalized with Heparin sulfate proteoglycans[38]. Further studies by the same group led to the elucidation of the mechanisms of formation of these nanoclusters; the nano-clusters were formed due to activity of cortical actin[39].

he third technique is a tracking based method namely single particle tracking[40-41] (SPT). SPT is a technique in which the movement of individual fluorescent molecules is monitored for a considerable amount of time. The mean squared displacement (MSD) of the particle is calculated and diffusion coefficient can be extracted from the data.

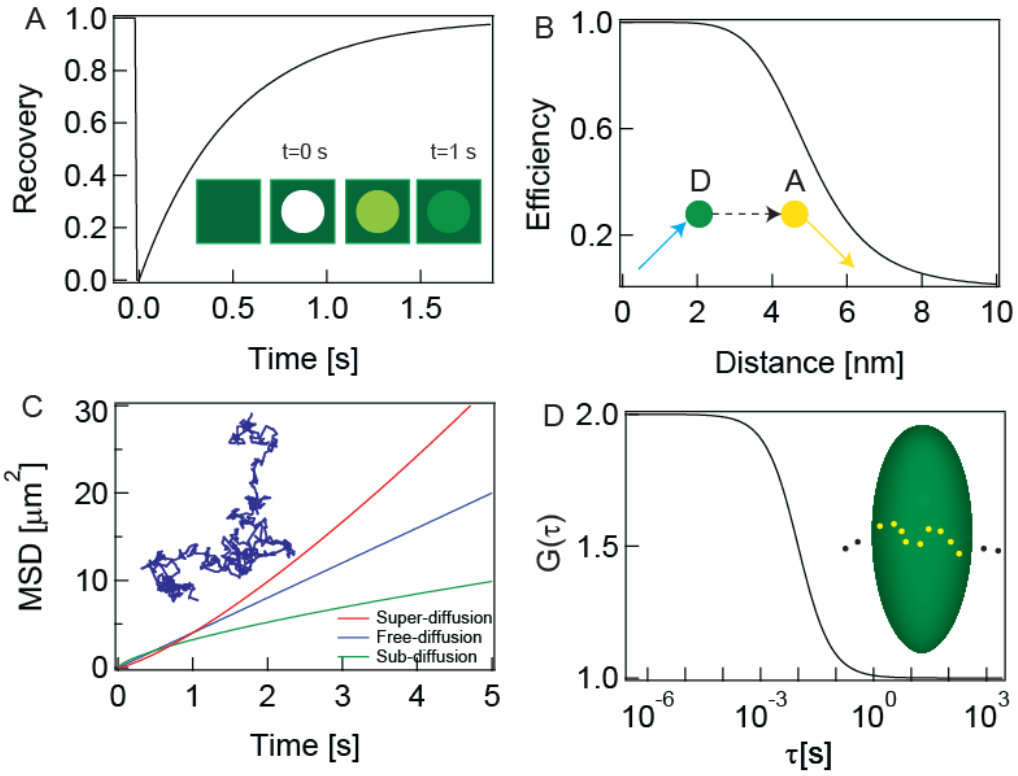

Fig. 1.1: Schematic of techniques to probe lipid rafts. A) Fluorescence Recovery After Photobleaching (FRAP): Here, the sample is photobleached and the recovery of fluorescence is monitored in the bleached area to measure the dynamics. B) Fluorescence Resonance Energy Transfer (FRET): Energy transfer between two different fluorescent molecules (labeled as D → Donor and A→ Acceptor respectively) is measured to yield information about the distance between the molecules. C) Single Particle Tracking (SPT): Individual fluorescent molecules are tracked for a considerable amount of time to yield information about the mode of diffusion exhibited by them. D) Fluorescence Correlation Spectroscopy (FCS): Fluctuations in fluorescence are analyzed to yield information about mobility.

Table 1-1: Summary of different techniques used to probe lipid rafts

Method	**Name of the technique**	**Information Obtained**
Photobleaching	FRAP, FLIP	Mobility
Energy transfer	FRET, Homo-FRET, FRET-FLIM	Distance
Tracking	SPT	Mobility and mode of diffusion
Correlation a) Temporal b) Spatial c) Spatiotemporal	a) Confocal FCS, DC-FCCS, SW-FCCS, sv-FCS, STED-FCS b) ICS, kICS c) Imaging FCS (TIRF-FCS, SPIM-FCS), RICS, STICS	Mobility, binding and organization

SPT also allows one to distinguish the mode of diffusion exhibited by the particle. The three modes of diffusion can be free, sub or super diffusion[42]. Single

particle tracking showed that raft associated proteins exhibited two different diffusing regimes (slow and fast), the slower diffusion correlated with the entry into raft associated regions[43]. SPT measurements led to observation of a novel type of movement of molecules on the cell membrane referred to as hop diffusion[44].

The last group of techniques discussed here are correlation based methods. Fluorescence correlation spectroscopy (FCS) was developed as a technique to measure the diffusion coefficients of molecules, to understand flow processes and to analyze the kinetics of reacting chemical systems[45-49]. In FCS, the underlying fluctuations arising due to any process are analyzed to determine the properties characteristic to that process; for instance, the diffusion coefficient of a molecule or the flow rate of molecules can be determined. The fluorescent intensity is temporally correlated with itself to yield the autocorrelation function. By fitting the autocorrelation function to theoretically derived models, the characteristic constant of the fluctuation process can be determined. Typically the experiment is performed in a small volume of 10^{-15} l. Instead of autocorrelation, cross-correlating the fluorescence from two different fluorescent probes led to the development of fluorescence cross-correlation spectroscopy (FCCS). Two different variants are currently in practice. If two different laser sources are used to excite the individual fluorophores, it is referred to as dual-color FCCS[50] (DC-FCCS). If a single excitation source is used, it is referred to as single wavelength FCCS[51] (SW-FCCS). DC-FCCS has been successfully used to monitor the endocytic pathway of cholera toxin[52]. A combined FRET and SW-FCCS study on live-cell membranes led to the identification of fraction of the cell surface receptor molecules existing as pre-formed dimers[53]. The same technique was used to probe the next step in the pathway where it indicated the existence of a certain level of downstream molecules interacting with the receptor without the binding of the ligand[54]. A detailed review of fluorescence cross-correlation spectroscopy can be found here[55].

Originally conceived as a temporal correlation technique, FCS was modified to perform correlation in the spatial domain under the name of Image Correlation Spectroscopy (ICS)[56]; reviewed here[57]. ICS is useful for estimating the number and size of aggregates. Modifications in ICS led to the creation of spatio-temporal ICS (STICS)[58] which has been used to measure protein diffusion and protein flow in living cells, but is sensitive to the photophysics of the labeled molecules, such as bleaching. The introduction of k space ICS (kICS) overcame this problem, as it was not sensitive to bleaching and blinking artifacts[59]. The main obstacle of the aforementioned ICS methods is that they are limited by the imaging rate of the microscope. As an alternative, Raster ICS (RICS) was developed to take advantage of the pixel/time structure within a raster scanning image, as obtained from confocal microscopy, to compute temporal correlations[60].

FCS has been successfully used to probe cell membranes and artificial lipid membranes. It has been used to probe the dynamics of lipids and proteins in living cell-membranes[61-62]. The interaction of antimicrobials peptides with lipid membranes has been investigated by FCS as well[63-65]. FCS has been performed in living cells to measure the diffusion behavior of membrane-associated molecules at the cell surface, and to gain information about segregation of these molecules into liquid ordered and liquid disordered states, since these have different characteristic diffusion coefficient[52, 66-67]. Cholesterol and sphingolipids cluster together leading to the formation of a liquid-ordered (L_o) phase which exhibits slow lateral diffusion while the rest of the membrane made up of phosphoglycerides diffuses faster and referred to as the liquid disordered (L_d) phase. The L_o and L_d phase can be distinguished based on the diffusion coefficient[52, 66-67]. Scanning FCS has been successfully used to study the slow diffusion of molecules on yeast cell membranes[68].

A variant in FCS namely spot variation FCS (sv-FCS) has been successfully used to characterize heterogeneity on cell membranes. Specifically, this technique yields insights about the two modes of confinement whether the membrane protein

under study is influenced by the actin cytoskeleton exhibiting hop diffusion or forms domains in the membrane exhibiting hindered diffusion[69]. In this technique, the spot size where FCS is being performed is varied at each experiment. With increase in area, the diffusion time scales linearly with the area in the case of free diffusion and when extrapolated to area of size zero, the diffusion time also scales down to zero. This is referred to as the FCS diffusion law. In cases, where no free diffusion is observed, a non-zero intercept is seen. For raft interactions, the intercept is positive while for interactions with the cytoskeleton, the intercept is negative. In a proof of principle study on biological systems, this technique was used to show that the diffusion of transferrin in the cell-membrane was influenced by the actin network while GPI anchored proteins were found in micro domains[70]. This was successfully used to characterize the importance of lipid rafts in Akt signaling pathway where it was established that these domains helped in signaling by recruiting Akt after accumulation of PIP3 in the membrane[71]. Studies on the serotonin 1A receptor using the same technique revealed that these proteins were influenced by the actin cytoskeleton leading to confinement in the membrane[72]. In a very recent study, sv-FCS was used to investigate the mechanisms of tolerance in NK cells and it was found that confinement of the activating receptors in domains led to tolerance[73]. A summary of the technique and its applications is available here[74]. A variant of sv-FCS was demonstrated wherein diffusion laws were calculated not by varying the size of the spot but by performing FCS at various axial positions (z) above and below the cell membrane[75].

Another way of looking at heterogeneity in cell membranes in fluctuation spectroscopy apart from diffusion laws is through the use of pair correlation functions (pCF). When two regions in space are correlated, the function exhibits a maximum which is indicative of the time taken to travel the distance between the two regions. This can be calculated theoretically from the diffusion equation. In the case, that the maximum is at a later time than the calculated value, it is indicative of a barrier to

diffusion. Pair-correlations have been successfully used to map barriers in a cell-membrane[76]. This method has been successfully used to map diffusion obstacles for a membrane marker called DiO and by fusing EGFP to a membrane targeting sequence. Apart from studies on cell-membrane, this method has been used to probe nuclear architecture and trafficking of molecules through nuclear pores[77-79]. The previous technique performed pair-correlation in the temporal domain. Upon performing the same in the spatial domain, the cluster size and distribution of cluster sizes can be obtained. This technique has been used on images obtained from super-resolution techniques like PALM and scanning electron microscopy (SEM). PC-PALM was successfully used to analyze the nanoscale distribution of GPI anchored proteins[80] while PC-SEM was used to study the molecular reorganization of the receptor IgE-FcεRI upon binding to the antigen[81].

The marriage of super resolution and FCS led to development of STED-FCS. STED is a super-resolution technique providing resolution in the order of 20 nm. In this technique, the fluorescence from a region greater than 20 nm is suppressed by a high power donut-shaped laser beam leading to improved resolution[82]. The first demonstrations of STED-FCS in 2005 showed a five time reduction in the measurement volume (25 al) when compared to confocal FCS[83]. Later this technique, proved the existence of trapping of GPI proteins and sphingolipids in <20 nm domains in a live-cell membrane unlike phosphoglycerolipids by spot variation STED-FCS[84]. This method has also been used recently to characterize the effects of various functional groups and chain lengths of various lipids on the trapping in cell membrane[85].

In all methods discussed so far, FCS systems generally use point detectors e.g., avalanche photodiodes (APD) or photomultiplier tubes (PMT) as detectors. Multiplexed FCS experiments have been performed using 2×2 Complementary Metal Oxide Semiconductor (CMOS) array based detection[86]. More recently, they have been performed on a 8×1 SPAD array[87]. But in many cases, FCS experiments need to

be performed on a large area to give an idea of membrane dynamics. EMCCD camera based Imaging FCS provides the necessary multiplexing advantage. EMCCD based FCS has first been demonstrated in a confocal mode. In this case, the EMCCD is mounted in an image plane of the microscope and the pinholes are defined by a cluster of pixels of the EMCCD for each laser beam[88-89]. This method therefore theoretically could have been used for up to ~300 confocal volumes. The method was extended by Sisan *et al.* by using a spinning disk microscope to provide the first FCS images in which each pixel in the image was correlated[90]. This method, however, requires the non-trivial synchronization of the spinning disk with the acquisition for FCS data if molecular processes are to be observed with high temporal resolution. EMCCD based detection has also been used in FCS measurements performed using multi channel confocal microscopy[91-92].

In earlier work from our group, we used the evanescent wave in Total Internal Reflection Fluorescence (TIRF) to study 2D surfaces with a time resolution of 4 ms allowing the resolution of lipid and protein dynamics at each pixel of an EMCCD camera[93] which led to the development of Imaging Total Internal Reflection-FCS (ITIR-FCS). The EMCCD camera has a time resolution of ~0.5 ms which is sufficient to resolve the dynamics on the cell membrane. Camera based FCS provides us the unprecedented advantage of observing the dynamics on a whole cell membrane at the same time. Apart from EMCCD cameras, sCMOS cameras have been used for Imaging FCS[94].

With the introduction of single plane illumination microscopy (SPIM)[95-96] and critical angle illumination[97-98] in FCS, the creation of the observation volumes was facilitated by selectively illuminating only a thin layer of the sample which lies in the focal plane of the detection objective in a 3D sample. A thin light sheet created in SPIM using cylindrical lenses[99] provides optical sectioning inside a cell and multiplexed FCS measurements can be performed at surfaces away from the cover

slide. ITIR-FCS and SPIM-FCS have already been used to quantitate mobility at many contiguous points on living cells using autocorrelation functions.

To summarize the methods mentioned above, several techniques have a high temporal resolution but are limited to measurements of a single or at most a few spots. Alternatively, there are a variety of image based spatial correlation techniques, but these have poor or anisotropic temporal resolution. ITIR-FCS bridges these regimes by providing good isotropic spatial and temporal resolution simultaneously. In ITIR-FCS the spatial resolution is diffraction limited as in other FCS techniques and the temporal resolution is limited by the frame rate of the imaging device.

In this thesis, ITIR-FCS is being extended to ITIR-FCCS enabling one to calculate cross-correlations apart from autocorrelations and to extract parameters from the same. This thesis has three parts; the first is a theoretical exploration of Imaging FCS, followed by a computational study and the last part discussed the applications in Imaging FCS.

After a detailed description of spatiotemporal correlation spectroscopy in the second chapter, the third chapter is a theoretical and experimental study to derive a suitable data analysis model to extract accurate and precise mobility parameters from Imaging FCS. In this work, we derive generalized expressions for cross-correlation between any two areas of any size and shape on a CCD chip and for the observation volume in Imaging FCS. The fitting models were tested using experiments. The fitting models yielded reliable estimates of mobility parameters from experimental data. In conventional FCS, calibration experiments are performed to determine the point spread function of the microscope using standard fluorescent dyes of known diffusion coefficient. The diffusion coefficient of unknown molecules is determined based on the PSF obtained from calibration experiments. Imaging FCS is a calibration free method which means that the value of PSF can be determined from experiments without the need for any external calibration. Hence in the second part of this chapter, four different methods to determine the PSF are compared. The major advantage of

imaging FCS is multiplexing leading to the observation of many different areas at the same time. This helps in understanding heterogeneity in diffusion in the system under study. It has been suggested earlier that differences in the forward and backward correlations, here termed ΔCCF, could be used to characterize non-equilibrium systems or anisotropic translocation[100-102]. By using ΔCCF values for neighboring pixels, we investigate heterogeneity in cell membranes for the first time. Hence, the third part of this chapter provides methods to characterize the heterogeneity of the cell membrane from Imaging FCS.

No systematic investigation on the effects of various instrumental factors on camera based FCS has been performed so far. Hence the fourth chapter describes the simulations to study the effects of experimental parameters on the accuracy and precision of the estimates of mobility and heterogeneity from imaging FCS. Simulations demonstrate that the heterogeneity caused due to domains as small as 100 nm (below the optical resolution limit) can be resolved by Imaging FCS.

The fifth chapter describes the applications of imaging FCS which were carried out. The technique was used to check whether lipid bilayers can form on different surfaces. It was used to study the effects of antimicrobials and detergents on lipid bilayers. Mobility and organization of membrane proteins were probed by imaging FCS. The last part describes the coupling of imaging FCS with impedance spectroscopy.

Unlike single point FCS which yields only mobility, imaging FCS provides not only mobility but also other metrics to characterize the heterogeneity of membranes and proved to be a valuable biophysical tool to characterize the dynamics and organization of lipids and proteins on the membranes of living cells.

2 Fluorescence Correlation Spectroscopy: Theory, Instrumentation and Data Analysis

Consider a simple system in equilibrium, say, particles diffusing freely in a solution. Such free diffusion is referred to as Brownian motion[103] after the discoverer who first observed such a phenomenon of pollen grains moving in water under the microscope. This random molecular motion is due to the collisions of pollen grains with water molecules. A formal description of Brownian motion was provided by Albert Einstein in 1905[104].

Any system even under thermal equilibrium exhibits fluctuations in the distance covered by each particle in a particular time. If, suppose, the system under thermal equilibrium is perturbed by an external force, then the system returns to equilibrium at a certain characteristic time depending on the process bringing it back to equilibrium dissipating the external perturbation. Similarly, for systems in equilibrium without any perturbation, spontaneous fluctuations disturb the equilibrium locally and these random fluctuations are dissipated at the same characteristic time as though it was perturbed by external forces. Hence, in order to determine the characteristic time constant, two complementary approaches can be performed; disturb the system out of equilibrium and observe how the disturbance is dissipated or observe the local fluctuations in equilibrium. Typically, the fluctuations are characterized mathematically by correlation functions of the relevant fluctuating physical properties. These concepts are well-known in Statistical Mechanics and referred to as the fluctuation dissipation theorem[105].

Now returning to the case of pollen grains in solution, the characteristic time constant is that of the diffusion coefficient which is a measure of the mobility of the molecule. As stated there are two different ways to obtain the same, (i) a destructive and (ii) a non-destructive method. The non-destructive method would be counting the number of pollen grains in a certain volume and then calculating the fluctuations in

the number of pollen grains. These fluctuations would then be analyzed using correlation functions to determine the mobility. The second, destructive method is to disturb the system out of equilibrium by removing the pollen grains in a certain volume and to count the number of pollen grains in the same volume till it reaches equilibrium. Based on how fast the perturbation was dissipated, the mobility of the pollen grains can be determined. The aforementioned two methods, if performed using fluorescent molecules are termed fluorescence correlation spectroscopy (FCS) and fluorescence recovery after photobleaching (FRAP) respectively. The rest of this chapter is a detailed description of fluorescence correlation spectroscopy.

The first application of fluctuation spectroscopy was the determination of size of polymers by observing the light scattered by them. This was referred to as dynamic light scattering (DLS)[106]. The fluctuations in intensity are recorded. These fluctuations vary around the average value of zero and hence are difficult to analyze and interpret. A convenient way to analyze them would be to use the autocorrelation function of these fluctuations which decays at a rate inversely proportional to the mobility. DLS was not capable of monitoring chemical reactions and hence fluorescence was used to probe the progress of a reaction. This led to the creation of fluorescence correlation spectroscopy to analyze binding reactions. Initially, FCS was developed as a complementary technique to DLS where FCS was used for monitoring chemical reactions[45, 47] and DLS for determination of size and molecular mass. But, the sensitivity, selectivity, reduction in background due to Stokes' shift of fluorescence led to the increased usage of FCS over DLS in Chemistry and Biology over the years[107].

2.1 Fluorescence correlation spectroscopy

Fluorescence correlation spectroscopy (FCS) is a technique used to study diffusion processes, flow processes and chemical kinetics[108]. In FCS, the underlying fluctuations arising due to these processes are analyzed to determine the properties

characteristic of that process. By analyzing the fluctuations in fluorescent trace, the diffusion coefficient of a molecule or the binding constant of molecules can be determined. In FCS, the fluorescent intensity is temporally autocorrelated to yield the autocorrelation function. The initial measurements in FCS were plagued by high background fluorescence leading to long measurement times since they were being performed in large volumes[107].

The initial measurements in FCS had a large number of molecules being observed at the same time leading to difficulties in performing experiments. The first measurements of FCS using a confocal microscope led to a renaissance in the field[109]. The pinhole in a confocal microscope, effectively blocks out-of-focus fluorescent light, thus reducing the background considerably. The pinhole creates an effective volume of 10^{-15} l in which the FCS measurements are made[110]. The fluctuations in this small volume are observed and they are autocorrelated. Molecules diffuse in and out of this small volume. The introduction of confocal microscopy in FCS made this technique single molecule sensitive.

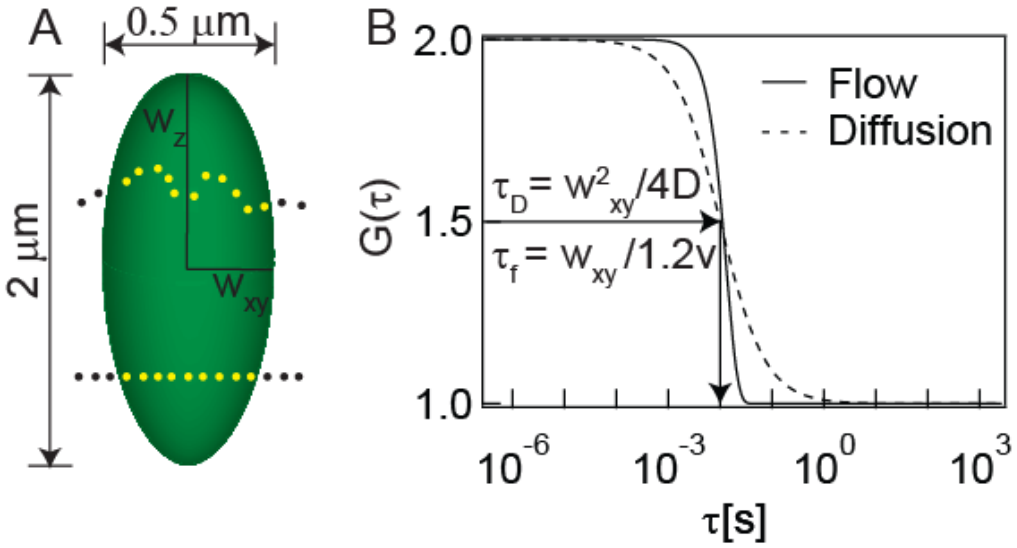

Fig. 2.1: Processes probed by FCS. The dimensions of the ellipsoidal confocal volume are determined by the diffraction theory of light. It is known from diffraction theory that $w_z > w_{xy}$. This discrepancy in resolution among *x*, *y* and *z* axes makes the volume ellipsoidal instead of spherical. As seen in B, two different processes take the same time to reach the half maximum. The shape can be used to determine the process. Flow processes exhibit an exponential decay while diffusion processes exhibit a hyperbolic decay.

The dimensions of the confocal volume are shown in Fig. 2.1 A. As seen in Fig. 2.1 B, the shape of the autocorrelation curve provides information about the type of the underlying molecular process causing the fluctuations. The mobility parameters shown in the figure for diffusion and flow are discussed later in the theory section.

Typical correlation curves obtained in FCS are shown in Fig. 2.2 A and B. *G(τ)* is the autocorrelation function of intensity which decays with lagtime *τ*. A faster decay of the autocorrelation function in this case represents a faster diffusion of the molecule under observation. The curves are characterized by τ_D which is the time taken for the correlation to decay to half the value of the maximum. The amplitude is inversely proportional to the number of particles in the observation volume. Thus FCS provides information about mobility and also about the number of particles in the small volume.

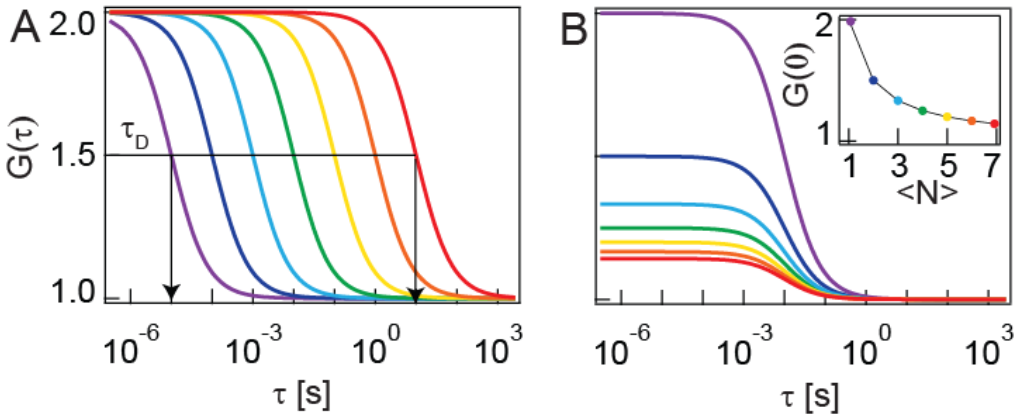

Fig. 2.2: Determination of mobility and number of particles by FCS. A is a plot of representative correlation functions decreasing in mobility from violet to red. A decrease in mobility is manifested as a slower decay in the correlation curves. The time taken to decay to half the maximum value is shown in all the curves. B is a plot of correlation curves with increasing number of particles (violet to red) in the observation volume. The amplitude of the correlation drops as the number of particles increase as seen in the inset.

2.1.1 Introduction to autocorrelation

The autocorrelation $\left(G(\tau)\right)$ is a measure of the self-similarity in time of the intensity trace $\left(I(t)\right)$ and is given by:

$$G(\tau) = \frac{\langle I(t)I(t+\tau)\rangle}{\langle I(t)\rangle^2} \qquad \textbf{2-1}$$

Self-similarity between any two mathematical functions can be quantitated by calculating the area common under their curves. The mutual area under the curve between the intensity trace and the same trace slided by an offset (τ) is quantitated for various values of τ in FCS. The fluorescence trace is made up of peaks at random positions with each peak corresponding to a fluorescent burst. The curves overlap to a larger extent at smaller offsets than when the offsets are larger as seen in Fig. 2.3. At smaller offsets, the broadened fluorescent peaks overlap with themselves. At larger offsets, the probability that peaks will overlap with other peaks is lower than that at smaller offsets.

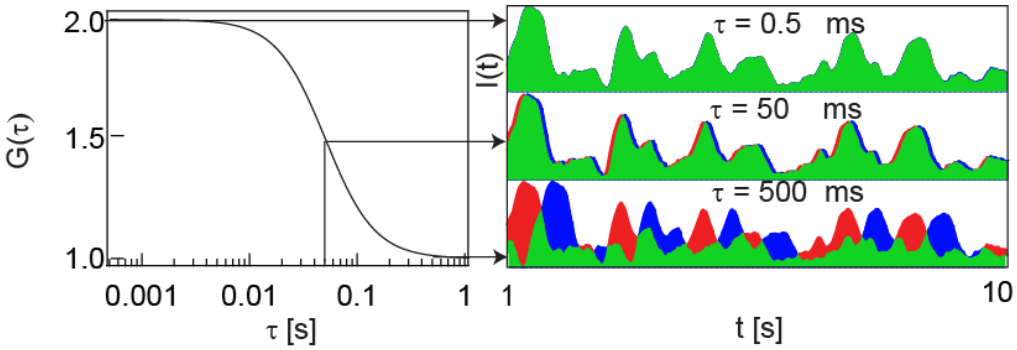

Fig. 2.3: Autocorrelation is a measure of self-similarity. The fluorescent trace is shown in red, the trace with an offset is shown in blue and the common area under the curve is shown in green. At smaller τ, the peaks overlap with themselves producing a very high amount of autocorrelation which is not the case at larger τ.

2.1.2 Theory of FCS

FCS is used to probe systems at thermal equilibrium. The statistical properties (e.g. mean and variance) do not vary with time for processes at thermal equilibrium. Such processes are referred to as stationary processes. A mathematical discussion of stationarity is found here[111]. Assuming stationarity[110] in such processes, the autocorrelation function (Eq. 2-1) can be redefined as,

$$G(\tau) = \frac{\langle I(t)I(t+\tau)\rangle}{\langle I(t)\rangle^2} = \frac{\langle I(0)I(\tau)\rangle}{\langle I(t)\rangle^2} \qquad \textbf{2-2}$$

Fluctuations are defined as deviations from the mean value. Mathematically $\delta I(t) = I(t) - \langle I(t) \rangle$. Using this definition, Eq. 2-2 can be rewritten as

$$G(\tau) = \frac{\left\langle \left(\delta I(0) + \langle I(t) \rangle \right) \left(\delta I(\tau) + \langle I(t) \rangle \right) \right\rangle}{\langle I(t) \rangle^2} \qquad \textbf{2-3}$$

$$= \frac{\left\langle \delta I(0)\delta I(\tau) + \langle I(t) \rangle \left(\delta I(\tau) + \delta I(0) \right) + \langle I(t) \rangle^2 \right\rangle}{\langle I(t) \rangle^2} = \frac{\langle \delta I(0)\delta I(\tau) \rangle}{\langle I(t) \rangle^2} + 1$$

The value of $\langle \delta I(0)\delta I(\tau) \rangle$ can be determined for various illumination profiles. The derivation is performed in 1D first and later can be extended for the three dimensions. Let the illumination be characterized by a Gaussian beam $\left(I(x) = I_0 e^{-\frac{2x^2}{w_0^2}} \right)$. Here *WO* is the e^{-2} radius of the Gaussian beam. The observed fluorescent intensity depends on the illumination profile and that of the concentration of the fluorophore *C*. The intensity at position *x* is related to the instantaneous concentration through $I(x,t) = q \int_{-\infty}^{\infty} I(x) C(x,t)\, dx$ where *q* is the efficiency of detection. The time averaged concentration is given by $\langle I(t) \rangle = \langle C \rangle q \int_{-\infty}^{\infty} I(x)\, dx = \langle C \rangle q I_0 w_0 \sqrt{\frac{\pi}{2}}$. Using the above definitions, the fluctuations at different positions *x* and *x'* can be written as

$$\delta I(x,0) = q \int_{-\infty}^{\infty} I(x) \delta C(x,0)\, dx \quad ; \quad \delta I(x',\tau) = q \int_{-\infty}^{\infty} I(x') \delta C(x',\tau)\, dx' \qquad \textbf{2-4}$$

Using Eq. 2-4, Eq. 2-3 can be rewritten as

$$\frac{\langle \delta I(0)\delta I(\tau)\rangle}{\langle I(t)\rangle^2} = \frac{2\langle \delta I(0)\delta I(\tau)\rangle}{\pi \langle C\rangle^2 q^2 {I_0}^2 w_0^2} \qquad \textbf{2-5}$$

$$= \frac{2\left\langle q^2 \int_{-\infty}^{\infty} I(x)\delta C(x,0)\,dx \int_{-\infty}^{\infty} I(x')\delta C(x',\tau)\,dx' \right\rangle}{\pi \langle C\rangle^2 q^2 {I_0}^2 w_0^2}$$

$$= \frac{2}{\pi \langle C\rangle^2 w_0^2} \int_{-\infty}^{\infty}\int_{-\infty}^{\infty} e^{-\frac{2x^2}{w_0^2}} e^{-\frac{2x'^2}{w_0^2}} \langle \delta C(x,0)\delta C(x',\tau)\rangle\, dx dx'$$

The value of $\langle \delta C(x,0)\delta C(x',\tau)\rangle$ can be determined by principles of mass transfer from position *x* and *x'* in a time of *τ*. This expression is a measure of correlation in concentration between those at lagtime of *0* with those later at a lagtime of *τ*. This is referred to in the literature as the diffusion propagator.

2.1.2.1 Derivation of diffusion propagator

The diffusion propagator can be derived based on Fick's laws of diffusion. The first law states that the flux (mass per unit area per unit time ($kgm^{-2}s^{-1}$) is proportional to the concentration gradient along the direction $\left(J \propto -\frac{\partial C}{\partial x} = -D\frac{\partial C}{\partial x} \right)$ where the constant of proportionality is defined as the diffusion coefficient (*D*) of the substance. It depends on the viscosity of the medium (*η*), temperature (*T*) and the radius of the diffusing substance (*R*) (assuming it to be a sphere) according to the Stokes Einstein's equation $\left(D = \frac{k_B T}{6\pi\eta R} \right)$ where k_B is the Boltzmann's constant (k_B = 1.38×10^{-23} JK^{-1}). The second law can be derived from the law of conservation of mass. The rate of change in concentration is equal to the flux gradient. Combining first and second laws, we get;

$$\frac{\partial C}{\partial t} = -\frac{\partial J}{\partial x} = D\frac{\partial^2 C}{\partial x^2} \qquad \textbf{2-6}$$

In cases, where there is directed movement along with diffusion, the flux gradient must be modified by the addition of the flux due to the movement along with

the flux due to the diffusion. The flux is a product of concentration and velocity in the case of directed movement $\left(J = vC\right)$;

$$\frac{\partial C}{\partial t} = -\frac{\partial J}{\partial x} = D\frac{\partial^2 C}{\partial x^2} - v\frac{\partial C}{\partial x} \qquad \textbf{2-7}$$

This yields the generalized advection-diffusion equation (In the literature, this is also referred to as convection-diffusion equation). For convenience, the notations can be rewritten using the following convention. The temporal and spatial derivatives are indicated by subscripts of *t* and *x* respectively.

$$C_t = DC_{xx} - vC_x \qquad \textbf{2-8}$$

The partial differential equation can be solved by using Fourier transforms. Converting from *x* space to reciprocal space (k_r here);

$$\widehat{C_t} = ik_r D\widehat{C_x} - ik_r v\widehat{C} = -k_r^2 D\widehat{C} - ik_r v\widehat{C} = -\left(k_r^2 D + ik_r v\right)\widehat{C} \qquad \textbf{2-9}$$

where $\widehat{C}$ represents the Fourier transform of the concentration function (concentration in inverse space). The above simplification can be made by using properties of the Fourier transform as stated in Appendix 1. Fourier transformation has reduced the partial differential equation into a linear differential equation in time; $\widehat{C} = \widehat{C}\left(0\right)e^{-\left(k^2 D + ik_r v\right)t}$. In order to complete the derivation, initial conditions need to be specified. An instantaneous point source at $t=t_0$ and $x=x_0$ can be modeled using a Dirac Delta function[112]. Hence $C\left(0\right) = \delta\left(x - x_0\right), \widehat{C}\left(0\right) = \frac{e^{ik_r x_0}}{\sqrt{2\pi}}$

$$\widehat{C} = \frac{e^{ikx_0 - \left(k_r^2 D + ik_r v\right)t}}{\sqrt{2\pi}} \qquad \textbf{2-10}$$

Taking the inverse Fourier transform: $C\left(t\right) = \frac{e^{-\frac{\left(x - x_0 + vt\right)^2}{4Dt}}}{\sqrt{4\pi Dt}}$.

Substituting the above term in Eq. 2-5, we get

$$\frac{\langle \delta I(0)\delta I(\tau)\rangle}{\langle I(t)\rangle^2} = \frac{2}{\pi \langle C\rangle w_0^2 \sqrt{4\pi D\tau}} \int_{-\infty}^{\infty}\int_{-\infty}^{\infty} e^{-\frac{2x^2}{w_0^2}} e^{-\frac{2x'^2}{w_0^2}} e^{-\frac{(x-x'+v\tau)^2}{4D\tau}}\, dxdx' \qquad \textbf{2-11}$$

$$= \frac{e^{-\left(\frac{v\tau}{\sqrt{4D\tau+w_0^2}}\right)^2}}{\langle C\rangle \sqrt{\pi}\sqrt{4D\tau+w_0^2}}$$

The details of the integration are provided in Appendix 2. The equation can be rewritten in 3 dimensions to yield the final solution of the autocorrelation function.

$$G(\tau) = 1 + \frac{e^{-\frac{(v_x\tau)^2+(v_y\tau)^2}{4D\tau+w_{xy}{}^2} - \frac{(v_z\tau)^2}{4D\tau+w_z{}^2}}}{\langle C\rangle \pi^{\frac{3}{2}} \left(4D\tau + w_{xy}{}^2\right)\sqrt{4D\tau + w_z{}^2}} \qquad \textbf{2-12}$$

Eq. 2-12 calculates the autocorrelation for systems exhibiting diffusion and flow. In the case of flow process, D=0 and in the case of diffusion, v_x=v_y=v_z=0.

$$G(\tau)_{flow} = 1 + \frac{1}{2\sqrt{2}\langle C\rangle V_c} e^{-\left(\frac{(v_x\tau)^2+(v_y\tau)^2}{w_{xy}{}^2} + \frac{(v_z\tau)^2}{w_z{}^2}\right)} \qquad \textbf{2-13}$$

where V_c is the confocal volume and is evaluated below.

$$V_c = \int_{-\infty}^{\infty}\int_{-\infty}^{\infty}\int_{-\infty}^{\infty} e^{-2\left(\frac{(x^2+y^2)}{w_{xy}{}^2} + \frac{z^2}{w_z{}^2}\right)} dxdydz = \left(\frac{\pi}{\sqrt{2}}\right)^{\frac{3}{2}} w_{xy}{}^2 w_z = \left(\frac{\pi}{\sqrt{2}}\right)^{\frac{3}{2}} w_{xy}{}^3 k \qquad \textbf{2-14}$$

where k is a measure of the ellipticity of the confocal volume. It is the ratio of axial length to the radial width $\left(k = \frac{w_z}{w_{xy}}\right)$.

$$G(\tau)_{diffusion} = 1 + \frac{1}{\langle C\rangle \pi^{\frac{3}{2}} w_{xy}{}^2 w_z \left(\frac{4D\tau}{w_{xy}{}^2}+1\right)\sqrt{\frac{4D\tau}{w_z{}^2}+1}} \qquad \textbf{2-15}$$

$$= 1 + \frac{1}{2\sqrt{2}\langle C\rangle V_c \left(\frac{\tau}{\tau_D}+1\right)\sqrt{\frac{\tau}{k^2\tau_D}+1}}$$

where $\tau_D = \frac{{w_{xy}}^2}{4D}$ is defined as diffusion time, the average transit time taken to travel the observation volume.

2.1.2.2 Derivation of observation volume

Substituting $\tau=0$ in Eq. 2-3*;*

$$G(0) = 1 + \frac{\left\langle (\delta I(0))^2 \right\rangle}{\left\langle I(t) \right\rangle^2} = 1 + \frac{\int_{-\infty}^{\infty}\int_{-\infty}^{\infty} I(r) I(r') \left\langle \delta C(r,0)\delta C(r',0) \right\rangle dr dr'}{\left\langle C \right\rangle^2 \left(\int_{-\infty}^{\infty} I(r)\, dr \right)^2} \qquad \textbf{2-16}$$

We are dealing with dilute solutions at equilibrium; hence the concentrations at two different points in space are independent of each other and not correlated to each other. Hence the expression $\left\langle \delta C(r,0)\delta C(r',0) \right\rangle$ is equal to $\left\langle C \right\rangle \delta(r-r')$.

$$G(0) = 1 + \frac{\int_{-\infty}^{\infty}\int_{-\infty}^{\infty} I(r) I(r') \delta(r-r')\, dr dr'}{\left\langle C \right\rangle \left(\int_{-\infty}^{\infty} I(r)\, dr \right)^2} = 1 + \frac{\int_{-\infty}^{\infty} \left(I(r) \right)^2 dr}{\left\langle C \right\rangle \left(\int_{-\infty}^{\infty} I(r)\, dr \right)^2} \qquad \textbf{2-17}$$

$$= 1 + \frac{1}{\left\langle C \right\rangle V_{eff}} = 1 + \frac{1}{N}$$

where V_{eff} is the effective volume of observation in FCS and N is the number of particles in the observation volume. Thus V_{eff} is defined as

$$V_{eff} = \frac{\omega_1^2}{\omega_2} \quad \omega_n = \int_{-\infty}^{\infty} \left(I(r) \right)^n dr \qquad \textbf{2-18}$$

$$\omega_1 = \int_{-\infty}^{\infty}\int_{-\infty}^{\infty}\int_{-\infty}^{\infty} e^{-2\left(\frac{\left(x^2+y^2\right)}{{w_{xy}}^2} + \frac{z^2}{{w_z}^2} \right)} dx dy dz = \left(\frac{\pi}{\sqrt{2}} \right)^{\frac{3}{2}} {w_{xy}}^2 w_z = \left(\frac{\pi}{\sqrt{2}} \right)^{\frac{3}{2}} {w_{xy}}^3 k$$

$$\omega_2 = \int_{-\infty}^{\infty}\int_{-\infty}^{\infty}\int_{-\infty}^{\infty} e^{-4\left(\frac{\left(x^2+y^2\right)}{{w_{xy}}^2} + \frac{z^2}{{w_z}^2} \right)} dx dy dz = \left(\frac{\pi}{4} \right)^{\frac{3}{2}} {w_{xy}}^2 w_z = \left(\frac{\pi}{4} \right)^{\frac{3}{2}} {w_{xy}}^3 k$$

$$V_{eff} = \frac{\left(\left(\frac{\pi}{2}\right)^{\frac{3}{2}} kw_{xy}^3\right)^2}{\left(\frac{\pi}{4}\right)^{\frac{3}{2}} kw_{xy}^3} = \pi^{\frac{3}{2}} kw_{xy}^3 = 2^{\frac{3}{2}}\left(\frac{\pi}{2}\right)^{\frac{3}{2}} kw_{xy}^3 = 2^{\frac{3}{2}} V_c \qquad \textbf{2-19}$$

It has to be noted that N is the number of particles in the effective observation volume and not the particles only in the confocal volume. Particles outside the confocal volume as well contribute to the detected fluorescence. Eq. 2-17 shows that V_{eff} can be determined by setting τ=0 in the expression for ACF.

2.2 Image Correlation Spectroscopy (ICS)

In Image Correlation Spectroscopy[56], the images are spatially instead of temporally correlated as in FCS. The derivation of the spatial autocorrelation function $r(\xi)$ in ICS is similar to FCS except the conspicuous absence of the diffusion propagator term. ξ is the lagspace analogous to lagtime in FCS.

The autocorrelation is typically calculated using Fourier transforms by means of Wiener-Khinchin theorem[113]. The Wiener-Khinchin theorem states that the power spectral density of a wide-sense stationary process is given by the Fourier transform of the autocorrelation. The power-spectral density is defined as the product of the Fourier transforms of the process and its complex conjugate. The assumptions of the Wiener-Khinchin theorem holds good here since the processes we intend to observe are strictly stationary. Wide-sense stationarity is a subset of strictly stationary.

$$r(\xi) = F^{-1}\left(F_x\left(I(x)\right) \times F_x^*\left(I(x)\right)\right) \qquad \textbf{2-20}$$

The intensity can be assumed to be a Gaussian function. The Fourier transform of a Gaussian function is another Gaussian.

$$I(x) = e^{-\frac{2x^2}{w_0^2}} \Rightarrow \quad F_x\left(I(x)\right) = \sqrt{\frac{\pi w_0^2}{2}} e^{-\frac{(\pi\xi w_0)^2}{2}} \Rightarrow r(\xi) = \frac{\pi w_0^2}{2} F^{-1}\left(e^{-(\pi\xi w_0)^2}\right) \qquad \textbf{2-21}$$

$$\Rightarrow r(\xi) = \frac{\pi w_0^2}{2} e^{-\left(\frac{\xi}{w_0}\right)^2}$$

$$r(\xi,\eta) = r_0 e^{-\left(\frac{\xi^2+\eta^2}{w^2}\right)} + r_\infty \qquad \textbf{2-22}$$

The above derivation was carried out in 1D, extended to 2D which is typically the case. By fitting to a 2-dimensional correlation function, the value of the PSF-w_0, can be calculated. r_0 is the amplitude and like FCS, it is related to the number of particles, ξ and η are lag distances in the x and y directions respectively. r_∞ is the correlation at longer lag distances.

2.3 Imaging FCS-Illumination schemes

The heart of Imaging FCS lies in the illumination scheme to create the small observation volume. Fluctuations are difficult to record in a large volume. The various ways to create a small observation volume include confocal, two photon, TIRF, variable angle TIRF and SPIM. The last three methods (TIRF, variable angle TIRF and SPIM) were used in this thesis and are discussed in detail here. In all the three cases, the z sectioning is provided by the illumination whereas the x, y sectioning is provided by the pixels of the electron multiplying CCD (EMCCD) camera in the detection. A detailed description of EMCCDs is provided at Sec. 2.5.3.

2.3.1 Total Internal Reflection

Whenever light passes from an optically denser medium to an optically rarer medium, it moves away from the normal to surface of separation between the media. When the angle of incidence exceeds the critical angle, the entire light gets reflected at the interface in the denser medium. This phenomenon, leads to the creation of an exponentially decaying wave referred to as the evanescent wave in the optically rarer medium providing z sectioning. This is sufficient to illuminate the molecules on the cell-membrane as seen in Fig. 2.4 B. The advantage of using this method is that it reduces the background noise due to the rest of the cell since only the cell-membrane is illuminated. FCS performed using Total Internal Reflection is referred to as TIR-FCS. A theoretical discussion on TIRF is provided below.

2.3.1.1 Theory

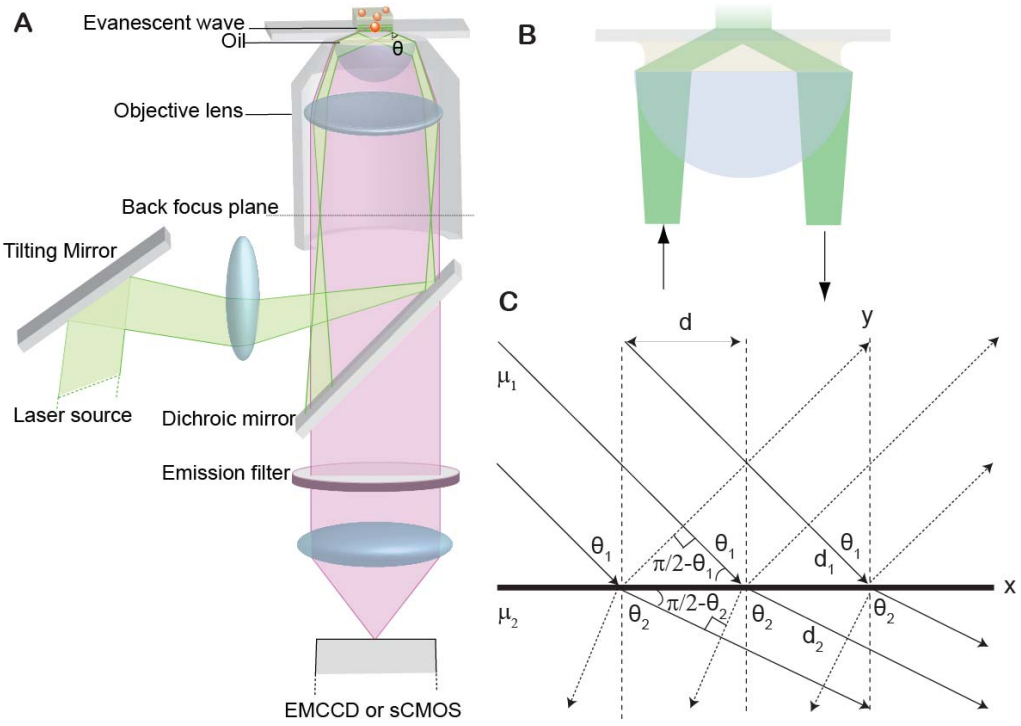

Fig. 2.4: Total Internal Reflection: Principles and Instrumentation. A is a schematic of the ITIR/IVA-FCS set up. B is a schematic showing the evanescent wave and the super-critical angle illumination in ITIR-FCS. C shows the plane waves and their wave fronts for a mathematical description of total internal reflection. A is an adaptation from an original figure prepared by Ping Liu from the lab.

Consider a light wave travelling from an optically denser medium with refractive index μ_1 (at an angle of θ_1 to the normal) to an optically rarer medium with refractive index μ_2. The rays are refracted at the interface. Let θ_2 be the angle of refraction. The plane waves are shown in solid lines and the wavefronts are shown in dashed lines in Fig. 2.4 C. The geometry from the same suggests that,

$$\cos\left(\frac{\pi}{2}-\theta_1\right)=\frac{d_1}{d} \quad \cos\left(\frac{\pi}{2}-\theta_2\right)=\frac{d_2}{d} \qquad \textbf{2-23}$$

d_1 and d_2 are distances travelled in medium μ_1 and μ_2 respectively. Hence they can be related to the velocity of light in the media (v_1 and v_2). The velocity of light in individual media can be obtained from the refractive indices of the media.

$$\frac{d_1}{\cos\left(\frac{\pi}{2}-\theta_1\right)}=\frac{d_2}{\cos\left(\frac{\pi}{2}-\theta_2\right)} \Rightarrow \frac{v_1 t}{\sin\theta_1}=\frac{v_2 t}{\sin\theta_2} \Rightarrow \frac{c}{\mu_1 \sin\theta_1}=\frac{c}{\mu_2 \sin\theta_2} \qquad \textbf{2-24}$$

Hence the law of refraction can be stated as $\mu_1 \sin\theta_1 = \mu_2 \sin\theta_2$. This is referred as Snell's law. It can be rewritten as $\theta_2 = \sin^{-1}\left(\frac{\mu_1}{\mu_2}\sin\theta_1\right)$. Since, $\mu_1 > \mu_2$, θ_2 is always greater than θ_1. Hence the wave always moves away from the normal in the case when it is travelling from denser to rarer medium and vice versa.

Mathematically, the arcsin function *($\sin^{-1} x$)*, is defined only for -1≤ x≤ 1. For, values of x>1, the function is not defined. Hence $\frac{\mu_1}{\mu_2}\sin\theta_1 \le 1$. The value of the angle of incidence for which $\theta_2=\pi/2$ (sin π/2=1), is referred to as critical angle or grazing angle. At the critical angle ($\theta_c = \sin^{-1}\left(\frac{\mu_2}{\mu_1}\right)$), the refracted ray grazes the interface of separation between the two media. For angles greater than the critical angle, the refracted ray is imaginary and the entire light gets reflected off the interface and this phenomenon is referred to as total internal reflection. Light is an electromagnetic radiation and hence at an interface, electrical and magnetic fields cannot be discontinuous. This leads to the creation of an exponentially decaying, standing wave called evanescent wave extending into the optically rarer medium. The penetration depth of the evanescent wave can be derived from the principles of electromagnetic theory. Consider the propagating electric field in the rarer medium with wave vector $\vec{k}$ $\left(|k| = \frac{2\pi}{\lambda}\right)$, angular frequency ω. In the 2D case, as seen in Fig. 2.4 C,

$$\overrightarrow{E_t} = \overrightarrow{E_{0t}} e^{i\left(\vec{k}.\vec{r}-\omega t\right)} = \overrightarrow{E_{0t}} e^{i\left(k_{2_x}x + k_{2_y}y - \omega t\right)} \qquad \textbf{2-25}$$

From the laws of trigonometry,

$$\overrightarrow{E_t} = \overrightarrow{E_{0t}} e^{i\left(k_2\cos\left(\frac{\pi}{2}-\theta_2\right)x + k_2\sin\left(\frac{\pi}{2}-\theta_2\right)y - \omega t\right)} = \overrightarrow{E_{0t}} e^{i\left(k_2\sin(\theta_2)x + k_2\cos(\theta_2)y - \omega t\right)} \qquad \textbf{2-26}$$

$$= \overrightarrow{E_{0t}} e^{i\left(k_2\sin(\theta_2)x + k_2 y\sqrt{1-\sin^2(\theta_2)} - \omega t\right)}$$

Applying Snell's law (2-24) to Eq. 2-26,

$$\overrightarrow{E_t} = \overrightarrow{E_{0t}} e^{i\left(k_2 \frac{\mu_1}{\mu_2}\sin(\theta_1)x + k_2 y\sqrt{1-\left(\frac{\mu_1}{\mu_2}\right)^2 \sin^2(\theta_1)} - \omega t\right)} \quad \textbf{2-27}$$

Eq. 2-27 describes the propagating electric field in the rarer medium for any plane wave at an angle of incidence θ_1 to the normal. In the case of total internal reflection, the term $\sqrt{1-\left(\frac{\mu_1}{\mu_2}\right)^2 \sin^2\theta_1}$ is imaginary since $\sin\theta_1 > \frac{\mu_2}{\mu_1}$. Hence

$$\overrightarrow{E_t} = \overrightarrow{E_{0t}} e^{i\left(k_2 \frac{\mu_1}{\mu_2}\sin(\theta_1)x + ik_2 y\sqrt{\left(\frac{\mu_1}{\mu_2}\right)^2 \sin^2(\theta_1) - 1} - \omega t\right)} = \overrightarrow{E_{0t}} e^{i\left(k_2 \frac{\mu_1}{\mu_2}\sin(\theta_1)x - \omega t\right)} e^{-yk_2\sqrt{\left(\frac{\mu_1}{\mu_2}\right)^2 \sin^2(\theta_1) - 1}} \quad \textbf{2-28}$$

$$= \overrightarrow{E_{0t}} e^{i\left(k_2 \frac{\mu_1}{\mu_2}\sin(\theta_1)x - \omega t\right)} e^{-y\frac{2\pi}{\lambda_2}\sqrt{\left(\frac{\mu_1}{\mu_2}\right)^2 \sin^2(\theta_1) - 1}} = \overrightarrow{E_{0t}} e^{i\left(k_2 \frac{\mu_1}{\mu_2}\sin(\theta_1)x - \omega t\right)} e^{-y\frac{2\pi}{\lambda}\sqrt{\mu_1^2 \sin^2(\theta_1) - \mu_2^2}}$$

where λ and λ_2 are the wavelengths of light in vacuum and the rarer medium respectively. In the case of $\theta_1 > \theta_c$, the electric field propagates in the x direction and is non-propagating in the y direction. The depth of penetration of the evanescent wave in the y direction can be determined by calculating the intensity from the electric field.

$$I = \left|\overrightarrow{E_{ty}}\right|^2 = I_0 e^{-y\frac{4\pi}{\lambda}\sqrt{\mu_1^2 \sin^2(\theta_1) - \mu_2^2}} = I_0 e^{-\frac{y}{d_p}} \quad \textbf{2-29}$$

The penetration depth (d_p) is defined as the distance where the intensity of the evanescent decays to e^{-1} times the intensity at the interface and it is given by Eq. 2-30.

$$d_p = \frac{\lambda}{4\pi\sqrt{\mu_1^2 \sin^2(\theta_1) - \mu_2^2}} = \frac{\lambda}{4\pi\sqrt{NA^2 - \mu_2^2}} \quad \textbf{2-30}$$

The term $\mu_1 \sin(\theta_1)$ is referred to as the numerical aperture of the objective of the microscope (NA). The numerical aperture is a dimensionless number and is a measure of the light gathering ability of the microscopy. It is related to the resolving power of the objective. The resolution is derived from the diffraction limit. The

resolution is given by the formula $\frac{\lambda}{2NA}$. Hence, for higher resolution, higher *NA* objectives are beneficial. The value of *NA* can be increased by increasing μ_1 or θ_1. The maximum value of θ_1 is $\pi/2$. Hence the maximum value of $\sin(\theta_1)$ is 1. It has to be remembered that, with increasing θ_1, the objective has to be very close to the sample and $\theta_1 = \pi/2$ would be a lens of focal length zero which is not possible. Hence, due to practical limitations, $\sin(\theta_1)$ is 0.95. So, a $NA>1$ can never be achieved if the medium is air (referred to as dry objective).

In order to increase the *NA*, wet objectives are used; a drop of water or oil with refractive index of 1.33 and 1.53 respectively is placed over the objective. It has to be remembered that the above considerations are from conventional microscopy. In the case of TIRF, in order for the penetration depth to be a real number, the *NA* must be greater than the refractive index of the rarer medium. Typically, TIRF imaging is performed in a glass-water interface; hence the numerical aperture of the objective must be greater than the refractive index of water (1.33). Hence, typically, TIRF is performed using an oil immersion objective with 1.45 or higher N.A. The refractive index of the oil must match the refractive index of the glass in the objective lens. Mismatches in the refractive index will lead to spherical aberration. For a wavelength of 514 nm, 1.45 *NA*, glass-water interface, Eq. 2-30 is evaluated to be 70 nm.

2.3.2 Variable angle FCS

Recently, other related illumination schemes with sectioning capability have been introduced for imaging and FCS. Variable angle epi-fluorescent Microscopy (VAEM)[114] and Highly Inclined and Laminated Optical Sheet (HILO) microscopy were utilized for imaging of plant cells and single molecule imaging, respectively[115-116].

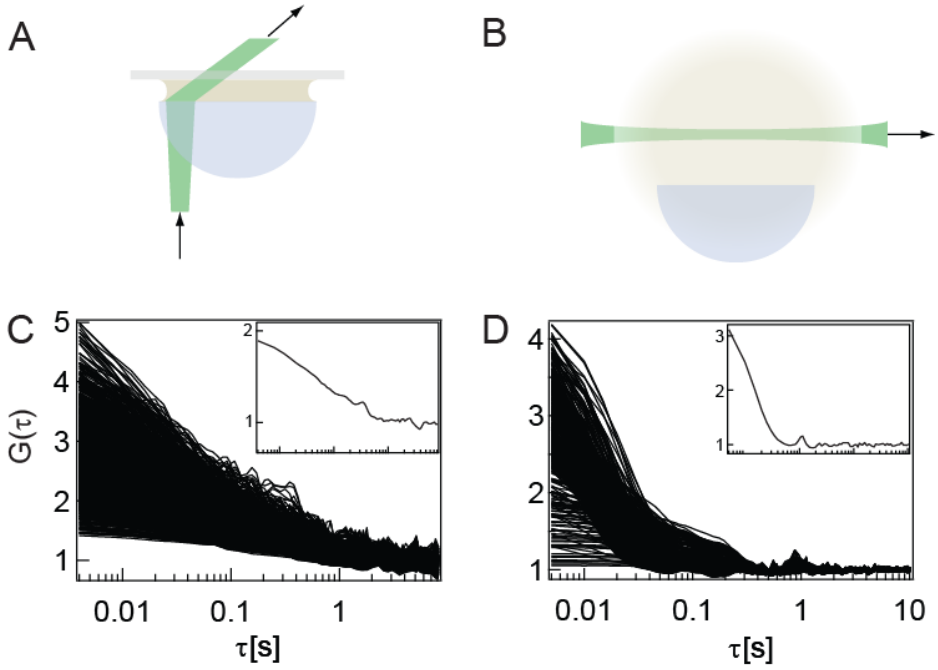

Fig. 2.5: Illumination schemes in camera based FCS. IVA-FCS is performed just by decreasing the angle of incidence to values less than the critical angle leading to selective excitation in the bulk sample as seen in A. B is a schematic of SPIM illumination where the fluorophores are excited by a diffraction limited light sheet. A and B are capable of exciting fluorophores in a physiologically relevant 3D environment inside biological samples. C is a set of representative autocorrelations from beads diffusing in solution. D was obtained by recording fluctuations of fluroscence of beads injected into the bloodstream of a zebrafish embryo. The dataset in D was a kind gift from Dr. Shi Xianke from the lab.

Critical angle illumination based FCS was demonstrated on fluorescent beads[97]. At sub-critical, oblique angles of illumination, the refracted light is just above the surface of separation sufficient to illuminate fluorophores away from the surface in the bulk sample. The use of sub-critical angles reduces the background considerably and provides volume isolation in the bulk suitable to perform FCS. Performing FCS in such illumination conditions is referred to as IVA-FCS (Imaging Variable Angle-FCS). IVA-FCS does not need any separate add-on apparatus to a TIRF microscope. In comparison with ITIR-FCS, IVA-FCS has the advantage of increased penetration depth into bulk of the sample away from the surface of separation.

2.3.3 Single Plane Illumination Microscopy

In SPIM-FCS, the volume isolation is provided by a diffraction-limited light sheet created using a cylindrical lens. Cylindrical lenses focus the light onto a line unlike the more commonly used spherical lenses which focus the light onto a single point. This facilitates selective illumination of only a thin layer of the sample away from the cover slide[95] which lies in the focal plane of the detection objective. The thickness of the light sheet can be varied by changing the numerical aperture of the objective used. Since these techniques only illuminate the parts of the sample which are observed[95, 99], the background and cross-talk between the detection elements is greatly reduced making FCS in an imaging mode possible even on live-cells and within living organisms.

2.4 Imaging FCS-experimental set up

The measurements were performed using two different objective type TIRF microscopes built around inverted microscopes with high *NA* objectives as shown in Fig. 2.4 A. The fluorophores were excited with laser light from a dual color laser source after passing through a suitable excitation filter. Light was directed to an EMCCD mounted on the left port by a dichroic mirror and emission filter. The details of the instrumentation are provided in Table 2-1. A maximum angle of 72.5° was achievable using the systems since $NA<0.95$. The critical angle for the glass-water interface is 61.7°. This provides a 10° range to perform TIRF. A description about image acquisition is given in Sec. 2.5.3. Spatial and temporal correlations were calculated from image stacks acquired by the EMCCD camera. 10000 frames were obtained on a suitable ROI with the minimum possible acquisition time of the EMCCD camera.

Table 2-1: Characteristics of TIRF instruments used in the thesis

	Set up-I	**Set up-II**
Microscope	Axiovert 200M, Carl Zeiss, Singapore	IX-71, Olympus, Singapore
Objective	Oil, 60X, NA 1.45, TIRFM, Olympus, Singapore	Oil, 100X, NA 1.45, TIRFM, Olympus, Singapore
Laser	Dual Calypso, Cobolt, Photonitech Pvt Ltd, Singapore, λ_{em}=491, 532 nm	Dual color air-cooled ion, Spectra-Physics, 185-F02, CA, USA, λ_{em}= 488, 514 nm
Dichroic mirror	560DRLP, Omega, Brattleboro, VT, USA	524DRLP, Olympus, Singapore
Emission filter	595AF60, Omega	524LP, Olympus
Excitation filter	XL08, Omega	FF01-513/17-25 Semrock, Rochester, NY, USA
EMCCD	Cascade II: 512, Photometrics, Tucson, AZ, USA	Andor iXON 860
Acquisition software	Metamorph, Universal Imaging Corporation, PA, USA	Andor Solis (Ver: 4.9.30000.0)
Chip Size	8.2×8.2 mm^2	3.1×3.1 mm^2
Pixel size	16×16 μm^2	24 x 24 μm^2
	Image Plane: 284×284 nm^2	Image Plane: 240×240 nm^2
Pixels	512×512	128×128
Best time resolution	4 ms for 21×21 pixels ROI	0.56 ms for 21×21 pixels ROI
Maximum angle	72.5º	72.5º

2.5 Imaging FCS-detection

Detection in Imaging FCS is achieved by the usage of fast and sensitive cameras. Two different sensing technologies are available today: CCD and CMOS.

2.5.1 CCD

As suggested by the name, the basic principle of charge coupled detector (CCD) lies in the charge coupling of neighboring pixel units so that they can be transferred and read out serially. There are two parts in a chip, a photoactive region and a storage region in order to increase the frame rate of the device. After capturing an image, the data is transferred to the storage part by charge coupling.

Depending on the location of the storage region, the CCDs are classified into interline CCD and frame transfer CCD. In an interline CCD, every second column is used for storage. The data from active columns is passed on to the storage column placed next to it. Every pixel in each of the storage column is read serially later. In a frame transfer region, a half of the chip is designated for storage since an entire frame is transferred in a single shot. From the storage area, the image is read one column at a time. An entire column of data is transferred to readout registers and then each pixel in this column is read serially. Once, a particular column is read, the data from the next column is read by the readout registers.

The advantage of using interline or frame transfer CCDs is that the data can be read from the storage region while another image can be captured by the active pixels. The configuration (active area and a storage area) increases the frame rate when compared to full frame CCDs which do not have a specific storage area.

2.5.2 ICCD

CCD technology was originally not used for single molecule detection. The next variant in CCD technology was intensified CCD (ICCD) camera, in which the signal passes through an amplification step using a micro channel plate. The incoming photons hit a photocathode where they are converted to electrons. Later,

these electrons move through a multi channel plate where multiplication occurs and hit a phosphor screen where they are converted to photons again and they strike the CCD chip. This technology was not used for single molecule detection because of the lower quantum efficiency (QE) that was offered by it. The presence of a photocathode reduces the QE in ICCD. Further, this cannot be used for Imaging FCS because of the loss in spatial resolution. During the movement in the multi channel plate, secondary electrons are created. Hence the electrons from one pixel may create secondary electrons in neighboring pixels as well leading to an increase in cross talk and a loss in spatial resolution.

2.5.3 EMCCD

Unlike a CCD, electron multiplying CCD (EMCCD) cameras have an amplification step after the readout step (Fig. 2.8). Amplification happens due to impact ionization of electronic charge. Every pixel in each line is read serially after letting the signal in each to pass through a multiplication register. A device is single molecule sensitive if the photons from single molecules are differentiable from the background. This was made possible by the introduction of cooled EMCCDs. Cooling the EMCCD to -80°C by thermoelectric pump elements incorporating Peltier effect, reduces the thermal noise. The second way to reduce the noise was by the incorporation of the electron multiplying step of impact ionization similar to that observed in the APD. The third reason for increased sensitivity is back illumination. In the conventional architecture referred to as front illumination, the photo detection unit is buried in the silicon chip. This leads to a loss in QE. There is further reduction by covering the active area with connection circuitry. In the case of back illumination, the light is allowed to fall from the back side by removing some of the bulk silicon in which the detection unit is embedded and the circuitry is behind the active area. This increases the quantum efficiency (QE) when compared to the front illuminated EMCCD. The QE of a front illuminated EMCCD is 50% while that of the back illuminated is 95%.

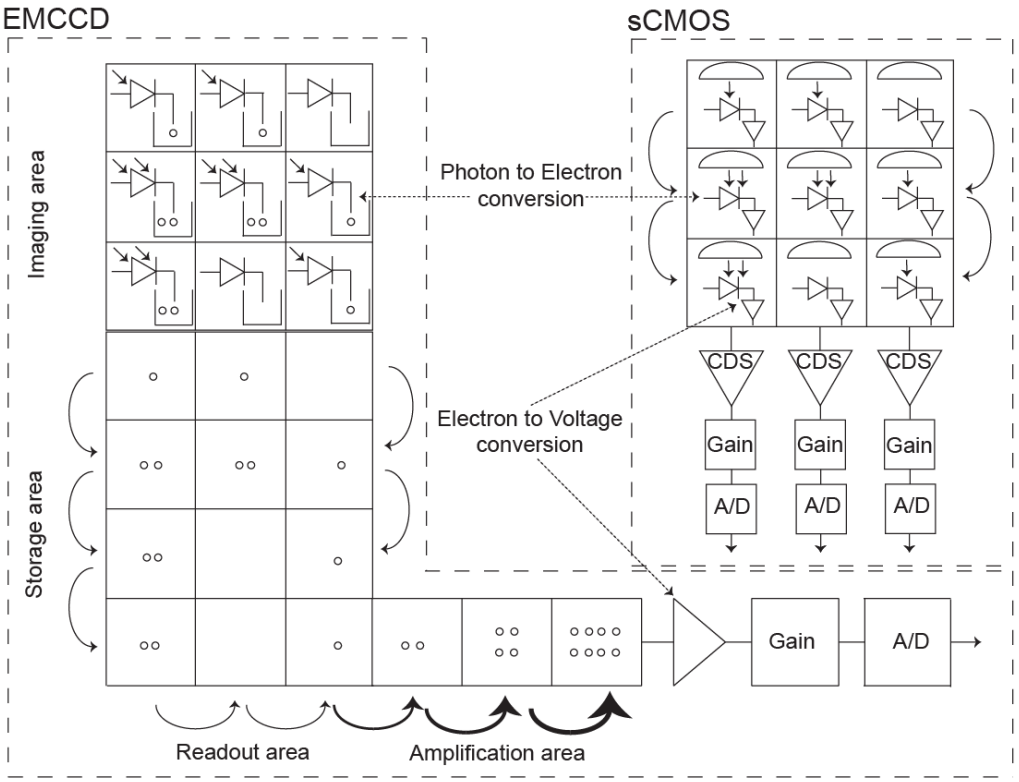

Fig. 2.6: Schematic of EMCCD and sCMOS architecture. The major differences between EMCCD and sCMOS in the readout and amplification are evident here. The figure is an adaptation of schematics of EMCCD and sCMOS provided here[117-118].

2.5.4 sCMOS

Scientific CMOS (sCMOS) is based on a complementary metal oxide semiconductor (CMOS) architecture. CMOS offers superior frame rates when compared to CCD and a very large field of view. Current CMOS can provide up to 4 Megapixel on a chip. The higher frame rate is possible since the data is read in a column parallel arrangement. CMOS sensors suffer from an inherent variability and smaller fill factor which is a ratio of the active refractive area of the chip to the total area of the chip. Unlike a CCD, the electronic signal obtained after the photon impingement are immediately converted to a voltage and amplified individually in each pixel. Each pixel is fitted with an individual amplifier and this leads to an inherent variability in the signal.

Apart from that, since each pixel has to be manufactured with an amplifier attached to it, the contact area for the photons of the silicon substrate is reduced. Both the factors contribute to lower signal to noise ratio. This was modified by the

introduction of scientific CMOS (sCMOS) cameras. They are also referred to as CCD/CMOS hybrid cameras. The fill factor is resolved by the use of micro lenses which focus the light on to the active area of the substrate. The pixels show variability since each of them has different amplifiers. This was resolved by the use of correlated double sampling (CDS). In CDS, at each step, the value of the pixel is set to a predetermined reference value and then the photon impingement is bound to occur leading to signal. The value of signal is the difference between the value of the reference and readout. In short, apart from differences in manufacturing and architecture, sCMOS offers parallel readout while EMCCD offers serial readout and as a result, sCMOS offers higher frame rates than EMCCD. In a nutshell, sCMOS offers smaller pixel sizes and higher frame rates while EMCCD offers higher sensitivity.

2.5.5 Characterization of noise in EMCCD and sCMOS

The noise sources can be classified into those which are common to EMCCD and sCMOS and those which are not. Shot noise, readout noise, dark noise, and A/D conversion noise are common noise sources in EMCCD and sCMOS whereas the multiplication step contributes to the noise only in the EMCCD.

The shot noise present in both cameras is due to inherent statistical fluctuations in the amount of photons detected. This can be modeled by a Poisson distribution with its mean equal to its variance. Hence the SNR is $\sqrt{N}$. It is dependent upon the QE of the detector. As a result, the back illuminated and front illuminated devices differ in the shot noise. Even an ideal detector is shot noise limited, hence it would be sufficient, if the detector has lower readout and dark noise. Any device becomes shot noise limited at very low light levels. The read out noise happens due to higher frame rates and higher number of pixels being sampled. This can occur at two stages, in the conversion of electrons to a voltage signal or at the analog to digital converter. The read out noise can be controlled by increasing the

gain in an EMCCD. sCMOS has higher readout noise (injection of unwanted electrons to the signal) when compared to EMCCD.

The dark noise is due to the thermal energy in the detector. This can be controlled by cooling the EMCCD. There is another noise in CCD called CIC which is clock induced charge or spurious noise. This is due to random single electrons generated during the charge coupled transfer. This is present in all CCDs but is important only in EMCCD since in conventional CCDs, this would be buried in the dark noise due to the absence of cooling. The last source of noise is the multiplicative noise. The last step in an EMCCD, the electron multiplication process due to impact ionization, is a stochastic process and leads to an inherent noise in the signal. This has been mathematically studied[119]. This is similar to the multiplication noise in an avalanche photodiode[120-121].

2.5.5.1 Multiplicative noise in EMCCD

The excess noise factor[119] is defined in EMCCD literature as $F^2 = \frac{\sigma_{out}^2}{M^2 \sigma_{in}^2}$

where M is the mean gain, σ_{in}^2 and σ_{out}^2 are the variances of the input and output signal respectively. In the case that there is no noise added by the multiplication process, the value of F is 1. In reality, the stochastic multiplication leads to the addition of noise and hence the value of F needs to be quantitated. Let $n\left(\sigma_n^2\right)$ and m $\left(\sigma_m^2\right)$ be the mean (variance) number of electrons into and out of a single multiplication stage. The gain (g) is defined as m/n. Assuming g is independent of n, and applying rules of error propagation, we get $\left(\frac{\sigma_m}{m}\right)^2 = \left(\frac{\sigma_n}{n}\right)^2 + \left(\frac{\sigma_g}{g}\right)^2$. If α be the probability of multiplication, $\alpha = g - 1$. The gain can be treated as a binomial process. Hence the variance in number of electrons added $\sigma_{added}^2 = n\alpha\left(1-\alpha\right)$. The variance of gain can be rewritten using the relation above as $\sigma_g^2 = \frac{\sigma_{added}^2}{n^2} = \frac{\alpha\left(1-\alpha\right)}{n}$

. Hence the variance at the end of every stage can be rewritten as $\sigma_m^2 = (1+\alpha)^2 \sigma_n^2 + n\alpha(1-\alpha)$. Let there be N multiplication steps in the EMCCD. Let S_{in} and S_{out} be the input and output signal respectively. Let the signal be shot noise limited. Hence the variance of S_{in} is equal to the signal itself. The variance at the end of every stage can be computed by applying the formula above sequentially.

$$\begin{aligned} N=1 \quad & \sigma_{out}^2 = S_{in}\left(1+\alpha^2+2\alpha+\alpha-\alpha^2\right) = S_{in}(1+3\alpha) \\ N=2 \quad & \sigma_{out}^2 = S_{in}(1+\alpha)\left[(1+\alpha)(1+3\alpha)+\alpha(1-\alpha)\right] \\ & = S_{in}(1+\alpha)\left(2\alpha^2+5\alpha+1\right) \end{aligned} \qquad \textbf{2-31}$$

This can be generalized for any value of N.

$$\sigma_{out}^2 = S_{in}(1+\alpha)^{N-1}\left(2(\alpha+1)^N+\alpha-1\right) = \frac{S_{in}M(2M+\alpha-1)}{\alpha+1} \qquad \textbf{2-32}$$

where $M = (1+\alpha)^N$. Hence the value of excess noise factor can be rewritten as

$$F^2 = \frac{\sigma_{out}^2}{M^2\sigma_{in}^2} = \frac{\sigma_{out}^2}{M^2 S_{in}} = \frac{1}{M}\left(\frac{2M+\alpha-1}{\alpha+1}\right) \qquad \textbf{2-33}$$

$$= \frac{1}{M}\left(\frac{2M+M^{\frac{1}{N}}-2}{M^{\frac{1}{N}}}\right) = \frac{1}{M}+\left(\frac{2(M-1)}{M^{\frac{1}{N}+1}}\right)$$

For high N and M, the value of $F^2=2$. Hence the excess noise factor (F) is quantified as $\sqrt{2}$.

2.5.6 Signal to Noise Ratio in imaging systems

The effective signal to noise ratio (S/N ratio)[122] can be computed by taking the ratio of the signal to sum of the noise sources in quadrature. The signal is given by the expression; $S = QE \times M \times P$ where QE is the quantum efficiency, P is the number of photons and M is the net EM gain. The effective noise is the sum in quadrature of shot noise, read out noise, dark current, clock induced charge and the multiplicative noise. $N = \sqrt{P_r^2 + F^2 \times M \times \left(P + P_d^2 + P_{cic}^2\right)}$. Hence the signal to noise ratio can be quantified as

$$\frac{S}{N} = \frac{QE \times M \times P}{\sqrt{P_r^2 + F^2 \times M \times \left(P + P_d^2 + P_{cic}^2\right)}} \qquad \textbf{2-34}$$

$$= \frac{QE \times P}{\sqrt{\left(\frac{P_r}{M}\right)^2 + F^2 \times \left(QE \times P + P_d^2 + P_{cic}^2\right)}}$$

The above expression shows that the net EM gain plays a significant role in reducing the effects of the readout noise on the overall noise. In the case of sCMOS camera, $F=M=1$ and $P_{cic}=0$. The detector characteristics of an EMCCD and a sCMOS camera are listed in the next page and the S/N is calculated for both cameras. The S/N ratio graph is shown in Fig. 2.8 A. The figure illustrates that for the characteristics described in Table 2-2, the EMCCD closely resembles an ideal detector which proves that the EMCCD is only shot noise limited.

Instead, a sCMOS does not perform as efficient as an EMCCD. But, it is to be remembered that the sCMOS has smaller pixels than an EMCCD. Hence, the difference in S/N ratio could just be attributed to the pixel size. Hence, the SNR of a hypothetical EMCCD is plotted with all the characteristics as in Table 2-2 except with a pixel size comparable to that sCMOS. Even, in this case, the hypothetical EMCCD outperforms sCMOS. Though the SNR plots merge at higher photon counts, at photon counts frequently observed in FCS experiments, it is found that EMCCD is better. This might mainly be attributed to the lower QE and higher read out noise of the sCMOS when compared to the EMCCD.

Four different cameras were used in the experiments described in this thesis. They are Cascade II: 512 and Evolve 512 (Photometrics, Tucson, AZ, USA), Andor iXON 860 (ANDOR, Belfast, UK) and Orca Flash 2.8 (Hamamatsu Photonics, Hamamatsu city, Japan).

Table 2-2: Characteristics of EMCCD and sCMOS cameras plotted in Fig. 2.8 A

	EMCCD: Andor iXON 860[123]	sCMOS: Hamamatsu Flash Orca 2.8[124]
Full Resolution	128×128	1920×1440
Speed	128×128 513 fps 64×64 943 fps	1920×1440 45.4 fps 1920×80 540 fps
Pixel Size	24×24 µm	3.6×3.6 µm
Chip Size	3.1×3.1 mm	6.9×5.2 mm
QE at 514 nm	0.95	0.65
EM Gain	1-1000	-
Analog Gain	10	8
Readout noise	0.3 e^- $pixel^{-1}$ (EM Gain: 200)	3 e^- $pixel^{-1}$
Full Well Capacity	800, 000 e^-	18000 e^-
Dark Current	0.002 e^- $pixel^{-1}s^{-1}$	0.5 e^- $pixel^{-1}s^{-1}$* (Data from model Flash 4.0)
CIC	0.05 e^- $pixel^{-1}s^{-1}$	-
Pixels at 500 fps	~16000	~160000
Multiplicative Noise	1.4x	-
A/D convertor	16 bit	12 bit
Max Readout rate	10 MHz	Varies with illumination size
Min illumination time	Cannot be set independently. Determined by frame rate*.	20 µs

*The illumination time in an EMCCD can be evaluated. Consider a typical frame rate of 0.56 ms for a 21×21 region. This includes the frame transfer time and the illumination time. As described in the principles of EMCCD operation, the read out is performed by reading individual lines. Hence 128×21 pixels need to be read. Assuming that the camera is operated at the fastest readout (improves the frame rate but increases the readout noise as well) of 10 MHz, it would take 128*21/10^7=0.26 ms for read out. Hence the illumination time is 0.56-0.26=0.3 ms.

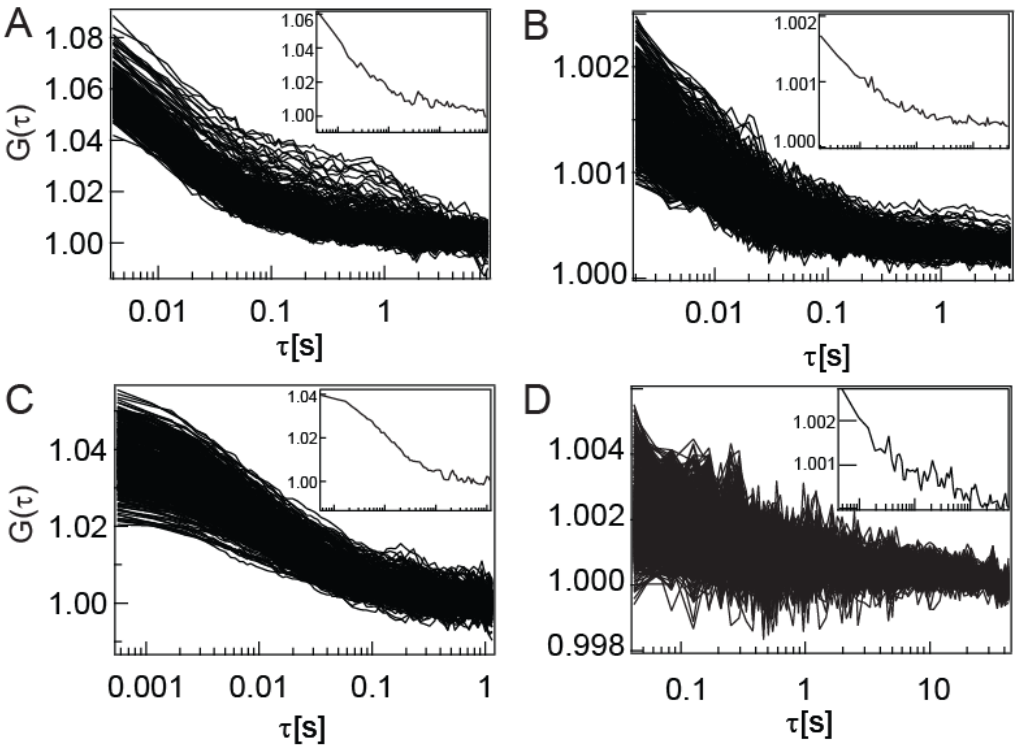

Fig. 2.7: Representative autocorrelation curves from different cameras. Four different cameras were tested during the course of the project. Representative correlation functions from all the cameras show that Imaging FCS can be performed using them. A, B and C are lipid bilayers samples probed by Imaging FCS using Cascade, Evolve and Andor EMCCD cameras respectively. D is a set of correlation curves calculated using images of fluorescent beads captured by Hamamatsu sCMOS camera. The inset shows a single autocorrelation in each case.

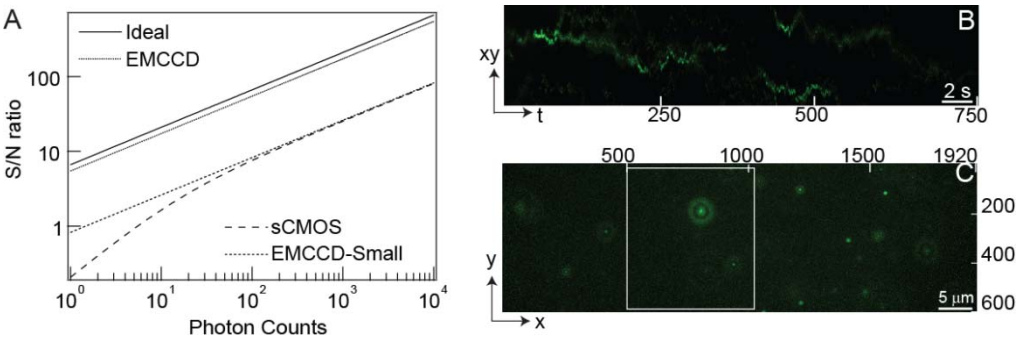

Fig. 2.8: Comparison of EMCCD and sCMOS cameras. A shows that sCMOS outperforms EMCCD in signal to noise ratio. B is a kymograph showing the paths of individual beads. C is a single image obtained from a stack captured by sCMOS showing the differences in area captured between an EMCCD and sCMOS. Typical area captured in EMCCD at the same frame rate is shown in the box.

Note the advancement in technology with time. Cascade II: 512 had the best time resolution of 4 ms while Evolve has 2 ms. With better time resolution, the plateau of autocorrelation can be captured. The improved time resolution between Evolve and Andor is only due to the less number of pixels ($1/16^{th}$) in Andor when

compared to Evolve leading to shorter readout time. With better time resolution, the plateau of autocorrelation can be captured. As discussed earlier, the current day models of sCMOS do not have the best S/N ratio to do correlation and hence the autocorrelations obtained from the fluctuations in fluorescence of beads in Fig. 2.7 D appears noisy. Due to limited QE, FCS could not be performed with conventional fluorophores but could be performed with very bright particles like beads. Though SNR is limiting in sCMOS using current day technology, it is bound to improve in the years to come. sCMOS provides the unprecedented advantage of multiplexing. For the first time, we were able to measure more than 1 million autocorrelations. Here, we show that by using a sCMOS camera, we can record 1,152,000 (1920×600) autocorrelation functions at 25 fps. A projection of a set of 750 frames from the stack displays the diffusion paths made by different beads as in Fig. 2.8 B. Due to very large field of view, individual particles can be tracked for a very long time as seen by the fluorescent traces. The dramatic improvement in the field of view can be understood by observing the white box in Fig. 2.8 C which is a 512x512 region, typical of EMCCD based field of view at the same frame rate of sCMOS.

2.6 Imaging FCS-calculation of correlation functions

Correlations are performed on a stack of multiple images acquired at different time points. Each image is made up of a certain number of pixels and each pixel has an associated intensity value. These are typically stored as a *.tiff file. The intensity values from the multi-plane tiff file are written into an intensity array of dimensions n, w_i, l_i where n is the number of frames, w_i is the number of rows in the image and l_i is the number of columns in the image. Each measurement has a background value associated which originates from camera, environment and sample related issues. The background value can be determined by a background file which was acquired without excitation of the fluorophores or the background value can be entered directly into software or can be set to the minimum value of the stack being correlated. For a

full frame data treatment, the correlation is performed at each pixel and upon completion the output consists of $w_i \times l_i$ number of correlation curves. Binning is a procedure in which intensity in adjacent pixels get added up. In case, binning is performed, the output consists of $\left\lfloor \frac{w_i}{bin} \right\rfloor \times \left\lfloor \frac{l_i}{bin} \right\rfloor$ number of correlations where $\lfloor x \rfloor$ is the largest integer less than or equal to x.

2.6.1 Correlation: Types and architecture

Correlations are performed between pixels which had been acquired at different times and/or locations. The acquisition time of the first frame is set to $t = 0$. The pixels in the frame are correlated individually with pixels in another frame that was acquired at $t = \tau$. The difference between the acquisition times of these two frames being correlated, τ, is referred to as lag time.

There are a number of important time scales for the calculation of the correlations. First, the frame rate of the camera limits the time resolution, and this time per frame is referred to as $\Delta\tau$. Note that this time includes the illumination of the camera as well as the readout time. All other time scales are multiples of this basic unit time $\Delta\tau$. Second, the measurement has to be taken over a certain acquisition time t_{acq}. Third, the correlations are calculated for different lagtimes τ ($0 < \tau < t_{acq}$). Fourth, at different lagtimes τ, the width over which the intensity signal is integrated before the correlation is calculated can vary and is referred to as the bin width[125-126]. Currently, there are two correlator architectures: linear and semi-logarithmic.

2.6.1.1 Linear correlation

In linear correlation mode, the correlations are calculated at linearly increasing lagtimes $\tau = m\Delta\tau$ where m ranges from *0* to *M-1*, if the correlations are calculated for M lagtimes. The bin width for each lagtime is kept constant at $\Delta\tau$. Theoretically, the last point of the correlation is the acquisition time (t_{acq}). It is not advisable to calculate the correlation till t_{acq} since the number of data points to average is very few as the lagtime approaches t_{acq}. To display correlations from $t = 0$

to $t = t_{end}\left[t_{end} < t_{acq}\right], t_{end}/\Delta\tau + 1$, number of calculations need to be done. Substituting typical values, $\Delta\tau$ = 0.5 ms, t_{end}=1.0235 s, 2048 correlations at individual lag times need to be performed. For linear correlation, the lagtime is

$$\tau_{\text{linear}}(m) = m\Delta\tau \quad \forall\left\{m \in \mathbb{N} \mid 0 \le m \le \frac{t_{end}}{\Delta\tau}\right\} \qquad \textbf{2-35}$$

Where $\mathbb{N}$ is the set of natural numbers.

2.6.1.2 Semi-logarithmic correlation

The semi-logarithmic correlator architecture is used more frequently since this architecture covers a larger range of lagtimes than the linear correlator using less number of computations. This correlator architecture is based on the multi-tau algorithm[125]. In the most common configuration, the first 16 correlations are at linearly increasing lagtimes $\tau = m\Delta\tau$ where *m* ranges from 0 to 15 with a bin width of $\Delta\tau$. The next set of 8 correlations possess linearly spaced lagtimes at intervals of $2\Delta\tau$ beginning with $(15+2)\Delta\tau$ and a bin width of $2\Delta\tau$. The next set of 8 correlations possess lagtimes at intervals of $4\Delta\tau$ beginning with $(31+4)\Delta\tau$ and a bin width of $4\Delta\tau$. This is repeated for bin widths of $8\Delta\tau$, $16\Delta\tau$, $32\Delta\tau$, $64\Delta\tau$ and $128\Delta\tau$. The last calculated lag time is at $(2048-1)\Delta\tau$. Substituting $\Delta\tau$=0.5 ms, a lag time of 1.0235 s can be achieved by just 72 (16+(8-1)×8) correlations. The same lagtime needs 2048 correlations in the linear configuration. The above example was for the configuration of a (16, 8) multi tau correlator but can be directly extended to any *(p, q)* correlator structure. In a *(p, q)* correlator, the first *p* correlations are at linearly increasing lagtimes $\tau = m\Delta\tau$ where *m* ranges from *0* to *p-1* with a bin width of $\Delta\tau$. The next *q* groups possess *p*/2 lagtimes with bin width and lagtime intervals which double from group to group. In this way a particular lagtime is always the sum of all the bin widths of the previous lagtimes. A *(p, q)* correlator calculates a correlation function at $h = [p+(q-1)\times q/2]$ number of lagtimes. The minimum number of frames (Fr_{min}), needed for a *(p,q)* correlator is

$$Fr_{\min} = p + \frac{p}{2}\sum_{i=1}^{q-1} 2^i \qquad \textbf{2-36}$$

For a (16, 8) correlator, Fr_{min}=2048. Although 2048 frames are sufficient to carry out the correlations, it is advised to perform the correlation with higher number of frames in order to increase the precision of the calculated correlation. Typically, correlations are calculated using 10000 frames. A detailed description of the semi-logarithmic correlator is available elsewhere[108, 126]. Thus the lagtime in this architecture can be represented by the formula below.

$$\tau_{\text{semilog}}(m) = \qquad \textbf{2-37}$$

$$\begin{cases} m\Delta\tau & \forall\{m \in \mathbb{N} \mid 0 \le m < p\} \\ \left(2^{\left(\left\lfloor \frac{2m}{p} \right\rfloor - 1\right)}\left(m - \left\lfloor \frac{2m}{p} \right\rfloor \frac{p}{2} + \frac{p}{2} + 1\right) - 1\right)\Delta\tau & \forall\left\{m \in \mathbb{N} \middle| p \le m < p + (q-1)\frac{q}{2}\right\} \end{cases}$$

There are two ways, by which the correlation can be calculated, using the sums of products method or by using Fourier transforms[127]. Here, the correlations are calculated using the former method. The continuous expression for correlation in Eq. 2-1 is converted to discrete form and implemented in the program as in Eq. 2-38 for the linear and the first cycle of the semi-logarithmic architecture. Symmetric normalization is performed where each correlation is normalized by only those intensity values used in the calculation of the autocorrelation[125].

$$G(k\Delta\tau) = \frac{(n-k)\sum_{i=0}^{n-k-1} I(i\Delta\tau)\, I((i+k)\Delta\tau)}{\sum_{i=0}^{n-k-1} I(i\Delta\tau) \sum_{i=k}^{n-1} I(i\Delta\tau)} \qquad \textbf{2-38}$$

$$\forall\{k \in \mathbb{N} \mid 0 \le k < x\}\begin{Bmatrix} \text{linear}: x = \dfrac{t_{end}}{\Delta\tau} \\ \text{Semi-logarithmic}: x = p \end{Bmatrix}$$

In the case of semi-logarithmic architecture, the multi tau algorithm is implemented[125-126]. Stacks which have acquisition times which are integer multiples of $\Delta\tau$ are created by summation and the correlations are calculated in these stacks as

shown in 2-39. The correlations are calculated for *p/2* points at arithmetically progressing time intervals at twice (2^l) the time resolution, $\Delta\tau$, of the camera. This is followed for *p/2* points with a time difference of four times (2^2) the time resolution. This is repeated till the time difference has reached 2^{q-1} times the time resolution.

$$G\left(\left(2^l\left(k+\frac{p}{2}+1\right)-1\right)\Delta\tau\right)= \qquad \textbf{2-39}$$

$$\frac{\left(\left\lfloor\frac{n}{2^l}\right\rfloor-k-\frac{p}{2}\right)\sum_{i=0}^{\left(\left\lfloor\frac{n}{2^l}\right\rfloor-k-\frac{p}{2}-1\right)}\sum_{j=2^l\times i}^{(2^l\times(i+1)-1)} I(j\Delta\tau)\sum_{j=2^l\times\left(i+k+\frac{p}{2}\right)}^{\left(2^l\times\left(i+k+\frac{p}{2}+1\right)-1\right)} I(j\Delta\tau)}{\sum_{i=0}^{\left(\left\lfloor\frac{n}{2^l}\right\rfloor-k-\frac{p}{2}-1\right)}\sum_{j=2^l\times i}^{(2^l\times(i+1)-1)} I(j\Delta\tau)\sum_{i=0}^{\left(\left\lfloor\frac{n}{2^l}\right\rfloor-k-\frac{p}{2}-1\right)}\sum_{j=2^l\times\left(i+k+\frac{p}{2}\right)}^{\left(2^l\times\left(i+k+\frac{p}{2}+1\right)-1\right)} I(j\Delta\tau)}$$

$$\forall\left\{k,l\in\mathbb{N}\,\middle|\,\begin{matrix}0\le k<\frac{p}{2}\\ 1\le l<q\end{matrix}\right\}$$

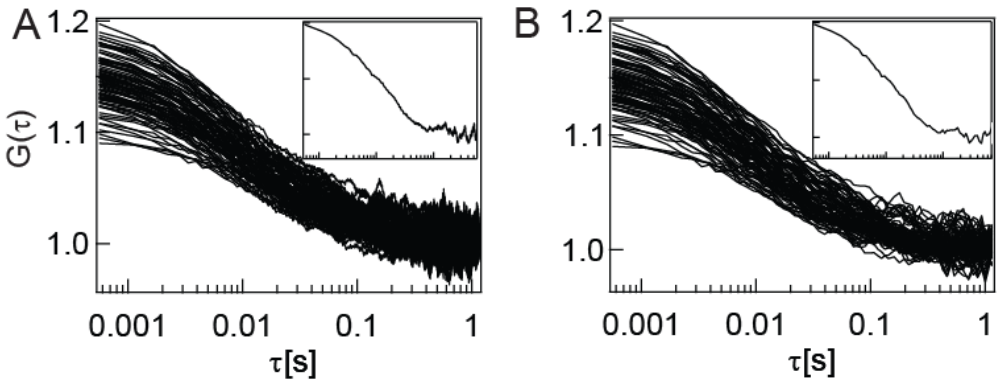

Fig. 2.9: Representative ACFs from different correlator architectures. A and B are autocorrelations from linear and semi-logarithmic architecture respectively. A was calculated from 2048 channels while B was calculated from 72 channels. Both the set of curves resemble each other. Hence, a semi-logarithmic correlator is preferred since it provides memory and data-handling advantages over the linear correlator.

2.7 Imaging FCS-data analysis by ImFCS

Presently, to the best of our knowledge, no commercially available software can read in image stacks and calculate correlations in each pixel of the image stack. Hence, an open-source program, ImFCS, was created that allows the user to read-in the intensity files from different CCDs, to automatically calculate the temporal

autocorrelations and temporal and spatial cross-correlations, to fit all data with a set of predefined models and to display images and histograms of all parameters. The program, ImFCS, is written in C++ for Windows XP/Vista, and is linked to the widely available commercial software IgorPro (WaveMetrics Inc, Lake Oswego, OR, USA) to provide a graphical interface for the user. This software is available for download at http://staff.science.nus.edu.sg/~chmwt/ImFCS.html. The functionalities of the software and a screen shot are shown in Fig. 2.10 and Fig. 2.11 respectively.

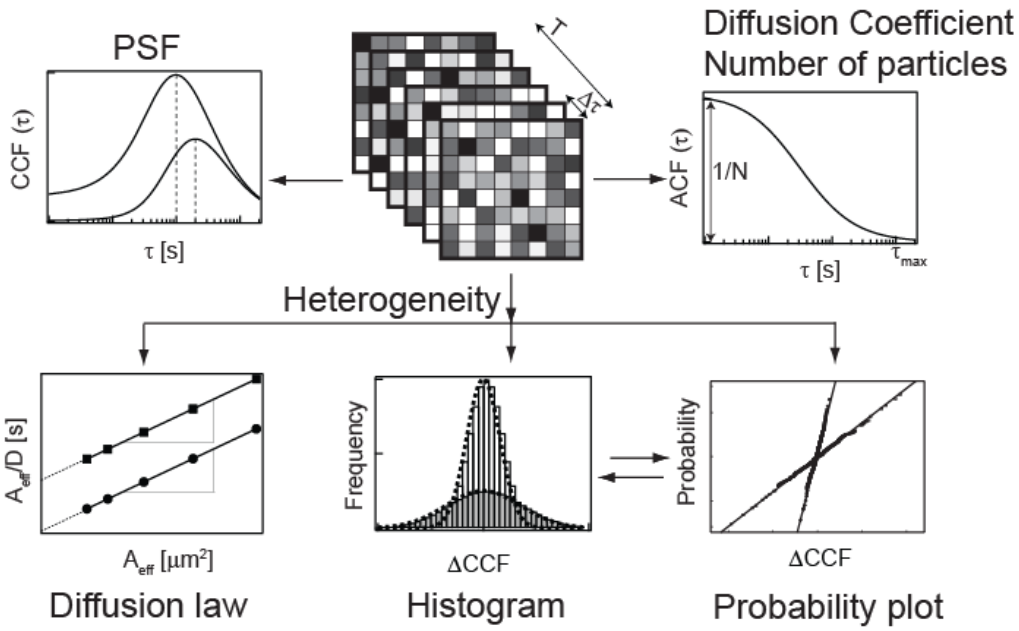

Fig. 2.10: Readouts in Imaging FCS. Imaging FCS is a method to mobility and number of particles. It can be determined by fitting temporal autocorrelations or by spatiotemporal cross-correlations or by spatial autocorrelations. The organization of molecules can be inferred by using diffusion laws and Δ*CCF* histograms and probability plots.

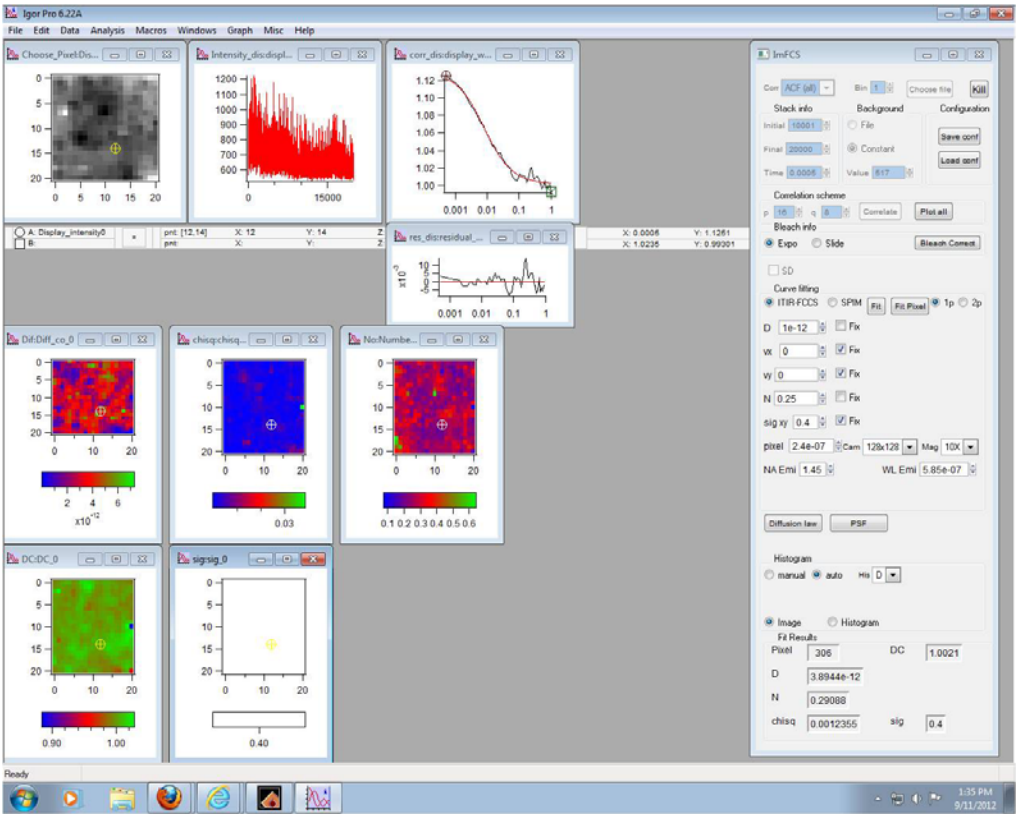

Fig. 2.11: Screen shot of ImFCS

3 Estimation of mobility, number of particles, PSF and heterogeneity by Imaging FCS

Camera based FCS is characterized by an illumination area which is a convolution between the square area of the pixel (a^2) and the point spread function (PSF). Theoretical expressions incorporating the effect of the PSF on the autocorrelation function in camera based FCS is available only for autocorrelation. But the usage of EMCCD permits one to perform cross-correlation between any two areas. In this work, we derive a generalized expression for cross-correlation between any two areas of any size and shape on a CCD chip incorporating the effect of PSF and use the same expression to extract diffusion coefficient and velocity parameters for 3 different types of transport (diffusion, flow, diffusion and flow). In order to quantitate the absolute number of particles contributing to the correlation, the effective volume of observation incorporating the effects of PSF needs to be obtained. Hence, in the next step, an expression for effective observation volume in camera FCS is determined. All the aforementioned expressions are determined first in 2-dimensions for TIRF based camera FCS and then later extended for 3D SPIM based camera FCS. The expressions for cross-correlations are validated using experiments later. This is followed by providing guidelines for effective fitting of cross-correlation data. Finally, new methods to probe heterogeneity from Imaging FCS data are discussed.

3.1 Materials and Methods

3.1.1 Reagents

Palmitoyl-2-oleoyl-sn-glycero-3-phosphocholine(POPC),1,2-dipalmitoyl-sn-glycerol-3-phosphoethanolamine-N-(lissamine rhodamine B sulfonyl) ammonium salt (Rho-PE), 1-Palmitoyl-2-Oleoyl-*sn*-Glycero-3-[Phospho-*rac*-(1-glycerol)] (Sodium Salt) (POPG), 1,2-Dipalmitoyl-*sn*-Glycero-3-Phosphoethanolamine-N-(Cap Biotinyl) Sodium Salt (Biotinyl Cap PE), 1,2-dilauroyl-*sn*-glycero-3-phosphocholine (DLPC) and 1,2-distearoyl-sn-glycero-3-phosphocholine (DSPC) were obtained from Avanti

Polar lipids (Alabaster, AL). Quantum dot Q21511MP was purchased from Molecular Probes, Invitrogen, Singapore (QD-585). Hellmanex was purchased from Hellma GmbH & Co, KG (Mullheim, Germany). Avidin was obtained from Invitrogen (Singapore).

3.1.2 Preparation of clean cover slides

Cover slides were sonicated in hellmanex detergent for 30 minutes. They were sonicated in 2 M H_2SO_4 for 30 minutes. This was followed by sonication in de-ionized water for 15 minutes twice. They were rinsed and stored in technical ethanol and air-dried before use.

3.1.3 Preparation of Supported Lipid Bilayers (SLB)

POPC was prepared as stock in $CHCl_3$. Rho-PE (concentration-0.01 mol% to the total lipid) was mixed with POPC for measurements. The solvent was subjected to vacuum evaporation for 1 hour. Deionized (DI) water was added to make 0.5 mM lipid suspension. 500 µl of the suspension was sonicated for 15 minutes to form vesicles. 200 µl of the sonicated suspension was dispensed onto a cleaned dry cover slide and incubated for 2 hours at 60 ºC for the formation of bilayers. This was followed by cooling for 30 minutes. The lipid aggregates above the bilayer were washed by replacing the solution 10 times with DI water.

3.1.4 Preparation and Immobilization of GUVs

GUVs were prepared and immobilized according to protocols described elsewhere[128]. The protocol is described in brief here. POPG was prepared as stock in $CHCl_3$ (5.19 mM). A known amount of POPG was dissolved in $CHCl_3$ to obtain the required stock concentration. 0.5 mM POPG was mixed with 5% Biotinyl-cap-PE and 0.01% Rho-PE and the solvent was subjected to vacuum evaporation for 1 hour. Rho-PE was added to fluorescently label the Giant Unilamellar Vesicles (GUVs) whereas Biotinyl-cap-PE was added to immobilize the GUVs on cover slide by avidin-biotin chemistry. PBS was added to make a lipid suspension and the sample was incubated at 37 ºC overnight to produce GUVs. Avidin (0.5 mg/ml) was added to the cover slide

and dried by heating at 60 ºC. Later, the POPG GUV solution was added to the cover slide. Biotinyl-Cap-PE present in the GUVs bound to the avidin on the cover slide, thus immobilizing the GUVs. The GUVs thus obtained, which were spread on the cover slide as a double bilayer due to the strong avidin-biotin interaction, were used for ITIR-FCS. The sizes of GUVs were determined by light microscopy.

3.1.5 Preparation of supported mixed lipid bilayers

DLPC and DSPC were prepared as stock in $CHCl_3$. Rho-PE (concentration-0.01%) was mixed with DLPC/DSPC (1:1 mol/mol) for measurements. The solvent was subjected to vacuum evaporation for 1 hour. Deionized (DI) water was added to make 0.5 mM lipid suspension. 500 µl of the suspension was sonicated for 15 minutes to form vesicles. 200 µl of the sonicated suspension was dispensed onto a cleaned dry cover slide and incubated for 2 hours at 60 ºC for the formation of bilayers. This was followed by cooling for 30 minutes. The lipid aggregates above the bilayer were washed by replacing the solution 10 times with DI water. The transition temperature of DLPC and DSPC are -1 and 55 ºC respectively. Hence DLPC forms the liquid disordered phase (L_d) and DSPC forms the liquid ordered phase (L_o) at room temperature. The fluid phase region in the mixed lipid bilayer is labeled by Rho-PE. The measurements are performed at room temperature where they are phase separated.

3.1.6 Diffusion and simulated flow measurements

Diffusion measurements were performed on lipid bilayers. For the measurement of directed movement, further referred to as flow, a QD-585 of concentration 1 nM was immobilized onto a cover slide and was air-dried. A Scan IM 120x100 motorized stage (Marzhauser Wetzlar GmbH & Co.KG, Wetzlar-Steindorf, Germany) was used to move the cover slide at a nominal velocity of 10 µm/s or 100 µm/s (referred to as slow flow or fast flow respectively). For the combination of diffusion and directed transport, lipid bilayers were prepared as described above on

clean cover slides and the motorized stage was used to move the cover slide at a velocity of 10 μm/s.

3.2 Theory

Correlations can be calculated for any pixel or combination of pixels on the EMCCD chip_as in Fig. 3.1. The PSF of a microscope can be approximated as a Gaussian Function with center x_0 and width w_0

$$I\left(x,x_0\right)=I_0 e^{-\frac{2\left(x-x_0\right)^2}{w_0^2}};w_0=\frac{w\lambda_{em}}{NA} \quad \textbf{3-1}$$

where λ_{em} is the wavelength of emission and NA is the numerical aperture and w_0 is a numerical value of PSF to be determined by fitting. The Gaussian functions are separable and can be multiplied to express the point spread function in the x-y plane[129-130].

$$I\left(x,x_0,y,y_0\right)=I\left(x,x_0\right)\times I\left(y,y_0\right) \quad \textbf{3-2}$$

It was suggested that $w_0=0.42$ as the best approximation of the Gaussian to the Bessel function of the PSF of a microscope[129-132]. However, this approximation was derived for imaging applications and might have to be adapted depending on the application[130]. In addition, this approximation did not take account of any molecular dynamics, noise due to an EMCCD. Due to the noise level for EMCCD cameras, this theoretical value cannot be achieved and a value of at least 0.6 is expected[133]. This is because of the noise factor as discussed in Sec. 2.5.5.1. In our case this value, underestimates the size of the PSF, especially in the case of particles moving fast compared to the acquisition time of the camera. Therefore this value might underestimate the cross-talk between neighboring pixels and fitting of this parameter is a better approach.

3.2.1 Derivation of a General Fitting Model for cross-correlation

The normalized cross-correlation function (CCF) for a stationary system has been defined earlier in Sec. 2.1.1 as

$$G(\tau) = \frac{\left\langle \delta F(0) \delta F'(\tau) \right\rangle}{\left\langle F(t) \right\rangle \left\langle F'(t) \right\rangle} + 1 = g(\tau) + 1 = g(\tau) + G_\infty \qquad \textbf{3-3}$$

where $F(t)$ and $F'(t)$ are the fluorescence signals in the two areas to be cross-correlated. Theoretically, the above expression for $G(\tau)$ converges to 1 for long correlation times. However, how well the function converges to 1 for long times depend on the length of the measurements. Due to the limited number of measurement points, the actual values usually vary slightly from 1. Therefore, we introduce the fitting parameter G_∞ instead of the value 1. This leads in our experience to better fits. It is this function we use for fitting all ACF and CCF data. In the following we derive the different forms of $g(\tau)$ for different shapes of the detection areas and for different processes including diffusion and flow.

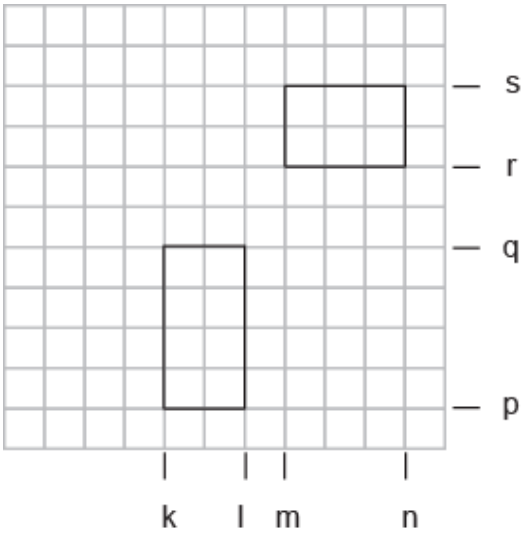

Fig. 3.1: Schematic representation of the regions on a CCD chip. These regions were used in the calculation of cross-correlation discussed in Sec. 3.2.1.

Here the cross-correlation is carried out between rectangular regions as shown in Fig. 3.1. *k, l, m, n, p, q, r, s* denote the location of the region of correlation on the chip. The fluorescence intensity and its fluctuations in the first area of cross correlation can be expressed using the *PSF* and the surface concentration *C* as

$$F(t) = \int_p^q \int_k^l \int_{-\infty}^{\infty} \int_{-\infty}^{\infty} I(x, x_0) I(y, y_0) C(x, y, t) \, dx dy dx_0 dy_0 \qquad \textbf{3-4}$$

Similarly, the signal and its fluctuations in the second area of correlation can be expressed as

$$F'(t)=\int_{r}^{s}\int_{m}^{n}\int_{-\infty}^{\infty}\int_{-\infty}^{\infty} I\left(x',x_0'\right)I\left(y',y_0'\right)C\left(x',y',t\right)dx'dy'dx_0'dy_0' \qquad \textbf{3-5}$$

The time average of the fluorescence signals can be calculated using 3-4 and 3-5.

$$\left\langle F'(t)\right\rangle=\left\langle C\right\rangle\int_{p}^{q}\int_{k}^{l}\int_{-\infty}^{\infty}\int_{-\infty}^{\infty} I\left(x,x_0\right)I\left(y,y_0\right)dxdydx_0dy_0 \qquad \textbf{3-6}$$

$$=\left\langle C\right\rangle\frac{I_0^2w_0^2\pi}{2}\left(l-k\right)\left(q-p\right)$$

$$\left\langle F'(t)\right\rangle=\left\langle C\right\rangle\int_{r}^{s}\int_{m}^{n}\int_{-\infty}^{\infty}\int_{-\infty}^{\infty} I\left(x',x_0'\right)I\left(y',y_0'\right)dx'dy'dx_0'dy_0' \qquad \textbf{3-7}$$

$$=\left\langle C\right\rangle\frac{I_0^2w_0^2\pi}{2}\left(n-m\right)\left(s-r\right)$$

Using, Eqs. 3-6 and 3-7, 3-3 can be rewritten as

$$g(\tau)=\frac{4}{\left\langle C\right\rangle^2\left(l-k\right)\left(q-p\right)\left(n-m\right)\left(s-r\right)I_0^4w_0^4\pi^2}\times \qquad \textbf{3-8}$$

$$\int_{r}^{s}\int_{p}^{q}\int_{m}^{n}\int_{k}^{l}\int_{-\infty}^{\infty}\int_{-\infty}^{\infty}\int_{-\infty}^{\infty}\int_{-\infty}^{\infty}$$

$$I\left(x,x_0\right)I\left(y,y_0\right)I\left(x',x_0'\right)I\left(y',y_0'\right)f(x,y,x',y',\tau)dxdx'dydy'dx_0dx_0'dy_0dy_0'$$

The expression for autocorrelation is separable and in the *x* direction, it is

$$g(\tau)=g_x(\tau)g_y(\tau) \qquad \textbf{3-9}$$

$$g_x(\tau)=\frac{2}{\left\langle C\right\rangle\left(l-k\right)\left(n-m\right)I_0^2w_0^2\pi}\times \qquad \textbf{3-10}$$

$$\int_{m}^{n}\int_{k}^{l}\int_{-\infty}^{\infty}\int_{-\infty}^{\infty} I\left(x,x_0\right)I\left(x',x_0'\right)P\left(x,x',\tau\right)dxdx'dx_0dx_0'$$

where *P(x, x', τ)* is the diffusion propagator as stated in Sec. 2.1.2.1.

$$g_x(\tau)=\frac{1}{\sqrt{\langle C\rangle}(l-k)(n-m)w_0^2\pi^{\frac{3}{2}}\sqrt{D\tau}}\times \qquad \textbf{3-11}$$
$$\int_m^n\int_k^l\int_{-\infty}^{\infty}\int_{-\infty}^{\infty} e^{-\frac{2(x-x_0)^2}{w_0^2}-\frac{2(x'-x'_0)^2}{w_0^2}-\frac{(x-x'+v_x\tau)^2}{4D\tau}}\,dxdx'dx_0dx_0'$$

The details of the derivation are given in Appendices 3 and 4. The solution to the integral is given in Eq. 3-12

$$g_x(\tau)=\frac{1}{2\sqrt{\langle C\rangle}(l-k)(n-m)}\times \qquad \textbf{3-12}$$
$$\left(\begin{array}{l}\sqrt{\frac{w_0^2+4D\tau}{\pi}}\left(e^{-\left(\frac{l-m+v_x\tau}{\sqrt{w_0^2+4D\tau}}\right)^2}-e^{-\left(\frac{l-n+v_x\tau}{\sqrt{w_0^2+4D\tau}}\right)^2}-e^{-\left(\frac{k-m+v_x\tau}{\sqrt{w_0^2+4D\tau}}\right)^2}+e^{-\left(\frac{k-n+v_x\tau}{\sqrt{w_0^2+4D\tau}}\right)^2}\right)\\ +(l-m+v_x\tau)\,erf\left(\frac{l-m+v_x\tau}{\sqrt{w_0^2+4D\tau}}\right)-(l-n+v_x\tau)\,erf\left(\frac{l-n+v_x\tau}{\sqrt{w_0^2+4D\tau}}\right)\\ -(k-m+v_x\tau)\,erf\left(\frac{k-m+v_x\tau}{\sqrt{w_0^2+4D\tau}}\right)+(k-n+v_x\tau)\,erf\left(\frac{k-n+v_x\tau}{\sqrt{w_0^2+4D\tau}}\right)\end{array}\right)$$

For square regions of $n\times n$ binning with side length a where $a=n\times d$ (where d is the side length of a single pixel in object space). If two regions of the same size are separated by r_x in the x direction and r_y in the y direction, the above general expression can be simplified by replacing $k=0$, $l=a$, $m=r_x$, $n=a+r_x$, $p=0$, $q=a$, $r=r_y$, $s=a+r_y$ to yield the following form

$$g_x(\tau)=\frac{1}{2\sqrt{\langle C\rangle a^2}}\times \tag{3-13}$$

$$\left(\begin{array}{l}\sqrt{\frac{w_0^2+4D\tau}{\pi}}\left(e^{-\left(\frac{a-r_x+v_x\tau}{\sqrt{w_0^2+4D\tau}}\right)^2}-2e^{-\left(\frac{r_x-v_x\tau}{\sqrt{w_0^2+4D\tau}}\right)^2}+e^{-\left(\frac{a+r_x-v_x\tau}{\sqrt{w_0^2+4D\tau}}\right)^2}\right)\\ +\left(a-r_x+v_x\tau\right)erf\left(\frac{a-r_x+v_x\tau}{\sqrt{w_0^2+4D\tau}}\right)+\left(a+r_x-v_x\tau\right)erf\left(\frac{a+r_x-v_x\tau}{\sqrt{w_0^2+4D\tau}}\right)\\ -2\left(r_x-v_x\tau\right)erf\left(\frac{r_x-v_x\tau}{\sqrt{w_0^2+4D\tau}}\right)\end{array}\right)$$

The above expression is a generalized expression for cross-correlation between different areas on the EMCCD chip for diffusion and flow. The expression for diffusion can be obtained by setting v_x=0.

$$g_x(\tau)_{diffusion}=\frac{1}{2\sqrt{\langle C\rangle a^2}}\times \tag{3-14}$$

$$\left(\begin{array}{l}\sqrt{\frac{w_0^2+4D\tau}{\pi}}\left(e^{-\left(\frac{a-r_x}{\sqrt{w_0^2+4D\tau}}\right)^2}-2e^{-\left(\frac{r_x}{\sqrt{w_0^2+4D\tau}}\right)^2}+e^{-\left(\frac{a+r_x}{\sqrt{w_0^2+4D\tau}}\right)^2}\right)\\ +\left(a-r_x\right)erf\left(\frac{a-r_x}{\sqrt{w_0^2+4D\tau}}\right)+\left(a+r_x\right)erf\left(\frac{a+r_x}{\sqrt{w_0^2+4D\tau}}\right)\\ -2r_x erf\left(\frac{r_x}{\sqrt{w_0^2+4D\tau}}\right)\end{array}\right)$$

The expression for autocorrelation can be obtained by setting r_x=0.

$$g_x(\tau)_{diffusion}=\frac{1}{\sqrt{\langle C\rangle a}}\left(\frac{\sqrt{w_0^2+4D\tau}}{a\sqrt{\pi}}\left(e^{-\left(\frac{a}{\sqrt{w_0^2+4D\tau}}\right)^2}-1\right)+erf\left(\frac{a}{\sqrt{w_0^2+4D\tau}}\right)\right) \tag{3-15}$$

The expressions for cross-correlation between two areas for diffusion and flow in 2D are provided in Appendices 5 and 6. In two dimensions, the expression for autocorrelation can be obtained from Eq. 3-15.

$$g(\tau)=\frac{1}{\langle C\rangle a^2}\left(\frac{\sqrt{w_0^2+4D\tau}}{a\sqrt{\pi}}\left(e^{-\left(\frac{a}{\sqrt{w_0^2+4D\tau}}\right)^2}-1\right)+erf\left(\frac{a}{\sqrt{w_0^2+4D\tau}}\right)\right)^2 \quad \textbf{3-16}$$

The above expression can be modified by the introduction of a dimensionless parameter which is a ratio of the pixel size to the sum of the PSF and the mean squared displacement during the observation time$\left(p(\tau)\right)$.

$$g(\tau)=\frac{1}{\langle C\rangle a^2}\left(erf\left(p(\tau)\right)+\frac{\left(e^{-(p(\tau))^2}-1\right)}{\sqrt{\pi}\,p(\tau)}\right)^2 \quad ;p(\tau)=\frac{a}{\sqrt{4D\tau+w_0^2}} \quad \textbf{3-17}$$

3.2.2 Effective Volume in Camera-FCS

In the following derivations for the effective volume, the integrations are performed in 1D and adapted for the 2D case by simple multiplication. As with Eq. 3-18, the integrals in the calculation of effective volume are also separable when expressed in Cartesian co-ordinates. In Imaging FCS, the illumination profile is a convolution between the square pixel ($W_{SP}(x)$) and the point spread function ($W_{PSF}(x)$) which is assumed to be a Gaussian (an approximation of Bessel function)[129]. Uniform illumination is assumed inside the square pixel with size a extending from $-a/2$ to $a/2$. The pixel is convolved with a Gaussian illumination profile.

$$W_{SP}(x)=\begin{bmatrix}1 & -\frac{a}{2}\le x\le\frac{a}{2}\\ 0 & \text{Otherwise}\end{bmatrix} \quad \textbf{3-19}$$

$$W_{PSF}(x)=I_0e^{\frac{-2x^2}{w_0^2}}$$

$$W(x)=W_{SP}(x)\otimes W_{PSF}(x)=\frac{w_0I_0}{2}\sqrt{\frac{\pi}{2}}\left(erf\left(\frac{a-2x}{\sqrt{2}w_0}\right)+erf\left(\frac{a+2x}{\sqrt{2}w_0}\right)\right)$$

The effective volume in FCS was defined earlier in Sec. 2.1.2.2. The integrals ω_1 and ω_2 are calculated below. The details of the integration are provided in Appendices 7-10.

$$\omega_1 = \int_{-\infty}^{\infty} \frac{W(x)}{W(0)} dx = \frac{1}{2erf\left(\frac{a}{\sqrt{2}w_0}\right)} \int_{-\infty}^{\infty} erf\left(\frac{a-2x}{\sqrt{2}w_0}\right) + erf\left(\frac{a+2x}{\sqrt{2}w_0}\right) dx \qquad \textbf{3-20}$$

$$= \frac{a}{erf\left(\frac{a}{\sqrt{2}w_0}\right)}$$

$$\omega_2 = \int_{-\infty}^{\infty} \left(\frac{W(x)}{W(0)}\right)^2 dx = \frac{1}{\left(2erf\left(\frac{a}{\sqrt{2}w_0}\right)\right)^2} \times \qquad \textbf{3-21}$$

$$\int_{-\infty}^{\infty} \left(erf\left(\frac{a-2x}{\sqrt{2}w_0}\right) + erf\left(\frac{a+2x}{\sqrt{2}w_0}\right)\right)^2 dx = \frac{a\left(erf\left(\frac{a}{w_0}\right) + \frac{w_0}{a\sqrt{\pi}}\left(e^{-\frac{a^2}{w_0^2}} - 1\right)\right)}{\left(erf\left(\frac{a}{\sqrt{2}w_0}\right)\right)^2}$$

Using Eqs. 3-20 and 3-21, the effective volume can be evaluated.

$$\text{Effective dimension in 1D} = \frac{a}{erf\left(\frac{a}{w_0}\right) + \frac{w_0}{a\sqrt{\pi}}\left(e^{-\frac{a^2}{w_0^2}} - 1\right)} \qquad \textbf{3-22}$$

$$\text{Effective area in TIRF-FCS } A_{eff} = \frac{a^2}{\left(erf\left(\frac{a}{w_0}\right) + \frac{w_0}{a\sqrt{\pi}}\left(e^{-\frac{a^2}{w_0^2}} - 1\right)\right)^2} \qquad \textbf{3-23}$$

Eq. 3-23 was obtained by extending the expression in Eq. 3-22 in 1D to 2D. It can be seen that the effective area can be obtained by setting τ=0 in 3-17 as expected from theoretical considerations as stated in Sec. 2.1.2.2. The value of diffusion time in Imaging FCS is given by the expression $\tau_D = \frac{A_{eff}}{4D}$. The expression of effective area needs to be substituted into the expression for autocorrelation to compute the absolute number of molecules contributing to the fluorescence in the area being observed.

The effective volume in the case of TIRF-FCS can be evaluated by integrating the exponential decaying stationary wave in the 'z' direction and multiplying it with the effective area.

$$\omega_1 = I_0 \int_{-\infty}^{\infty} e^{-\frac{z}{d}} dz = I_0 d \qquad \textbf{3-24}$$

$$\omega_2 = I_0 \int_{-\infty}^{\infty} e^{-\frac{2z}{d}} dz = \frac{I_0 d}{2} \qquad \textbf{3-25}$$

Here '*d*' is the penetration depth of the evanescent wave.The effective '*z*' dimension can be evaluated to be '*2d*'. Hence the observation volume in 3D can be parameterized as

$$\text{Effective volume in TIRF-FCS } V_{eff} = \frac{2da^2}{\left(erf\left(\frac{a}{w_0}\right) + \frac{w_0}{a\sqrt{\pi}}\left(e^{-\frac{a^2}{w_0^2}} - 1 \right) \right)^2} \qquad \textbf{3-26}$$

3.2.3 Fitting models in TIRF-FCS

The autocorrelation function given by Eq. 3-16 can be rewritten using Eq. 3-23 as follows

$$g(\tau) = \frac{A_{eff}}{a^2 N}\left(erf\left(\frac{a}{\sqrt{4D\tau + w_0^2}}\right) + \frac{\sqrt{4D\tau + w_0^2}}{a\sqrt{\pi}}\left(e^{-\frac{a^2}{4D\tau + w_0^2}} - 1 \right) \right)^2 \qquad \textbf{3-27}$$

where $N = \langle c \rangle A_{eff}$

$$g(\tau) = \frac{1}{N}\left(\frac{erf\left(\frac{a}{\sqrt{4D\tau + w_0^2}}\right) + \frac{\sqrt{4D\tau + w_0^2}}{a\sqrt{\pi}}\left(e^{-\frac{a^2}{4D\tau + w_0^2}} - 1 \right)}{erf\left(\frac{a}{w_0}\right) + \frac{w_0}{a\sqrt{\pi}}\left(e^{-\frac{a^2}{w_0^2}} - 1 \right)} \right)^2 \qquad \textbf{3-28}$$

$$G(\tau)=\frac{1}{N}\left(\frac{erf\left(p(\tau)\right)+\frac{\left(e^{-(p(\tau))^2}-1\right)}{\sqrt{\pi}\,p(\tau)}}{erf\left(p(0)\right)+\frac{\left(e^{-(p(0))^2}-1\right)}{\sqrt{\pi}\,p(0)}}\right)^2+G_\infty \qquad \textbf{3-29}$$

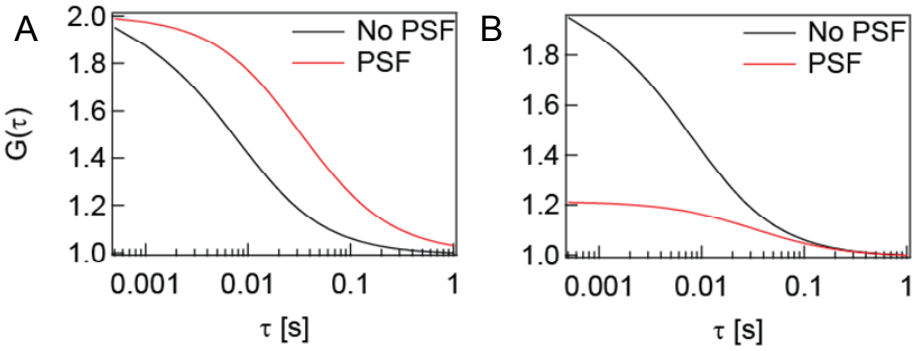

Fig. 3.2: Change in observation volume due to the PSF. A is a calculation of the correlation with and without the contribution of PSF. The calculation of the correlation function without PSF was performed by setting w_0=0. The increase in observation volume is manifested as a slower rate of decay. In B, the non-normalized autocorrelation curves indicate the increase in number of particles with the increase in observation volume.

3.2.4 Fitting models in SPIM-FCS

In the case of SPIM-FCS, evaluation needs to be performed in the z direction as well due to presence of finite thickness light sheet in the z direction. Hence the integration is performed from $-\infty$ to ∞ and the light sheet is modeled as a Gaussian with center m and w_z being the e^{-2} radius. The details of the integration are provided in Appendix 11.

$$g_z(\tau)=\frac{1}{\langle C\rangle\langle I(z,z_0)\rangle^2}\int_{-\infty}^{\infty}\int_{-\infty}^{\infty}I(z,z_0)I(z',z_0')P(z,z',\tau)\,dz\,dz' \qquad \textbf{3-30}$$

$$=\frac{1}{\langle C\rangle\sqrt{\pi}\sqrt{w_z^2+4D\tau}}$$

Hence the autocorrelation function in the z direction can be evaluated as follows.

$$G(\tau)=\frac{1}{a^2\sqrt{\pi}\langle c\rangle w_z}\times \left(erf\left(\frac{a}{\sqrt{4D\tau+w_0^2}}\right)+\frac{\sqrt{4D\tau+w_0^2}}{a\sqrt{\pi}}\left(e^{-\frac{a^2}{4D\tau+w_0^2}}-1\right)\right)^2\left(1+\frac{4D\tau}{w_z^2}\right)^{-\frac{1}{2}}+G_\infty \quad \textbf{3-31}$$

Similar to the case of the 2D TIRF, the observation volume needs to be evaluated in order to evaluate the absolute number of particles contributing to the fluorescence.

$$\omega_1=I_0\int_{-\infty}^{\infty}e^{-2\left(\frac{z-m}{w_z}\right)^2}dz=I_0 w_z\sqrt{\frac{\pi}{2}} \quad \textbf{3-32}$$

Hence effective volume in SPIM-FCS is

$$V_{eff}=\frac{\sqrt{\pi}a^2 w_z}{\left(erf\left(\frac{a}{w_0}\right)+\frac{w_0}{a\sqrt{\pi}}\left(e^{-\frac{a^2}{w_0^2}}-1\right)\right)^2} \quad \textbf{3-33}$$

The autocorrelation in SPIM-FCS (Eq. 3-31) can be rewritten as

$$g(\tau)=\frac{1}{\langle C\rangle V_{eff}}\times \frac{\left(erf\left(\frac{a}{\sqrt{4D\tau+w_0^2}}\right)+\frac{\sqrt{4D\tau+w_0^2}}{a\sqrt{\pi}}\left(e^{-\frac{a^2}{4D\tau+w_0^2}}-1\right)\right)^2\left(1+\frac{4D\tau}{w_z^2}\right)^{-\frac{1}{2}}}{\left(erf\left(\frac{a}{w_0}\right)+\frac{w_0}{a\sqrt{\pi}}\left(e^{-\frac{a^2}{w_0^2}}-1\right)\right)^2} \quad \textbf{3-34}$$

$$g(\tau)=\frac{1}{N}\left(1+\frac{4D\tau}{w_z^2}\right)^{-\frac{1}{2}}\left(\frac{erf\left(p(\tau)\right)+\frac{\left(e^{-(p(\tau))^2}-1\right)}{\sqrt{\pi}p(\tau)}}{erf\left(p(0)\right)+\frac{\left(e^{-(p(0))^2}-1\right)}{\sqrt{\pi}p(0)}}\right)^2 \quad \textbf{3-35}$$

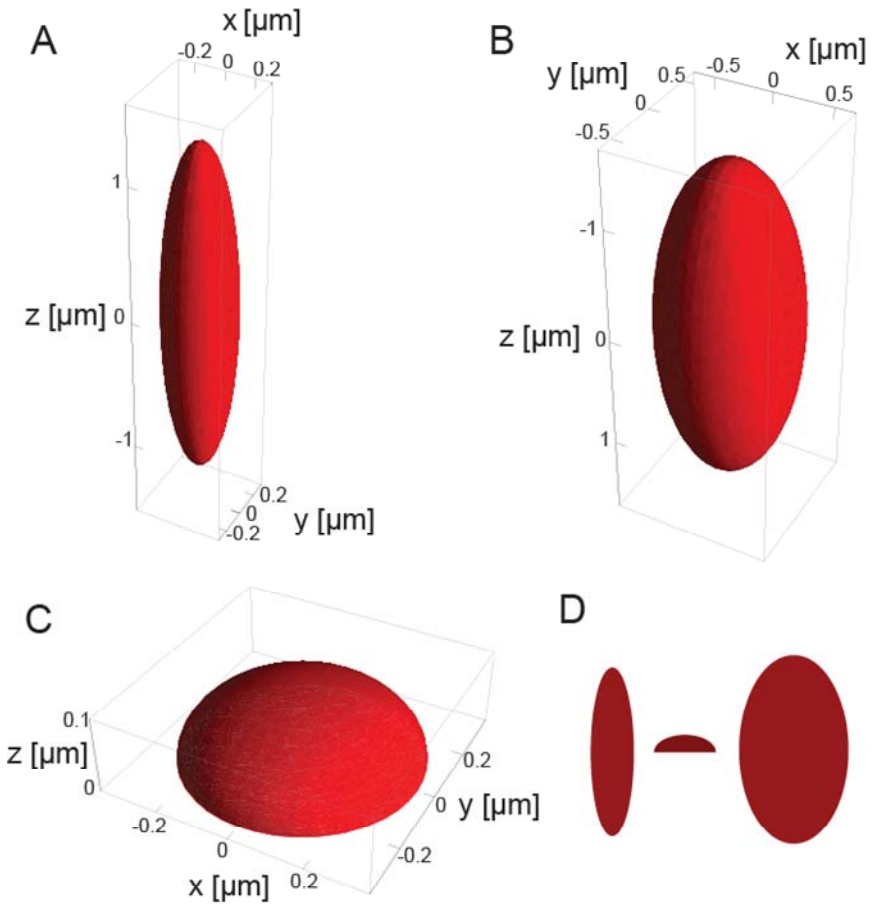

Fig. 3.3: Schematic representation of Observation volume. A, B and C are observation volumes in confocal, SPIM and TIRF respectively. D is a plot of the observation volume drawn to the same scale.

3.3 Results and Discussion

The first part describes the various methods to characterize mobility and number density from imaging FCS (Sec. 3.3.1) while the second part describes the various methods to characterize heterogeneity from Imaging FCS data (Sec. 3.3.2).

3.3.1 Mobility and Number density from Imaging FCS

The system and newly derived fitting models for ITIR-FCS were tested using supported lipid bilayers and samples with quantum dots fixed to a cover slide. By moving these samples with an automated microscope stage we could create situations for diffusion, active transport and a combination of the two.

3.3.1.1 Calibration of mechanical microscope stage

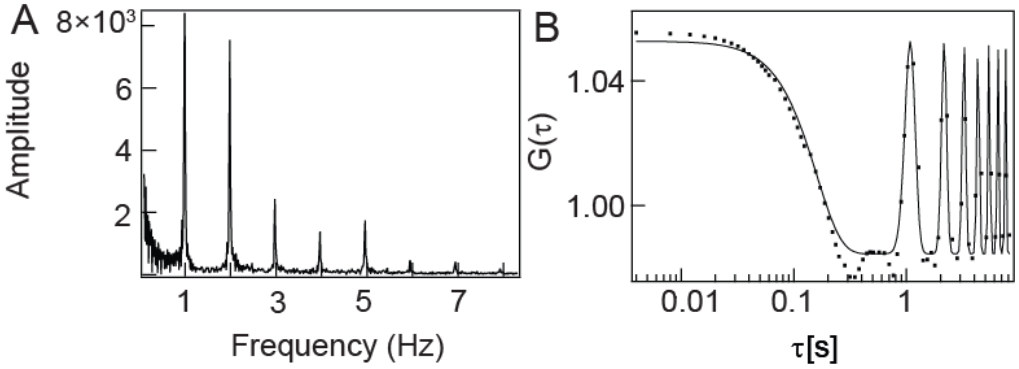

Fig. 3.4: Calibration of microscope stage. A is a plot of Fourier Transform of one pixel of the camera. It shows the frequency to be 1 Hz. B shows the periodic autocorrelation function. $\left(\frac{10}{2/200} \frac{\mu m / s}{mm/parts} = 1 \quad Hz \right)$

We decided to calibrate the microscope stage by using a micrometer scale (2 mm scale in 200 parts) which was moved with a speed of 10 μm/s through the field of view. The scale was illuminated using the microscope halogen lamp and wide field images were recorded. Since the scale consists of a periodic array of black stripes on a transparent background, we first calculated the proper fitting function for the FCS measurements (Appendix 12). This calibration was performed since it involves non-fluorescent samples and hence fluorescence related artifacts in flow can be avoided. Since the scale was moved in the *x*-direction, the data was fitted with $r_x = r_y = v_y = 0$. The retrieved velocity was 9.26 μm/s. This shows that the microscope stage moves as expected.

3.3.1.2 Autocorrelation analysis of flow and diffusion processes

Autocorrelation functions were computed and fitted to retrieve diffusion coefficient *(D),* velocity of flow *(v),* convergence value of correlation function at longer lag times (G_∞) and the e^{-2} radius of PSF (w_0). In this chapter, the computations are performed in a 3×3 binned area (852×852 nm^2) since it corresponds to the typical pinhole size used in confocal FCS. The overall quality of fits using the derived fitting models to the autocorrelation of diffusion is very good, as seen in Fig. 3.5 A and D. Fitted autocorrelation function (ACF) for data of samples that exhibit only flow show

deviations from the data (Fig. 3.5 B and C). There are several reasons for these deviations. Firstly, the data in these cases contains higher harmonics as evidenced by the regular peaks in the tail of the ACF. We attribute this to the stepping motor of the automated microscope stage which does not move over the full distance in one linear movement. This is supported by the intensity traces for these measurements (Fig. 3.5 B and C insets).

Secondly, these measurements were conducted on air dried samples of quantum dots and part of the ACF, in particular at short times, are possibly related to photophysical properties of the quantum dots which can exhibit blinking behavior on a similar time scale as the timescale of measurement, i.e. milliseconds[134]. The qualitative analysis (from Fig. 3.5 B and C) suggests that for flow processes, the fitting is not good. From the quantitative analysis, (Table 3-1), it is seen that, the autocorrelation cannot be fitted to determine D, N, v and w_0 simultaneously. The standard deviation exceeds the mean which might suggest two different things, either the value of the parameter is zero or the parameters cannot be fitted independently.

We know that none of the parameters are expected to have a value of zero, hence it is seen that the parameters cannot be determined from a single autocorrelation function. The transport coefficients are strongly linked to the PSF. The fitting parameters are correlated that it is impossible to fit both of them independently. It is referred to as the identifiability problem in curve-fitting. The χ^2 fitting space does not have a minimum which can be reached. Instead the surface is flat and a broad range of values can be fitted. The error in the fitted parameter is the inverse of the curvature of the χ^2 surface. For a flat profile, the curvature is zero and hence the error is high. In such cases, a small change in initial parameters leads to very drastic differences in the output parameters. The correlation matrix which is a normalized version of the covariance matrix can be used to diagnose identifiability problems. The diagonal elements are always 1 and any off-diagonal elements greater than the value of ±0.99 indicates difficulty in curve-fitting.

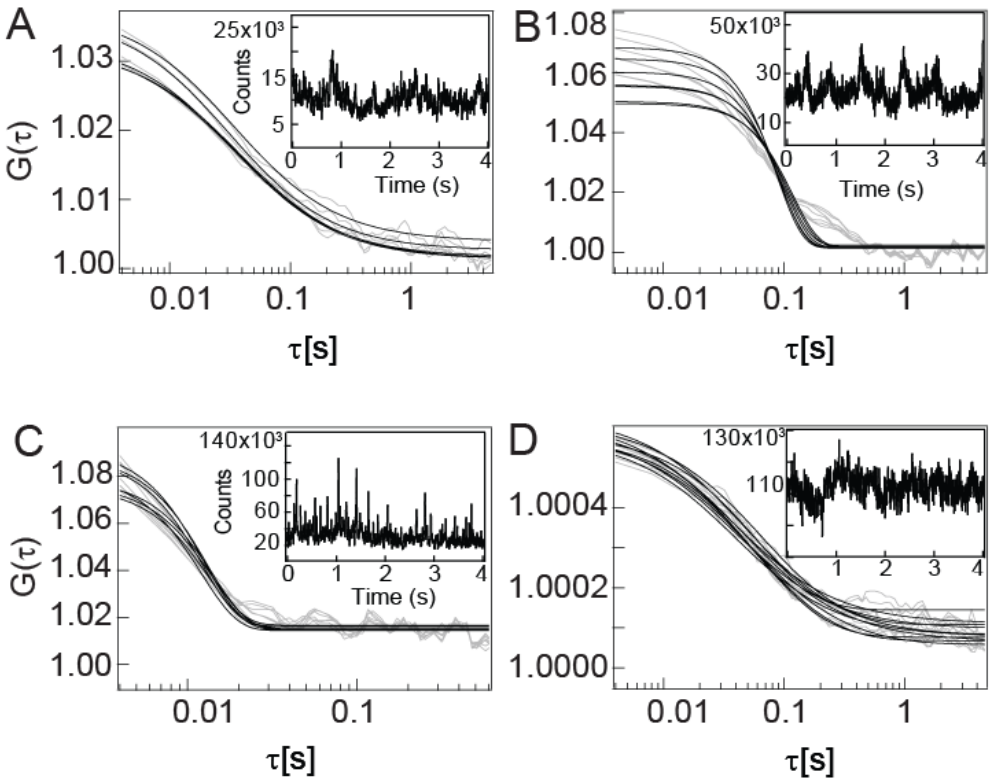

Fig. 3.5: Autocorrelations of systems exhibiting diffusion and/or flow. The black lines are the fits to the data (gray lines). Lipid diffusing on a supported lipid bilayer (diffusion), immobilized quantum dots moved with a velocity of 10 μm/s (slow flow), immobilized quantum dots moved with a velocity of 100 μm/s (fast flow) and lipid diffusing on a supported lipid bilayer moved with a velocity of 10 μm/s (diffusion and flow) are shown in A, B, C and D respectively. The flow data, created by moving a microscope stage with a stepping motor at speeds of 10 and 100 μm/s, causes some periodic artifacts in the intensity traces (insets) and deviations of the ACFs from their theoretically predicted form as seen here.

Table 3-1: Parameters retrieved from autocorrelations

Correlation type	D (μm^2/s)	v (μm/s)	w
Diffusion	2.9 ± 4.2	-	0.40 ± 0.08
Slow flow	-	10 ± 14	1.94 ± 3.80
Fast flow	-	97 ± 170	2.10 ± 5.00
Diffusion and flow	3.9 ± 4.5	9 ± 4.8	1.76 ± 1.46

mean ± standard deviation where the standard deviation is the standard deviation associated with the global fitting of the data and not the standard deviation from various trials.

The covariance matrix in this case is shown in Table 3-2. It is seen that generally D and N which measure two different properties in FCS are assumed to independent, but due to the presence of PSF, they are inversely related to each other. This can also be understood by performing a first order Taylor's series expansion of the autocorrelation function. The details are provided in Appendix 13.

$$g(\tau) = \frac{a^2}{\sqrt{\pi}} \frac{1}{\left(\frac{4D\tau}{w_0^2} + 1\right) N w_0^2} \qquad \textbf{3-36}$$

As seen from Eq. 3-36 and Table 3-2, an increase in PSF led to an increase in D and a decrease in N as seen in Fig. 3.6. Hence it is crucial to accurately determine the PSF in order to obtain correct estimates of D and N. Further, in the case of diffusion, the PSF cannot be less than the theoretical prediction in EMCCD of 0.6 as seen in Table 3-1. Hence, we need to resort to cross-correlation to estimate the PSF and the transport properties.

3.3.1.3 Cross-correlation functions (CCF) for diffusion and flow

Cross-correlations were performed for systems exhibiting diffusion, flow, and a combination of diffusion and flow, on areas of 3×3 binning for reasons described in Sec. 3.3.1.2. In the cases where flow is present in the system, the flow direction was along the horizontal positive x direction. The dependence of the cross-correlation on the relative position of two areas in space was investigated by choosing the central pixel and cross-correlating this central pixel with all surrounding pixels in all directions. This procedure allowed us to study simultaneously CCFs with different angles in respect to the flow.

In the rest of the thesis, we refer to the CCF between two areas A and B, in which B is displaced with respect to A along the positive x- or y-direction, as the forward CCF or CCF_{AB} if the correlation has been calculated as $\langle F_A(t)F_B(t+\tau)\rangle$ and as the backward CCF or CCF_{BA} if the correlation has been calculated as $\langle F_B(t)F_A(t+\tau)\rangle$.

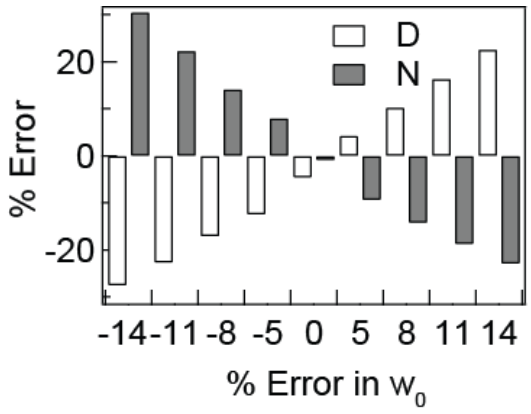

ACF	D	N	PSF
D	1	-1	1
N	-1	1	-1
PSF	1	-1	1

Fig. 3.6: An error in *PSF* leads to an error in *D* and *N*. The errors in *D* and *N* are of a simulated autocorrelation curve are inversely related. The details of the simulation are provided in Sec. 4.1.1. **Table 3-2: ACF Covariance matrix.** This is supported by the correlation matrix obtained while fitting an autocorrelation curve which shows a positive (negative) correlation between *PSF* and *D* (*N*).

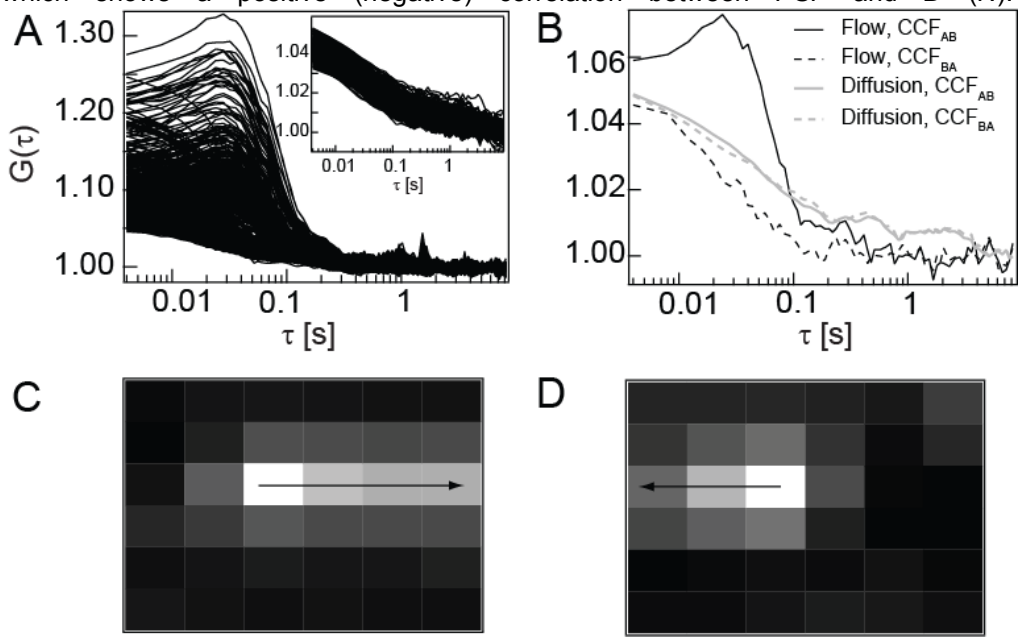

Fig. 3.7: Forward and backward cross-correlations of diffusion and flow. 2 distinct populations are seen only in A and not in the inset since the forward cross-correlation along the direction of flow exhibit a peak while the cross-correlation against the direction of flow does not. The forward and backward cross-correlations in diffusion shown in the inset in A do not exhibit any differences since diffusion is a random process. Characteristic forward and backward cross-correlations from the above two processes are shown in B. The maps in C and D show the values of the maxima of the CCF between the center pixel and the surrounding pixels for flow only. C (D) represents the values for flow along the horizontal +*x* (-*x*) direction.

This means in our setup, for instance, that forward CCFs along the *x* direction are parallel and backward CCFs along the *x* direction are anti-parallel to the flow direction. The presence of flow can be easily identified in a forward CCF, i.e. the CCF along the flow direction, by the appearance of a peak, representing the transition

time of a particle from area *A* to area *B*. This peak is absent in the backward CCF. In the *y* direction, forward and backward CCFs are not expected to show any peaks since they are orthogonal to the flow in our case. For diffusion in an isotropic phase, the forward and backward CCFs are symmetric.

Pseudo-autocorrelations in flow measurements

To calculate the spatial cross correlation between two binned regions, the "cross talk" of the fluorescence intensity originating from one of the binned regions and contributing to the fluorescence intensity of the other region must be evaluated. A distance of 4 pixels has been suggested for EMCCD based system[93]. Since, the spatiotemporal cross correlations performed here are less than 4 pixels; there arises a pseudo-autocorrelation in these calculations. When the distance between the regions of separation decreases, the cross talk increases, as a result, there is a higher contribution of the pseudo-autocorrelation term to the evaluated cross-correlation function. The issue of pseudo-autocorrelation has been tackled by subtracting the forward and the backward cross-correlations[100, 135-136]. The correlation in the direction against the flow is a decaying curve which is only due to the pseudo-autocorrelation between these two regions. Hence for the analysis of measurements of flowing samples in the absence of diffusion, the backward CCF is subtracted from the forward CCF. If this analysis is performed for directed transport then the characteristic peak for flow in the CCF becomes more symmetric. For all other measurements no subtraction is performed since the subtraction removes all information on processes, such as diffusion, which contribute equally to the forward and backward CCFs.

Split integration

The correlation between two arbitrary areas, each one defined by a group of pixels on a CCD, can be expressed as the sum of all possible correlations between the two groups of pixels of the two areas. Therefore, the correlation between two areas *A* and *B* containing *m* and *n* pixels in arbitrary arrangement, respectively, is just the sum of all possible correlations $m \times n$ between all pixels of these two areas. In this case the

correlations have to take account of the basic size of a pixel d=284 nm and of the distances in x and y direction between the m and n pixels $r_{x,mn}$ and $r_{y,mn}$.

$$G_{AB}(\tau) = \sum_{i=1}^{m}\sum_{j=1}^{n} g(\tau; r_{x,ij}, r_{y,ij}) + G_{\infty} \qquad \textbf{3-37}$$

The cross correlations of 3×3 binned regions with overlap, i.e. regions which are separated by only one or two pixels can be suitably decomposed to reveal the cross- and the autocorrelations. The values recovered from the fit indicate that the values recovered from the cross-correlation are closer to the expected value whereas the value retrieved from the autocorrelation is not precise and accurate. Only the ACF has a higher standard deviation when compared to the mean similar to the data in Table 3-1. This analysis suggests that cross-correlation must be performed between non-overlapping regions. Since we performed the cross-correlation with 3×3 binning, areas have to be shifted by at least 3 pixels to avoid overlap. The above analysis can be extended to cross-correlations between regions of any shape and size. In the case of non-rectangular regions, the regions must be broken down into its constituent rectangular or square regions and the cross-correlation has to be carried down between the smaller regions.

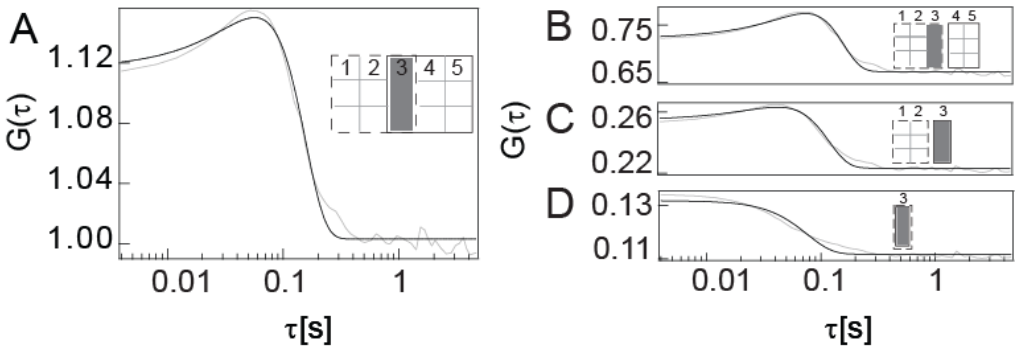

Fig. 3.8: Decomposition of correlation into auto-and cross-correlations. A shows the CCF for the full areas. This CCF is calculated between the lines (1, 2, 3) and (3, 4, 5). This CCF can be decomposed into CCFs between lines (1, 2, 3) with lines (4, 5) in B, the CCF between lines (1, 2) and line (3) in C and the ACF of the overlapping line (3) in D. The sum of the correlations in B, C and D result in the correlations in graph A for fits (black lines) and data (gray lines). Please note that the correlations for the sub regions in B, C and D have all been normalized to the total intensity and thus will not individually converge to G_{∞} =1 at long times, although their sum does.

Table 3-3: Decomposition of a CCF into its constituent ACF and CCFs

Correlation type	v (μm/s)	w
Total CCF (Fig. 3.8 *A*)	10 ± 0.3	2.46 ± 0.18
Constituent CCF – 1 (Fig. 3.8 *B*)	9.6 ± 0.2	2.08 ± 0.08
Constituent CCF – 2 (Fig. 3.8 *C*)	10 ± 0.4	2.02 ± 0.18
ACF (Fig. 3.8 *D*)	13 ± 495	2.06 ± 94.8

The standard deviation reported is the standard deviation obtained due to the curve fitting and is not the standard deviation due to many trials.

Table 3-4: Influence of w_0 on fitting of CCF

Type	w	D (μm^2/s)	v (μm/s)
Diffusion	0	4.9 ± 0.5	--
	0.42	4.6 ± 0.5	--
	Fitting parameter	2.6 ± 0.1	--
Slow Flow	0	--	No convergence
	0.42	--	9.1 ± 0.3
	Fitting parameter	--	8.9 ± 0.3
Fast Flow	0	--	No convergence
	0.42	--	90 ± 7.6
	Fitting parameter	--	94 ± 6.9

Fitting cross-correlation data

The major difficulty in fitting autocorrelation data was that the simultaneous fitting of D, N, v and w_0 was not possible. Hence the effect of w_0 was first studied on the cross-correlation of 3×3 binned non-overlapping CCF. It is seen from Table 3-4 that flow parameters are not affected by w_0 irrespective of whether w was fixed at 0.42 or as a fitting parameter. But, it is seen that in the case of diffusion, the value of the PSF plays an important role in determining the value of D. In the case of cross-correlation of diffusion, if w is not left as a free parameter, instead fixed at 0 or 0.42,

it cannot fit the raw data properly. This can be seen from the residuals. The fits are shown for w_0=0 in Fig. 3.9. Similar fits were observed for w=0.42. Hence the convergence of w was checked in the next section.

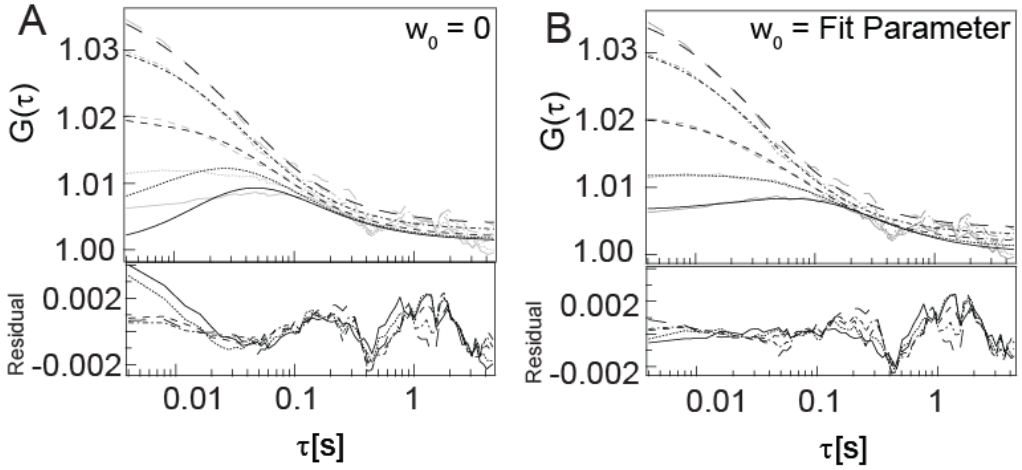

Fig. 3.9: Influence of w_0 on fitting of CCF. ACF and CCF along the horizontal of 3×3 binned regions of lipid diffusing on a 2D lipid bilayer (diffusion) fitted with equation in Appendix 6. w_0 was fixed at 0 in A whereas it was a fit parameter in B. The residuals are plotted below the respective graphs. As seen in the figure, w_0 =0 gives us acceptable fits in the case of 3×3 binned data from a system exhibiting diffusion or auto-correlation and overlapping cross-correlation. In the case of w_0 as a fitting parameter, w converges to a value of 1.78 ± 0.02 if only the non overlapping regions are considered. The gray lines represent the data while the black lines represent the fits.

Convergence of w_0 in cross-correlation

The covariance matrix was used to check whether CCF could be used to independently fit parameters. As stated earlier in Sec. 3.3.1.2, for covariances less than ±0.99, no identifiability problems are observed. The entries in the covariance matrix are less than ±0.99 as seen in Table 3-5. Hence D and PSF are independent to each other as expected since they measure two different molecular parameters. The chi squared function obtained after curve-fitting exhibits a single minimum for cross-correlation enabling any non-linear fitting algorithm to successfully fit D, N and PSF independently unlike the autocorrelation function. The data presented is that of a simulated correlation curve. The details of the simulation are presented in Sec. 4.1.1. The simulation was actually performed with D=7 $\mu m^2/s$ and w=1.2. The cross-correlation function reaches the minimum exactly. Thus these simulated results suggest that any fitting program can accurately and precisely determine D and PSF

from cross-correlation functions. This is because in the case of cross-correlation, *D* is determined from the position of the peak and the peak position is predominantly determined only by *D* and is independent of PSF. The broadening of the peak is influenced by the point spread function.

Parameters from cross-correlation data

Non-overlapping cross-correlations were calculated and data were fitted with equations in Appendices 5 and 6. The overall quality of fits with 4-6 parameters is very good, as seen in Fig. 3.11.

Velocity

The retrieved speed obtained from cross-correlation analysis is close to the expected value of 10 and 100 μm/s in the cases of slow and fast flow, respectively as in Table 3-6. In the case of diffusion and flow, the retrieved value for the velocity is not as accurate as the value retrieved for the flow only case. In the case of diffusion and flow, the retrieved velocity, show somewhat lower values with higher error than when only flow is present, although the values fall into the expected range. This is very likely a problem of distinguishing flow and diffusion by a fit and depends on which of the two processes dominates. It can also be influenced by the separation between the two cross-correlated areas, because of the different time dependence of the displacement of diffusion and flow.

Table 3-5: Covariance matrix of cross-correlation function

CCF (3x3)	*D*	*N*	*PSF*
D	1	0.01	-0.65
N	0.01	1	0.06
PSF	-0.65	0.06	1

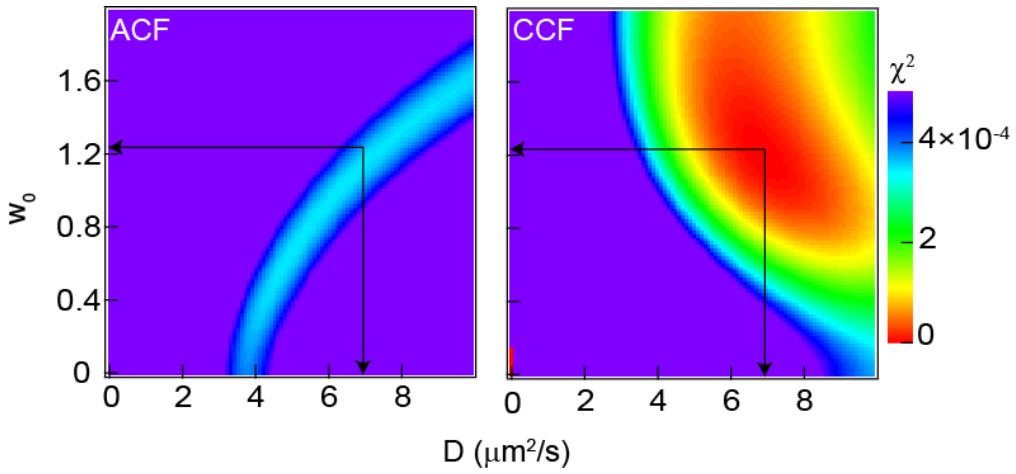

Fig. 3.10: CCF converges to a single minimum in χ^2. The values of *D* and *PSF* ($w=w_0\lambda/NA$) were fixed at the indicated values and the fitting was carried out for *N* and G_∞ for simulated functions of autocorrelation (ACF) and cross-correlation (CCF). (Sec. **4.1.1**). The χ^2 obtained after fitting is plotted above. The positions of the values of w_0 and *D* used in the calculation are shown by the arrows. The figure indicates that there is a single minimum in χ^2 in the case of CCF which can be reached by a curve fitting program unlike the ACF.

G_∞

Systematic deviations in G_∞ are expected for samples exhibiting bleaching. Here all the values in are close to the theoretical value of 1 as expected since the intensity traces do not show any bleaching as seen in the insets in Fig. 3.5.

PSF

Since the PSF of the microscope is finite in size, and on the order of the pixel size of our EMCCD, it has to be taken account of in the fitting of the CCFs. When w_0 was used as a fitting parameter, it can be observed that the values obtained for *w* are larger than the expected value of 0.42[129-132] as seen in Table 3-6. There are various possible reasons for the larger value of w_0.

1. Firstly, the side lobes of the diffraction pattern, in which ~ 10% of the emission is found, are still contributing to the pseudo-autocorrelation found in the CCFs of neighboring pixels[137-139].
2. Secondly, the samples measured are not ideally fulfilling the *z=0* condition which was assumed in the derivations up to now. Deviations of the *z* position

would increase cross talk between neighboring pixels due to the changes in the emission pattern in the image plane at z=0.

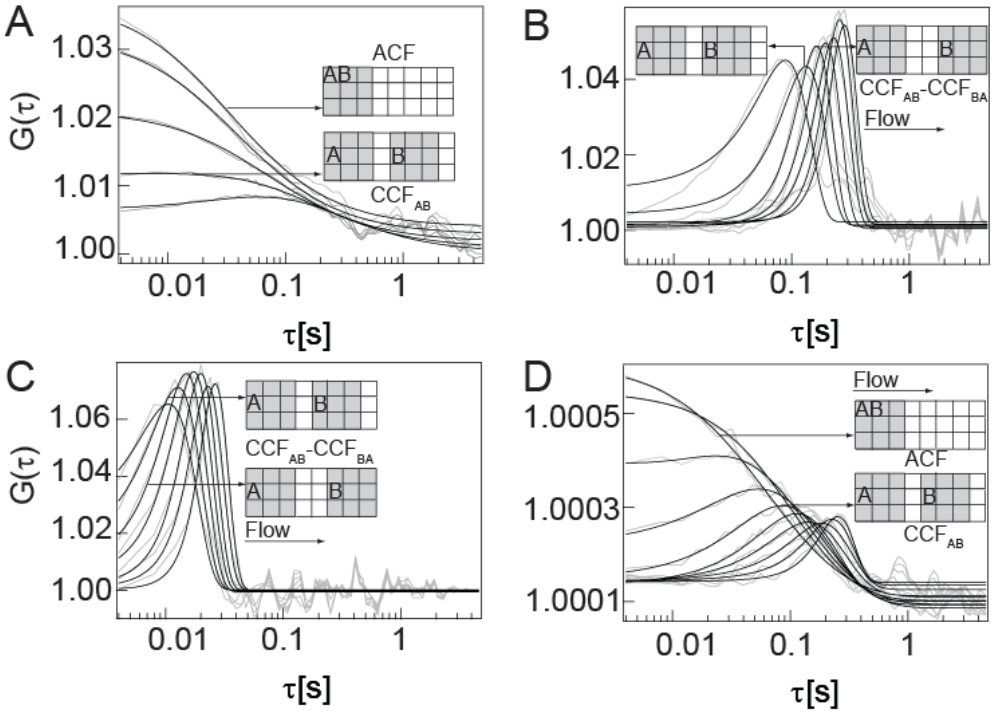

Fig. 3.11: Auto- and cross-correlations of diffusion and/or flow. The black lines are the fits to the data (gray lines). The insets are examples explaining the size and displacement of the two areas in the particular correlation functions. All correlations were performed on 3×3 binned regions. ACF and CCF along the diffusion, backward correlation subtracted CCF (CCF_{AB} - CCF_{BA}) along the horizontal of non overlapping regions of slow flow, backward correlation subtracted CCF (CCF_{AB} - CCF_{BA}) along the horizontal of non overlapping regions of fast flow and ACF and CCF along the horizontal for diffusion and flow are shown in A, B, C and D respectively.

Table 3-6: Parameters retrieved from cross-correlation functions

Parameter	Diffusion	Slow flow	Fast flow	Diffusion and flow
D [μm^2/s]	2.6 ± 0.1	--	--	1.6 ± 0.9
v [μm/s]	--	8.9 ± 0.3	94 ± 6.9	8.4 ± 1.5
G_∞	1.0005 ± 0.0003	1.001 ± 0.0006	0.9998 ± 0.0002	1.0001± 0
w	1.78 ± 0.02	1.48 ± 0.40	1.92 ± 0.24	2.12 ± 0.78

3. The expression for w_o was defined for paraxial optics. But at angles of incidence greater than the critical angle, this assumption is invalid and hence

the Gaussian expression for non-paraxial optics has to be used which has a factor of 0.44 instead of 0.42[129-132].

4. It is known earlier that the finite pixel size contributes to the blurring and decreases the localization accuracy[140]. This effect has been modeled by assuming the pixel to be a 2D uniform distribution and molecule can have its center anywhere in the field. This contributes to an uncertainty in the localization of the molecule. From probability theory, it is known that the standard deviation of a uniform distribution is $\frac{a}{\sqrt{12}}$ (Appendix 14). The same result can also be proved by deriving the variance of the convolved intensity distribution derived earlier (Eq. 3-19). The details of the derivation are in the Appendix 15. In our case this is evaluated to be 242 nm.
5. The finite exposure time also contributes to a blurring of the PSF. The effects have been quantified in the case of diffusion recently[141] and it is equal to $\sqrt{\frac{Dt_E}{3}}$ where t_E is the exposure time. In the case of flowing samples, the distance travelled during the exposure is vt_E and this contributes to the blurring.
6. Finally, the noise added by the EMCCD multiplication process has been effectively quantified and described in detail in Sec. 2.5.5.1and hence an excess noise factor of $\sqrt{2}$ needs to used.

All the individual noise sources have been quantified and added in quadrature. The exposure time was calculated to be 3 ms. At 10MHz, to transfer a 512×20 region, it would take 1 ms. For a time per frame of 4 ms, at 1 ms transfer time, the exposure time is 3 ms. The velocity was used at the set velocity of 10 and 100 μm/min. The D was assumed to 1.5 $\mu m^2/s$. It is seen here that CCF 3×3 bin 3 pixels apart yields estimations of *PSF* which are comparable to the estimated value based on theoretical consideration of noise factors as seen in Table 3-7 for

all the 4 cases. But it is seen that, the pixellation noise is 3 times of the theoretical value of *PSF* since 3×3 binning is used. Hence, in order to reduce the uncertainty in *PSF*, 2×2 or 1×1 binning needs to be done. From Table 3-4, it is known that *PSF* does not play a very important role to accurately determine the velocity if they are cross-correlated at longer distances when compared to the *PSF*. This is not true in diffusion. The solution to diffusion equation as in Sec. 2.1.2.1 shows that the number of particles drops as the squared exponential of the distance of separation between the cross-correlation regions. Hence, the CCF must be performed at non-overlapping regions close to each other. Hence *PSF* plays the most crucial role in diffusion.

Table 3-7: Uncertainty propagation in *PSF*

Error terms	Diffusion (nm)	Slow flow (nm)	Fast flow (nm)	Diffusion flow (nm)
Theoretical (nm)	89	89	89	89
Pixellation noise (nm)	242	242	242	242
Blurring due to diff (nm)	39	-	-	39
Blurring due to flow (nm)	-	30	300	30
σ_{final} (nm)	260	260	396	263
Multiplicative noise (nm)	364	364	554	368
w_0 (nm)	728	728	1108	736
Calculated w	1.78	1.78	2.6	1.82
Obtained	1.78 ± 0.02	1.48 ± 0.40	1.92 ± 0.24	2.12 ± 0.78
% Error	0	17	26	-16

The calculations were first performed using the PSF given in the references therein which used a different convention for the Gaussian as in Appendix 15 and they were converted in the last step. The width of both the Gaussians are inter-convertible. The width of the Gaussian in 3-1 is two times the width of the Gaussian described in appendix 15.

Influence of *PSF* in diffusion

This raises the question of how dependent the recovered sample properties are on the value of w_0. Hence to understand the effects of w_0 on cross-correlation, the data was subjected to binning of 3 different sizes [1, 2, and 3]. Cross-correlations of regions separated by 3 pixels along a line were chosen as the tool to understand the importance of w_0 in diffusion. The diffusion coefficient was fixed and allowed to vary from 2 to 4 $\mu m^2/s$ and w_0 was fixed and allowed to vary from 0.8 to 1.6 in different fitting trials. The goodness of fit can be ascertained by the χ^2 value of the fit. A large value of χ^2 indicates a poor fit of the model to the collected data. A contour plot of the value of χ^2obtained after fitting was made for all the 3 binned pixel sizes. The contour plot clearly reveals that the w_0 value converges after fitting (Fig. 3.12). There is a clear minimum which is observed in the contour plots.

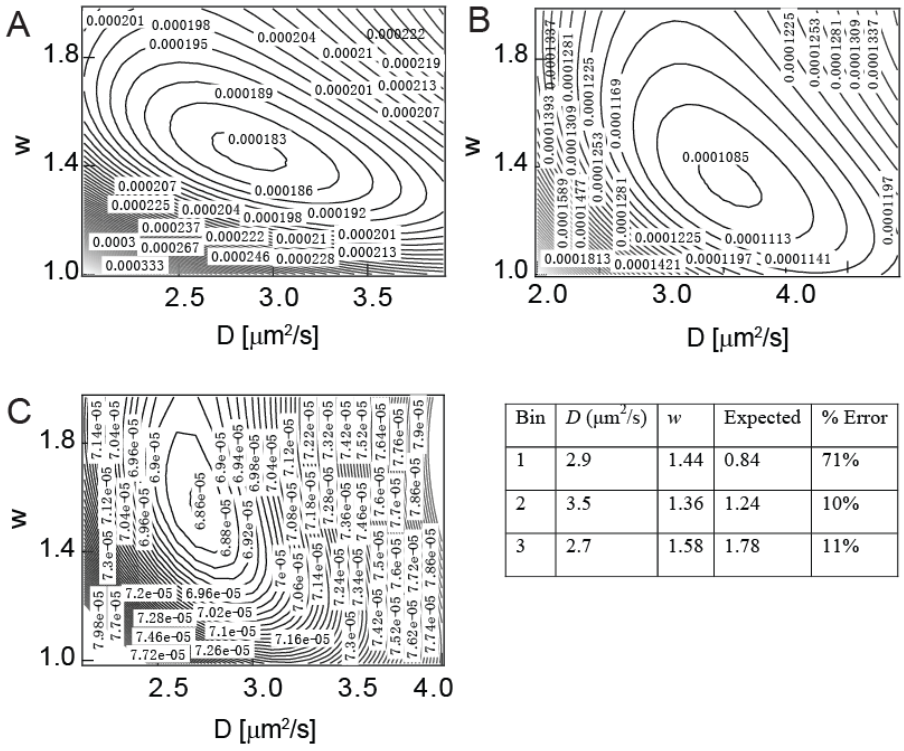

Bin	D ($\mu m^2/s$)	w	Expected	% Error
1	2.9	1.44	0.84	71%
2	3.5	1.36	1.24	10%
3	2.7	1.58	1.78	11%

Fig. 3.12: Contour plots of χ^2 value of CCFs. The areas were separated by 3 pixels for diffusion. The values are plotted against different values of w_0 and D for binning sizes of 1×1, 2×2 and 3×3 in A, B and C respectively. **Table 3-8: Error in *PSF* from CCF at different binning sizes.** D and w values obtained for the fitted curve with the minimum χ^2 when the fitting was carried out with D allowed to vary from 2 to 4 $\mu m^2/s$ and $w_{allowed}$ to vary from 0.4 to 0.8 for various binning sizes of cross-correlation of regions separated by 3 pixels for system undergoing diffusion

This analysis reveals that D can be fitted simultaneously in the presence of w_0 in the case of diffusion. As the size of the bin increases from 1 to 3, the expected w increases due to increase in localization uncertainty as expected. But it is seen that the experimental w does not follow the same trend as the calculated w. At the current sensitivity of EMCCD cameras, the SNR is not sufficient to get accurate estimations of PSF and hence the diffusion coefficients from CCF are not reliable as well. The CCF provides independent estimations of D, N and PSF unlike ACF but the estimations are not accurate due to the current day limitations of S/N ratios of the cameras. Hence, we need other methods to determine the PSF. Three different methods (ACF, ICS, fit free CCF) to find PSF are discussed below.

Determination of PSF by autocorrelation method

The autocorrelation doesn't yield reliable estimates only when all three parameters -D, N and PSF are free. But, when one of the values is fixed, they can be fitted independently of each other. Specifically, when the PSF is fixed for 1×1, the covariance between D and N is -0.9. As stated earlier, for values less than ± 0.99, there are no identifiability problems. Hence, upon fixing the PSF to a value, D and N can be fitted independently to each other. This raises the question of finding the value to fix PSF. Prior to the experiment, since the value of PSF is not known, an iterative method can be used.

The autocorrelation functions at different binned areas needs to be calculated (1×1 to 5×5). D is an intrinsic parameter of the particle and hence is independent of the binning area used to calculate the D. The data at various bin areas are fitted with various values of the PSF. D is an increasing or decreasing function of bin area for values of PSF less or greater than the PSF of the system respectively. The reasons for this behavior are discussed in detail in Sec. 3.3.1.2. The value of PSF which yields a D independent of the bin area is the PSF of the system. The discussion in the next chapter (Sec.4.2.1.1) shows that this D is the absolute diffusion coefficient of the molecule. This method is shown in Fig. 3.13 A where the PSF was fixed at 2 different

values, the theoretical value of 0.42 and the value obtained from CCF as in Table 3-6. It is seen that both the values do not yield a constant *D* with increasing bin size from Fig. 3.13 A. Instead, when the *PSF* was fixed at 0.7, the value of obtained *D* is constant with increasing bin size. Hence a value of 0.7 is the *PSF* of the system and the average *D* is 1.5 ± 0.6 $\mu m^2/s$.

The same method can be implemented differently. For bin areas>>*PSF*, *D* is independent of *PSF*. This can be seen from Fig. 3.13 C and D where the detection profiles were plotted for 2 different values of *a* for a fixed w_0. In the case where the size of the pixel is comparable to the *PSF*, the detection profile resembles the *PSF* as in C. Instead, it resembles the pixel size when the pixel size is five times that of the *PSF* as in D. Hence *D* obtained from autocorrelation of such areas is the reliable and absolute *D* since it can be fitted only by the knowledge of the pixel size. This *D* can then be used to determine the *PSF* from autocorrelation where bin areas are comparable to the size of the *PSF*. The value of *D* obtained from 5×5 binned data is 1.5 ± 0.6 $\mu m^2/s$. This method retrieves a value of 0.7 ± 0.4 for the *PSF* by fixing the *D* at 1.5 $\mu m^2/s$ for 1×1 binned data. The expected values of PSF incorporating the effects of the finite pixel size for various bin sizes were calculated and shown in Table 3-8. The value of PSF retrieved by this method (0.7) is close to the expected value based on theory of 0.84 (Table 3-8) when compared to CCF which yielded a value of 1.44.

Determination of PSF by Image Correlation method

Spatial cross-correlation can be performed to estimate the *PSF* by using ICS fitting models (Eq. 2-22). Typically, 20×20 pixel regions are captured in Imaging FCS. Such small regions do not yield reliable estimates from ICS which requires larger regions. A 32×32 region yields estimates with 10% relative error[142]. In this case, the value obtained is 0.62 ± 0.2 and the fit along with the raw data is shown in Fig. 3.13 B.

Determination of PSF by fit-free method

Cross-correlation functions can be used to estimate the absolute *D* of the molecule without any calibration or without any data fitting. When cross-correlations are performed between pixels which are separated by a certain distance, the cross-correlation function exhibits a peak, which shows the average time it takes for the particles to diffuse from the first pixel to the other pixel as seen in Fig. 3.15. For free diffusion,

$$D = \frac{(ma)^2}{4\tau_{G(\tau)_{\max}}} \qquad \textbf{3-38}$$

where the pixels being cross-correlated are separated by *m* pixel units and $\tau_{G(\tau)max}$ is the value of lagtime at which the cross-correlation function exhibits a maximum. For a simulated *D* of 1 $\mu m^2/s$, *m*=2 and 3 yield *D* of 1.01 ± 0.36 and 0.95 ± 0.30 $\mu m^2/s$ respectively. Hence this method yields accurate and absolute *D*. This *D* can later be used to determine the *PSF* from autocorrelation of areas where the bin area is comparable to the size of *PSF*.

This method is the fastest when compared to others since there is no data fitting and any automatic peak finding program can be used to obtain the position of the peaks. Here, the *findpeak* function in Igor Pro© was used to identify the peaks from the cross-correlation curves. There are two factors contributing to the error in this method. Firstly, the peaks must be clearly distinguishable for any peak finding function to discriminate it from the rest of the correlation function. The distinguishability of the peaks is dependent on the S/N ratio and can possibly lead to larger standard deviations for this method. Hence, currently this method is limited to simulated data (Sec. 4.1.1). Secondly, the broadening of the peak is dependent upon the bin width used to calculate the correlation at and around the peak position. Peaks which appear at lagtimes calculated using binwidths much higher than the time resolution of the camera cannot be distinguished. The advantages and disadvantage of

each of the methods are discussed in Table 3-9. With improvement in sensitivity of cameras, CCF based methods would be the best since they are fast and yield estimates of *D*, *N* and *PSF* from single fits without the need for any iteration.

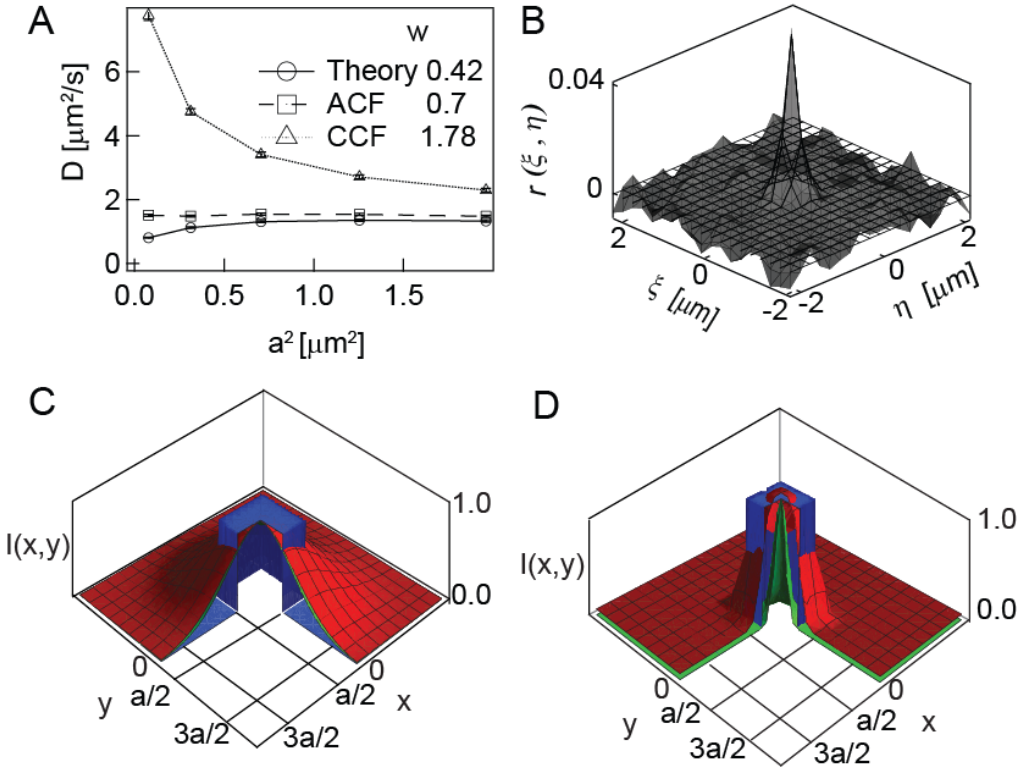

Fig. 3.13: PSF determination by autocorrelation and ICS methods. A is a plot of the *D* obtained from 5 different bin sizes with *w* fixed at 3 different values. At the theoretical value of 0.42, the diffusion coefficients increase with bin size. At the value obtained from CCF, they decrease with increasing bin size. The value of *w* which yields a constant *D* was found to be 0.7. B is a plot of the spatial autocorrelation function and its fit. The detection profile in TIRF-FCS was plotted for 2 different values of *a*/*w* by changing the value of *a*. In C, the value of *a*/*w* was set to 1.5 whereas it was set to 7.5 in D. At higher values, as in D, the profile shown in red resembles the pixel shown in blue. Instead, at lower values, the red profile resembles the *PSF* shown in green. Hence, bin areas>>*PSF*, *D* is independent of *PSF* and can be determined only by the knowledge of pixel size.

Table 3-9: Summary of various methods to determine PSF

Method	Value	Advantage	Disadvantage
ACF	0.7	Most accurate	It is an iterative process.
CCF-fitting	1.78	*D*, *N* and *PSF* from single fit	Inaccurate estimates at current SNR of cameras
CCF-findpeak	-	Fit free	Not feasible using the SNR of current cameras
ICS	0.62	Can be done on every image in the stack	Needs more than 20×20 region for accurate analysis

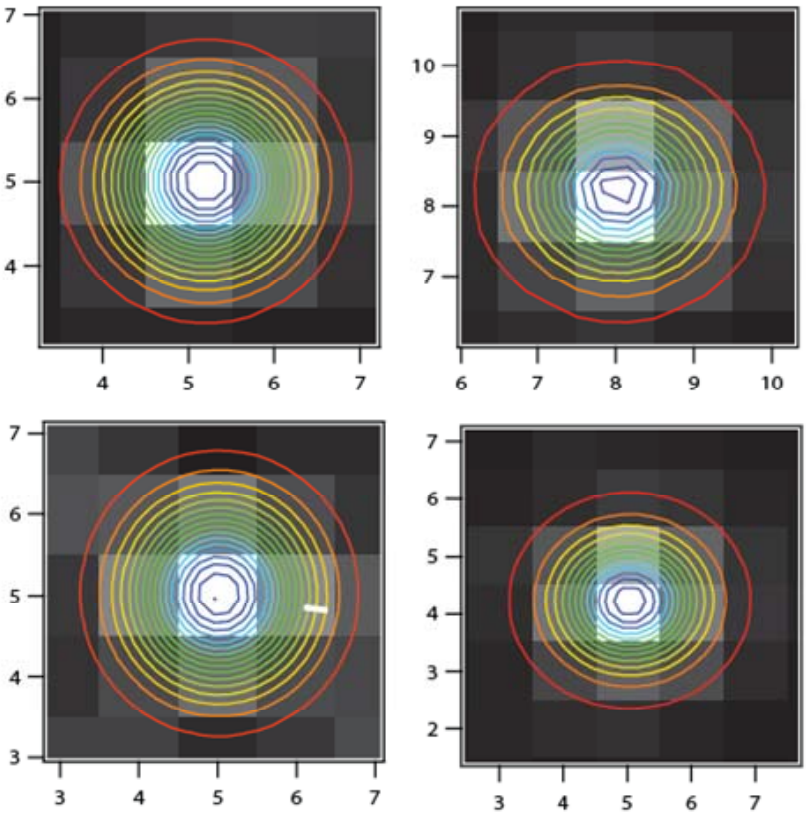

Fig. 3.14: Cross-validation of PSF measurements: The value of the PSFs obtained were cross-checked by imaging 40 nm beads and fitting a 2D Gaussian to each of them. The ACF analysis provided a PSF of 320 nm whereas this methods provides a PSF of 334 nm indicating that the values obtained from the ACF method are quite reliable.

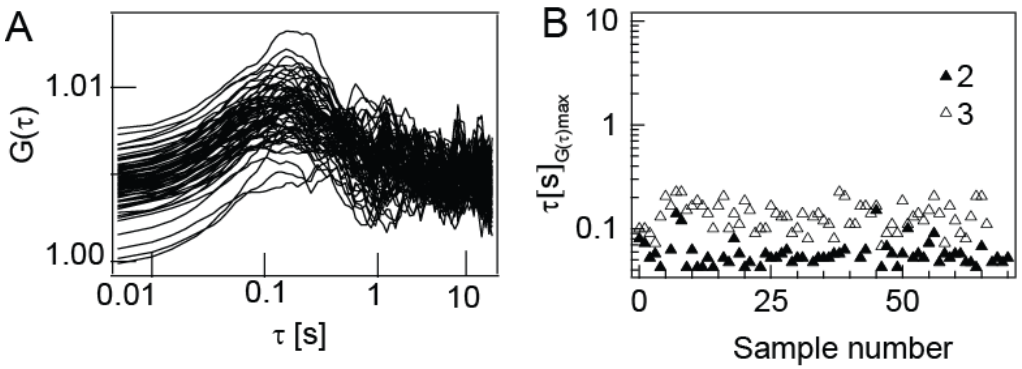

Fig. 3.15: Fit free determination of PSF. The cross-correlations between different pixels yield a peak which provides an estimate of the transit time needed to traverse the distance. Using distance-time relationships of free diffusion, accurate *D* can be estimated. This *D* can be used to estimate the *PSF* of a system from autocorrelation functions. A shows a set of cross-correlation functions for regions 3 pixels apart. B shows the peak positions for samples, where the distance between the pixels are 2 and 3.

Diffusion coefficient

Diffusion in lipid bilayers was modeled by Saffman and Delbrück and they derived an expression for the diffusion coefficient[143].

$$D = \frac{k_B T}{4\pi\mu_m h}\left(\ln\left(\frac{\mu_m h}{\mu_w R}\right) - 0.5772\right) \qquad \textbf{3-39}$$

with k_B = 1.38×10^{-23} JK^{-1}. The height (h) of a POPC bilayers has been measured and is found to be 3.5 nm[144]. The radius can be determined from the partial molecular volume of POPC. Theoretical and experimental studies found the molecular volume to be 1.25 nm^3 [145]. Assuming the lipid to be a cylinder, the cross-sectional area is found to be 0.71 nm^2 which shows that the radius (R) is 0.5 nm. The viscosity of water[146] (μ_w) at 298 K and at atmospheric pressure is 0.9 mPa s. The viscosity (μ_m) of POPC bilayers[147] has been measured to be 0.18 Pa s. Substituting these values, the diffusion coefficient is found to be, 6 $\mu m^2/s$. Since the measurements are made on SLBs, it is known that the diffusion is hindered due to the presence of the support and the diffusion coefficients are lower by a factor 2[148]. Hence the effective diffusion coefficient predicted from theory is 3 $\mu m^2/s$.

The diffusion coefficient has been estimated by two calibration free methods, namely z scan FCS[148-149] and two-focus FCS (2f FCS)[150] to be 2-4 $\mu m^2/s$. The D has been found be 1.8 and 4 $\mu m^2/s$ using FRAP and SPT[128]. Overall, the value of the value of D obtained from autocorrelation (1.5 ± 0.6 $\mu m^2/s$) is comparable to the values obtained from theory and literature. But, it is lower than those measured from other techniques. This could be attributed to the limited time resolution of the EMCCD (4 ms) used in this measurement. It is shown in a later section (Sec. 5.2.2) that with better time resolution (0.5 ms), the obtained D (2.6 ± 1.0 $\mu m^2/s$) is close to the expected value from theory and literature.

Number of particles

The autocorrelation analysis reveals the number density of the particles to be 50 μm^{-2}. As discussed above, the cross-sectional area is 0.71 nm^2, theoretically, in an area of 1 μm^2, assuming complete coverage by the lipid molecules, the surface will be covered by 1.4×10^6 lipid molecules. The dye to lipid ratio is 0.01% in the experiments. Hence the surface will be covered by $0.01\times0.01\times1.4\times10^6 = 140$ dye molecules. Hence theoretically, the number density is expected to be 140 μm^{-2}. This value is in the same order as that obtained from the experiments of 50 μm^{-2}.

3.3.1.4 Comparison of CCF versus ACF

Although autocorrelation analysis can be used to determine the flow and diffusion parameters, the direction of flow cannot be determined using autocorrelation analysis. Cross-correlations need to be performed in order to determine the direction of flow. Hence it is necessary to resort to cross-correlation analysis to retrieve flow parameters. In the case of flow, the cross-correlation has to be carried out between areas which are more than 3 pixels apart. In this case, the distance does not have a very strong influence on the amplitude, in particular when the CCF is calculated along the flow direction. At longer distances, the effect of w_0 is reduced and hence accurate and precise parameters for the velocity can be obtained.

In the case of diffusion, the effect of w_0 is negligible only when cross-correlations are calculated at longer distances than w_0. But, in those cases, the amplitude drops considerably. Hence, in diffusion, autocorrelations are the best way to obtain diffusion coefficients. These autocorrelations cannot be independently fitted for *PSF*, *D* and *N*. The *PSF* has to be determined first from the autocorrelation and then fixed to yield estimates of *D* and *N* from autocorrelation.

It should be noted that the diffusion coefficient as well as the size of the point spread function are extracted from the fit directly and a separate calibration is not needed for ITIR-FCS. This is an advantage compared to single spot FCS measurements, since the measured diffusion coefficients and flow velocities are not

dependent on the accurate knowledge of the diffusion coefficient of a standard dye. Therefore, ITIR-FCS is a calibration-free method to retrieve the parameters of flow and diffusion. This is unlike conventional FCS where the diffusion coefficient is not measured directly but is determined over the diffusion time which is dependent on the width of the confocal volume. While this section was a detailed discussion on two of the estimates from Imaging FCS, mobility and number, the next section is a discussion on the third parameter obtained from Imaging FCS-heterogeneity.

3.3.2 Methods to characterize the heterogeneity from Imaging FCS

The cell membrane is a complex organization made up of hundreds of lipid species and thousands of different proteins. Initially, the cell membrane was assumed to be a homogenous sea of lipids in which the proteins were embedded referred to as fluid-mosaic model[4]. Currently, the lipid rafts model states that that certain lipids and proteins arrange themselves into domains of various sizes below the optical resolution limit bringing in heterogeneity into the structure of the cell membrane[5-6]. Heterogeneity in Imaging FCS can be characterized by two different methods, using diffusion laws[69] and ΔCCF.

3.3.2.1 Diffusion law

The diffusion law states that the average transit time of a tracer molecule through circular areas of different sizes scale linearly with the size of the area for free diffusion. Theoretically, when extrapolated to an area of size zero, a transit time of zero is expected. Any non-zero transit time upon extrapolation is an indication of heterogeneity. The diffusion law is obtained by plotting diffusion time against the observation area. Specifically, a positive intercept is an indication of domains leading to hindered diffusion. This could be explained by the fact that, in the presence of domains, while the probe area is on the same size of the domain, the observed diffusion coefficient is that inside the domain. Hence, the diffusion time is longer than the case when the area of observation is much larger than the domain size, that the observed diffusion time is that of the bulk membrane leading to a shorter

diffusion time. This non-linearity can be approximated with a line with a positive intercept. A negative intercept is indicative of hindered diffusion due to a meshwork. The molecule is trapped in individual areas of mesh and cannot cross the borders of the mesh freely. As a result, when the observation area is the same area of individual mesh entities, the tracer exhibits free diffusion with a shorter diffusion time when compared to when the observation area is bigger than the mesh where it exhibits hindered diffusion due to the trapping effects of the mesh. As a result, the intercept is negative.

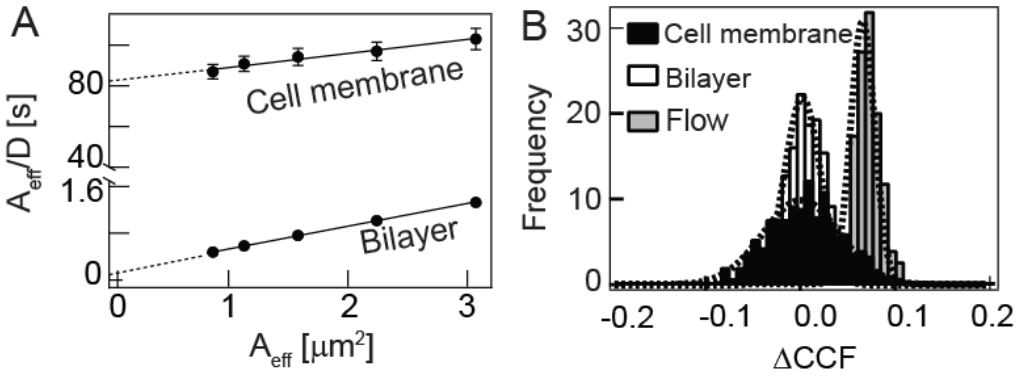

Fig. 3.16: Heterogeneity metrics from Imaging FCS. A is a plot of diffusion laws from simulated data. A simulated domain model of cell membrane has a positive intercept while a simulated lipid bilayer has an intercept of zero. Details of the simulation are in Sec. 4.1. B is a distribution of *ΔCCF* values from diffusing and flowing samples. The average *ΔCCF* value is zero in the case of diffusing samples while flowing samples have a non-zero *ΔCCF* value. In the case of diffusing samples, the cell-membrane has a broader distribution when compared with the distribution obtained from a lipid bilayer indicating that the cell-membrane sample is more heterogenous when compared with the lipid bilayers.

The FCS diffusion law has been already successfully demonstrated in *z*-scan[151-152], super-resolution[153-154], and spot variation[155] based FCS techniques. In ITIR-FCS, these measurements are particularly easy to perform since in an image various detection areas can be selected by pixel binning post-acquisition, i.e. the grouping of single pixels into larger areas by summing their values. The minimum observation area $A_{1,\,eff}$ which can be acquired in imaging FCS is the single pixel size a^2 convoluted with the *PSF (i.e.,* $A_{1,\,eff} = a^2 \otimes PSF$*)*, where a is the side length of a pixel. For n×n binning the observation area $A_{n,\,eff} = (n \times a)^2 \otimes PSF$. Pixel binning can

be performed even after the measurement and thus a single measurement contains all possible detection areas that are multiples of the size of a single pixel. Thus a single ITIR-FCS measurement is sufficient for a test of the diffusion law.[156]

3.3.2.2 *ΔCCF* distribution

Differences in cross-correlation function have been used in a variety of ways to characterize systems away from equilibrium. It has been used to measure the amount of flux in a chemical reaction[101], to perform temporal ordering of events of proteins involved in a pathway[157] and to separate the different layers of flow in turbulent flow[158]. Here, we use the same metric to characterize the differences in diffusion behavior between adjacent pixels and to separate the pixels which show pure diffusion from those which don't. The cross-correlation between adjacent pixels is calculated and subtracted from one another, the area under the curve is calculated and the distribution of all the values is plotted. In the case of systems exhibiting isotropic diffusion, the forward and the backward correlations are identical because particles are free to diffuse randomly and follow no particular direction (Fig. 3.7 A and B). In such a case, when the forward correlation is subtracted from the backward correlation, a flat profile is obtained. For an ideal, free diffusion, such a distribution will be a delta function centered at zero. But due to the finite length of the time-series data collected, there is an inherent broadening and a distribution centered at zero is obtained for free diffusion. The broadening is increased for systems with heterogeneity. The width of the distribution serves as a metric for heterogeneity (Fig. 3.16 B).

For non-isotropic processes like flow, the correlation in the direction of the flow, exhibits a maxima at the time it takes to travel from the first region to the second region being correlated. The intensity observed in any pixel is a sum total of the intensity of the pixel and the contributions of cross-talk from pixels which are separated from each other at distances on the order of the PSF. This cross-talk leads to a pseudo-autocorrelation term. Hence, the correlation in the direction against the

flow is a decaying curve which is only due to the pseudo-autocorrelation between these two regions. Hence, the subtracted correlation profiles are not flat leading to the area under the resulting curve being a non-zero number. Thus *ΔCCF* distribution serves as a way to distinguish processes exhibiting directed transport alone or in combination with other processes. The reader is referred to Appendix 16 for a theoretical treatment of the above phenomenon.

$$\Delta CCF = \int_0^{\Psi} \left(CCF_{AB}(\tau) - CCF_{BA}(\tau) \right) \quad d\tau \qquad \textbf{3-40}$$

where Ψ is the maximum lag time

Hence the *ΔCCF* approach can in principle be used to map membrane dynamics. In order to test this idea, we performed several measurements. First, on flattened GUVs the most prominent boundary is the boundary of the vesicle and the solution phase, and the *ΔCCF* images clearly show these boundaries and possibly other boundaries on the vesicles (Fig. 3.17). Second, mixed lipid bilayers consisting of a liquid ordered and a liquid disordered phase, showed phase boundaries which can be detected by *ΔCCF* images (Fig. 3.18). Third, we performed measurements on live-cells under different conditions (Fig. 3.19).

ΔCCF maps of immobilized lipid vesicles

The original intensity image of the GUV is plotted alongside the *ΔCCF* images with 1×1 and 3×3 binning for comparison (Fig. 3.17). The *ΔCCF* images clearly distinguish the GUV from the external surroundings. The 1×1 binned image resembles the original intensity image. It is to be noted that these are flattened GUVs on the cover slide and are hence multilamellar. The results presented here will not differ based on the lamellarity of the lipid preparations. Values on the labeled GUV membrane are similar and the GUV is seen as a smooth surface.

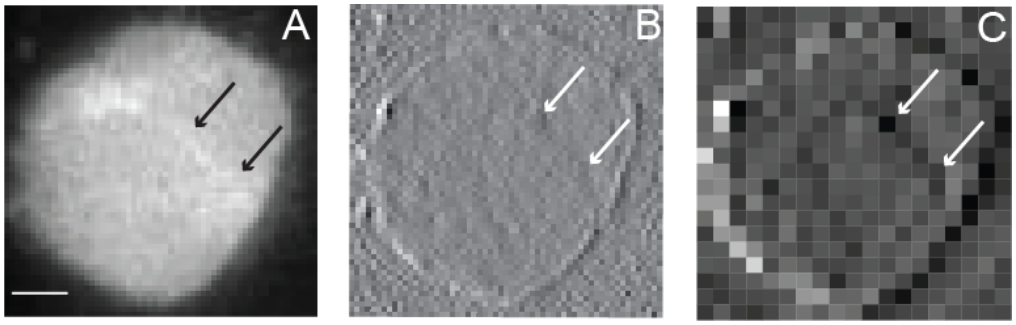

Fig. 3.17: Detection of borders by *ΔCCF*. Image of a surface immobilized GUV is shown in A. The GUV is flat due to the strong interaction between biotinylated lipids and surface immobilized avidin. For B and C, we calculated CCF_{AB}-CCF_{BA} along the horizontal for neighboring non-overlapping pixels. The results were integrated to obtain one single value which we refer to as *ΔCCF*. The scale used in these graphs reaches from the minimum (black) to the maximum (white) values thus obtained. In general black values are negative and white values positive. B is a *ΔCCF* map of 1×1 binned data for the GUV in A. C is a *ΔCCF* map of 3×3 binned data for the GUV in A. The borders and areas on the vesicle membrane (arrows) can be clearly distinguished according to their different diffusion behavior. It should be noted that in general the diffusion behavior does not have to be analogous to the intensity image. The scale bar represents 3 µm.

However, outside the vesicle, the CCFs are determined only by noise and consequently the *ΔCCF* fluctuates freely. The boundary of the vesicles can be easily detected. The *ΔCCF* image for 3×3 binning shows clearly the boundary of the GUV. The left and the right boundaries appear differently since the transition at the two boundaries is not the same due to our definition of the forward and backward CCFs. In the left boundary, the correlation of the liquid phase is subtracted from the correlation of the lipid phase whereas in the right boundary, the lipid phase is subtracted from the liquid phase. Interestingly, there are some more boundaries visible within the GUV membrane, albeit not as visible as the vesicle boundary. These boundaries, observable as well in the intensity images, may correspond to regions with a different diffusion coefficient which were created during vesicle immobilization (see arrows in Fig. 3.17). It has to be noted that the GUVs presented here are immobilized and spread on surfaces and hence these are multilamellar structures. This method will yield borders irrespective of whether the GUVs are bilayer or multilayered structures since only systematic deviations in diffusion processes are imaged by *ΔCCF*.

ΔCCF images on supported mixed lipid bilayers

The original intensity image of the phase separated bilayer is plotted alongside the *ΔCCF* images for comparison (Fig. 3.18 A and B). The *ΔCCF* images clearly distinguish the L_o and L_d regions. The bottom region is characterized by homogenous values of *ΔCCF* while the top region is characterized by a broader distribution of *ΔCCF* values. The L_o region appears more granular when compared to the L_d region. This is in agreement with the CCF values of GUVs where the labeled GUV was characterized by homogenous values while the outside appeared more granular. The cross correlations and autocorrelations for this measurement are provided in Fig. 3.18 C, D, E and F.

Characterization of cell membrane organization by *ΔCCF*

The distributions of the different lipid classes that make up cell membranes, including sphingolipids, cholesterol and glycerophospholipids, are highly heterogeneous. The membrane exhibits a range of diffusion coefficients due to the presence of regions of lower mobility called "lipid rafts" embedded in a fluid phase of higher mobility. Lipid rafts have been reviewed in recent literature[6].

A definition coined at the 2006 Keystone symposium on lipid rafts and cell function states, "lipid rafts are small (10-200 nm), heterogeneous, highly dynamic, sterol- and sphingolipid-enriched domains that compartmentalize cellular processes"[5]. MβCD is commonly used to disrupt rafts as it extracts cholesterol from membranes. Reducing cholesterol content in cell membranes leads to a mislocalization of raft associated proteins, and the loss of raft-like diffusion behavior[66, 159-160]. For the investigation of the cell membrane organization, we used SHSY5Y neuroblastoma cells, labeled with the sphingolipid binding domain (SBD) of the amyloid peptide Aβ. SBD was recently shown to have a similar diffusion behavior on cell membranes as Cholera Toxin B and thus functions as a good raft marker[66].

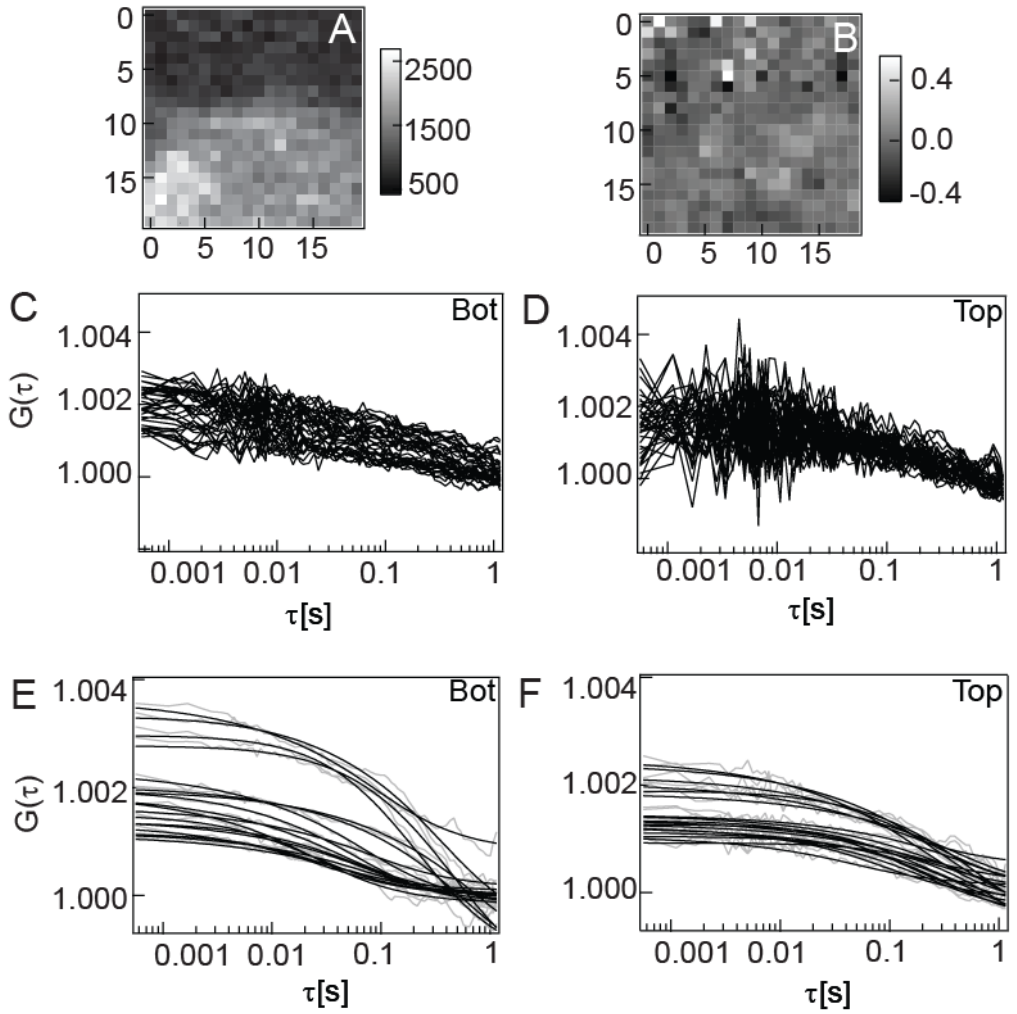

Fig. 3.18: Detection of borders between phase separated regions by ΔCCF. The image of a phase separated mixed lipid bilayers is shown in A. Rho-PE preferentially labels the L_d phase (bottom part) compared to the L_o phase (top part). *ΔCCF* image of the mixed lipid bilayer in A is shown in B. C and D show the cross-correlation functions on the L_d and L_o respectively. The CCFs in the unlabeled L_o are noisier than the labeled L_d phase. E and F show the ACFs for the L_o (D = 0.35 ± 0.31 μm^2/s) and L_d (D = 1.38 ± 1.25 μm^2/s) phase respectively.

The diffusion coefficient can be used as a measure of the fluidity of the membrane. Upon addition of MβCD, the average diffusion coefficient of membrane bound SBD-TMR (0.7 ± 1.1 μm^2/s) increases over a time interval of 30 minutes by about a factor 2-3 (1.7 ± 1.1 μm^2/s). Accordingly, the diffusion coefficient histograms show a progressive shift towards higher diffusion coefficients (Fig. 3.19 G). This is consistent with the expectation that there is an increase in lateral mobility of raft related lipids and proteins on the cell membrane after cholesterol removal. In all cases, the large standard deviation of the diffusion coefficients indicates strong

variations in the diffusion coefficients on the cell membrane, in agreement with the partitioning of SBD into different lipid regions[66]. This interpretation is consistent with the dynamic partitioning raft model proposed earlier[161-163]. These experiments show that cholesterol content is important for the raft-like behavior of SBD. Possible changes in the large scale organization of the membrane after cholesterol extraction were investigated by the means of *ΔCCF* images and their frequency histograms (Fig. 3.19 except G). Without MβCD addition, the *ΔCCF* images of SBD-TMR labeled cells are characterized by a high granularity (Fig. 3.19 A-C*)*. There is a sudden decrease in granularity for *ΔCCF* images after incubating the cells with MβCD for 10 minutes (Fig. 3.19 D). The granularity then gradually increases with time until after 30 min of incubation, when it reaches a similar range to that of non-treated cells (Fig. 3.19 F).

Therefore, while the fluidity of the membrane, as characterized by the diffusion coefficient, increases within 30 minutes of MβCD addition due to cholesterol removal, the membrane reorganizes and reaches a similar state as non-treated cells during the same time period, as shown by the *ΔCCF* distribution. A possible explanation for the change in *ΔCCF* distributions upon drug treatment is the change of the membrane equilibrium during drug action. SBD has been shown to be internalized by SHSY5Y cells and MβCD treatment disturbed SBD internalization[66]. The normally wide *ΔCCF* distribution may arise from restriction or direction of SBD diffusion due to cytoskeletal confinements[164]; alternatively, internalization may act as a sink for SBD, leading to wider, non-isotropic values of *ΔCCF*. Internalization inhibition, as seen in MβCD treated cells, may result in a disruption of this flux and thus narrower distributions.

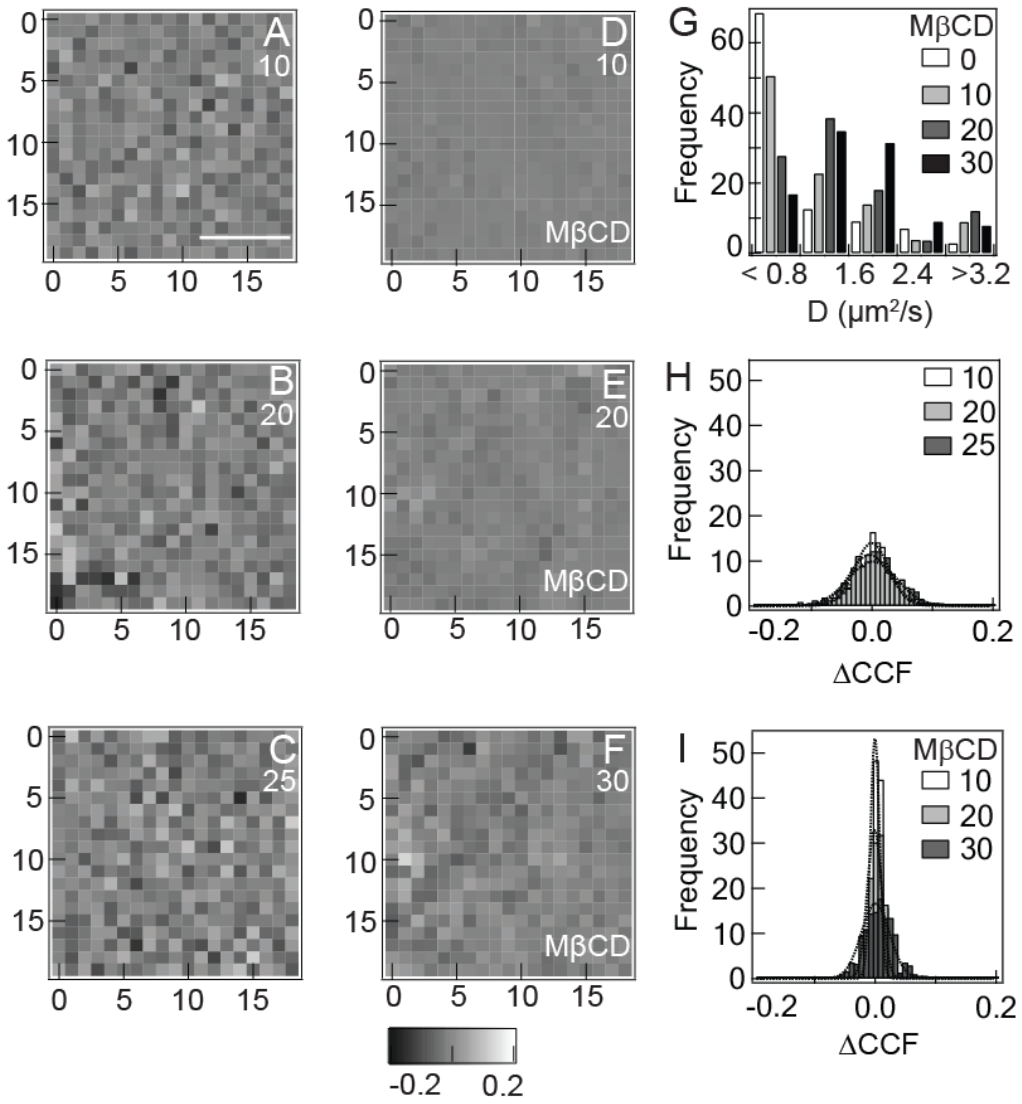

Fig. 3.19: Effect of MβCD on *D* and *ΔCCF* of SBD labeled cells. *ΔCCF* images of cells labeled with SBD-TMR. A-C show the images for non-treated control cells. D-F show the *ΔCCF* images for cells treated with MβCD after various times of incubation. Images in A-C are very heterogeneous. Upon addition of drugs, the images become less granular and the heterogeneity is restored to various degrees after increased incubation of the drug as seen in F. The heterogeneity in these images is comparable with the heterogeneity as seen in images A-C. G shows the histograms of *D* at various times of incubation with MβCD for SBD-TMR. H and I are *ΔCCF* histograms after various incubation times for SBD-TMR labeled cells without or with treatment with MβCD respectively. Gaussian fits to the distribution are indicated in dotted lines. The dataset used in the analysis was a kind gift from Dr. Manoj Manna from the lab.

In both normal and inhibited cases, though, the average of the *ΔCCF* distribution is zero since there is no macroscopic flux in the system. Therefore, changes in internalization would result in an altered membrane organization and transport patterns at least on the time scales of the drug action until new membrane equilibrium is reached. This is consistent with earlier findings that MβCD treatment

leads to an overall loss of cholesterol dependent membrane lipid domains, and to a re-organization of the remaining non-extracted lipids, but does not change the original properties of the membrane[165]. It should be noted that other reports found an indirect release of glycerophospholipids[166-167]. As a result of the disorganization in the membrane upon cholesterol removal[166] and it has been hypothesized that some compensatory changes in membrane lipid composition could occur after cholesterol depletion[167] which could be an explanation for our findings.

3.4 Conclusion

In this work, we introduce ITIR-FCCS as an extension of ITIR-FCS for the investigation of transport and diffusion processes in cell membranes. An expression for auto- and cross-correlations for areas of any arbitrary shape and size on an EMCCD chip was derived, and the resulting ITIR-FCCS calculations were applied to molecular systems exhibiting different combinations of flow and diffusion. The diffusion coefficients extracted are in good agreement with other reported measurements and the measured flow velocities are close to the expected values. The method is calibration free since the PSF can be determined from the data itself. We studied anisotropic translocation in GUVs and mixed lipid bilayers to demonstrate that membrane organization can in principle be studied by determining the difference of the forward and backward correlations in so-called *ΔCCF* images. Furthermore, using the *ΔCCF* approach, we demonstrated that cell membrane organization and heterogeneity can be observed by using markers for lipid microdomains. ITIR-FCCS gives adequate spatial and temporal resolution to be able to measure membrane dynamics in a calibration free manner, and thus presents a powerful biophysical tool to provide novel insights into transport phenomena and membrane organization.

4 Accuracy and precision of estimates of mobility, number and heterogeneity from Imaging FCS

A variety of theoretical and simulation studies have been performed in FCS to understand the effects of various factors in the collection, analysis and the interpretation of data. Pioneering work on the statistical accuracy of FCS was performed by Koppel[168] who proved that the S/N ratio in FCS can be improved by increasing the counts per molecule per second (*cps*) and not the total counts per second and is independent of the number of particles[168]. The above expression was later modified to include the effect of lower concentrations[169], Gaussian illumination profiles and transport processes other than diffusion[170]. Later, analytical expressions were derived which decomposed the error in FCS into two terms, the standard deviation and the bias[171]. The noise has also been experimentally quantified where the effects of concentration, intensity and measurement times on the autocorrelation function were studied[172]. Apart from theoretical and experimental studies, the effects of fluorophore saturation[173], molecular orientation[174], total measurement time[175], membrane curvature[176], minimum and maximum lagtime[177] on the autocorrelation have also been investigated computationally. Simulations have not only been used to study the effects of various experimental parameters on the autocorrelation curves, but also used to minimize the effects of distortion volume on parameter estimation leading to the development of numerical fluorescence correlation spectroscopy (NFCS)[178-179]. There have been simulation studies on the correlation in the spatial domain and in which the effects of sampling, background noise and photobleaching were investigated[142, 180]. Simulations have also shed valuable insights for parameter extraction from FCS data. Few of the major findings include: the diffusion coefficient of the faster diffusing particle must be at least 1.6 times that of the slower one for resolution into two different species[181], weighted data fit provided more accurate estimations of D than non-weighted ones[126] and curve-fitting based on an Bayesian

approach preferred simpler diffusion models to more complicated models avoiding over fitting of the data[182-183].

To the best of our knowledge, no systematic investigation on the effects of various instrumental factors on camera based FCS has been performed. Hence this chapter is a simulation study, aimed at studying the effects of different parameters on the estimates of D and N in imaging FCS and provides guidelines for efficient experimental design. The major advantage of imaging FCS is multiplexing leading to the observation of many different areas at the same time. This helps in understanding heterogeneity in diffusion in the system under study. Heterogeneity in imaging FCS is analyzed by calculation of diffusion laws[69] (Sec. 3.3.2.1) and ΔCCF functions (Sec. 3.3.2.2). The last part of the article compares the two methods for quantifying heterogeneity. Hence, it is shown here that imaging FCS can provide reliable estimates of mobility and concentration and can provide valuable insights into the organization of biomolecules in a membrane.

4.1 Methods

The codes for the simulations were written in Microsoft Visual Studio 2008© (Version 9.0.30729.1 SP). They were run in a high performance work station with 96 GB RAM and 64 bit Windows© operating system equipped with 12 processors. Data analysis were carried out in Igor Pro 6.22A© (Wavemetrics Inc., OR, USA and Matlab R2011a© (MathWorks, Natick, MA, USA). The various places where each software was used are indicated in the text.

4.1.1 Free diffusion simulations

A certain number of particles (N_t) were uniformly distributed in a circle of radius (R_s=4 μm) and the particles were allowed to diffuse within the circle. To simulate EMCCD based detection, a 20×20 square grid (a=240 nm) resembling the pixellated chip was superimposed onto the circular region. The center of the pixellated region coincided with the center of the circle. The diameter of the circular

region was made longer than the diagonal of the square region. The *ran2()* function was used to generate two random numbers U_1 and U_2 from the standard uniform distribution. *ran2()* is a "random number generator of L'Ecuyer with Bays-Durham shuffle and added safeguards"[127]. Using these two random numbers, the position $\left(x_{0,i}, y_{0,i}\right)$ of each particle were determined according to the transformation

$$\left(x_{0,i}, y_{0,i}\right) = \left(R_s\sqrt{U_{1_i}}\cos\left(2\pi U_{2_i}\right), R_s\sqrt{U_{1_i}}\sin\left(2\pi U_{2_i}\right)\right) \forall \left\{i \in \mathbb{N} \middle| 0 \le i < N_t\right\} \quad \textbf{4-1}$$

To simulate diffusion, a random displacement was added to each of the particle from its current position in each frame. Two random numbers (z and U_3) were drawn from a standard normal distribution and a standard uniform distribution using *gasdev()* and *ran2()* respectively. *gasdev()* yields normally distributed random numbers using uniformly distributed random numbers obtained from *ran2()* after the Box-Muller transformation[127]. The new positions of the particles were determined by adding

$$P\left(x, y, \Delta\tau\right) = \frac{1}{4\pi D\Delta\tau} e^{-\frac{(x-x_0)^2+(y-y_0)^2}{4D\Delta\tau}}, \left\langle r^2 \right\rangle = 4D\Delta\tau \quad \textbf{4-2}$$

$$\left(x_{i+1,j}, y_{i+1,j}\right) = \left(x_{i,j} + \sqrt{\left\langle r^2 \right\rangle} z_{i,j}\cos\left(2\pi U_{3_{i,j}}\right), y_{i,j} + \sqrt{\left\langle r^2 \right\rangle} z_{i,j}\sin\left(2\pi U_{3_{i,j}}\right)\right)$$

$$\forall \left\{ \begin{array}{c} i \in \mathbb{N} \middle| 0 \le i < n \\ j \in \mathbb{N} \middle| 0 \le j < N_t \end{array} \right\}$$

where $\Delta\tau$ is the time per frame. Whenever a particle left the region due to diffusion, another particle was added at another random position on the periphery of the circular region, thus keeping the number concentration of the particles, a constant. But, it has to be noted that the number of particles in each pixel varied due to the diffusion process being simulated. To simulate the fluorescence emission, a Poisson distributed random number was chosen with a mean set as the *cps* for each molecule using the *poidev()*[127]. Each photon was distributed across the airy disc for each particle. A Gaussian profile was used as an approximation to the Bessel airy disc[129]. Two uniformly distributed random numbers U_4 and U_5 were obtained from r*an2()*.

The position $(x_{i,j,k}, y_{i,j,k})$ of each of the photons were determined and for every photon, a unit increment was performed to the existing intensity at that pixel.

$$I(x,y)=\frac{1}{2\pi\sigma^2}e^{-\frac{(x-x_0)^2+(y-y_0)^2}{2\sigma^2}} \qquad \textbf{4-3}$$

$$I\left(\left\lfloor\frac{x_{i,j}+\sigma\sqrt{-2\ln(U_{4_{i,j,k}})}\cos\left(2\pi U_{5_{i,j,k}}\right)}{a}\right\rfloor,\left\lfloor\frac{y_i+\sigma\sqrt{-2\ln(U_{4_{i,j,k}})}\sin\left(2\pi U_{5_{i,j,k}}\right)}{a}\right\rfloor\right)=$$

$$I\left(\left\lfloor\frac{x_{i,j}+\sigma\sqrt{-2\ln(U_{4_{i,j,k}})}\cos\left(2\pi U_{5_{i,j,k}}\right)}{a}\right\rfloor,\left\lfloor\frac{y_i+\sigma\sqrt{-2\ln(U_{4_{i,j,k}})}\sin\left(2\pi U_{5_{i,j,k}}\right)}{a}\right\rfloor\right)+1$$

$$\forall\left\{\begin{array}{c} i\in\mathbb{N}\,|\,0\le i<n \\ j\in\mathbb{N}\,|\,0\le j<N_t \\ k\in\mathbb{N}\,|\,0\le k<poidev(cps)\end{array}\right\}$$

where $\lfloor\rfloor$ is the floor function.

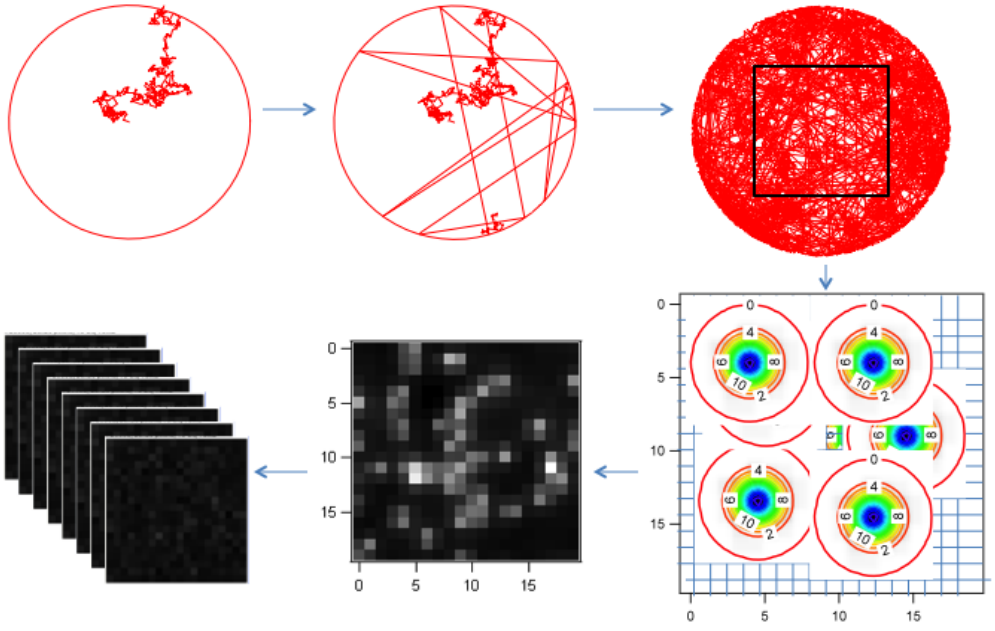

Fig. 4.1: Schematic of the simulations. Random-walk simulations of particles are carried out. If a particle moves out of the simulation area, a new particle is added at a random position. This is repeated for all the particles. At each position, a Gaussian mask is incorporated to simulate the effects of PSF. This leads to the creation of a single image. This is repeated for all the images in the stack.

4.1.2 Domain simulations

Non-overlapping circular domains of radii 100 nm with 50% coverage were uniformly distributed in the circular simulation area of R_s=5 µm. The centers of these domains were determined in a similar way to Eq. 4-1. These set of simulations were

characterized by the probability to exit a domain P_{out}. A random number from the standard uniform distribution was drawn and the particle was permitted to move into any domain freely, but move out of the domain only if the drawn random number was less than the value set to P_{out}. The D of the particle inside and outside the domain were D_{in} and D_{out} respectively ($D_{in}<D_{out}$). For this set of simulations, the following parameters were used: a=280 nm, PSF=250 nm, n=10000, $\Delta\tau$=5 ms, cps=40 kHz and N_t=1000. $\Delta\tau$ was chosen in such a way that $\Delta\tau/\tau_D$ was less than 0.1. Here the range of $\Delta\tau/\tau_D$ used was 0.0005-0.05.

Table 4-1: Parameters used in the simulations

Parameter	Description
a	Pixel side length of the EMCCD
A_{eff}	Effective area of observation
cps	Average number of photons emitted per second per molecule
n	Number of frames
N	Number of particles diffusing in the effective area
N_t	Number of particles diffusing in the entire simulation region
R_s	Radius of the simulation region
T	Total measurement time $T = n\,\Delta\tau$
T_{min}	Minimum total measurement time for a particular error level
$\Delta\tau$	Time resolution of the EMCCD
w_0	Point spread function
τ	Lagtime
τ_{max}	Last point in the lagtime till which the correlation is calculated
τ_D	Diffusion time $\tau_D = \frac{A_{eff}}{4D}$

4.2 Results and discussion

The results and discussion has two sections. The first section deals with dependence of accuracy and precision of the mobility and number density estimates

on experimental factors (Sec. 4.2.1) while the second section deals with those of the heterogeneity estimates (Sec. 4.2.2).

4.2.1 Effect of instrumental factors on mobility and number density

The effects of *PSF*, maximum lagtime, total measurement time, number of frames and cps are studied and discussed below. The values of the parameters were: *cps*=60 kHz, D=1 $\mu m^2/s$, N_t=900, a=240 nm and they were chosen to match experimentally observed values. The a was chosen same as the pixel size of the Andor EMCCD camera used in experiments (Table 2-2). The e^{-2} radius of the *PSF* was chosen to be 320 nm to match it with experimentally measured value from autocorrelation based determination of PSF. A value of 0.7 in Table 3-9 corresponds to a PSF of ~300 nm.

4.2.1.1 Effect of $\Delta\tau$, T and *PSF*

Typically, Imaging FCS is performed using 10,000 frames and hence the effect of $\Delta\tau$ was studied for the same number of frames. The error versus $\Delta\tau$ shows a parabolic profile in Fig. 4.2 A. The fitting was performed using 3-17 for the autocorrelation functions. It was shown in Sec. 3.3.1.3 that the value of *PSF* has to be fixed in order to obtain D and N. Hence, the *PSF* was fixed at the simulated value for the analysis below. It should also be noted that, whenever the *PSF* was fixed at a higher or lower value to the simulated *PSF*, the D decreased or increased with increasing bin size respectively and was constant only when it was fixed at the correct *PSF*. This indicates that the diffusion coefficient obtained from this method is absolute and only the absolute diffusion coefficient is constant with increasing bin size.

There is a broad range of values of $\Delta\tau/\tau_d$ which yields accurate estimates of D (errors within 10%). For values of $\Delta\tau>\tau_d/10$, the error increases beyond 10%. The effect is more drastically seen for N than for D. The value of N is predominantly determined by the shorter lagtimes of the correlation curve. The shorter lagtimes are extrapolated to τ=0 which yields the value of N.

$$\frac{\Delta\tau}{\tau_d} < 0.1 \qquad \textbf{4-4}$$

It is quite surprising that the error is high when the values of $\Delta\tau/\tau_d$ are low. It is also seen that for a given $\Delta\tau$ and T, the error associated with the estimate of D decreases with an increase in D (Fig. 4.2 C). In the simulation described above, varying the *cps* (one order higher or lower) could not yield any appreciable change in error (Fig. 4.2 D) indicating that the error associated with D is not due to lower signal to noise ratio and we are not limited by the brightness of the molecule at the simulated scenario. Instead, varying the *PSF* value yielded changes in error. The error increases with an increase in *PSF* size (Fig. 4.2 E). At low D or low $\Delta\tau$, an increase in error is observed. The dimensionless parameter, $w_0^2/D\Delta\tau$ is the critical parameter controlling the precision of the observed estimate of D. This parameter measures the ratio between the point spread function and the mean squared displacement ($4D\Delta\tau$) of the particle in the particular frame. The error is lower when the displacement per frame is higher than the uncertainty in localization due to the PSF. This has been known in the single parameter tracking literature as "reduced localization error"[184]. Hence, ways to increase the precision would be to reduce w_0 experimentally or increase $\Delta\tau$,. Care has to be taken in order to not increase $\Delta\tau$ to levels higher than those described by the previous inequality ($\Delta\tau < \tau_d/10$) so that it leads to a loss in accuracy. If this is not experimentally feasible, the other way to reduce the error would be to increase the total acquisition time ($T=n\Delta\tau$). This is demonstrated in Fig. 4.2 F where an increase in T led to an increase in precision of the estimated value. This was also observed by Ries *et al,* where it was observed that due to slow diffusion in membranes, longer measurement times and not increased brightness yielded accurate correlation curves[185]. Though, it may be tempting to increase T to higher levels to reduce the error to the desired levels, the practical limitation will be the photostability of the dye.

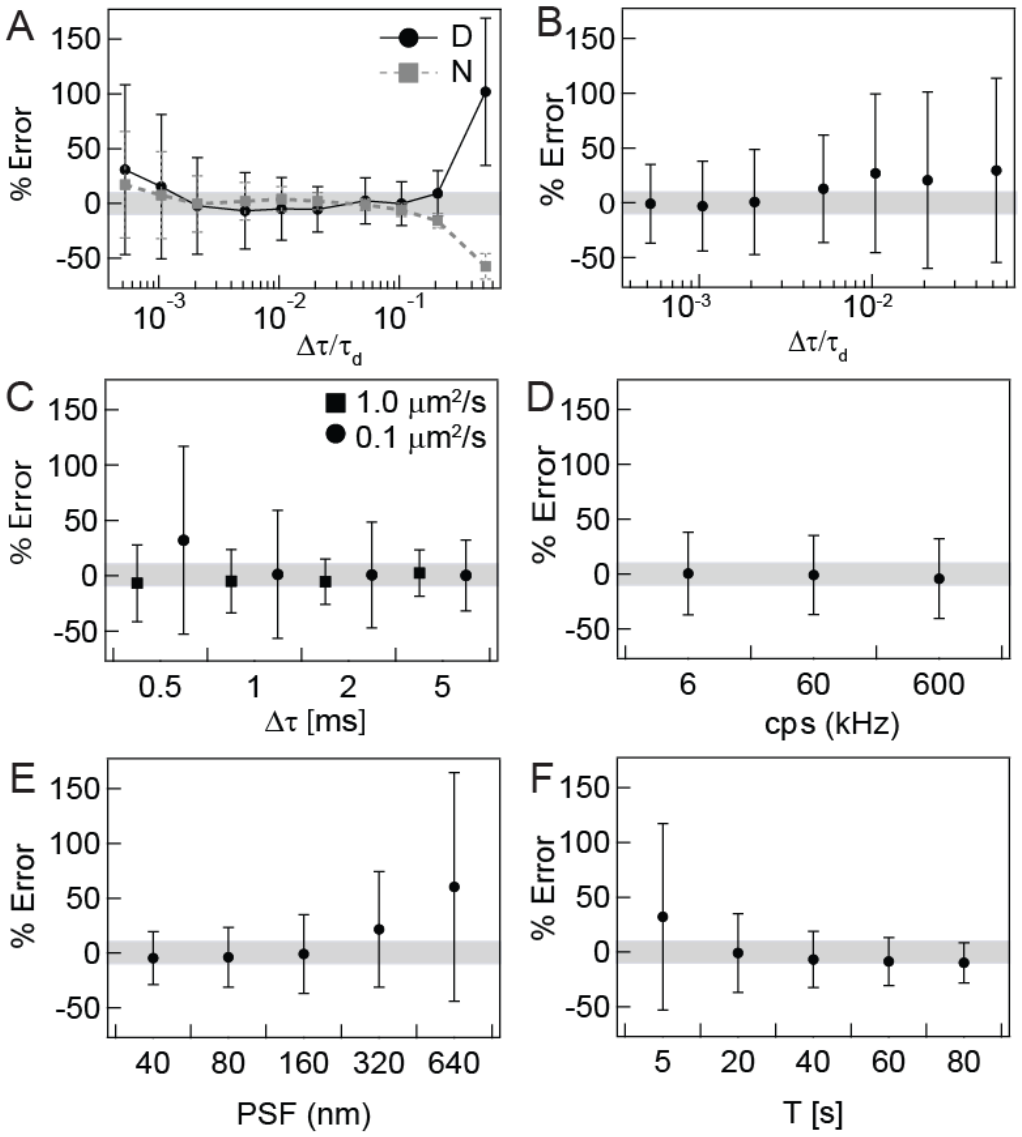

Fig. 4.2: Dynamic range of time resolution in Imaging FCS. The errors in *D* and *N* obtained at various time resolutions for a simulated stack of n=10000, D=1 μm^2/s, *cps*=60 kHz and N_t =900 in a circular area of R=4 μm with a EMCCD detection grid of 20×20 pixels with *a*=240 nm and *PSF* of 320 nm. The parameters were chosen as close to experiments as possible. The error in A shows a parabolic profile. There is a critical $\Delta\tau/\tau_D$ beyond which error starts increasing. At lower $\Delta\tau/\tau_D$ values the error can be overcome by increasing *n*. The grey box indicates 10% error from the simulated value. B shows that for a fixed *T, PSF, D* and *cps*, it is advisable to use n_{max} and $\Delta\tau_{min}$. The precision decreases with an increase in $\Delta\tau$. Upon reaching, $\Delta\tau=\tau_D$, there is a decrease in accuracy and precision. For the same error levels, *T* increases with an increase in $\Delta\tau$. C shows that there is a decrease in precision of the estimates with a decrease in *D* for the same *n* and $\Delta\tau$ ($\Delta\tau<\tau_D$ in both the cases) as seen in A. The precision cannot be increased by increasing the *cps* as in D. An increase in PSF causes a decrease in precision for the same *D*, *n* and $\Delta\tau$ as seen in E. F shows that the precision can be increased by increasing the *T* for the same *D*, *n, PSF* and $\Delta\tau$. The critical factor controlling the precision of the estimate is $w_0^2/D\Delta\tau$.

A practical suggestion, for cases where photobleaching is limiting, as suggested by Fig. 4.2 B, is to acquire the maximum number of images at the lowest experimentally accessible $\Delta\tau$. For a given *T, D* and *PSF*, the error increases with increasing $\Delta\tau$ and higher number of frames are required for obtaining the same level of error.

The precision of the estimate of *D* is affected by the size of the pixel in object space. The pixel size can be calculated by dividing the physical size of the pixel by the magnification of the objective. The choice of the pixel size is dependent upon two different effects. Firstly, a reduction in the pixel size (*a*) in object space provides better precision because this leads to increased sampling. The effects of pixel size on localization error has been quantified earlier and it has been shown that the finite pixel size of *a* leads to a localization error of $a^2/12$[186]. The error decreases with an increase in the ratio between displacement per frame and pixel size. The pixel size in object space can be made as small as possible by employing a high magnification objective or by choosing array detectors with small physical pixel sizes. The data presented here is in accordance with earlier reports in Raster Image Correlation Spectroscopy (RICS) which suggested that spatial oversampling (higher than the Nyquist criterion) is required for an accurate estimation of PSF by image based correlation techniques[187]. An optimal pixel size of ~50 nm was suggested for RICS. Secondly, in cases where imaging is performed at sub-optimal signal to noise ratio, an increase in the pixel size (by software or hardware binning) leads to an increase in the signal to noise ratio since this leads to increased photon counts. Hence an increase in pixel size leads to an increase in precision of the estimate. These competing effects must be borne in mind while choosing the pixel size.

The simulations performed here helped us in understanding the uncertainties and errors associated with *D* and *N*. Generally, distributions in *D* and *N* are used to characterize the heterogeneity of any sample. The statistical question to be put forth

in such a condition is whether the spread in D and N are significantly larger than the "inherent width"[188].

There have been many theoretical studies on FCS about optimal $\Delta\tau$. All these papers report optimal $\Delta\tau$ needed in terms of τ_D. τ_D was defined as $A_{eff}/4D$ in the case of imaging FCS in Sec. 3.2.2. A parabolic profile for the error versus $\Delta\tau$ has also been obtained by Degiorgio *et al*[189] for intensity correlation spectroscopy and by Brenner *et al* for number fluctuation spectroscopy[190]. The estimate of $\Delta\tau_{max}$ for imaging FCS is in the same order of $\Delta\tau_{max}$ for other techniques. For instance, Tchiernak *et al*[177] reported a $\Delta\tau_{max}$ of $2/3*\tau_D$ for confocal FCS whereas Kolin *et al*[180] provided a value of $1/2*\tau_D$ for TICS. Further, Kolin *et al* state that for $\Delta\tau$ within the suggested regime, the total number of sampled images in the stack determines the precision, similar to the data presented here. In the case of T_{min}, simulations and experiments in photon correlation spectroscopy[175] and in rotation correlation spectroscopy[188] have yielded a value of $100\tau_D$. For a D=1 $\mu m^2/s$, $\tau_D \sim= 100$ *ms*, hence for $\Delta\tau$=1ms, 10,000 frames are sufficient according to the suggestions above. More number of frames are necessary for molecules with D<1 $\mu m^2/s$ as stated earlier. The results are in agreement with those reported by Saffarian *et al*[171] that even without shot noise, the S/N ratio is strongly dependent upon the finite T of the experiment.

4.2.1.2 Effect of spatial sampling and total measurement time on PSF determination

In the analysis earlier, the effects of PSF were studied on the estimates of D. It was assumed in those analyses that the value of PSF was accurately known. But, the PSF needs to be determined for each system for accurate determination of D in camera-based FCS. Three different methods to determine PSF based on autocorrelation, cross-correlation and image correlation were discussed earlier (Sec. 3.3.1.3). The effect of experimental parameters (pixel size and total measurement time) on the determination of PSF from Imaging FCS is discussed here.

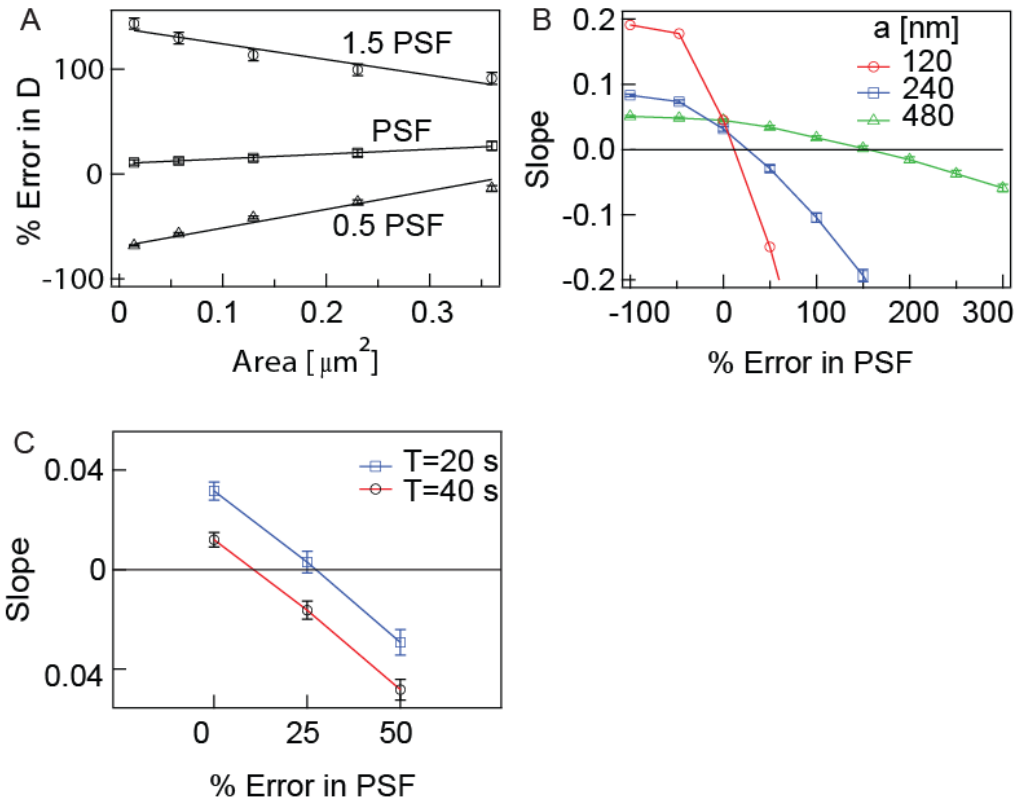

Fig. 4.3: Effect of spatial sampling and *T* on PSF determination. A) Determination of PSF by autocorrelation method B) Effect of pixel sizes on the determination of PSF C) Effect of total measurement time on the determination of PSF

The procedure to determine PSF from autocorrelation based method in brief is provided below. The autocorrelation functions at different binned areas needs to be calculated (1×1 to 5×5). *D* is an intrinsic parameter of the particle and hence is independent of the binning area used to calculate the *D*. The data at various bin areas are fitted with various values of the *PSF*. *D* is an increasing (positive slope) or decreasing (negative slope) function of bin area for values of *PSF* less or greater than the *PSF* of the system respectively. The value of *PSF* which yields a *D* independent of the bin area is the *PSF* of the system. As seen in the figure above, the value of PSF which yields a slope of zero is the PSF of the system.

The effects of pixel size on the accuracy of the PSF were studied by simulations. The PSF was fixed at 320 nm and the autocorrelation based method was

used to determine the PSF. Three different pixel sizes (120, 240 and 480 nm) were checked for the accuracy of the PSF obtained. PSF was varied across a wide range of values spanning those below and above the simulated PSF. As expected, for PSFs < simulated PSF, the slope was positive and vice versa for all the three cases. Theoretically, all the three pixel sizes are expected to have a zero crossing on the x-axis when the error is zero. But the zero crossing, displays a trend. The lines asymptotically converge to zero percent error indicating that the finite spatial sampling has an effect on the value of the PSF obtained by autocorrelation based method. This is in accordance with earlier reports that the finite pixel size of a leads to a localization error of $a^2/12$[186].

As the pixel size increases, the accuracy of the PSF obtained decreases. A pixel value of 120 nm yields the smallest error of ~15% among the three. The ratio between the smallest pixel and the PSF is 37.5%. For accurate PSF determination in imaging[191] and RICS[187], a ratio of at most 17% between the smallest and PSF is suggested. This difference might explain the observed error in PSF determination here from Imaging FCS. This suggests that spatial oversampling over Nyquist criterion is necessary for accurate determination of PSF from Imaging FCS.

4.2.1.3 Effect of τ_{max} and N

For proper estimation, at least up to 3 decades of lagtime need to be fitted ($1000\Delta\tau$). The results are summarized as a schematic in Fig. 4.4 B. Although the τ_{max} is less than earlier reports ($\tau_{max}>5000\tau_D$ for solutions[177] in confocal FCS), we find that $\tau_{max}>100\tau_D$ is sufficient for Imaging FCS in our case. In the case of N, up to 2000 particles/μm^2 yield estimates within 10% error (Fig. 4.4 A). For N>2000 μm^{-2}, there is a loss in accuracy due to decrease in amplitude of the correlation functions. The dependence of the signal to noise on N has been studied analytically, computationally and experimentally and the present findings agree with them that at higher concentrations, the S/N is independent of N and depends only on the cps, whereas at

lower concentrations it is dependent upon N[168-170, 172]. In the case when N<1 particle/μm^2, the increase in error due to a decrease in N can be compensated by a corresponding increase in *cps* for a particular error level as suggested by Koppel[168].

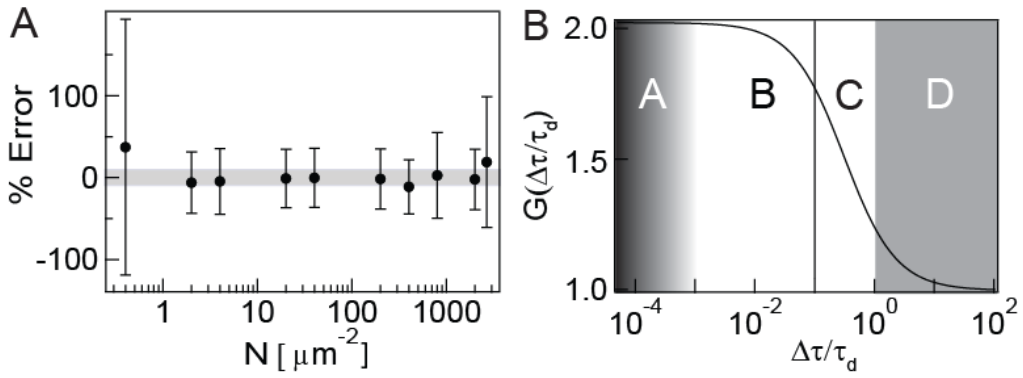

Fig. 4.4: Dependence of accuracy and precision of estimates on N and $\Delta\tau$. A shows that there is a large dynamic range in N which yields accurate and precise estimates of D and N. Generally, Imaging FCS is performed only in this regime. For N>2000 μm^{-2}, there is a loss in accuracy due to decrease in amplitude of the correlation functions. Fitting guidelines in Imaging FCS are summarized in B. For n=10000, the region A, shows the region dominated by error due to insufficient T. In the region A, more than 10000 frames are needed to obtain reliable estimates of D and N. Further, present day EMCCD cameras cannot reach regimes where $\Delta\tau/\tau_D$ >10^{-3}. The region B indicates the region where the first point in the correlation curve can be ($\Delta\tau/\tau_D$ =10^{-3}-10^{-1}), and depending upon the start of the curve, fitting has to be done for at the least 3 orders of τ. The solid black line indicates the position of maximum $\Delta\tau/\tau_D$ =0.1) yielding reliable estimates of D and N. The first point of correlation should not be in the regions to the right of this line (C and D). The white region (regions B and C) show the minimum region required to be fitted to obtain D and N accurately.

4.2.1.4 Guidelines in Performing an Imaging FCS experiment

The analysis presented in the previous sections enables one to put forth guidelines while designing an Imaging FCS experiment. The goal of any Imaging FCS is to provide the most accurate and reliable estimates of mobility and concentration.

1. The first step while designing an Imaging FCS experiment is to find the minimum time resolution of the camera ($\Delta\tau_{min}$).

2. The first step in the calibration of the microscope is the calculation of the pixel size (a) of the EMCCD camera in the object space. The physical pixel

size of the EMCCD is provided by the manufacturer. Based on that *a* can be calculated.

a = physical pixel size/Magnification of the objective used

3. **Calibration of the microscope**

After calculating the pixel size, the next step is the calculation of the PSF of the microscope. The PSF can be done in any of the three ways described earlier[8]. In the case of autocorrelation based calibration, a sample whose diffusion coefficient (*D*) is approximately known and which exhibits free diffusion needs to be chosen. To begin with, as a rule of thumb, the diffusion time can be calculated by the expression: $\tau_{d,\ approx} = a^2/4D$. The measurements must be made using a time resolution of the camera which is at least ten times faster than that of the above value. This procedure will yield the value of PSF. Once PSF and *a* are known, the effective area (A_{eff}) of each pixel can be estimated. Thus the system is calibrated.

4. Choice of parameters

1. The density of the particles must be in the range of 10-1000 $\mu m^{-2.}$
2. Suitable EM gain has to be used which will not lead to a saturation of the pixels in the EMCCD chip.
3. The choice of pixel size is discussed in detail in the next section.

5. For an unknown sample, if an approximate *D* is known, the time resolution must be at the least 10 times smaller than the τ_d ($\tau_{d\ =}\ A_{eff}/4D$). At least 10000 frames need to be taken. In case, the sample does not photobleach, more frames are recommended since the error reduces with increase in number of frames. In case, even an approximate diffusion coefficient is not known, a series of time resolutions has to be tested at 10000 frames such that the

average D does not vary with the time resolution. Then the time resolution with the lowest error has to be chosen. If the error is same across a variety of time resolutions, the lowest time resolution has to be chosen since this reduces the amount of illumination on the sample reducing phototoxicity and photobleaching.

6. Then for a given amount of T, images need to be captured at different time resolutions ($\Delta\tau_{min,}$ $2\Delta\tau_{min}$, $5\Delta\tau_{min}$, $10\Delta\tau_{min}$). In case, if the sample is shot noise limited, the error will decrease until a time resolution ($\Delta\tau_{optimum}$) where it is no longer shot noise limited. If not, the best time resolution will exhibit the lowest possible error.
7. In the next step, the T_{max} has to be identified after which the sample starts photobleaching.
8. At this $\Delta\tau_{optimum}$, $T_{max}/\ \Delta\tau_{optimum}$ number of frames need to be captured for consistent estimates of mobility.
9. Upon calculation, the fitting has to be done at the least 3 orders of correlation time (typically, $\Delta\tau$ to $2000\Delta\tau$).

4.2.2 Effect of instrumental factors on heterogeneity

Heterogeneity in Imaging FCS can be characterized using diffusion laws (Sec. 3.3.2.1) and ΔCCF (Sec. 3.3.2.2). The influence of the experimental parameters on the heterogeneity metrics needs to be investigated, before they are applied to study heterogeneous systems. Hence, diffusion laws and ΔCCF analysis were performed for the same set of data as in Fig. 4.2.

4.2.2.1 Effect of experimental parameters on diffusion laws

Various binning were carried out from 1×1 to 5×5. The binned areas overlapped with each other. The diffusion law was visualized by plotting A_{eff}/D vs A_{eff}. Standard error of the mean was used to perform a weighted fit. Typical diffusion laws for D=1 and 0.1 $\mu m^2/s$ are shown in Fig. 4.5 A. The slope of the diffusion law is

the reciprocal of *D*. Fig. 4.5 D shows the error in *D* across the values of $\Delta\tau/\tau_D$ tested. The first two points are limited by the number of frames. The error at higher $\Delta\tau$ is not as significant as those obtained from autocorrelation. This is because, the *D* obtained in diffusion law is an average from 1×1-5×5 autocorrelations. The higher $\Delta\tau$ values do not yield reliable estimates of *D* in the case of 1×1. Due to an increased τ_D, the higher bins yield accurate estimates of *D.* Hence on average, the error is reduced in the case of the slope when compared to the autocorrelation. Fig. 4.5 E shows the intercept values obtained from the diffusion laws. There is a certain range of $\Delta\tau/\tau_D$ values which yield intercepts as expected as close to zero. The grey box indicated an error of *10* ms here and an error of 10% from the simulated value in the case of *D*. As the case above, the intercepts at smaller $\Delta\tau/\tau_D$ are limited by number of frames and hence non-zero intercepts are seen.

It is observed that the intercepts have a higher error in the case of lower *D* as in Fig. 4.5 G. This can be overcome by increasing the number of frames. As seen in Fig. 4.6 A, the intercept progressively decreases and reaches zero with increase in *T*. Generally, positive intercepts indicate the presence of domains in the observation area. The positive intercept obtained at lower mobility should not be immediately misinterpreted with the confinement in a domain. Suitable biological controls need to be done to confirm the statement above.

4.2.2.2 Effect of experimental parameters on *ΔCCF* distributions

Traditionally, *ΔCCF* is characterized by the second or fourth moments of the distribution, standard deviation or kurtosis respectively. Typical *ΔCCF* distributions are shown in Fig. 4.5 B. The present simulation studies suggest that the second moment of *ΔCCF* is affected not only by the heterogeneity of the system but also by the mobility of the particles. Slow moving particles have a higher width when compared to fast moving particles as in Fig. 4.5 H. While calculating the kurtosis, it is inherently assumed here that the *ΔCCF* distributions are Gaussian. *ΔCCF* distribution of particles undergoing free diffusion is expected to be a normal distribution. For all

the other cases, the distribution is not expected to be a Gaussian. Hence the inherent assumption while calculating kurtosis is not justified in all the cases. *ΔCCF* distributions are also affected by the $\Delta\tau$ of the data. Increasing $\Delta\tau$ has increasing values of standard deviation as in Fig. 4.5 H. With differences in $\Delta\tau$, different areas of the curve are subtracted and hence different standard deviations are obtained. Even subtracting the same temporal regions from experiments with different $\Delta\tau$ yield different values since the same region has different levels of statistical noise for different $\Delta\tau$. Hence, there arose needs to develop *ΔCCF* methods which are mobility and $\Delta\tau$ independent and assume no prior assumptions of the distribution of the data.

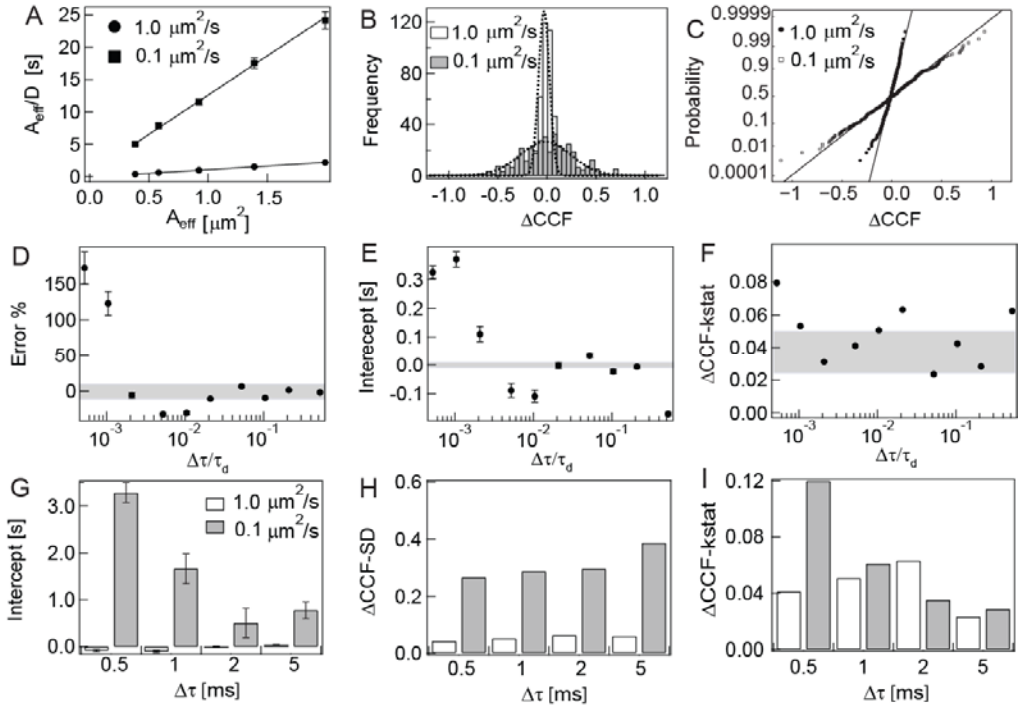

Fig. 4.5: Heterogeneity estimates from Imaging FCS. Representative diffusion laws, *ΔCCF* distributions and normal probability plots for D=1.0 and 0.1 μm^2/s are shown in A, B and C respectively. The simulations described in Fig. 4.2 were analyzed for heterogeneity. The slope of the diffusion law is inversely proportional to the D and the error in D is seen in the figure D. E is a plot of the intercepts obtained from diffusion laws. F shows the *kstat* values of the same set of simulations. The grey box shows the mean and one standard deviation of *kstat* values obtained from 380 values sampled from a standard normal distribution. F indicates that *kstat* on the average shows the distributions to be normal for simulations of free diffusion. This suggests that diffusion laws and *ΔCCF* distributions can be obtained for the indicated $\Delta\tau$ values. G indicates that the intercepts are dependent upon D. This dependence can be reduced by increasing the T as discussed in Fig. 4.4. The standard deviation of *ΔCCF* distribution depends upon D of the sample and $\Delta\tau$ of the system as seen in H. This can be overcome by using *kstat* as a metric to characterize the distribution which is independent of $\Delta\tau$ as in I.

As stated earlier, the *ΔCCF* values are normally distributed for particles undergoing free diffusion. Hence any method which systematically characterizes deviations from normal distribution serves to quantitate the heterogeneity in diffusion in the system. Hence any given *ΔCCF* distribution needs to be tested for its normality. Here, Lilliefors test[192], an adaptation of the Kolmogrov-Smirnov test is used to test for the normality of the distribution (Matlab© function *lillietest*). The Kolmogrov-Smirnov test compares the current distribution to any distribution whose parameters need to be specified prior to the test. Lilliefors test compares the given distribution to any distribution using the mean and standard deviation from the data itself. Here, the data is compared to a Gaussian distribution. In order to perform this test, the cumulative distributions of *ΔCCF* and that of the Gaussian calculated from the *ΔCCF*'s parameters are calculated. The test statistic is referred to as *kstat*. *kstat* is a distance measure between the two distributions. For a given *ΔCCF* value, the proportion of values less than the given value is computed for a Gaussian and for the observed distribution. The maximum of the absolute difference between the values is referred to as *kstat* $\left(kstat = \max_x \left|CDF_{\Delta CCF} - CDF_{Gaussian}\right|\right)$.

As the raw data is directly used to perform the test without any histogram calculations, it is scale free. For $\Delta\tau$>0.5 ms, it is seen from Fig. 4.5 I that molecules exhibiting different mobility have similar values of *kstat*. The same figure also shows that *kstat* values from samples simulated with different $\Delta\tau$ have similar values indicating that it is $\Delta\tau$ free. The test is non-parametric and makes no inherent assumptions about the distribution of the data. Hence the use of normality testing over the use of moments of the distribution is recommended to compare the heterogeneity between various samples. Similar to the diffusion law, Lilliefors test shows deviations from normal distribution in case of samples with low mobility (Fig. 4.5 I, $\Delta\tau$=0.5 ms*)*. As the case with diffusion laws, it can be overcome by increasing *T* (Fig. 4.6 B). When comparing diffusion law and normality tests (Fig. 4.6), it is seen

that both of them depend on *T*. But, in the case of samples with lower mobility, the diffusion laws need longer *T* than normality tests to converge to the expected value. In the simulated regime, for samples with slower mobility, it is seen that the intercepts converge to zero, but even at very large experimentally accessible *T*, the intercepts are higher than those obtained from faster mobility. This is not the case with *kstat* whereas, at lower mobility, with increasing T, the *kstat* values decrease and are comparable to those obtained from faster mobility (Fig. 4.3 and Fig. 4.4).

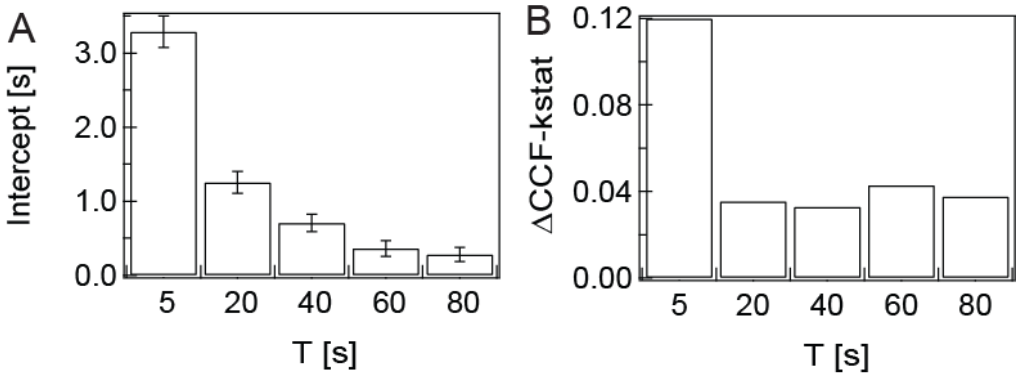

Fig. 4.6: Dependence of heterogeneity estimates on T. At low *D*, an increase in *T* leads to a decrease in intercepts (A) and *kstat* (B). The intercepts show a higher dependence on *T* than *kstat*.

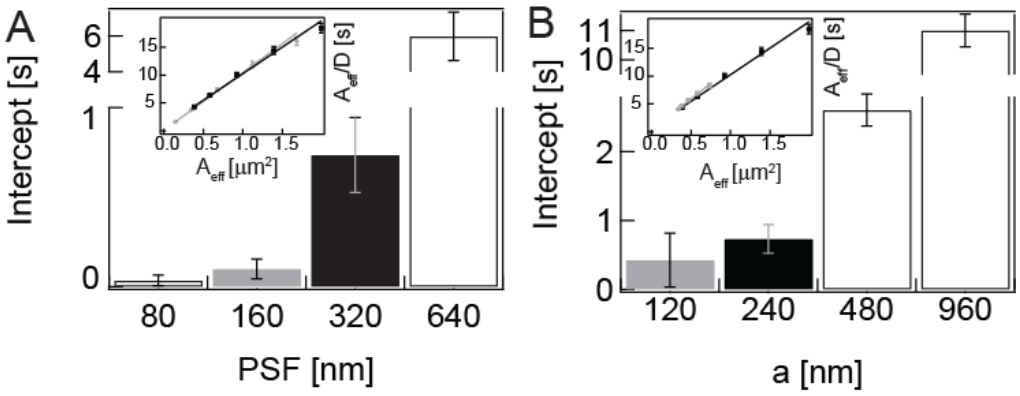

Fig. 4.7: Dependence of heterogeneity estimates on detection area. A) and B) show two different ways to reduce the detection area. The detection area can be reduced by either reducing the PSF or the pixel size. The FCS diffusion laws at two different PSFs or pixel sizes are shown in the insets in grey or black corresponding to those values with bars filled in grey or black respectively.

4.2.2.3 Effect of total measurement time, PSF and pixel size on intercepts in the FCS diffusion law

A reduction in pixel size or the PSF leads to a reduction in the observation area thereby reducing the values of A_{eff}/D and hence the intercepts obtained are close to the expected value of zero as in the figure above.

There are two factors governing the precision of the FCS diffusion law, the distance of the first point on the x-axis from zero and the spacing between the points. Both factors stated above are determined by A_{eff}. The primary factor affecting the distance of the first point from zero and the spacing between them are PSF and pixel size, respectively. The figures show that a two times reduction in PSF at a given pixel size (a = 240 nm, w_0 = 160 and 320 nm) is more effective in reducing the intercept than a two times reduction in pixel size at a given PSF (a = 120 and 240 nm, w_0 = 320 nm). Super resolution techniques need to be implemented in order to reduce the PSF to levels below the diffraction limit.

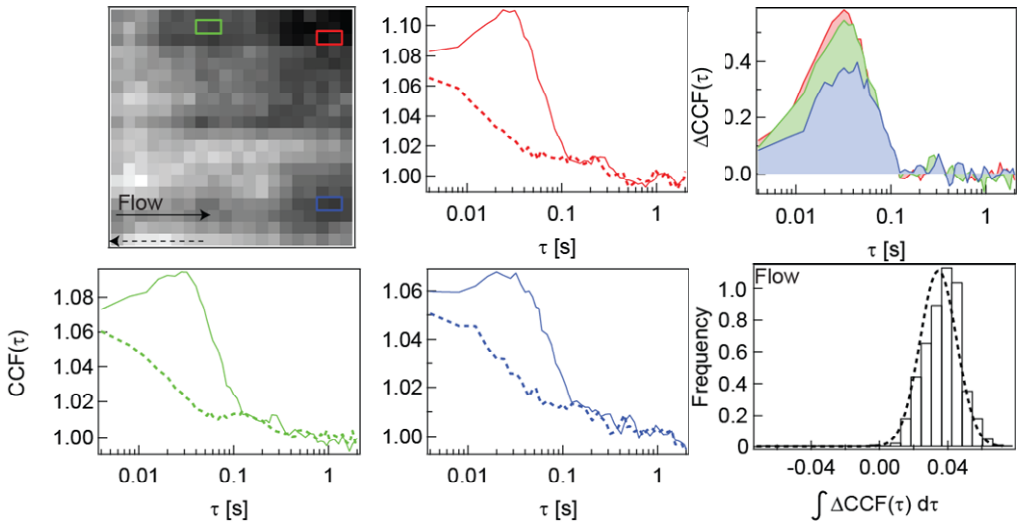

Fig. 4.8: ΔCCF distributions for flow. The forward and backward cross-correlations for three different pixel positions labeled in red, blue and green are shown in continuous and broken lines respectively. The difference between the forward and backward cross-correlation along with the distribution is shown as well in the extreme right panels.

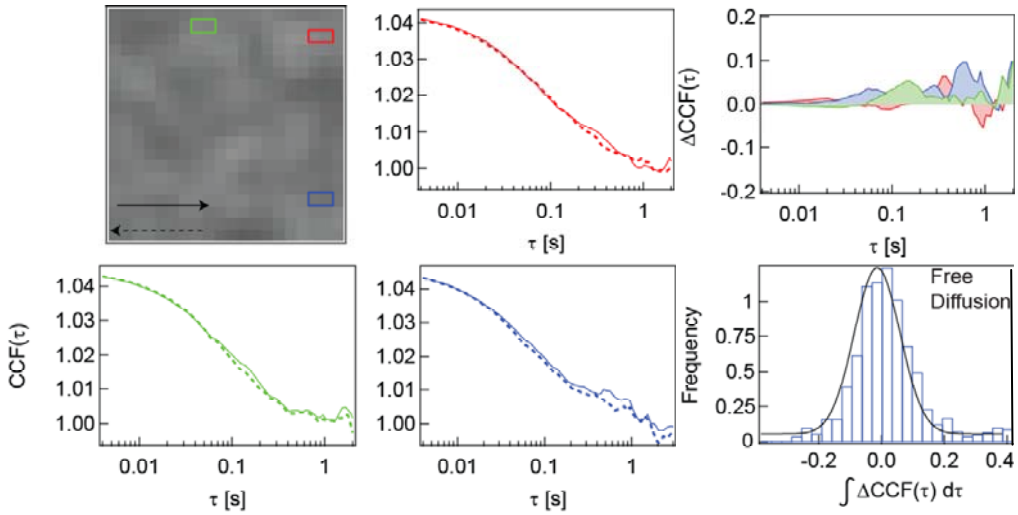

Fig. 4.9: ΔCCF distributions for diffusion. The corresponding functions for diffusion are shown here. The same convention as the previous figure is adopted. The symmetric ΔCCF distribution is seen here.

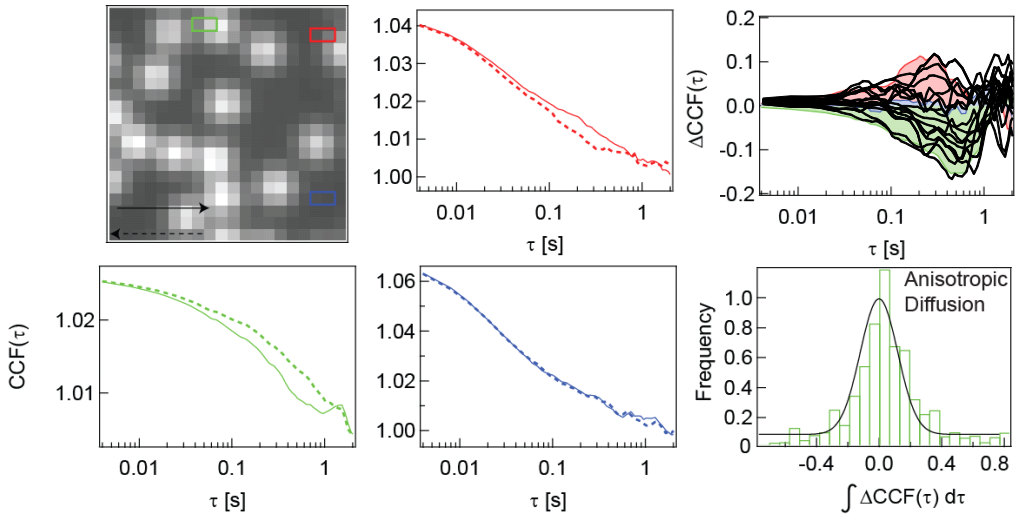

Fig. 4.10: ΔCCF distributions for anisotropic diffusion. The corresponding functions for anisotropic diffusions are shown here. The same convention as the previous figure is adopted. The symmetric ΔCCF distribution is seen here. Unlike, free diffusion, the forward and the backward correlations do not overlap with each other in all the pixels.

4.2.3 Heterogeneity estimates from simulations with domains

After establishing the error limits of the heterogeneity metrics with experimental parameters, they were tested on simulations with domains. When the ratio of D_{out} to D_{in} was kept at *100* with a D_{out} of *10* $\mu m^2/s$ and P_{out} was systematically varied from $5e^{-5}$ *to 1.0*, the average D increases with increase in P_{out} as expected (Fig. 4.12 F). The trapping efficiencies of the domains are inversely related to P_{out}. With an increase in $P_{out,}$ a decrease in intercept value (τ_{int}) was seen.

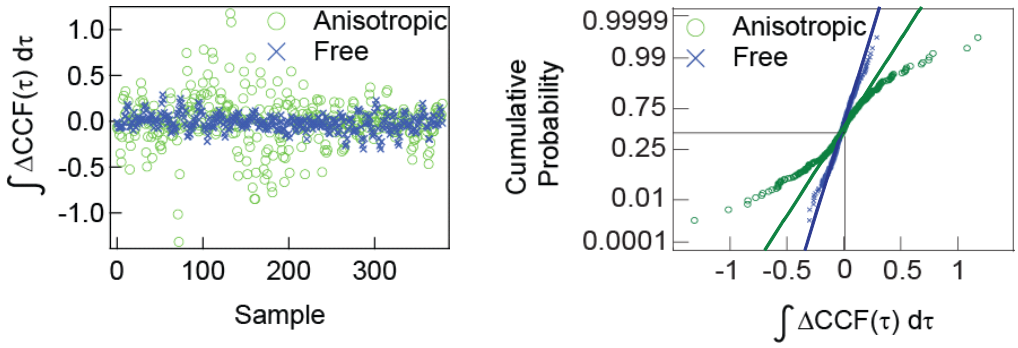

Fig. 4.11: Demonstration of Kolmogrov-Smirnov test. The ΔCCF values for free and anisotropic diffusion are plotted here. The corresponding cumulative probability function is shown later. The thick lines indicate the theoretical Gaussians in the cumulative probability function. The deviations from Gaussian are very evident for tanisotropic

This is expected, since the intercept values are an indicator of the average time the molecule spends in the domain. As P_{out} increases, the trapping time decreases and hence the intercept decreases as seen here[63]. As described in Sec. 4.2.2.1, intercepts have higher error with a decrease in D. Hence the obtained intercepts could be artifacts of the slow mobility of the particles. It has been shown earlier that a lower D can give rise to non-zero intercepts in the diffusion law. In order to ascertain the fact that the intercepts displayed are those of trapping and not mere errors due to the lack of sufficient T, free diffusion corresponding to the average D obtained by fitting the autocorrelations from the previous case were simulated. The data obtained from such simulations are plotted as points for bilayers in Fig. 4.12 A-E. It is seen that, the slow mobility in turn contributes to the obtained non-zero intercept. But, the trapping increases the intercepts to levels higher than that of slow mobility only. The same set of data was also analyzed for heterogeneity using normality tests. Similar to the intercepts, the *kstat* values are affected by T. But the trapping increases the *kstat* values to distinguish it from those which are affected by slow diffusion only. For the simulated domain coverage of 50%, the value of P_{out} at max of *1%* shows differences in intercepts and *kstat* values between the simulations those of the bilayer and those of the domains. For P_{out} values greater than *1%*, it is difficult to distinguish the effects of trapping and slow mobility. The data in Fig. 4.12

D and E show that, the ratio of D_{out} to D_{in} needs to be at least *50* to differentiate the effects of trapping and slow mobility in the case of domains of size 100 nm at P_{out}=5e^{-5}. The value is reduced in the case of domains with larger radii. For a comparison, the raw data is plotted in the form of histograms and the standard deviation of these *ΔCCF* distributions is plotted in Fig. 4.12 C since all the measurements were performed with the same $\Delta\tau$. Unlike *kstat*, the standard deviations are a monotonically decreasing function with decreasing *D* in the case of bilayers similar to the intercepts from diffusion law and unlike *kstat* from the normality tests. The merits and demerits of both the methods are discussed below.

Table 4-2 Comparison of methods to quantitate heterogeneity

Diffusion law	ΔCCF-normality test
Performed by fitting autocorrelation data	Performed on raw cross-correlation data and hence it is faster since fitting data to non-linear models is avoided
It can differentiate the effects of domains and meshwork	It cannot individually differentiate modes of diffusion since only systematic differences in normality is measured
It cannot differentiate flow and diffusion processes.	*ΔCCF* distributions can differentiate flow and diffusion processes by the position of the mean.
The raft partition coefficient* $(K)^{193}$ needs to be at least 1000 in order to differentiate hindered diffusion due to traps from mere slow diffusion.	The raft partition coefficient $(K)^{193}$ needs to be at least 10000 to differentiate hindered diffusion due to traps from mere slow diffusion. This indicates that the normality tests need stronger trapping to confirm the presence of heterogeneity when compared to diffusion laws.
A positive intercept obtained in the case of domain in diffusion law. But, a positive intercept is observed even with particles that diffuse slowly which can be avoided by increasing the measurement time (*T*). In the case of 0.1 μm^2/s, a measurement time of 80 s is needed in order to differentiate whether the intercept is an artifact of slow diffusion or trapping	An increased *kstat* value is seen in the case of domain in ΔCCF-normality test. But, an increased *kstat* value is observed even with particles that diffuse slowly which can be avoided by increasing the measurement time. In the case of 0.1 μm^2/s, a measurement time of 20 s is needed in order to differentiate whether the intercept is an artifact of slow diffusion or trapping. This suggests that the diffusion laws have a higher dependence on *T* than normality tests.
Provides an estimate of global heterogeneity in the system	Provides an estimate of local heterogeneity in the system

*The partition coefficient[193] was defined as $K = \frac{D_{out}}{D_{in}P_{out}}$.

The table indicates that diffusion laws and both methods have advantages and limitations. Since both the metrics (intercept and *kstat*) can be quantified from the same raw data, it is advisable to quantitate both the local and global heterogeneity in the system.

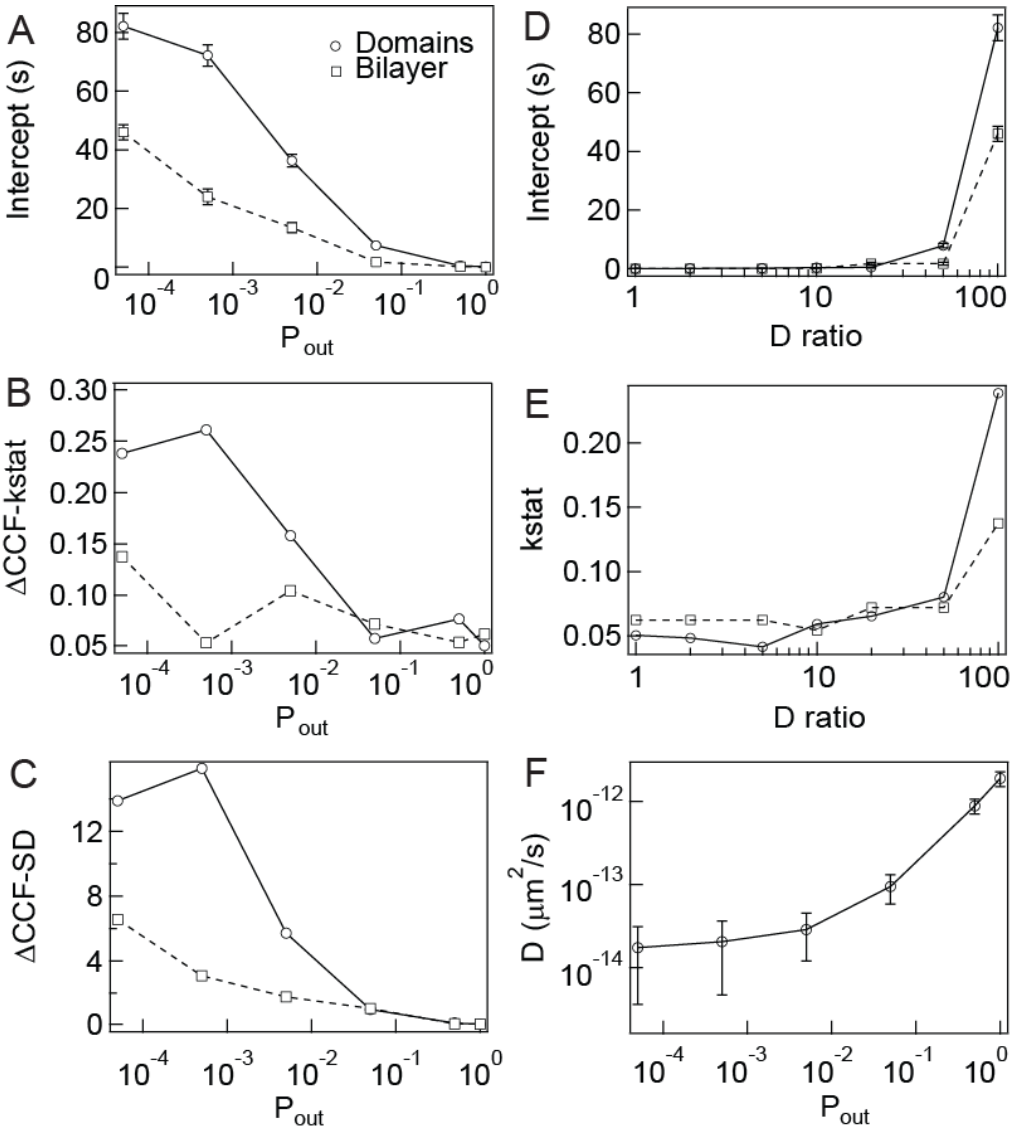

Fig. 4.12: Estimation of heterogeneity for simulations with domains. A is a plot of the intercepts of diffusion law from Imaging FCS. As the trapping efficiency decreases (P_{out} increases), there is a reduction in the intercept. The autocorrelation was performed to yield the average *D*. Free diffusion simulations of the obtained average *D* were performed. The intercepts from the two sets of simulations are compared in A to ascertain that trapping increases the value of intercepts. B is a plot of *kstat* for the same set of data. As above, trapping introduces non-normality leading to an increase in *kstat* than those introduced due to slow mobility. Both the data show differences between trapping and slow mobility when P_{out}<1%. C is a plot of the standard deviation of the *ΔCCF* distributions of the data shown in B. For a $P_{out}=5e^{-5}$ and D_{out}=10 μm^2/s, the intercepts and *kstat* increase with decreasing levels of D_{in} (*D* ratio = D_{out}/D_{in}) as seen in figs. D and E respectively. An increase in P_{out} leads to a decrease in trapping efficiently consequently leading to an increase in *D* as seen in F for a fixed ratio of D_{out} to D_{in} of 100 for the same set of data shown in A-C.

4.3 Conclusion

Simulations were used to ascertain the effects of various instrumental parameters on the accuracy and precision of the mobility, number density and heterogeneity parameters obtained from Imaging FCS. This helps to estimate the error in the estimates beforehand using the chosen parameters. Guidelines are provided for efficient experimental design. An accurate expression for the effective area was provided leading to the definition of τ_D. For accurate estimation of D and N, $\Delta\tau<\tau_D/10$. The precision is inversely related to $w_0^2/D\Delta\tau$. In cases, where it is not possible to reduce $w_0^2/D\Delta\tau$, an increase in T leads to an increase in precision. For a given T, it is advisable to use n_{max} and $\Delta\tau_{min}$. The S/N ratio is dependent upon counts per molecule per second and not counts per second as already established in FCS[168]. At low N, the decrease in S/N ratio can be compensated by an increase in counts per molecule per second. The S/N ratio decreased for high number of particles in the observation region. Heterogeneity can be ascertained in Imaging FCS by diffusion laws and ΔCCF distributions. Diffusion laws provide an estimate of the global heterogeneity of the sample whereas normality tests provide an estimate for the local heterogeneity of the sample. It is seen that both methods have merits and demerits. Since diffusion laws and ΔCCF-normality tests can be performed from the same raw data, it is advisable to quantitate heterogeneity by both methods to obtain a complete picture of the heterogeneity of the system being probed. The simulations performed here helped in understanding the uncertainties and errors of the estimates from Imaging FCS allowing one to put forth the statistical question whether the observed spread in D and N is significantly larger than the inherent uncertainty. The measurements and simulations in this thesis so far indicate that Imaging FCS provides reliable estimates of D, N and heterogeneity of the sample and is a valuable biophysical tool to study the same. The next chapter describes various applications of Imaging FCS.

5 Applications of mobility, number density and heterogeneity estimates obtained from Imaging FCS

The previous chapters discussed the various methods to determine the mobility and number density estimates from Imaging FCS along with the accuracy and precision of those estimates. The various experimental applications from which mobility, number and heterogeneity were determined using Imaging FCS are discussed here. The applications are classified into three sections. The first section describes a biological application where Imaging FCS was used to probe the organization of a membrane protein called EGFR. This is followed by a chemical application where Imaging FCS was used to study the formation of bilayers on different surfaces and the action of antimicrobials on them. The next instrumental application focuses on the coupling of Imaging FCS with impedance spectroscopy.

5.1 Materials and methods

The details of the plasmids, the graphene films and the diamond transistors are provided in Appendix 17. Melittin and magainin were purchased from Sigma Aldrich (Singapore) and were used as received.

5.1.1 Transfection and Imaging of cell-membrane proteins

The cells were grown in 35 mm fluorodishes with cover glass bottom obtained from World Precision Instruments Inc (Sarosota, FL, USA). Chemical transfection using FuGENE©6 (Promega Pte Ltd, Singapore) was performed. 3 µl of the transfection reagent was mixed with 1 µg of the plasmid. Imaging was carried out in indicator free media. The media composition and growth conditions of the CHO cells used are described here[53].

5.1.2 Preparation of lipid bilayers on nanodiamond and graphene

The protocol to prepare bilayers on glass has been described earlier in Sec. 3.1.3. The following modifications were made to the original protocol. The lipid bilayers were prepared in the similar chambers as in Sec. 5.1.1 instead of cover slides. The concentration of Rho-PE was 0.02% for bilayers grown on graphene. The lipid

samples on nanodiamond and graphene were subjected to vacuum evaporation for 1 hour. Prior to lipid addition, the flasks were cleaned in piranha reagent (H_2O_2:H_2SO_4::3:1). The sonication was performed for 45 minutes and incubated at 60 ºC for 3 hours. 2-6 ml of the suspension was sonicated for 30-45 minutes to form vesicles. Nanodiamond and graphene were fixed over the cover glass bottom in the chamber using silicone rubber. It is crucial to soak the CVD graphene sample in distilled water for a day prior to deposition of biomimetic membranes for better membrane formation. This is to prevent a widespread adsorption of unfused lipid vesicles rather than formation of a spatially uniform membrane. The lipid membrane must be wetted in buffer solution all the time to prevent disintegration.

5.2 Results and discussion

This section discusses three different applications of Imaging FCS. The first section describes the use of single molecule sensitive Imaging FCS to probe the mobility and heterogeneity of a membrane protein called EGFR on live-cells expressing the transfected protein at physiological concentration levels. The second application describes the use of Imaging FCS as an assay tool to monitor the formation and disruption of lipid bilayers on various surfaces of different hydrophobicities. The third application is our approach at combinatorial microscopy where we describe the coupling of Imaging FCS with impedance spectroscopy.

5.2.1 Live-cell imaging of membrane dynamics

The cell membrane separates the cell from the exterior environment and has a multitude of tasks such as transporting nutrients in and metabolic wastes out of cells and communicating signals from the cell exterior[2]. Many diseases are manifestations of the constituents of the cell membrane failing to perform their designated tasks and membrane proteins are major drug targets[194]. Imaging FCS can investigate the diffusion behavior of membrane proteins and lipids on an entire cell membrane in a single measurement. By correlating the data in the different pixels over time, Imaging FCS provides diffusion coefficients and concentrations of lipids and proteins in

artificial and cell membranes along with the heterogeneity of the sample from a single data set. All the investigations of temporal dynamics using Imaging FCS are on a scale of the resolution limit since we wanted to investigate membrane organization on the smallest accessible level. The spatial information was added by the cross-correlation of pixel pairs. Here, we study the diffusion and organization of two different proteins, PMT and EGFR using Imaging FCS.

5.2.1.1 EGFR

EGFR (Epidermal growth factor receptor) is a member of the tyrosine kinase family of receptors. The four proteins observed so far have been named ErbB 1-4[195]. ErbB1 is referred to as EGFR. Mutations in EGFR leading to over-expression have been implicated in a variety of cancers, for instance, lung cancer[196]. The clinical importance of these mutations can be understood by the amount of research in the field; a search in PUBMED for "EGFR + cancer" retrieves 14000 hits.

EGFR has been shown to reside in membrane microdomains[197-201]. These proteins are found in caveolar and non-caveolar lipid rafts. A specific targeting sequence of the protein has been isolated which is responsible for the movement of these proteins to lipid rafts[202]. Generally one-third to one-half of the total population of EGFR appears to be localized to lipid rafts[203].

5.2.1.2 PMT

The plasma membrane targeting sequence from the X-linked retinitis pigmentosa protein RP2[204] was used as a negative control. The N-terminal sequence of the protein responsible for membrane targeting is MGCFFSKRRK. This sequence has been conserved across a variety of organisms. Glycine at position 2 is the site for myristoylation and cysteine at position 3 is the site for palmitoylation.

5.2.1.3 Experimental details

CHO cells were chosen for the experiments in order to avoid artifacts from endogenously expressed EGFR proteins (ErB1). Only a very low amount of ErB2 is known to be expressed by CHO cells[53, 205]. CHO cells are a very good model system

to study EGFR dynamics since they have low levels of endogenous expression The CHO cells were transfected with the proteins coupled with a fluorescent protein (GFP in this case). The fluorescent proteins were cloned into the C terminus of the proteins. The functionality of the proteins has already been tested earlier in our lab[53].

5.2.1.4 Mobility of membrane proteins on live-cells

The diffusion coefficient is a measure of the fluidity of the membrane. The previous studies have found the diffusion coefficient of EGFR on the cell membranes of CHO cells to be 0.38 ± 0.13 $\mu m^2/s$[53-54]. Here it is found to be 0.2 ± 0.1 $\mu m^2/s$ which is comparable given the fact that the measurements are performed in the bottom membrane accessible by TIRF-FCS which has reduced mobility when compared to the upper membrane accessible by confocal FCS. The diffusion is hindered due to the presence of the support and the diffusion coefficients are reduced by a factor of two[148]. The large SD of the diffusion coefficients indicates strong variations in the diffusion coefficients on the cell membrane, in agreement with the partitioning of EGFR into different lipid regions[203]. Methods to reduce the SD were discussed in greater detail in the previous chapter. The mobility of PMT (0.6 ± 0.3 $\mu m^2/s$) is higher than that of EGFR on the cell membrane given the differences in size between both proteins.

The white pixels in Fig. 5.1 C and D indicate curves for which the fits didn't reach convergence. Since, the software ImFCS (Sec. 2.7) written during the project provides information from every pixel, the reasons for the non-convergence at those pixels can be retrieved. The two regions that are not fitted are characterized by a sudden rise in intensity lasting for around 2 seconds during the 40 second acquisition period. The intensity rise is twice the average intensity during all the other times. The sudden increase in intensity could be attributed to aggregates of fluorescent proteins diffusing on the membrane. Such problems can be overcome by implementing automatic FCS analysis algorithms in ImFCS for removal of unwanted peaks

corrupting the curves[206]. At certain cases, there are traces which exhibit a loss in fluorescence with time. This may be the case where the molecule is immobile on the cell membrane and hence the pixels exhibit bleaching. An option to correct for loss incurred due to bleaching is available in the software.

Bleach correction

One of the most common problems encountered in camera based FCS is the irreversible loss in fluorescence intensity during acquisition referred to as bleaching. At very high intensity decay rates, the correlation curves are dominated by bleaching instead of underlying fluctuations in the system. The easiest way to identify bleaching is by visual inspection of intensity trace which shows a gradual loss in fluorescence. Bleaching is evident in autocorrelations as well. Autocorrelation curves affected by bleaching are characterized by non-convergence of the curves. The fitted value of G_∞ is not close to the expected theoretical value of one[207]. Typically, any deviation greater than 3% from the value of one is an indication of photobleaching. Upon fitting, the diffusion coefficients retrieved for curves affected by bleaching is around 2 orders of magnitude lower than the expected value. It is necessary to correct the affected intensity traces before the calculation of autocorrelation. It is assumed that the decay of fluorescence can be modeled by a bi-exponential curve[208].

$$F(t) = F_0 + A_1 e^{-\left(\frac{t-t_0}{\tau_1}\right)} + A_2 e^{-\left(\frac{t-t_0}{\tau_2}\right)} \qquad \textbf{5-1}$$

Then the raw data at any instant is multiplied by the ratio of F_0 (fit parameter from Eq. 5-1) to that of the fitted value at the same instant. The corrected data is used further for the calculation of correlation.

5.2.1.5 Number density of membrane proteins on live-cells

This technique allows one to obtain the number of particles in each pixel. Here, the number density of EGFR was found to be ~160 μm^{-2}. The average diameter of CHO-K1 cell is found to be ~13 μm[209-211]. Assuming the cell to be a hemisphere, the total surface area is given by $3\pi r^2$ where r is the radius of the hemisphere. The

surface area of the cell membrane is calculated to be 400 μm^2. Hence the total number of receptors in the cell membrane is found to be ~64,000 molecules/cell.

5.2.1.6 Heterogeneity of membrane proteins on live-cells

As discussed in Sec. 3.3.2, the heterogeneity in Imaging FCS can be determined from diffusion laws and *ΔCCF* distributions at physiological concentrations avoiding artifacts of over-expression induced clustering. The diffusion law for EGFR in Fig. 5.1 E shows a positive intercept while an intercept close to zero is obtained for PMT indicating that EGFR prefers to partition in to domains while PMT does not. The average intercepts from diffusion laws for four different measurements clearly confirm the fact that EGFR does partition into rafts. This is corroborated by *ΔCCF* distributions which exhibit a non-normal distribution for EGFR but a normal distribution for PMT. For the same set of four measurements above, the *kstat* values agree with the fact that EGFR exhibits hindered diffusion while PMT exhibits free diffusion. This is in agreement with data provided in the literature that EGFR localizes to microdomains[197-201].

Thus it is established here that this technique allows one to display quantitative images of cell dynamics with the contrast being *D*, *N* or heterogeneity apart from the conventional intensity.

5.2.2 Imaging FCS-a tool to study membrane formation and disruption

Supported lipid bilayers (SLBs) are excellent synthetic models to study membrane dynamics and the effects of chemical and biological agents on them. The physical properties of the bilayers like integrity, continuity and dynamic fluidity serve as a read-out of the interaction between the agents and the membrane. Two characteristic features indicative of a good lipid bilayer are spatial uniformity and lateral mobility[211]. The spatial uniformity can be probed using fluorescence imaging. FCS serves as a sensitive optical detection method for lateral mobility.

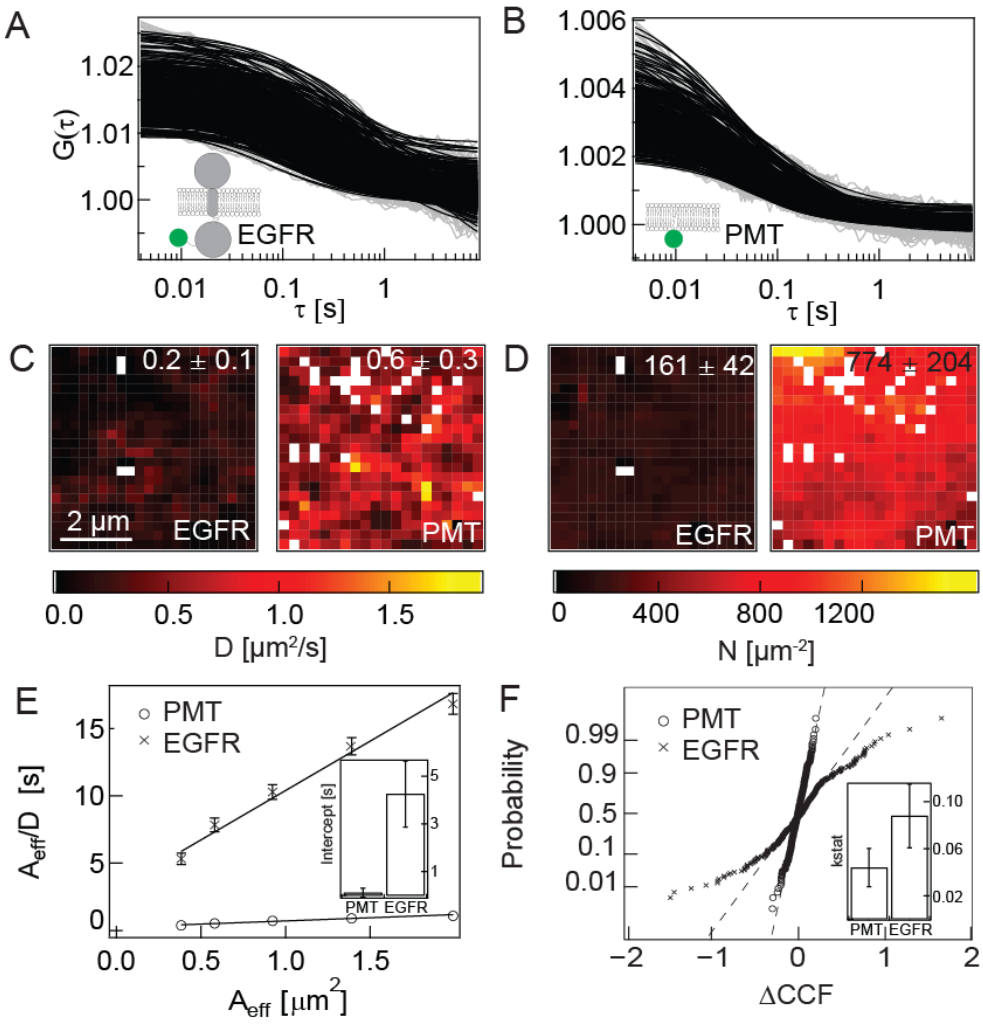

Fig. 5.1: Membrane dynamics probed by Imaging FCS. The lower membrane of cells grown on a cover-slide is imaged by a TIRF microscope. The autocorrelation curves of EGFR and PMT are shown in A and B. These curves are fitted to predefined models and the analysis yields the diffusion coefficient (*D*) of the particle and the number of particles (*N*) in each pixel of the image. The results are plotted as heat maps. This technique allows one to display quantitative images of cell dynamics with the contrast being *D* and *N* apart from the conventional intensity (Figs. C and D). E and F show the diffusion law and *ΔCCF* distribution respectively of EGFR and PMT. The insets in E and F show the average value of intercept and *kstat* from diffusion law and *ΔCCF* distribution respectively for PMT and EGFR. It is evident that both the metrics clearly classify EGFR as a domain associated protein and PMT as a protein exhibiting free diffusion.

The advantage of using FCS in this study is that the diffusion coefficient obtained as a readout from FCS is a direct measure of the roughness of the surface. The length scales probed by FCS provide a measure of nanoscopic uniformity while FRAP could only provide uniformity at longer length scales. Hence it is advantageous to use FCS to characterize lipid bilayers on different surfaces. FCS has already been used to probe the formation of lipid bilayers on nanodiamond[212].

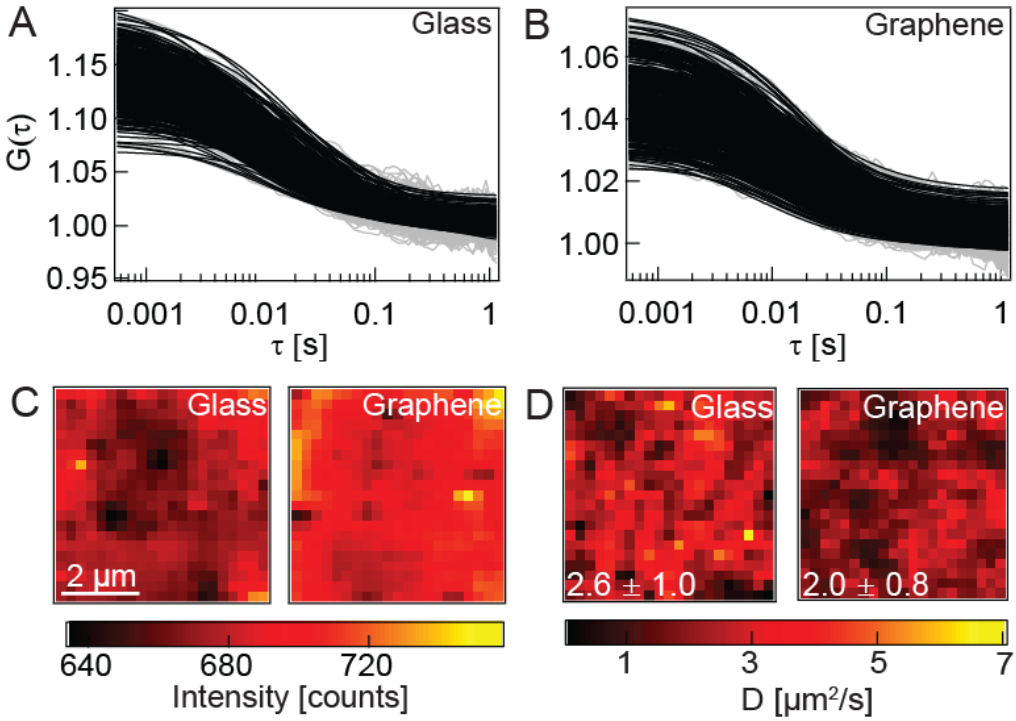

Fig. 5.2: Supported lipid bilayers on graphene. ACFs of membranes on glass and graphene are shown in A and B. The figures show all 441 correlation curves captured in a 21 × 21 pixel region of interest on the EMCCD camera. The labeling ratio of Rho-PE/POPC was 0.01% for glass and 0.02% for graphene; the sample was excited with 2 mW at a wavelength of 514 nm; the recording time was 5.6 s for 10000 frames. All data were fitted with Eq. 3-17. The intensity images of the bilayers which quantify spatial uniformity are shown in C. The diffusion coefficient images which quantify mobility are shown in D.

In order to measure fluidity by ITIR-FCS, the substrate must be optically transparent and has a high refractive index (higher than that of water in order to obtain TIR (explained in Sec. 2.3.1). Since, ITIR-FCS measures membrane fluidity at many points simultaneously, it can be used as a probe for spatial uniformity as well. Another advantage of using ITIR-FCS to characterize the bilayers on surfaces is that it is a surface sensitive technique and avoids background noise due to the contributions from the bulk liquid away from the interface. Here, ITIR-FCS has been used to show that continuous lipid bilayers (above the optical resolution limit) can be formed on graphene films.

The D of POPC membranes on graphene and glass were found to be 2.0 ± 0.8 $\mu m^2/s$ and 2.6 ± 1.0 $\mu m^2/s$ respectively. The obtained D for glass is closer to the

Saffman-Delbrück model[143] since these measurements have been performed with a faster camera with a time resolution of 0.5 ms. The lipid mobilities of membranes on graphene is close to that of glass (Fig. 5.2 A, B and D), which is surprising in view of the hydrophobic character of graphene[213].

The average intensity images of the bilayers on glass and graphene are shown in Fig. 5.2 C. The spatial uniformity of membranes atop graphene and glass is evident in Fig. 5.2 D in which the diffusion coefficient images show relatively constant membrane diffusivity. Such findings provide new insights into the compatibility of graphene with biomimetic membrane fluidity. The diffusion coefficients are in agreement with the values reported in literature using other methods, e.g. z-scan FCS and 2-focus FCS[128, 148-150]. As expected, G_∞ is close to unity in all cases indicating that there is no photobleaching. Although any conventional imaging technique would have provided the intensity image (Fig. 5.2 C), only ITIR-FCS can provide the diffusion coefficient image where physical properties (here roughness) can be used as a contrast measure. The good lateral mobility of biomimetic membrane on graphene suggests that a trapped water layer may exist between the graphene and biomimetic membrane.

The ability to form lipid bilayers makes graphene an ideal candidate as a biosensor for testing the action of biological and chemical agents that disrupt the membranes of bacteria. It is known that the composition of eukaryotic and bacterial cell membranes are different[214]. Bacterial cell membranes are enriched in negatively charged lipids and hence supported lipid bilayers which contain such lipids, for instance POPG are considered good mimics of bacterial membranes[212, 214]. Hence graphene surfaces were tested for possibility of formation of POPC-POPG membranes.

POPC and POPG molecules are zwitterionic and negatively charged respectively. POPC:POPG bilayers are very similar in their structural properties including thickness and global order as the acyl chains for POPC and POPG are the

same[215]. However, a significant decrease in *D* was observed for 33 mol % of POPG lipids (1.1± 0.5 $\mu m^2/s$) when compared to only POPC bilayers on graphene. However, the lower *D* can be attributed to the increase in local viscosity due to extensive hydrogen bonding[216].

Here, ITIR-FCS has been used to show that continuous lipid bilayers can be formed on graphene. Regardless of the types of graphene film used, supported lipid bilayers can be successfully formed on them. This shows that graphene with its high electrical conductivity and optical transparency allows the possibility of fabricating a dual-mode optical and electrical detection system.

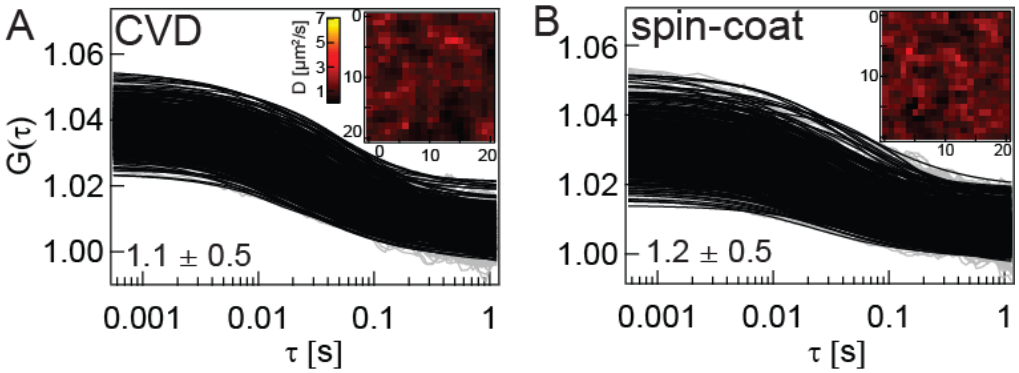

Fig. 5.3: Mimics of bacterial membrane grown on graphene. The entire set of autocorrelation curves in grey and the fits in black are shown for Rho-PE labeled POPC:POPG (2:1) bilayers grown on graphene made using two different methods, CVD and spin-coat respectively are shown in A and B. The insets show the corresponding D images drawn on the same scale as Fig. 5.2. The images are darker than those in Fig. 5.2 indicating the reduction in diffusion coefficient.

5.2.2.1 Action of antimicrobials probed by Imaging FCS

The action of antimicrobials on lipid bilayers can be studied in real time using Imaging FCS and hence the same technique was used to elucidate the mechanism of action of magainin 2 and melittin on membranes. Upon insertion into the membrane, the antimicrobials lead to a change in the fluidity of the membrane leading to a change in the diffusion coefficient of the membrane.

Magainin 2 is a 23-residue cationic peptide extracted from the skin of the African frog *Xenopus laevis*[217-218]. It adopts a primarily α-helical structure upon binding to negatively charged membranes by electrostatic attraction. Magainin 2 has

two binding states in a membrane; a surface state at low peptide concentration in which it adsorbs parallel to the membrane surface and a transmembrane pore-forming state at high peptide concentration[219-220]. The mechanism of peptide-induced membrane perforation has been a subject of much debate. There is increasing experimental evidence of membrane thinning as a precursor stage to pore formation[219, 221-226].

Here, membrane thinning can be observed from Imaging FCS as well. Membrane thinning and bilayer disruption leads to a loss of fluorescent lipids from the supported lipid bilayer. Hence, the number of particles decreases upon the addition of the peptide as seen in the histogram of number of particles after the addition of magainin (Fig. 5.4 B). The second evidence of membrane thinning is from the fact that the diffusion coefficient of 2:1 POPC:POPG bilayers decreases upon incubation with the peptide. Diffusion in the lower leaflet is slower than the upper leaflet due to the attachment to the substrate. The reduction in *D* is also attributed to the fact that these peptides create pores in the membranes and the presence of such barriers to diffusion leads to a reduction in *D*. Hence the *D* decreases upon incubation with the peptide (Fig. 5.4 A).

Melittin is an antimicrobial peptide obtained from bee venom. Both magainin and melittin disrupt membranes in a similar fashion[227]. Corroborating the statement above is the fact that a reduction of *D* and *N* was also observed upon incubation with melittin (Fig. 5.4 E and F).

A decreased *D* after the addition of anti-microbial peptides to supported lipid bilayers has been observed earlier as well[228]. The addition of cryptdin-4 led to a 3 times reduction in the *D* of supported phospholipid bilayers[229]. Melittin and magainin led to a decrease of 60% in the diffusion coefficient upon binding to lipid membranes[230]. Earlier reports have also shown the significant loss of lipids upon melittin addition by complementary techniques like ellipsometry[231]. Thus Imaging FCS was used in the successful demonstration of both the lowering in diffusion

coefficient and number density due to the addition of antimicrobials simultaneously for the first time.

The detection system for the optical set up is an EMCCD camera. The best EMCCD cameras offer a time resolution of 0.5 ms which is sufficient to resolve events on the membrane before and after peptide addition. But, the dynamics of the peptide in the bulk solution prior to the incorporation into the membrane cannot be resolved by this tool. They can be overcome by cameras with higher time resolution. The time resolution of the cameras is increasing at an unprecedented rate and it is widely believed that newer EMCCD camera models will be in the market with better time resolution very soon to probe solution dynamics.

Here, the membrane thinning effect can be clearly observed from the AFM and epifluorescence images when 1 μM Magainin 2 was added to the negatively charged POPC/POPG membranes. Increasing peptide concentration results in membrane thinning, where a change in lipid thickness from ~ 5±1 nm (Fig. 5.4 C) to ~ 3±1 nm (Fig. 5.4 D) was detected.

5.2.3 Combined electrical and optical detection

The physical properties of the bilayers which serve as a read out of the interaction between the membrane disturbing agents and the lipid membranes can be readily quantified by a variety of techniques. The previous section demonstrated the usage of FCS and AFM. Apart from these two, they can be monitored by other fluorescence techniques like FRET, FRAP, FLIM or by scanning techniques like Scanning Probe Microscopy (SPM) or electrical techniques like impedance spectroscopy. A combination of the aforementioned techniques is used in order to completely understand the mechanism of activity of the agents on membranes since each technique measures a unique aspect of the reaction.

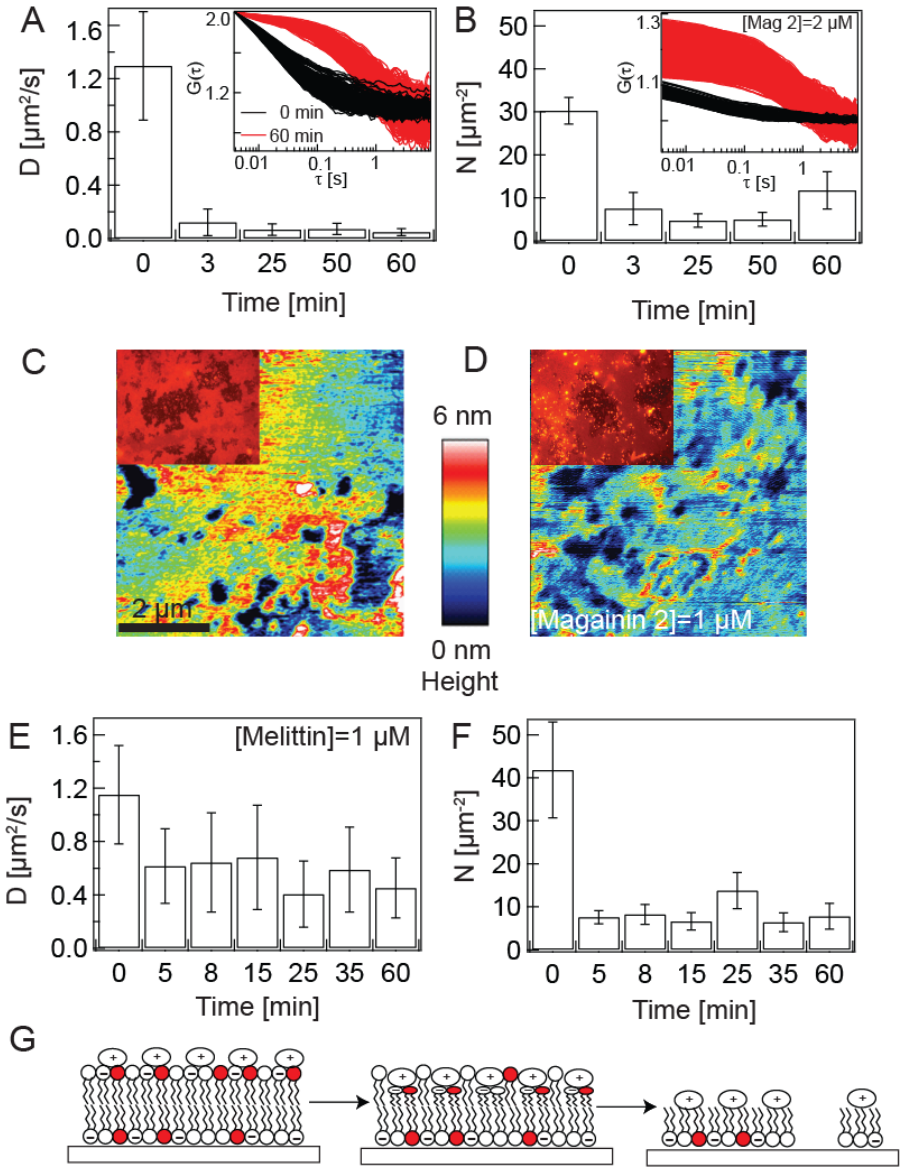

Fig. 5.4: Action of melittin and magainin probed by Imaging FCS. A and B show the reduction in *D* and *N* with time upon addition of magainin. The two sets of autocorrelations shown in the inset A are normalized for the number density and hence reveal the differences in diffusion behavior. The raw autocorrelations in inset B differ in the amplitude indicating a difference in the number of particles. C and D are AFM images of membrane before and addition of magainin-2 peptides respectively. A membrane thickness of 4-5 nm was obtained in C. Widespread membrane thinning effect where membrane thickness reduced to 2-3 nm and membrane disruption are evident in D. The Inset in D shows the epi-fluorescence image in which adsorption of peptides (represented by bright spots) was clearly observed at the periphery of the membranes. These bright spots are speculated to be due to the onset of membrane thinning in which adsorbed peptides push apart the lipid head groups on the top leaflet, causing these fluorescent lipids to be dislodged from the surface. Similar effects to A and B are observed upon melittin addition shown in E and F respectively. G is a schematic representation of the anti-microbial peptide action. Cationic peptides (ovals) bind to intact membrane. They push apart lipid head groups, resulting in membrane thinning effect. At higher concentration of peptides, there is a loss of the upper leaflet leading to a reduction in *D*, *N* and thickness.

Simultaneous measurement of the various properties by the different techniques can yield novel insights into the problem which cannot be solved by performing the measurements separately since the measured parameters at any time-point have a one-to-one correspondence to each other during synchronous sensing. Such combinatorial tools have been already constructed and demonstrated. A combined AFM/TIRFM for order parameter measurements and AFM/FCS for raft studies have been demonstrated[232-233]. A detailed review of such tools is provided here[234].

In this context, we introduce simultaneous optical detection by ITIR-FCS and electrical detection of the field-effect to elucidate the changes in fluidity and integrity of membranes induced by membrane disrupting agents. Single molecule sensitive ITIR-FCS enables the accurate determination of mobility of the bilayers and the space charge effect of semiconductors showing field effect response is an efficient way of probing the integrity of the bilayer. In the case of the chosen two techniques, the diffusion coefficient is used as a read out in ITIR-FCS. The reduction in diffusion coefficient of lipids diffusing on the membrane may be due to imperfections in bilayer or the aggregates in the bilayer or due to creation of pores after insertion of antimicrobial peptides (discussed in Sec. 5.2.2.1). This discrepancy can be solved by integrating this setup with a field-effect transistor (FET) configuration which shows a change in current if pores or imperfections in the bilayer were present. Hence these two techniques can be used in synergy for better understanding of membrane processes. We demonstrate the system by studying the action of melittin on phospholipid bilayers.

Conventionally, imaging is performed on fused silica, glass or mica. But these substrates are not electrically conductive and hence cannot be used for simultaneous optical and electrical detection[212]. On the other hand, materials used in electrical detection like indium tin oxide or gold are limited by their transparency and hence cannot be used for optical sensing[212]. The use of optically transparent and

electrically active nanocrystalline diamond with microscopic smoothness and sufficient hydrophilicity with proper surface treatment amenable to forming high quality biomimetic membranes led to the synergistic coupling of both the optical and electrical methods.

5.2.3.1 Principle of electrical detection of membrane dynamics

Electrical detection typically involves a FET which consists of a pair of source and drain regions bearing a conductive channel in between. Such source and drain contacts can be deposited onto the electrically active substrate via thermal or electron-beam lithography. A dielectric layer (usually aqueous electrolyte) is sandwiched in between a conductive gate and the conductive channel. The gate electrode serves to modulate the channel conductivity of the underlying semiconductor and could decrease or increase the current passing through the channel by varying the applied electric field. The p-type hole accumulation layer in intrinsic nanocrystalline diamond is used as the semiconductor here. The chemical/biological entity can potentially modulate the surface potential of the active channel and hence the change in channel conductivity can be correlated to their interaction. Such surface charge transfer process allows elucidation of mechanistic changes induced by chemical and biological agents to membranes.

5.2.3.2 Demonstration of simultaneous optical and electrical detection

A 2:1 POPC:POPG bilayer was prepared on a nanocrystalline diamond based sensor. Combined electrical and optical detection of the action of melittin on the bilayer was performed. A reduction in the diffusion coefficient is observed concomitant with a corresponding increase in the drain-source current as in Fig. 5.5. A detailed discussion of reduction of the diffusion coefficient upon melittin addition is described in Sec. 5.2.2.1. When the diamond surface is passivated by a lipid bilayer, negatively charged ions in the solution are prevented from reaching it. This results in a low drain-source current. However, upon addition of melittin, membrane disruption occurred, allowing negatively charged ions in the solution to interact with

the diamond surface, bring forth an increase in hole concentration by electrostatic interaction. In general, it is seen that with an increase in the extent of disruption of the lipid bilayer, the drain-source current of diamond correspondingly increases. However, at too high a concentration of cationic peptide, the drain-source current decreased due to electrostatic repulsion between cationic melittin and the hole accumulation layer in diamond.

It is also seen that at 0.5 μM melittin, the number of particles in the bilayers decreases, *D* stays constant and there is an increase in current. This suggests that at 0.5 μM, the peptides cause thinning and some perforations in the bilayers leading to increase in current and a loss in fluorescent particles. At 1 μM, the porosity increases leading to a reduction in *D*, increase in current and a higher degree of reduction in *N*. However, as the concentration increases beyond 1 μM, a decrease in drain-source current, coupled with a dramatic decrease in diffusion and number of fluorescent molecules are observed (See Sec. 5.2.2.1). This could be attributed to a membrane surface saturation of cationic peptide, extensive peptide-induced membrane agglomeration and direct contact between cationic peptides and the diamond surface.

It was concluded in the previous section that after membrane thinning, an imperfect monolayer of lipids is left on the substrate based on AFM and Imaging FCS. The electrical measurements suggest a passivation of the surface by melittin or possibly even direct contact between melittin and diamond surface could reduce the hole concentration of diamond. Hence, it is known that the height observed in the AFM in Sec. 5.2.2.1 is an average of the monolayer and that of the peptide bound to the surface. The above interpretation would not have been possible if the measurements had been made individually. The correlation in the results between the optical and electrical measurement helps in the elucidation of the action mechanism of melittin on bilayers and its concentration dependence.

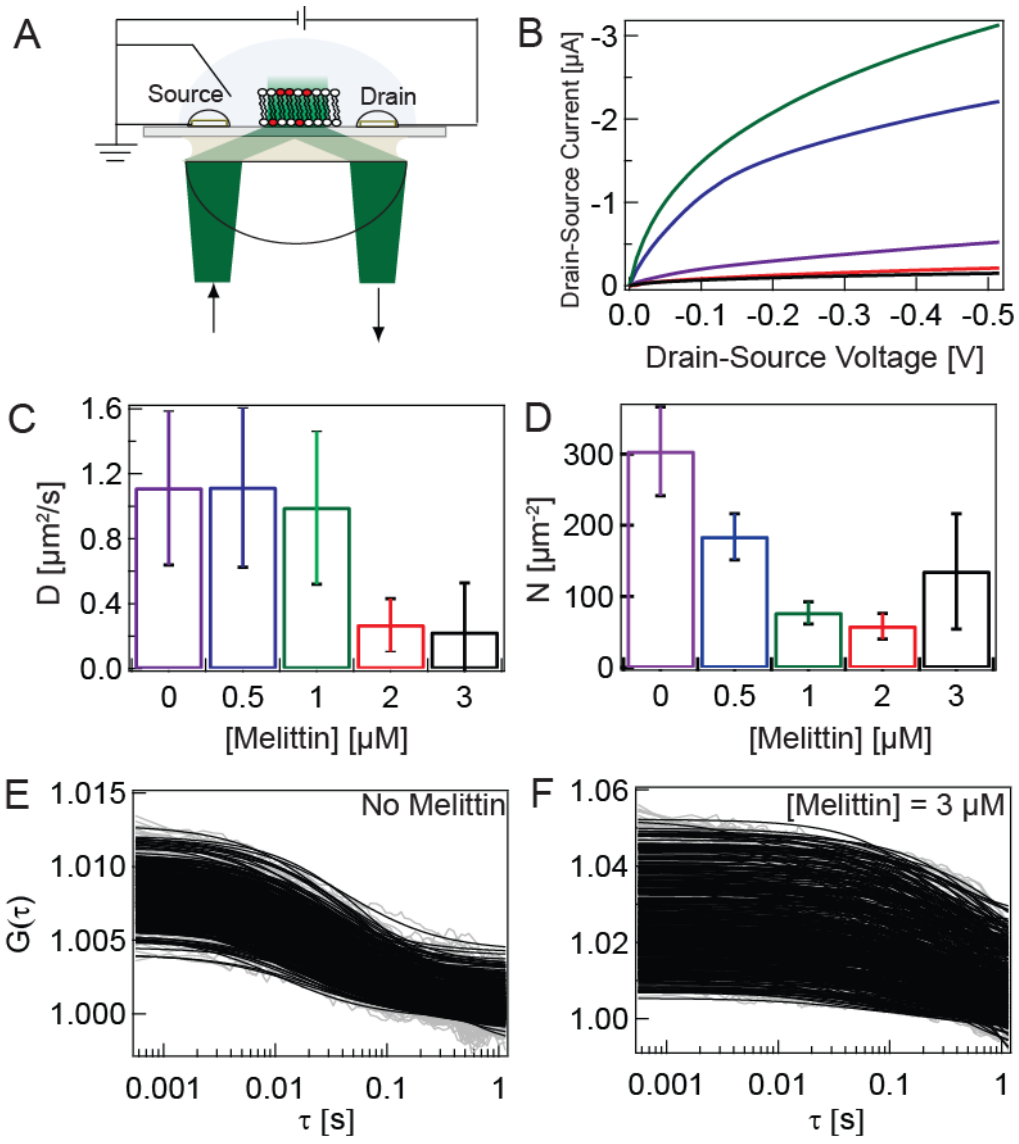

Fig. 5.5: Simultaneous electrical and optical detection. A is a schematic of the set up showing the presence of the source and drain electrodes along with the optically transparent and electrically active substrate. B is a plot of the drain source current at various peptide concentrations. C and D show the reduction in *D* and *N* upon peptide addition respectively. The entire set of autocorrelation curves is shown in grey along with the fits in black before and after addition of the peptide in E and F respectively.

It would have been ideal if the force, optical and electrical measurements would have been performed from a single sample. But in the current set-up, force measurements could not be coupled and hence only coupled optical and electrical measurements are reported here. The tool described here is a unique combination of different methods thus reducing the need for preparing the sample many times and provides novel insights into the investigated problem since two different physical properties namely membrane fluidity and continuity was monitored synchronously.

The tool developed here serves three purposes, as a screening device to isolate prospective antimicrobial candidates from a huge repertoire or for in-depth studies of mechanism or to determine the dosage for the chosen peptides.

5.3 Conclusion

Two different applications were discussed in this chapter. The first application showed the ability of the technique to display quantitative images of cell mobility and heterogeneity. Thus, this technique holds great promise as a single molecule sensitive tool to probe real-time membrane organization and dynamics in live-cells. The second application described the usage of this technique to study the action of antimicrobial peptides on different surfaces. The latest public health problem is antibiotics resistance to commercial generic antibiotic drugs. Hence antimicrobial peptides are seen as a potential treatment for bacterial infections since bacteria cannot develop resistance to these peptides as these peptides do not target a specific protein but act on the entire negatively charged membrane as a whole. Hence it is imperative to develop tools to properly quantify the peptide action on membranes. Simultaneous optical and electrical detection is an ideal tool that can be used for screening studies of antimicrobials on membranes.

6 Conclusion

Over the years, various technologies have revolutionized biological research. The ability to culture cells outside an organism was one of the major breakthroughs and led to *in vitro*[235] experimentation. This was later improved when *in situ*[236] experiments provided spatial information. Improvements in labeling technologies led to the development of *in vivo* measurements. The next improvement came with the introduction of *ex vivo* measurements on tissues from biological samples which bridged the gap between *in vitro* and *in vivo* measurements. The improvements in animal cell culture went hand in hand with the introduction of *in planta* experiments in the field of plant biology. The advances in data processing and computation led to a new era in biology referred to as *in silico*[237] biology. Each method of experimentation provides different insights into the same problem. The last two decades have seen a tremendous increase in the development of single molecule sensitive techniques in biological research which are collectively referred to as *in singulo*[238-240] methods.

Current research suggests that fixing cells leads to artifacts. Hence there is a need to study biological processes in live-cells. Further, in non-single molecule sensitive technique, the signal to noise ratio is increased by increasing the number of biomolecules, as a result, over-expression is performed. This thesis describes one such technique studying an ensemble of biomolecules in live-cell membrane at physiological concentrations using single molecule sensitive cameras called Imaging Total Internal Reflection FCS. ITIR-FCS is a technique which has been shown to quantitate mobility at many contiguous points on a cell membrane using autocorrelation functions.

In this thesis, ITIR-FCS was extended to ITIR-FCCS enabling one to calculate cross-correlations and to extract parameters from the same. Proof of principle ITIR-FCCS measurements were demonstrated on molecular systems

exhibiting different combinations of flow and diffusion (Sec. 3.3.1). The estimates of mobility and concentration were close to the expected value. The method is calibration free since the PSF can be determined from the data itself. Four different methods were discussed to calculate the PSF.

The ability to calculate cross-correlation enabled one to study heterogeneity in diffusion in GUVs and mixed lipid bilayers (Sec. 3.3.2). The heterogeneity was determined by computing the difference of the forward and backward correlations leading to the creation of *ΔCCF* distributions. After measurements in artificial lipid bilayers stated above, the *ΔCCF* imaging was used to probe the cell membrane organization and heterogeneity of a lipid microdomain marker called SBD. Apart from *ΔCCF*, heterogeneity can also be ascertained in Imaging FCS by diffusion laws (Sec. 3.3.2.1). Diffusion laws provide an estimate of the global heterogeneity of the sample whereas normality tests provide an estimate for the local heterogeneity of the sample.

After experimental Imaging FCS studies to probe mobility, concentration and heterogeneity, simulations were used to ascertain the effects of various instrumental parameters on the accuracy and precision of the same (Sec. 4.2). This enabled one to compute the error in the estimates beforehand using the chosen parameters. In a nutshell, it was found that the accuracy of D and N was dependent on $\Delta\tau$ and that the precision was inversely related to $w_0^2/D\Delta\tau$.

Currently it is seen that the heterogeneity in Imaging FCS is estimated using diffusion laws and *ΔCCF* images. Barriers have been detected using pair-correlation functions. Put together, pair correlation, diffusion law and *ΔCCF*, all these are quite good at understanding the heterogeneity of the system.

The advent of sCMOS, which provide a wider field of view, opens up unprecedented opportunities in Imaging FCS. The data can be obtained from multiple cells at the same time. More than million correlations can be calculated from a single

measurement. The smaller pixel sizes have an advantage in estimating the heterogeneity. Currently while calculating diffusion laws, the areas for which the calculations are performed are ~ 0.05, 0.25, 0.5, 1, 1.5 μm^2. Smaller pixel size would lead to better diffusion laws. In spite of a pixel size of ~ 50 nm, the first few binnings (upto 5×5), will be diffraction limited. In the current scenario, the first point is at 0.05 while the next point is at 0.25 μm^2. But with a pixel size of 50 nm, in between 0.05 and 0.25 μm^2, we can get 5 more points by performing 6-9 binning. As well, the biologically relevant length scales are close to the diffraction limit and hence determining diffusion laws with smaller pixel sizes close to the diffraction limit will provide more accurate estimations in the case of diffusion law.

Various applications of Imaging FCS were demonstrated in the last chapter. The first application demonstrated the usage of single molecule sensitive Imaging FCS to probe the dynamics and organization of a membrane protein at physiological concentrations (Sec. 5.2.1). The rest of the applications discussed in the chapter probed the mobility of lipids. Imaging FCS was used to study the formation of lipid bilayers on a variety of surfaces like nanodiamond and graphene (Sec. 5.2.2). The major advantage of using such surfaces is that these electrically conducting and optically active surfaces enable one to simultaneously probe the existence of the bilayer by electrical and optical means. This was demonstrated in the study of action of an anti-microbial called magainin 2 on bilayer surfaces.

This thesis showed proof of principle measurements coupling impedance measurements and FCS (Sec. 5.2.3). AFM could also be combined so that the underlying method can be probed by three different tools at the same time. The addition of polarizing optics would enable one to calculate order parameters as well. Recently, proof of principle experiments combining FCS and anisotropy measurements was demonstrated[241]. Hence, in the near future, from the same sample, mobility, concentration, heterogeneity, surface roughness, conductivity and order parameters can be determined.

Apart from determining number from autocorrelation analysis, the number can also be determined if the algorithms from number and brightness analysis are implemented in Imaging FCS. The brightness serves to quantitate the oligomeric state of the biomolecule. The advantage of implementing number and brightness analysis is that, it is performed on single images from the stack. As a result, at least the number of particles and brightness can be estimated in spite of photobleaching in samples.

This entire thesis discussed only autocorrelations and spatiotemporal cross-correlation. Implementing a two-color cross-correlation system will help in understanding the interactions of biomolecules. Currently, this technique enables one to obtain mobility, concentration and heterogeneity maps. With the implementation of two-color correlation, interaction maps will be possible to be obtained. Thus this technique will be a value addition to the arsenal of tools available today to study protein-protein interactions since it will yield information about interaction at physiological concentrations in live-cells.

The current day cameras have time resolution in the sub millisecond regime. Faster cameras will enable one to probe the dynamics of cytoplasmic molecules which diffuse at a rate faster than those attached to the membrane. The advent of faster cameras would also enable one to do Photon Counting Histogram (PCH). As a result, the concentration can be determined from three different methods, autocorrelation, N&B and PCH while the oligomerization can be determined from N&B and PCH. Hence, it is seen that this technique is a full data analysis package that can be used to extract a variety of meaningful biological information upon suitable statistical techniques using a single data set.

With faster cameras, superior memory capabilities, data is being generated in Imaging FCS at a rapid pace; hence there is a great need to develop automated data analysis tools. Automated fitting procedures need to be implemented. For example Bayesian analysis or artificial neural networks can be implemented to choose between

fitting models for instance, one particle, two particles or three particles fits. Currently, no hardware correlators are available either standalone or attached to an EMCCD. Hence on-chip data analysis can be done by performing the calculations in a PCI-card instead of performing it using the software offline.

ITIR-FCS gives adequate spatial and temporal resolution to be able to measure membrane dynamics in a calibration free manner, and thus presents a powerful biophysical tool to provide novel insights into transport phenomena and membrane organization. Thus, this technique holds great promise as a single molecule sensitive tool to probe real-time membrane organization and dynamics in live-cells. The introduction of SPIM-FCS enables one to perform measurements in the cytoplasm as well. With automated data-analysis and liquid handling methods, this technique has great potential to be used as an automated screening technique to assay for interactions in live-cells in the pharmaceutical industry.

Bibliography

1. S. Surade, M. Klein, P. C. Stolt-Bergner, C. Muenke, A. Roy, H. Michel, *Comparative analysis and "expression space" coverage of the production of prokaryotic membrane proteins for structural genomics*, *Protein Sci* **2006**, *15*. 2178-89

2. H. Lodish, A. Berk, C. Kaiser, M. Krieger, M. Scott, A. Bretscher, H. Ploegh, P. Matsudaira, in *Molecular Cell Biology* **2007**, 147-196.

3. M. van Engeland, L. J. Nieland, F. C. Ramaekers, B. Schutte, C. P. Reutelingsperger, *Annexin V-affinity assay: a review on an apoptosis detection system based on phosphatidylserine exposure*, *Cytometry* **1998**, *31*. 1-9

4. S. J. Singer, G. L. Nicolson, *The Fluid Mosaic Model of the Structure of Cell Membranes*, *Science* **1972**, *175*. 720-731

5. L. J. Pike, *Rafts defined: a report on the Keystone Symposium on Lipid Rafts and Cell Function*, *J. Lipid Res.* **2006**, *47*. 1597-1598

6. L. J. Pike, *The challenge of lipid rafts*, *Journal of Lipid Research* **2009**, *50*. S323-328

7. Y. Zhang, X. Li, K. A. Becker, E. Gulbins, *Ceramide-enriched membrane domains-Structure and function*, *Biochim. Biophys. Acta-Biomembr.* **2009**, *1788*. 178-183

8. A. J. Garcia-Saez, P. Schwille, *Fluorescence correlation spectroscopy for the study of membrane dynamics and protein/lipid interactions*, *Methods* **2008**, *46*. 116-122

9. K. Simons, J. L. Sampaio, *Membrane organization and lipid rafts*, *Cold Spring Harb Perspect Biol* **2011**, *3*.

10. C. Dietrich, L. A. Bagatolli, Z. N. Volovyk, N. L. Thompson, M. Levi, K. Jacobson, E. Gratton, *Lipid rafts reconstituted in model membranes*, *Biophys J* **2001**, *80*. 1417-28

11. P. Thomsen, K. Roepstorff, M. Stahlhut, B. van Deurs, *Caveolae are highly immobile plasma membrane microdomains, which are not involved in constitutive endocytic trafficking*, *Mol Biol Cell* **2002**, *13*. 238-50

12. R. G. Anderson, K. Jacobson, *A role for lipid shells in targeting proteins to caveolae, rafts, and other lipid domains*, *Science* **2002**, *296*. 1821-5

13. M. Suzuki, Y. Shinohara, Y. Ohsaki, T. Fujimoto, *Lipid droplets: size matters*, *J Electron Microsc* **2011**, *60*. S101-16

14. G. van Meer, A. I. de Kroon, *Lipid map of the mammalian cell*, *J Cell Sci* **2011**, *124*. 5-8

15. C. Osman, D. R. Voelker, T. Langer, *Making heads or tails of phospholipids in mitochondria*, *J Cell Biol* **2011**, *192*. 7-16

16. A. Shevchenko, K. Simons, *Lipidomics: coming to grips with lipid diversity*, *Nat Rev Mol Cell Biol* **2010**, *11*. 593-598

17. M. R. Wenk, *Lipidomics: New Tools and Applications*, *Cell* **2010**, *143*. 888-895

18. T. Zech, C. S. Ejsing, K. Gaus, B. de Wet, A. Shevchenko, K. Simons, T. Harder, *Accumulation of raft lipids in T-cell plasma membrane domains engaged in TCR signalling*, *Embo J* **2009**, *28*. 466-76

19. R. Henriques, C. Griffiths, E. Hesper Rego, M. M. Mhlanga, *PALM and STORM: unlocking live-cell super-resolution*, *Biopolymers* **2011**, *95*. 322-31

20. L. Zhong, G. Zeng, X. Lu, R. C. Wang, G. Gong, L. Yan, D. Huang, Z. W. Chen, *NSOM/QD-Based Direct Visualization of CD3-Induced and CD28-Enhanced Nanospatial Coclustering of TCR and Coreceptor in Nanodomains in T Cell Activation*, *PLoS ONE* **2009**, *4*. e5945

21. D. Fu, F. K. Lu, X. Zhang, C. Freudiger, D. R. Pernik, G. Holtom, X. S. Xie, *Quantitative chemical imaging with multiplex stimulated Raman scattering microscopy*, *J Am Chem Soc* **2012**, *134*. 3623-6

22. U. Schnell, F. Dijk, K. A. Sjollema, B. N. G. Giepmans, *Immunolabeling artifacts and the need for live-cell imaging*, *Nat Meth* **2012**, *9*. 152-158

23. D. Marguet, P.-F. Lenne, H. Rigneault, H.-T. He, *Dynamics in the plasma membrane: how to combine fluidity and order*, *EMBO J* **2006**, *25*. 3446-3457

24. E. Sezgin, P. Schwille, *Fluorescence Techniques to Study Lipid Dynamics*, *Cold Spring Harbor Perspectives in Biology* **2011**.

25. J. S. Goodwin, A. K. Kenworthy, *Photobleaching approaches to investigate diffusional mobility and trafficking of Ras in living cells*, *Methods* **2005**, *37*. 154-164

26. A. K. Kenworthy, B. J. Nichols, C. L. Remmert, G. M. Hendrix, M. Kumar, J. Zimmerberg, J. Lippincott-Schwartz, *Dynamics of putative raft-associated proteins at the cell surface*, *The Journal of Cell Biology* **2004**, *165*. 735-746

27. T. Foerster, *Intermolecular energy migration and fluorescence*, *Annals of Physics* **1948**, *2*. 55

28. P. Liu, S. Ahmed, T. Wohland, *The F-techniques: advances in receptor protein studies*, *Trends in Endocrinology & Metabolism* **2008**, *19*. 181-190

29. F. T. Chan, C. F. Kaminski, G. S. Kaminski Schierle, *HomoFRET fluorescence anisotropy imaging as a tool to study molecular self-assembly in live cells*, *Chemphyschem* **2011**, *12*. 500-9

30. J. N. Israelachvili, in *Intermolecular and Surface Forces (Third Edition)*, **2011**, pp 71-90.

31. B. H. Meyer, J.-M. Segura, K. L. Martinez, R. Hovius, N. George, K. Johnsson, H. Vogel, *FRET imaging reveals that functional neurokinin-1 receptors are monomeric and reside in membrane microdomains of live cells*, *Proc. Natl. Acad. Sci. U. S. A.* **2006**, *103*. 2138-2143

32. R. F. M. de Almeida, L. M. S. Loura, M. Prieto, *Membrane lipid domains and rafts: current applications of fluorescence lifetime spectroscopy and imaging*, *Chemistry and Physics of Lipids* **2009**, *157*. 61-77

33. J. Herreros, T. Ng, G. Schiavo, *Lipid Rafts Act as Specialized Domains for Tetanus Toxin Binding and Internalization into Neurons*, *Molecular Biology of the Cell* **2001**, *12*. 2947-2960

34. A. N. Bader, E. G. Hofman, J. Voortman, P. M. en Henegouwen, H. C. Gerritsen, *Homo-FRET imaging enables quantification of protein cluster sizes with subcellular resolution*, *Biophys J* **2009**, *97*. 2613-22

35. T. Friedrichson, T. V. Kurzchalia, *Microdomains of GPI-anchored proteins in living cells revealed by crosslinking*, *Nature* **1998**, *394*. 802-805

36. R. Varma, S. Mayor, *GPI-anchored proteins are organized in submicron domains at the cell surface*, *Nature* **1998**, *394*. 798-801

37. P. Sharma, R. Varma, R. C. Sarasij, Ira, K. Gousset, G. Krishnamoorthy, M. Rao, S. Mayor, *Nanoscale organization of multiple GPI-anchored proteins in living cell membranes*, *Cell* **2004**, *116*. 577-589

38. N. Vyas, D. Goswami, A. Manonmani, P. Sharma, H. A. Ranganath, K. VijayRaghavan, L. S. Shashidhara, R. Sowdhamini, S. Mayor, *Nanoscale organization of hedgehog is essential for long-range signaling*, *Cell* **2008**, *133*. 1214-27

39. D. Goswami, K. Gowrishankar, S. Bilgrami, S. Ghosh, R. Raghupathy, R. Chadda, R. Vishwakarma, M. Rao, S. Mayor, *Nanoclusters of GPI-Anchored Proteins Are Formed by Cortical Actin-Driven Activity*, *Cell* **2008**, *135*. 1085-1097

40. L. S. Barak, W. W. Webb, *Diffusion of low density lipoprotein-receptor complex on human fibroblasts*, *J Cell Biol* **1982**, *95*. 846-52

41. M. J. Saxton, K. Jacobson, *SINGLE-PARTICLE TRACKING:Applications to Membrane Dynamics*, *Annual Review of Biophysics and Biomolecular Structure* **1997**, *26*. 373-399

42. M. J. Saxton, K. Jacobson, *Single-particle tracking: Applications to membrane dynamics*, *Annu. Rev. Biophys. Biomolec. Struct.* **1997**, *26*. 373-399

43. F. Pinaud, X. Michalet, G. Iyer, E. Margeat, H.-P. Moore, S. Weiss, *Dynamic Partitioning of a Glycosyl-Phosphatidylinositol-Anchored Protein in Glycosphingolipid-Rich Microdomains Imaged by Single-Quantum Dot Tracking*, *Traffic* **2009**, *10*. 691-712

44. A. Kusumi, H. Ike, C. Nakada, K. Murase, T. Fujiwara, *Single-molecule tracking of membrane molecules: plasma membrane compartmentalization and dynamic assembly of raft-philic signaling molecules*, *Semin Immunol* **2005**, *17*. 3-21

45. E. L. E. Douglas Magde, Watt W. Webb,, *Fluorescence correlation spectroscopy. II. An experimental realization*, *Biopolymers* **1974**, *13*. 29-61

46. W. W. W. Douglas Magde, Elliot L. Elson,, *Fluorescence correlation spectroscopy. III. Uniform translation and laminar flow*, *Biopolymers* **1978**, *17*. 361-376

47. D. M. Elliot L. Elson, *Fluorescence correlation spectroscopy. I. Conceptual basis and theory*, *Biopolymers* **1974**, *13*. 1-27

48. E. Haustein, P. Schwille, *Fluorescence correlation spectroscopy: Novel variations of an established technique*, *Annu. Rev. Biophys. Biomolec. Struct.* **2007**, *36*. 151-169

49. O. Krichevsky, G. Bonnet, *Fluorescence correlation spectroscopy: the technique and its applications*, *Rep. Prog. Phys.* **2002**, *65*. 251-297

50. P. Schwille, F. J. Meyer-Almes, R. Rigler, *Dual-color fluorescence cross-correlation spectroscopy for multicomponent diffusional analysis in solution*, *Biophys J* **1997**, *72*. 1878-86

51. L. C. Hwang, T. Wohland, *Dual-color fluorescence cross-correlation spectroscopy using single laser wavelength excitation*, *Chemphyschem* **2004**, *5*. 549-51

52. K. Bacia, I. V. Majoul, P. Schwille, *Probing the endocytic pathway in live cells using dual-color fluorescence cross-correlation analysis*, *Biophys J* **2002**, *83*. 1184-93

53. P. Liu, T. Sudhaharan, R. M. L. Koh, L. C. Hwang, S. Ahmed, I. N. Maruyama, T. Wohland, *Investigation of the dimerization of proteins from the*

epidermal growth factor receptor family by single wavelength fluorescence cross-correlation spectroscopy, *Biophysical Journal* **2007**, *93*. 684-698

54. X. Ma, S. Ahmed, T. Wohland, *EGFR activation monitored by SW-FCCS in live cells*, *Front Biosci* **2011**, *3*. 22-32

55. L. C. Hwang, T. Wohland, *Recent advances in fluorescence cross-correlation spectroscopy*, *Cell Biochem Biophys* **2007**, *49*. 1-13

56. N. O. Petersen, P. L. Hoddelius, P. W. Wiseman, O. Seger, K. E. Magnusson, *Quantitation of membrane receptor distributions by image correlation spectroscopy: concept and application*, *Biophys. J.* **1993**, *65*. 1135-1146

57. D. L. Kolin, P. W. Wiseman, *Advances in image correlation spectroscopy: Measuring number densities, aggregation states, and dynamics of fluorescently labeled macromolecules in cells*, *Cell Biochem. Biophys.* **2007**, *49*. 141-164

58. B. Hebert, S. Costantino, P. W. Wiseman, *Spatiotemporal image correlation Spectroscopy (STICS) theory, verification, and application to protein velocity mapping in living CHO cells*, *Biophys. J.* **2005**, *88*. 3601-3614

59. D. L. Kolin, D. Ronis, P. W. Wiseman, *k-Space Image Correlation Spectroscopy: A Method for Accurate Transport Measurements Independent of Fluorophore Photophysics*, *Biophys. J.* **2006**, *91*. 3061-3075

60. M. A. Digman, P. Sengupta, P. W. Wiseman, C. M. Brown, A. R. Horwitz, E. Gratton, *Fluctuation Correlation Spectroscopy with a Laser-Scanning Microscope: Exploiting the Hidden Time Structure*, *Biophys. J.* **2005**, *88*. L33-36

61. J. G. Kay, M. Koivusalo, X. Ma, T. Wohland, S. Grinstein, *Phosphatidylserine Dynamics in Cellular Membranes*, *Molecular Biology of the Cell* **2012**.

62. H. Pick, A. K. Preuss, M. Mayer, T. Wohland, R. Hovius, H. Vogel, *Monitoring expression and clustering of the ionotropic 5HT3 receptor in plasma membranes of live biological cells*, *Biochemistry* **2003**, *42*. 877-84

63. L. Yu, L. Guo, J. L. Ding, B. Ho, S. S. Feng, J. Popplewell, M. Swann, T. Wohland, *Interaction of an artificial antimicrobial peptide with lipid membranes*, *Biochim Biophys Acta* **2009**, *2*. 333-44

64. P. Li, T. Wohland, B. Ho, J. L. Ding, *Perturbation of Lipopolysaccharide (LPS) Micelles by Sushi 3 (S3) Antimicrobial Peptide*, *Journal of Biological Chemistry* **2004**, *279*. 50150-50156

65. L. Yu, J. L. Ding, B. Ho, T. Wohland, *Investigation of a novel artificial antimicrobial peptide by fluorescence correlation spectroscopy: an amphipathic cationic pattern is sufficient for selective binding to bacterial type membranes and antimicrobial activity*, *Biochim Biophys Acta* **2005**, *1*. 29-39

66. S. Hebbar, E. Lee, M. Manna, S. Steinert, G. S. Kumar, M. Wenk, T. Wohland, R. Kraut, *A fluorescent sphingolipid binding domain peptide probe interacts with sphingolipids and cholesterol-dependent raft domains*, *Journal of Lipid Research* **2008**, *49*. 1077-1089

67. K. Bacia, D. Scherfeld, N. Kahya, P. Schwille, *Fluorescence correlation spectroscopy relates rafts in model and native membranes*, *Biophys. J.* **2004**, *87*. 1034-1043

68. J. Ries, P. Schwille, *Studying Slow Membrane Dynamics with Continuous Wave Scanning Fluorescence Correlation Spectroscopy*, *Biophysical Journal* **2006**, *91*. 1915-1924

69. L. Wawrezinieck, H. Rigneault, D. Marguet, P. F. Lenne, *Fluorescence correlation spectroscopy diffusion laws to probe the submicron cell membrane organization*, *Biophys. J.* **2005**, *89*. 4029-4042

70. P.-F. Lenne, L. Wawrezinieck, F. Conchonaud, O. Wurtz, A. Boned, X.-J. Guo, H. Rigneault, H.-T. He, D. Marguet, *Dynamic molecular confinement in the plasma membrane by microdomains and the cytoskeleton meshwork*, *Embo J* **2006**, *25*. 3245-3256

71. R. Lasserre, X.-J. Guo, F. Conchonaud, Y. Hamon, O. Hawchar, A.-M. Bernard, S. M. H. Soudja, P.-F. Lenne, H. Rigneault, D. Olive, G. Bismuth, J. A. Nunes, B. Payrastre, D. Marguet, H.-T. He, *Raft nanodomains contribute to Akt/PKB plasma membrane recruitment and activation*, *Nat Chem Biol* **2008**, *4*. 538-547

72. S. Ganguly, A. Chattopadhyay, *Cholesterol depletion mimics the effect of cytoskeletal destabilization on membrane dynamics of the serotonin1A receptor: A zFCS study*, *Biophys J* **2010**, *99*. 1397-407

73. S. Guia, B. N. Jaeger, S. Piatek, S. Mailfert, T. Trombik, A. Fenis, N. Chevrier, T. Walzer, Y. M. Kerdiles, D. Marguet, E. Vivier, S. Ugolini, *Confinement of Activating Receptors at the Plasma Membrane Controls Natural Killer Cell Tolerance*, *Sci. Signal.* **2011**, *4*. ra21-

74. H. T. He, D. Marguet, *Detecting nanodomains in living cell membrane by fluorescence correlation spectroscopy*, *Annu Rev Phys Chem* **2011**, *62*. 417-36

75. J. Humpolí ková, E. Gielen, A. Benda, V. Fagulova, J. Vercammen, M. vandeVen, M. Hof, M. Ameloot, Y. Engelborghs, *Probing Diffusion Laws within Cellular Membranes by Z-Scan Fluorescence Correlation Spectroscopy*, *Biophysical Journal* **2006**, *91*. L23-L25

76. M. A. Digman, E. Gratton, *Imaging barriers to diffusion by pair correlation functions*, *Biophys J* **2009**, *97*. 665-73

77. E. Hinde, F. Cardarelli, M. A. Digman, A. Kershner, J. Kimble, E. Gratton, *The impact of mitotic versus interphase chromatin architecture on the molecular flow of EGFP by pair correlation analysis*, *Biophys J* **2011**, *100*. 1829-36

78. F. Cardarelli, E. Gratton, *In vivo imaging of single-molecule translocation through nuclear pore complexes by pair correlation functions*, *PLoS ONE* **2010**, *5*.

79. E. Hinde, F. Cardarelli, M. A. Digman, E. Gratton, *In vivo pair correlation analysis of EGFP intranuclear diffusion reveals DNA-dependent molecular flow*, *Proc Natl Acad Sci U S A* **2010**, *107*. 16560-5

80. P. Sengupta, T. Jovanovic-Talisman, D. Skoko, M. Renz, S. L. Veatch, J. Lippincott-Schwartz, *Probing protein heterogeneity in the plasma membrane using PALM and pair correlation analysis*, *Nat Methods* **2011**, *8*. 969-75

81. S. L. Veatch, E. N. Chiang, P. Sengupta, D. A. Holowka, B. A. Baird, *Quantitative Nanoscale Analysis of IgE-FcepsilonRI Clustering and Coupling to Early Signaling Proteins*, *J Phys Chem B* **2012**, *2*. 2

82. S. W. Hell, *Toward fluorescence nanoscopy*, *Nat Biotech* **2003**, *21*. 1347-1355

83. L. Kastrup, H. Blom, C. Eggeling, S. W. Hell, *Fluorescence Fluctuation Spectroscopy in Subdiffraction Focal Volumes*, *Physical Review Letters* **2005**, *94*. 178104

84. C. Eggeling, C. Ringemann, R. Medda, G. Schwarzmann, K. Sandhoff, S. Polyakova, V. N. Belov, B. Hein, C. von Middendorff, A. Schonle, S. W. Hell, *Direct*

observation of the nanoscale dynamics of membrane lipids in a living cell, *Nature* **2009**, *457*. 1159-1162

85. V. Mueller, C. Ringemann, A. Honigmann, G. Schwarzmann, R. Medda, M. Leutenegger, S. Polyakova, V. N. Belov, S. W. Hell, C. Eggeling, *STED nanoscopy reveals molecular details of cholesterol- and cytoskeleton-modulated lipid interactions in living cells*, *Biophys J* **2011**, *101*. 1651-60

86. M. Gosch, A. Serov, T. Anhut, T. Lasser, A. Rochas, P. A. Besse, R. S. Popovic, H. Blom, R. Rigler, *Parallel single molecule detection with a fully integrated single-photon 2X2 CMOS detector array*, *Journal of Biomedical Optics* **2004**, *9*. 913-921

87. R. A. Colyer, G. Scalia, I. Rech, A. Gulinatti, M. Ghioni, S. Cova, S. Weiss, X. Michalet, *High-throughput FCS using an LCOS spatial light modulator and an 8 × 1 SPAD array*, *Biomed. Opt. Express* **2010**, *1*. 1408-1431

88. B. Kannan, J. Y. Har, P. Liu, I. Maruyama, J. L. Ding, T. Wohland, *Electron multiplying charge-coupled device camera based fluorescence correlation spectroscopy*, *Anal. Chem.* **2006**, *78*. 3444-3451

89. M. Burkhardt, P. Schwille, *Electron multiplying CCD based detection for spatially resolved fluorescence correlation spectroscopy*, *Opt. Express* **2006**, *14*. 5013-5020

90. D. R. Sisan, R. Arevalo, C. Graves, R. McAllister, J. S. Urbach, *Spatially resolved fluorescence correlation spectroscopy using a spinning disk confocal microscope*, *Biophys. J.* **2006**, *91*. 4241-4252

91. F. Bestvater, Z. Seghiri, M. S. Kang, N. Groener, J. Y. Lee, K.-B. Im, M. Wachsmuth, *EMCCD-based spectrally resolved fluorescence correlation spectroscopy*, *Optics Express* **2010**, *18*. 23818-23828

92. W. Song, S. Moon, B. C. Lee, C. S. Park, D. Y. Kim, H. S. Kwon, *Site-specific multipoint fluorescence measurement system with end-capped optical fibers*, *Appl. Optics* **2011**, *50*. 3529-3537

93. B. Kannan, L. Guo, T. Sudhaharan, S. Ahmed, I. Maruyama, T. Wohland, *Spatially resolved total internal reflection fluorescence correlation microscopy using an electron multiplying charge-coupled device camera*, *Anal. Chem.* **2007**, *79*. 4463-4470

94. S. M. Hashmi, M. Loewenberg, E. R. Dufresne, *Spatially extended FCS for visualizing and quantifying high-speed multiphase flows in microchannels*, *Optics Express* **2007**, *15*. 6528-6533

95. T. Wohland, X. Shi, J. Sankaran, E. H. K. Stelzer, *Single Plane Illumination Fluorescence Correlation Spectroscopy (SPIM-FCS) probes inhomogeneous three-dimensional environments*, *Opt. Express* **2010**, *18*. 10627-10641

96. J. Capoulade, M. Wachsmuth, L. Hufnagel, M. Knop, *Quantitative fluorescence imaging of protein diffusion and interaction in living cells*, *Nature Biotechnology* **2011**, *29*. 835-842

97. M. Matsumoto, T. Sugiura, K. Minato, in *Confocal, Multiphoton, and Nonlinear Microscopic Imaging III*, **2007**, vol. 6630, pp 63017-63017.

98. M. Matsumoto, T. Sugiura, K. Minato, *Illumination by Near-Critical-Angle Incidence for Imaging Fluorescence Correlation Spectroscopy with Electron-Multiplying Charge-Coupled Device Camera*, *Jpn. J. Appl. Phys.* **2010**, *49*. 3

99. J. Huisken, J. Swoger, F. Del Bene, J. Wittbrodt, E. H. K. Stelzer, *Optical Sectioning Deep Inside Live Embryos by Selective Plane Illumination Microscopy*, *Science* **2004**, *305*. 1007-1009

100. M. Brinkmeier, K. Dorre, J. Stephan, M. Eigen, *Two beam cross correlation: A method to characterize transport phenomena in micrometer-sized structures*, *Anal. Chem.* **1999**, *71*. 609-616

101. H. Qian, E. L. Elson, *Fluorescence correlation spectroscopy with high-order and dual-color correlation to probe nonequilibrium steady states*, *Proc. Natl. Acad. Sci. U. S. A.* **2004**, *101*. 2828-2833

102. H. Qian, S. Saffarian, E. L. Elson, *Concentration fluctuations in a mesoscopic oscillating chemical reaction system*, *Proc. Natl. Acad. Sci. U. S. A.* **2002**, *99*. 10376-10381

103. F. R. Hallett, P. A. Speight, R. H. Stinson, in *Introductory biophysics*, **1977**.

104. J. Renn, *Einstein's invention of Brownian motion*, *Annalen der Physik* **2005**, *14*. 23-37

105. R. Kubo, *The fluctuation-dissipation theorem*, *Reports on Progress in Physics* **1966**, *29*. 255

106. B. J. Berne, R. Pecora, in *Dynamic light scattering : with applications to chemistry, biology, and physics*, **2000**.

107. Elliot L. Elson, *Fluorescence Correlation Spectroscopy: Past, Present, Future*, *Biophysical Journal* **2011**, *101*. 2855-2870

108. X. Shi, T. Wohland, in *Nanoscopy and Multidimensional Optical Fluorescence Microscopy* **2010**.

109. D. E. Koppel, D. Axelrod, J. Schlessinger, *Dynamics of fluorescence marker concentration as a probe of mobility*, *Biophysical Journal* **1976**, *16*. 1315-1329

110. N. Thompson, **2002**, vol. 1, pp 337-378.

111. V. Krishnan, in *Probability and Random Processes*, **2005**.

112. E. Zauderer, in *Partial Differential Equations of Applied Mathematics*, **2006**, pp 253-331.

113. J. Stein, in *Digital Signal Processing: A Computer Science Perspective*, **2001**.

114. C. A. Konopka, S. Y. Bednarek, *Variable-angle epifluorescence microscopy: a new way to look at protein dynamics in the plant cell cortex*, *The Plant Journal* **2008**, *53*. 186-196

115. M. Tokunaga, N. Imamoto, K. Sakata-Sogawa, *Highly inclined thin illumination enables clear single-molecule imaging in cells*, *Nat Meth* **2008**, *5*. 159-161

116. M. Tokunaga, N. Imamoto, K. Sakata-Sogawa, *Addendum: Highly inclined thin illumination enables clear single-molecule imaging in cells*, *Nat Meth* **2008**, *5*. 455-455

117. http://www.andor.com/learning/digital_cameras/?docid=325.

118. http://sales.hamamatsu.com/assets/pdf/hpspdf/e_flashtec.pdf.

119. M. S. Robbins, B. J. Hadwen, *The noise performance of electron multiplying charge-coupled devices*, *Ieee Transactions on Electron Devices* **2003**, *50*. 1227-1232

120. J. N. Hollenhorst, *A theory of multiplication noise*, *Electron Devices, IEEE Transactions on* **1990**, *37*. 781-788

121. K. Matsuo, M. C. Teich, B. E. A. Saleh, *Noise properties and time response of the staircase avalanche photodiode*, *Electron Devices, IEEE Transactions on* **1985**, *32*. 2615-2623

122. *http://sales.hamamatsu.com/assets/pdf/hpspdf/Flash4-ChangingTheGame.pdf*.

123. *http://www.andor.com/scientific_cameras/ixon_emccd_camera/860_back-illuminated/*.

124. *http://sales.hamamatsu.com/assets/pdf/hpspdf/e_orcaFlashE01.pdf*.

125. K. Schaetzel, R. Peters, in *Secondary* ed. S. S. Kenneth. SPIE, 1991, vol. 1430, pp 109-115.

126. T. Wohland, R. Rigler, H. Vogel, *The standard deviation in fluorescence correlation spectroscopy*, *Biophys. J.* **2001**, *80*. 2987-2999

127. W. Press, B. Flannery, S. Teukolsky, W. Vetterling, in *Numerical Recipes in C: The Art of Scientific Computing*, **1992**.

128. L. Guo, J. Y. Har, J. Sankaran, Y. M. Hong, B. Kannan, T. Wohland, *Molecular diffusion measurement in lipid Bilayers over wide concentration ranges: A comparative study*, *Chemphyschem* **2008**, *9*. 721-728

129. B. Zhang, J. Zerubia, J.-C. Olivo-Marin, *Gaussian approximations of fluorescence microscope point-spread function models*, *Appl. Opt.* **2007**, *46*. 1819-1829

130. B. Zhang, J. Zerubia, J. C. Olivo-Marin, in *Secondary* ed. J. A. Conchello, C. J. Cogswell, T. Wilson. Spie-Int Soc Optical Engineering: San Jose, CA, 2006, pp K900-K900.

131. J. Ries, E. P. Petrov, P. Schwille, *Total internal reflection fluorescence correlation spectroscopy: Effects of lateral diffusion and surface-generated fluorescence*, *Biophys. J.* **2008**, *95*. 390-399

132. D. Thomann, D. R. Rines, P. K. Sorger, G. Danuser, *Automatic fluorescent tag detection in 3D with super-resolution: application to the analysis of chromosome movement*, *J. Microsc.-Oxf.* **2002**, *208*. 49-64

133. X. Michalet, O. H. Siegmund, J. V. Vallerga, P. Jelinsky, J. E. Millaud, S. Weiss, *Detectors for single-molecule fluorescence imaging and spectroscopy*, *J Mod Opt* **2007**, *54*. 239

134. R. F. Heuff, J. L. Swift, D. T. Cramb, *Fluorescence correlation spectroscopy using quantum dots: advances, challenges and opportunities*, *Phys. Chem. Chem. Phys.* **2007**, *9*. 1870-1880

135. Y. Blancquaert, J. Gao, J. Derouard, A. Delon, *Spatial fluorescence cross-correlation spectroscopy by means of a spatial light modulator*, *J. Biophotonics* **2008**, *1*. 408-418

136. P. S. Dittrich, P. Schwille, *Spatial two-photon fluorescence cross-correlation Spectroscopy for controlling molecular transport in microfluidic structures*, *Anal. Chem.* **2002**, *74*. 4472-4479

137. A. Santos, I. T. Young, *Model-based resolution: applying the theory in quantitative microscopy*, *Appl. Opt.* **2000**, *39*. 2948-2958

138. E. Dusch, T. Dorval, N. Vincent, M. Wachsmuth, A. Genovesio, *Three-dimensional point spread function model for line-scanning confocal microscope with high-aperture objective*, *J. Microsc.-Oxf.* **2007**, *228*. 132-138

139. G. Heuvelman, F. Erdel, M. Wachsmuth, K. Rippe, *Analysis of protein mobilities and interactions in living cells by multifocal fluorescence fluctuation microscopy*, *Eur. Biophys. J. Biophys. Lett.* **2009**, *38*. 813-828

140. R. E. Thompson, D. R. Larson, W. W. Webb, *Precise Nanometer Localization Analysis for Individual Fluorescent Probes*, *Biophysical Journal* **2002**, *82*. 2775-2783

141. H. Deschout, K. Neyts, K. Braeckmans, *The influence of movement on the localization precision of sub-resolution particles in fluorescence microscopy*, *Journal of Biophotonics* **2012**, *5*. 97-109

142. S. Costantino, J. W. D. Comeau, D. L. Kolin, P. W. Wiseman, *Accuracy and dynamic range of spatial image correlation and cross-correlation spectroscopy*, *Biophysical Journal* **2005**, *89*. 1251-1260

143. P. G. Saffman, M. Delbrück, *Brownian motion in biological membranes*, *Proceedings of the National Academy of Sciences* **1975**, *72*. 3111-3113

144. E. C. Yusko, J. M. Johnson, S. Majd, P. Prangkio, R. C. Rollings, J. Li, J. Yang, M. Mayer, *Controlling protein translocation through nanopores with bio-inspired fluid walls*, *Nat Nano* **2011**, *6*. 253-260

145. A. I. Greenwood, S. Tristram-Nagle, J. F. Nagle, *Partial molecular volumes of lipids and cholesterol*, *Chem Phys Lipids* **2006**, *143*. 1-10

146. J. Keslin, *Viscosity of Liquid Water in the Range—8 C to 150 C*, *J. Phys. Chem. Ref. Data* **1978**, *7*.

147. W. L. C. Vaz, D. Hallmann, R. M. Clegg, A. Gambacorta, M. Rosa, *A comparison of the translational diffusion of a normal and a membrane-spanning lipid in L_α phase 1-palmitoyl-2-oleoylphosphatidylcholine bilayers*, *European Biophysics Journal* **1985**, *12*. 19-24

148. M. Przybylo, J. Sykora, J. Humpolickova, A. Benda, A. Zan, M. Hof, *Lipid diffusion in giant unilamellar vesicles is more than 2 times faster than in supported phospholipid bilayers under identical conditions*, *Langmuir* **2006**, *22*. 9096-9099

149. A. Benda, M. Benes, V. Marecek, A. Lhotsky, W. T. Hermens, M. Hof, *How to determine diffusion coefficients in planar phospholipid systems by confocal fluorescence correlation spectroscopy*, *Langmuir* **2003**, *19*. 4120-4126

150. T. Dertinger, I. von der Hocht, A. Benda, M. Hof, J. Enderlein, *Surface sticking and lateral diffusion of lipids in supported bilayers*, *Langmuir* **2006**, *22*. 9339-9344

151. J. Humpolickova, E. Gielen, A. Benda, V. Fagulova, J. Vercammen, M. Vandeven, M. Hof, M. Ameloot, Y. Engelborghs, *Probing diffusion laws within cellular membranes by Z-scan fluorescence correlation spectroscopy*, *Biophys J* **2006**, *91*. L23-L25

152. S. Ganguly, A. Chattopadhyay, *Cholesterol Depletion Mimics the Effect of Cytoskeletal Destabilization on Membrane Dynamics of the Serotonin(1A) Receptor: A zFCS Study*, *Biophys J* **2010**, *99*. 1397-1407

153. C. Eggeling, C. Ringemann, R. Medda, G. Schwarzmann, K. Sandhoff, S. Polyakova, V. Belov, B. Hein, C. von Middendorff, A. Schonle, S. Hell, *Direct observation of the nanoscale dynamics of membrane lipids in a living cell*, *Nature* **2009**, *457*. 1159-1162

154. V. Mueller, C. Ringemann, A. Honigmann, G. Schwarzmann, R. Medda, M. Leutenegger, S. Polyakova, V. N. Belov, S. W. Hell, C. Eggeling, *STED Nanoscopy Reveals Molecular Details of Cholesterol- and Cytoskeleton-Modulated Lipid Interactions in Living Cells*, *Biophys J* **2011**, *101*. 1651-1660

155. V. Ruprecht, S. Wieser, D. Marguet, G. J. Schutz, *Spot Variation Fluorescence Correlation Spectroscopy Allows for Superresolution Chronoscopy of Confinement Times in Membranes*, *Biophys J* **2011**, *100*. 2839-2845

156. H. Huang, A. Pralle, *Continuous monitoring of membrane protein micro-domain association during cell signaling*, *arXiv:1101.5087v1* **2011**.

157. D. R. Sisan, D. Yarar, C. M. Waterman, J. S. Urbach, *Event Ordering in Live-Cell Imaging Determined from Temporal Cross-Correlation Asymmetry*, *Biophysical Journal* **2010**, *98*. 2432-2441

158. A. Jachens, J. Schumacher, B. Eckhardt, K. Knobloch, H. H. Fernholz, *Asymmetry of temporal cross-correlations in turbulent shear flows*, *Journal of Fluid Mechanics* **2006**, *547*. 55-64

159. R. Lasserre, X. J. Guo, F. Conchonaud, Y. Hamon, O. Hawchar, A. M. Bernard, S. M. Soudja, P. F. Lenne, H. Rigneault, D. Olive, G. Bismuth, J. A. Nunes, B. Payrastre, D. Marguet, H. T. He, *Raft nanodomains contribute to Akt/PKB plasma membrane recruitment and activation*, *Nat. Chem. Biol.* **2008**, *4*. 538-547

160. S. Mukherjee, F. R. Maxfield, *Membrane domains*, *Annu. Rev. Cell Dev. Biol.* **2004**, *20*. 839-866

161. F. Pinaud, X. Michalet, G. Iyer, E. Margeat, H. P. Moore, S. Weiss, *Dynamic Partitioning of a Glycosyl-Phosphatidylinositol-Anchored Protein in*

Glycosphingolipid-Rich Microdomains Imaged by Single-Quantum Dot Tracking, *Traffic* **2009**, *10*. 691-712

162. A. K. Kenworthy, B. J. Nichols, C. L. Remmert, G. M. Hendrix, M. Kumar, J. Zimmerberg, J. Lippincott-Schwartz, *Dynamics of putative raft-associated proteins at the cell surface*, *J. Cell Biol.* **2004**, *165*. 735-746

163. E. D. Sheets, G. M. Lee, R. Simson, K. Jacobson, *Transient confinement of a glycosylphosphatidylinositol-anchored protein in the plasma membrane*, *Biochemistry* **1997**, *36*. 12449-12458

164. A. Kusumi, C. Nakada, K. Ritchie, K. Murase, K. Suzuki, H. Murakoshi, R. S. Kasai, J. Kondo, T. Fujiwara, *Paradigm shift of the plasma membrane concept from the two-dimensional continuum fluid to the partitioned fluid: High-speed single-molecule tracking of membrane molecules*, *Annu. Rev. Biophys. Biomolec. Struct.* **2005**, *34*. 351-378

165. E. Ottico, A. Prinetti, S. Prioni, C. Giannotta, L. Basso, V. Chigorno, S. Sonnino, *Dynamics of membrane lipid domains in neuronal cells differentiated in culture*, *Journal of Lipid Research* **2003**, *44*. 2142-2151

166. S. Ilangumaran, D. C. Hoessli, *Effects of cholesterol depletion by cyclodextrin on the sphingolipid microdomains of the plasma membrane*, *Biochem. J.* **1998**, *335*. 433-440

167. J. S. Goodwin, K. R. Drake, C. L. Remmert, A. K. Kenworthy, *Ras diffusion is sensitive to plasma membrane viscosity*, *Biophys. J.* **2005**, *89*. 1398-1410

168. D. E. Koppel, *Statistical accuracy in fluorescence correlation spectroscopy*, *Physical Review A* **1974**, *10*. 1938

169. Q. Hong, *On the statistics of fluorescence correlation spectroscopy*, *Biophysical Chemistry* **1990**, *38*. 49-57

170. P. Kask, R. Gunther, P. Axhausen, *Statistical accuracy in fluorescence fluctuation experiments*, *European Biophysics Journal* **1997**, *25*. 163-169

171. S. Saffarian, E. L. Elson, *Statistical Analysis of Fluorescence Correlation Spectroscopy: The Standard Deviation and Bias*, *Biophys. J.* **2003**, *84*. 2030-2042

172. K. Starchev, J. Ricka, J. Buffle, *Noise on Fluorescence Correlation Spectroscopy*, *Journal of Colloid and Interface Science* **2001**, *233*. 50-55

173. G. Nishimura, M. Kinjo, *Systematic Error in Fluorescence Correlation Measurements Identified by a Simple Saturation Model of Fluorescence*, *Analytical Chemistry* **2004**, *76*. 1963-1970

174. F. Ye, M. M. Collinson, D. A. Higgins, *Molecular Orientation and Its Influence on Autocorrelation Amplitudes in Single-Molecule Imaging Experiments*, *Analytical Chemistry* **2007**, *79*. 6465-6472

175. E. J. Nijman, H. G. Merkus, J. C. M. Marijnissen, B. Scarlett, *Simulations and Experiments on Number Fluctuations in Photon-Correlation Spectroscopy at Low Particle Concentrations*, *Appl. Opt.* **2001**, *40*. 4058-4063

176. S. Milon, R. Hovius, H. Vogel, T. Wohland, *Factors influencing fluorescence correlation spectroscopy measurements on membranes: simulations and experiments*, *Chemical Physics* **2003**, *288*. 171-186

177. A. Tcherniak, C. Reznik, S. Link, C. F. Landes, *Fluorescence Correlation Spectroscopy: Criteria for Analysis in Complex Systems*, *Analytical Chemistry* **2009**, *81*. 746-754

178. M. J. Culbertson, J. T. B. Williams, W. W. L. Cheng, D. A. Stults, E. R. Wiebracht, J. J. Kasianowicz, D. L. Burden, *Numerical Fluorescence Correlation Spectroscopy for the Analysis of Molecular Dynamics under Nonstandard Conditions*, *Analytical Chemistry* **2007**, *79*. 4031-4039

179. J. D. Lam, M. J. Culbertson, N. P. Skinner, Z. J. Barton, D. L. Burden, *Information Content in Fluorescence Correlation Spectroscopy: Binary Mixtures and Detection Volume Distortion*, *Analytical Chemistry 83*. 5268-5274

180. D. L. Kolin, S. Costantino, P. W. Wiseman, *Sampling effects, noise, and photobleaching in temporal image correlation spectroscopy*, *Biophysical Journal* **2006**, *90*. 628-639

181. U. Meseth, T. Wohland, R. Rigler, H. Vogel, *Resolution of fluorescence correlation measurements*, *Biophysical Journal* **1999**, *76*. 1619-1631

182. J. He, S.-M. Guo, M. Bathe, *A Bayesian approach to the analysis of fluorescence correlation spectroscopy data I: Theory*, *Analytical Chemistry* **2012**.

183. S.-M. Guo, J. He, N. Monnier, G. Sun, T. Wohland, M. Bathe, *A Bayesian approach to the analysis of fluorescence correlation spectroscopy data II: Application to simulated and in vitro data*, *Analytical Chemistry* **2012**.

184. X. Michalet, *Mean square displacement analysis of single-particle trajectories with localization error: Brownian motion in an isotropic medium*, *Physical Review E 82*. 041914

185. J. Ries, P. Schwille, *New concepts for fluorescence correlation spectroscopy on membranes*, *Physical Chemistry Chemical Physics* **2008**, *10*. 3487-3497

186. R. E. Thompson, D. R. Larson, W. W. Webb, *Precise nanometer localization analysis for individual fluorescent probes*, *Biophys J* **2002**, *82*. 2775-83

187. C. M. Brown, R. B. Dalal, B. Hebert, M. A. Digman, A. R. Horwitz, E. Gratton, *Raster image correlation spectroscopy (RICS) for measuring fast protein dynamics and concentrations with a commercial laser scanning confocal microscope*, *J Microsc* **2008**, *229*. 78-91

188. C. Y. Lu, D. A. Vanden Bout, *Effect of finite trajectory length on the correlation function analysis of single molecule data*, *J. Chem. Phys.* **2006**, *125*. 9

189. V. Degiorgio, J. B. Lastovka, *Intensity-Correlation Spectroscopy*, *Physical Review A* **1971**, *4*. 2033-2050

190. S. L. Brenner, R. J. Nossal, G. H. Weiss, *Number fluctuation analysis of random locomotion-statistics of a smoluchowski process*, *J. Stat. Phys.* **1978**, *18*. 1-18

191. R. W. Cole, T. Jinadasa, C. M. Brown, *Measuring and interpreting point spread functions to determine confocal microscope resolution and ensure quality control*, *Nat Protoc* **2011**, *6*. 1929-41

192. H. W. Lilliefors, *On the Kolmogorov-Smirnov test for normality with mean and variance unknown*, *Journal of the American Statistical Association* **1967**. 399-402

193. S. Jin, A. S. Verkman, *Single Particle Tracking of Complex Diffusion in Membranes: Simulation and Detection of Barrier, Raft, and Interaction Phenomena*, *The Journal of Physical Chemistry B* **2007**, *111*. 3625-3632

194. S. Tan, H. T. Tan, M. C. M. Chung, *Membrane proteins and membrane proteomics*, *PROTEOMICS* **2008**, *8*. 3924-3932

195. X. Zhang, J. Gureasko, K. Shen, P. A. Cole, J. Kuriyan, *An allosteric mechanism for activation of the kinase domain of epidermal growth factor receptor*, *Cell* **2006**, *125*. 1137-49

196. D. Marquez-Medina, A. Gasol-Cudos, M. T. Taberner-Bonastre, J. C. Samame Perez-Vargas, A. Salud-Salvia, A. Llombart-Cussac, *Human Papillomavirus in Non-Small-Cell Lung Cancer: The Impact of EGFR Mutations and the Response to Erlotinib*, *Arch Bronconeumol* **2012**, *22*. 22

197. I. H. Jang, J. H. Kim, B. D. Lee, S. S. Bae, M. H. Park, P. G. Suh, S. H. Ryu, *Localization of phospholipase C-gamma1 signaling in caveolae: importance in EGF-induced phosphoinositide hydrolysis but not in tyrosine phosphorylation*, *FEBS Lett* **2001**, *491*. 4-8

198. S. V. Matveev, E. J. Smart, *Heterologous desensitization of EGF receptors and PDGF receptors by sequestration in caveolae*, *Am J Physiol Cell Physiol* **2002**, *282*. C935-46

199. C. Mineo, G. N. Gill, R. G. Anderson, *Regulated migration of epidermal growth factor receptor from caveolae*, *J Biol Chem* **1999**, *274*. 30636-43

200. C. Mineo, G. L. James, E. J. Smart, R. G. Anderson, *Localization of epidermal growth factor-stimulated Ras/Raf-1 interaction to caveolae membrane*, *J Biol Chem* **1996**, *271*. 11930-5

201. M. G. Waugh, D. Lawson, J. J. Hsuan, *Epidermal growth factor receptor activation is localized within low-buoyant density, non-caveolar membrane domains*, *Biochem J* **1999**, *337*. 591-7

202. M. Yamabhai, R. G. Anderson, *Second cysteine-rich region of epidermal growth factor receptor contains targeting information for caveolae/rafts*, *J Biol Chem* **2002**, *277*. 24843-6

203. L. J. Pike, X. Han, R. W. Gross, *Epidermal Growth Factor Receptors Are Localized to Lipid Rafts That Contain a Balance of Inner and Outer Leaflet Lipids*, *Journal of Biological Chemistry* **2005**, *280*. 26796-26804

204. J. P. Chapple, A. J. Hardcastle, C. Grayson, K. R. Willison, M. E. Cheetham, *Delineation of the plasma membrane targeting domain of the X-linked retinitis pigmentosa protein RP2*, *Invest Ophthalmol Vis Sci* **2002**, *43*. 2015-20

205. A. R. Zurita, P. M. Crespo, N. P. Koritschoner, J. L. Daniotti, *Membrane distribution of epidermal growth factor receptors in cells expressing different gangliosides*, *Eur J Biochem* **2004**, *271*. 2428-37

206. J. Ries, M. Bayer, G. Csucs, R. Dirkx, M. Solimena, H. Ewers, P. Schwille, *Automated suppression of sample-related artifacts in Fluorescence Correlation Spectroscopy*, *Optics Express* **2010**, *18*. 11073-11082

207. J. Ries, S. Chiantia, P. Schwille, *Accurate determination of membrane dynamics with line-scan FCS*, *Biophysical Journal* **2009**, *96*. 1999-2008

208. A. Delon, Y. Usson, J. Derouard, T. Biben, C. Souchier, *Photobleaching, Mobility, and Compartmentalisation: Inferences in Fluorescence Correlation Spectroscopy*, *J. Fluoresc.* **2004**, *14*. 255-267

209. W. Pilbrough, T. P. Munro, P. Gray, *Intraclonal protein expression heterogeneity in recombinant CHO cells*, *PLoS ONE* **2009**, *4*.

210. P. E. Thelwall, K. M. Brindle, *Analysis of CHO-K1 cell growth in a fixed bed bioreactor using magnetic resonance spectroscopy and imaging*, *Cytotechnology* **1999**, *30*. 121-32

211. D. Kuystermans, M. Al-Rubeai, *cMyc increases cell number through uncoupling of cell division from cell size in CHO cells*, *BMC Biotechnol* **2009**, *9*. 76

212. P. K. Ang, K. P. Loh, T. Wohland, M. Nesladek, E. Van Hove, *Supported Lipid Bilayer on Nanocrystalline Diamond: Dual Optical and Field-Effect Sensor for Membrane Disruption*, *Advanced Functional Materials* **2009**, *19*. 109-116

213. O. Leenaerts, B. Partoens, F. M. Peeters, *Water on graphene: Hydrophobicity and dipole moment using density functional theory*, *Physical Review B* **2009**, *79*.

214. L. Yu, J. L. Ding, B. Ho, S. S. Feng, T. Wohland, *Investigation of the mechanisms of antimicrobial peptides interacting with membranes by fluorescence correlation spectroscopy*, *The Open Chemical Physics Journal* **2008**, *1*. 62-79

215. D. J. Hirst, T. H. Lee, M. J. Swann, S. Unabia, Y. Park, K. S. Hahm, M. I. Aguilar, *Effect of acyl chain structure and bilayer phase state on binding and penetration of a supported lipid bilayer by HPA3*, *European biophysics journal : EBJ* **2011**, *40*. 503-14

216. L. Janosi, A. A. Gorfe, *Simulating POPC and POPC/POPG Bilayers: Conserved Packing and Altered Surface Reactivity*, *Journal of Chemical Theory and Computation* **2010**, *6*. 3267-3273

217. L. Yang, T. M. Weiss, R. I. Lehrer, H. W. Huang, *Crystallization of antimicrobial pores in membranes: Magainin and protegrin*, *Biophysical Journal* **2000**, *79*. 2002-2009

218. M. Zasloff, B. Martin, H. C. Chen, *ANTIMICROBIAL ACTIVITY OF SYNTHETIC MAGAININ PEPTIDES AND SEVERAL ANALOGS*, *Proceedings of the National Academy of Sciences of the United States of America* **1988**, *85*. 910-913

219. F. Y. Chen, M. T. Lee, H. W. Huang, *Evidence for membrane thinning effect as the mechanism for peptide-induced pore formation*, *Biophysical Journal* **2003**, *84*. 3751-3758

220. K. Matsuzaki, K. Sugishita, N. Ishibe, M. Ueha, S. Nakata, K. Miyajima, R. M. Epand, *Relationship of membrane curvature to the formation of pores by magainin 2*, *Biochemistry* **1998**, *37*. 11856-11863

221. W. T. Heller, T. A. Harroun, T. M. Weiss, L. Yang, A. J. Waring, R. I. Lehrer, H. W. Huang, *Membrane thinning induced by protegrin-1: Clues to the mode of antibacterial action*, *Biophysical Journal* **1999**, *76*. A215-A215

222. W. T. Heller, A. J. Waring, R. I. Lehrer, T. A. Harroun, T. M. Weiss, L. Yang, H. W. Huang, *Membrane thinning effect of the beta-sheet antimicrobial protegrin*, *Biochemistry* **2000**, *39*. 139-145

223. W. C. Hung, F. Y. Chen, C. C. Lee, Y. Sun, M. T. Lee, H. W. Huang, *Membrane-thinning effect of curcumin*, *Biophysical Journal* **2008**, *94*. 4331-4338

224. S. Ludtke, K. He, H. Huang, *Membrane thinning caused by magainin 2*, *Biochemistry* **1995**, *34*. 16764-16769

225. S. J. Ludtke, K. He, T. Harroun, W. T. Heller, H. W. Huang, *Lipid dependence of membrane thinning caused by magainin, melittin and alamethicin*, *Biophysical Journal* **1996**, *70*. SU425-SU425

226. A. Mecke, D. K. Lee, A. Ramamoorthy, B. G. Orr, M. M. B. Holl, *Membrane thinning due to antimicrobial peptide binding: An atomic force microscopy study of MSI-78 in lipid bilayers*, *Biophysical Journal* **2005**, *89*. 4043-4050

227. M.-T. Lee, W.-C. Hung, F.-Y. Chen, H. W. Huang, *Mechanism and kinetics of pore formation in membranes by water-soluble amphipathic peptides*, *Proceedings of the National Academy of Sciences* **2008**, *105*. 5087-5092

228. R. Machan, M. Hof, *Lipid diffusion in planar membranes investigated by fluorescence correlation spectroscopy*, *Biochim Biophys Acta* **2010**, *7*. 24

229. A. Miszta, R. Machan, A. Benda, A. J. Ouellette, W. T. Hermens, M. Hof, *Combination of ellipsometry, laser scanning microscopy and Z-scan fluorescence correlation spectroscopy elucidating interaction of cryptdin-4 with supported phospholipid bilayers*, *J Pept Sci* **2008**, *14*. 503-9

230. T. Sheynis, J. Sykora, A. Benda, S. Kolusheva, M. Hof, R. Jelinek, *Bilayer localization of membrane-active peptides studied in biomimetic vesicles by visible and fluorescence spectroscopies*, *Eur J Biochem* **2003**, *270*. 4478-87

231. R. Machan, A. Miszta, W. Hermens, M. Hof, *Real-time monitoring of melittin-induced pore and tubule formation from supported lipid bilayers and its physiological relevance*, *Chem Phys Lipids* **2010**, *163*. 200-6

232. S. Chiantia, J. Ries, N. Kahya, P. Schwille, *Combined AFM and two-focus SFCS study of raft-exhibiting model membranes*, *Chemphyschem* **2006**, *7*. 2409-2418

233. J. Oreopoulos, C. M. Yip, *Combined scanning probe and total internal reflection fluorescence microscopy*, *Methods* **2008**, *46*. 2-10

234. D. Axelrod, G. M. Omann, *Combinatorial microscopy*, *Nature Reviews Molecular Cell Biology* **2006**, *7*. 944-952

235. B. Alberts, A. Johnson, J. Lewis, M. Raff, K. Roberts, P. Walter, in *Molecular biology of the cell*, **2002**.

236. J. G. Gall, M. L. Pardue, *Formation and detection of RNA-DNA hybrid molecules ub cytological preparations*, *Proceedings of the National Academy of Sciences* **1969**, *63*. 378-383

237. A. Danchin, C. Médigue, O. Gascuel, H. Soldano, A. Hénaut, *From data banks to data bases*, *Research in Microbiology* **1991**, *142*. 913-916

238. C. Bustamante, *Unfolding single RNA molecules: bridging the gap between equilibrium and non-equilibrium statistical thermodynamics*, *Quarterly Reviews of Biophysics* **2005**, *38*. 291-301

239. C. Bustamante, *In singulo Biochemistry: When Less Is More*, *Annual Review of Biochemistry* **2008**, *77*. 45-50

240. P. R. Selvin, in *Single-molecule techniques: a laboratory manual*, **2008**.

241. T. A. Nguyen, P. Sarkar, J. V. Veetil, S. V. Koushik, S. S. Vogel, *Fluorescence polarization and fluctuation analysis monitors subunit proximity, stoichiometry, and protein complex hydrodynamics*, *PLoS One* **2012**, *7*. 30

242. S. Wang, P. K. Ang, Z. Wang, A. L. L. Tang, J. T. L. Thong, K. P. Loh, *High Mobility, Printable, and Solution-Processed Graphene Electronics*, *Nano Letters* **2009**, *10*. 92-98

243. P. K. Ang, M. Jaiswal, C. H. Y. X. Lim, Y. Wang, J. Sankaran, A. Li, C. T. Lim, T. Wohland, O. z. Barbaros, K. P. Loh, *A Bioelectronic Platform Using a Graphene−Lipid Bilayer Interface*, *ACS Nano* **2010**, *4*. 7387-7394

Appendix

Unless otherwise stated, the integrals are evaluated in mathematica.

1. **Fourier transforms in the derivation of diffusion propagator and ICS**

$$F_t\left(\frac{\partial C}{\partial t}\right) = isF_t(C)$$

$$F_t\left(\frac{\partial C}{\partial x}\right) = \frac{\partial}{\partial x}F_t(C)$$

$$F_x\left(e^{-ax^2}\right) = \sqrt{\frac{\pi}{a}}e^{-\left(\frac{\pi^2 k^2}{a}\right)}$$

2. **Derivation of autocorrelation function in FCS**

$$\frac{2}{\pi\langle C\rangle w^2\sqrt{4\pi D\tau}}\int_{-\infty}^{\infty}\int_{-\infty}^{\infty} e^{-\frac{2x^2}{w^2}}e^{-\frac{2x'^2}{w^2}}e^{-\frac{(x-x'+v\tau)^2}{4D\tau}}\,dxdx'$$

$$=\frac{2}{\pi\langle C\rangle w\sqrt{8D\tau+w^2}}\int_{-\infty}^{\infty} e^{-\frac{2x'^2}{w^2}}e^{-\frac{(-x'+v\tau)^2}{8D\tau+w^2}}\,dx' = \frac{e^{-\left(\frac{v\tau}{\sqrt{4D\tau+w^2}}\right)^2}}{\langle C\rangle\sqrt{\pi}\sqrt{4D\tau+w^2}}$$

3. **Formulae used in derivation for autocorrelation in Imaging FCS**

$$\int_{-\infty}^{\infty} e^{-\left(\frac{x-a}{b}\right)^2+\left(\frac{x-c}{d}\right)^2}dx = \frac{\sqrt{\pi}}{\sqrt{\left(\frac{1}{b^2}+\frac{1}{d^2}\right)}}e^{\frac{(a-c)^2}{b^2+d^2}}$$

$$\int_g^h e^{-\left(\frac{x-p}{q}\right)^2}dx = \frac{q\sqrt{\pi}}{2}\left(erf\left(\frac{h-p}{q}\right)-erf\left(\frac{g-p}{q}\right)\right)$$

$$\int_y^z erf\left(\frac{r-x}{s}\right)dx$$

$$=\frac{s}{\sqrt{\pi}}\left(e^{-\frac{(r-y)^2}{s^2}}-e^{-\frac{(r-z)^2}{s^2}}\right)+(r-y)erf\left(\frac{r-y}{s}\right)-(r-z)erf\left(\frac{r-z}{s}\right)$$

4. Autocorrelation in Imaging FCS

Using the formulae in Appendix 3, the integrals below are evaluated.

$$g_x(\tau)=\frac{1}{\sqrt{\langle C\rangle}(l-k)(n-m)w_0^2\pi^{\frac{3}{2}}\sqrt{D\tau}}\times$$

$$\int_m^n\int_k^l\int_{-\infty}^{\infty}\int_{-\infty}^{\infty} e^{-\frac{2(x-x_0)^2}{w_0^2}-\frac{2(x'-x'_0)^2}{w_0^2}-\frac{(x-x'+v_x\tau)^2}{4D\tau}}\,dx\,dx'\,dx_0\,dx_0'$$

$$=\frac{2}{\sqrt{\langle C\rangle}(l-k)(n-m)w_0\pi\sqrt{8D\tau+w_0^2}}\int_m^n\int_k^l\int_{-\infty}^{\infty} e^{-\frac{2(x'-x'_0)^2}{w_0^2}-\frac{(x_0-x'+v_x\tau)^2}{\frac{w_0^2}{2}+4D\tau}}\,dx'\,dx_0\,dx_0'$$

$$=\frac{1}{2\sqrt{\langle C\rangle}(l-k)(n-m)}\int_m^n erf\left(\frac{l-x_0'+v_x\tau}{\sqrt{w_0^2+4D\tau}}\right)-erf\left(\frac{k-x_0'+v_x\tau}{\sqrt{w_0^2+4D\tau}}\right)dx_0'$$

$$=\frac{1}{2\sqrt{\langle C\rangle}(l-k)(n-m)}\times$$

$$\left(\begin{array}{l}\sqrt{\frac{w_0^2+4D\tau}{\pi}}\left(e^{-\left(\frac{l-m+v_x\tau}{\sqrt{w_0^2+4D\tau}}\right)^2}-e^{-\left(\frac{l-n+v_x\tau}{\sqrt{w_0^2+4D\tau}}\right)^2}-e^{-\left(\frac{k-m+v_x\tau}{\sqrt{w_0^2+4D\tau}}\right)^2}+e^{-\left(\frac{k-n+v_x\tau}{\sqrt{w_0^2+4D\tau}}\right)^2}\right)\\ +(l-m+v_x\tau)erf\left(\frac{l-m+v_x\tau}{\sqrt{w_0^2+4D\tau}}\right)-(l-n+v_x\tau)erf\left(\frac{l-n+v_x\tau}{\sqrt{w_0^2+4D\tau}}\right)\\ -(k-m+v_x\tau)erf\left(\frac{k-m+v_x\tau}{\sqrt{w_0^2+4D\tau}}\right)+(k-n+v_x\tau)erf\left(\frac{k-n+v_x\tau}{\sqrt{w_0^2+4D\tau}}\right)\end{array}\right)$$

5. Cross-Correlation of flow in Imaging FCS

$$G(\tau)_{flow} = G_\infty + \frac{1}{4\langle C\rangle a^4}\times$$

$$\left(\frac{w_0}{\sqrt{\pi}}\left(e^{-\left(\frac{a-r_x+v_x\tau}{w_0}\right)^2} - 2e^{-\left(\frac{r_x-v_x\tau}{w_0}\right)^2} + e^{-\left(\frac{a+r_x-v_x\tau}{w_0}\right)^2}\right) - 2\left(r_x - v_x\tau\right)erf\left(\frac{r_x - v_x\tau}{w_0}\right)\right.$$
$$\left.+\left(a - r_x + v_x\tau\right)erf\left(\frac{a - r_x + v_x\tau}{w_0}\right) + \left(a + r_x - v_x\tau\right)erf\left(\frac{a + r_x - v_x\tau}{w_0}\right)\right)$$
$$\left(\frac{w_0}{\sqrt{\pi}}\left(e^{-\left(\frac{a-r_y+v_y\tau}{w_0}\right)^2} - 2e^{-\left(\frac{r_y-v_y\tau}{w_0}\right)^2} + e^{-\left(\frac{a+r_y-v_y\tau}{w_0}\right)^2}\right) - 2\left(r_y - v_y\tau\right)erf\left(\frac{r_y - v_y\tau}{w_0}\right)\right.$$
$$\left.+\left(a - r_y + v_y\tau\right)erf\left(\frac{a - r_x + v_y\tau}{w_0}\right) + \left(a + r_y - v_y\tau\right)erf\left(\frac{a + r_y - v_y\tau}{w_0}\right)\right)$$

6. Cross-Correlation of diffusion in Imaging FCS

$$G(\tau)_{diffusion} = G_\infty + \frac{1}{4\langle C\rangle a^4}\times$$

$$\left(\sqrt{\frac{w_0^2+4D\tau}{\pi}}\left(e^{-\left(\frac{a-r_x}{\sqrt{w_0^2+4D\tau}}\right)^2} - 2e^{-\left(\frac{r_x}{\sqrt{w_0^2+4D\tau}}\right)^2} + e^{-\left(\frac{a+r_x}{\sqrt{w_0^2+4D\tau}}\right)^2}\right) - 2r_x erf\left(\frac{r_x}{\sqrt{w_0^2+4D\tau}}\right)\right.$$
$$\left.+\left(a - r_x\right)erf\left(\frac{a - r_x}{\sqrt{w_0^2+4D\tau}}\right) + \left(a + r_x\right)erf\left(\frac{a + r_x}{\sqrt{w_0^2+4D\tau}}\right)\right)$$
$$\left(\sqrt{\frac{w_0^2+4D\tau}{\pi}}\left(e^{-\left(\frac{a-r_y}{\sqrt{w_0^2+4D\tau}}\right)^2} - 2e^{-\left(\frac{r_y}{\sqrt{w_0^2+4D\tau}}\right)^2} + e^{-\left(\frac{a+r_y}{\sqrt{w_0^2+4D\tau}}\right)^2}\right) - 2r_x erf\left(\frac{r_y}{\sqrt{w_0^2+4D\tau}}\right)\right.$$
$$\left.+\left(a - r_y\right)erf\left(\frac{a - r_y}{\sqrt{w_0^2+4D\tau}}\right) + \left(a + r_y\right)erf\left(\frac{a + r_y}{\sqrt{w_0^2+4D\tau}}\right)\right)$$

7. Integral w_1 in the calculation of observation volume

$$\int_{-\infty}^{\infty} erf\left[\frac{a-2x}{\sqrt{2}w_0}\right] + erf\left[\frac{a+2x}{\sqrt{2}w_0}\right] dx$$

$$= \left[\begin{array}{l} -\frac{(a-2x)}{2} erf\left[\frac{a-2x}{\sqrt{2}w_0}\right] \\ +\frac{(a+2x)}{2} erf\left[\frac{a+2x}{\sqrt{2}w_0}\right] - \frac{w_0}{\sqrt{2\pi}}\left(e^{-\frac{(a-2x)^2}{2w_0^2}} - e^{-\frac{(a+2x)^2}{2w_0^2}} \right) \end{array} \right]_{-\infty}^{\infty}$$

$$= \left[-\frac{(a-2x)}{2} erf\left[\frac{a-2x}{\sqrt{2}w_0}\right] + \frac{(a+2x)}{2} erf\left[\frac{a+2x}{\sqrt{2}w_0}\right] \right]_{-\infty}^{\infty}$$

$$= \left(2a + \left[x\left(erf\left[\frac{a-2x}{\sqrt{2}w_0}\right] + erf\left[\frac{a+2x}{\sqrt{2}w_0}\right] \right) \right]_{-\infty}^{\infty} \right) = 2a$$

8. Integral w_2 in the calculation of observation volume

$$\int_{-\infty}^{\infty}\left(Erf\left[\frac{a-2x}{\sqrt{2}w_0}\right]+Erf\left[\frac{a+2x}{\sqrt{2}w_0}\right]\right)^2 dx$$

Let $u=\dfrac{a+2x}{\sqrt{2}w_0}$ and $t=\dfrac{\sqrt{2}a}{w_o}$

$$Hence\ f(u)=Erf[t-u]+Erf[u]$$

$$\int_{-\infty}^{\infty}\left(f(x)\right)^2 dx=\frac{w_o}{\sqrt{2}}\int_{-\infty}^{\infty}\left(f(u)\right)^2 du$$

$$=\frac{w_o}{\sqrt{2}}\left(\left[u\left(f(u)\right)^2\right]_{-\infty}^{\infty}-2\int uf(u)f'(u)du\right)$$

$$=-\sqrt{2}w_0\int_{-\infty}^{\infty}uf(u)f'(u)du$$

$$\int_{-\infty}^{\infty}uf(u)f'(u)dx=\frac{2}{\sqrt{\pi}}\int_{-\infty}^{\infty}u\left(erf[u]+erf[t-u]\right)\left(e^{-u^2}-e^{-(t-u)^2}\right)du$$

$$\int_{-\infty}^{\infty}uerf[u]e^{-u^2}du=\frac{1}{\sqrt{2}}$$

$$\int_{-\infty}^{\infty}uerf[t-u]e^{-u^2}du=-\frac{e^{-\frac{t^2}{2}}}{\sqrt{2}}$$

$$-\int_{-\infty}^{\infty}uerf[u]e^{-(t-u)^2}du=-t\sqrt{\pi}erf\left[\frac{t}{\sqrt{2}}\right]-\frac{e^{-\frac{t^2}{2}}}{\sqrt{2}}\text{(Appendix 9)}$$

$$-\int_{-\infty}^{\infty}uerf[t-u]e^{-(t-u)^2}du=\frac{1}{\sqrt{2}}\text{(Appendix 10)}$$

$$=4a\left(erf\left[\frac{a}{w_0}\right]+\frac{w_0}{a\sqrt{\pi}}\left(e^{-\frac{a^2}{w_0^2}}-1\right)\right)$$

9. **Integral used in Appendix 8**

$$\int_{-\infty}^{\infty} x\,erf[x]\,e^{-(t-x)^2}\,dx \quad \text{Let } u = t-x$$

$$= \int_{-\infty}^{\infty} (t-u)\,erf[t-u]\,e^{-u^2}\,du$$

$$= t\int_{-\infty}^{\infty} erf[t-u]\,e^{-u^2}\,du - \int_{-\infty}^{\infty} u\,erf[t-u]\,e^{-u^2}\,du$$

$$= t\int_{-\infty}^{\infty} erf[t-u]\,e^{-u^2}\,du + \frac{e^{-\frac{t^2}{2}}}{\sqrt{2}}$$

From Keith Briggs* *et al*,

$$\int_{-\infty}^{\infty} e^{-(\alpha x+\beta)^2}\,erf[\gamma x+\delta]\,dx = \frac{\sqrt{\pi}}{\alpha}\,erf\left[\frac{\alpha\delta-\beta\gamma}{\sqrt{\alpha^2+\gamma^2}}\right]$$

$$= t\sqrt{\pi}\,erf\left[\frac{t}{\sqrt{2}}\right] + \frac{e^{-\frac{t^2}{2}}}{\sqrt{2}}$$

*http://keithbriggs.info/documents/erf-integrals.pdf

http://www.wilmott.com/messageview.cfm?catid=4&threadid=79097

10. Integral used in Appendix 8

$$\int_{-\infty}^{\infty} x\,erf[t-x]\,e^{-(t-x)^2}\,dx \quad \text{Let } u = t-x$$

$$= \int_{-\infty}^{\infty} (t-u)\,erf[u]\,e^{-u^2}\,du = t\int_{-\infty}^{\infty} erf[u]\,e^{-u^2}\,du - \int_{-\infty}^{\infty} u\,erf[u]\,e^{-u^2}\,du$$

$$\int_{-\infty}^{\infty} erf[u]\,e^{-u^2}\,du = 0 \quad \text{Hence} \int_{-\infty}^{\infty} x\,erf[t-x]\,e^{-(t-x)^2}\,dx = -\frac{1}{\sqrt{2}}$$

11. Autocorrelation in SPIM-FCS

$$\langle I(z,z_0)\rangle = \left(\int_{-\infty}^{\infty} I(z,z_0)\,dz\right)^2 = \frac{I_0^2\pi w^2}{2}$$

$$g_z(\tau) = \frac{1}{\langle C\rangle \pi^{\frac{3}{2}} w_z^2\sqrt{D\tau}} \int_{-\infty}^{\infty}\int_{-\infty}^{\infty} e^{-2\left(\frac{z-m}{w_z}\right)^2} e^{-2\left(\frac{z'-m}{w_z}\right)^2} e^{-\left(\frac{z-z'}{2\sqrt{D\tau}}\right)^2} dz\,dz'$$

$$= \frac{2}{\langle C\rangle \pi w_z\sqrt{w_z^2+8D\tau}} \int_{-\infty}^{\infty} e^{-\frac{(m-z')^2}{4D\tau+\frac{w_z^2}{2}}} e^{-2\left(\frac{z'-m}{w_z}\right)^2} dz' = \frac{1}{\langle C\rangle \sqrt{\pi}\sqrt{w_z^2+4D\tau}}$$

12. Cross-correlation in Periodic processes

The propagator for flow is given by

$$P\left(x,y\,|\,x',y',\tau\right)=\delta\left(x'-x-v_x\tau,y-y'-v_y\tau\right)$$

The propagator for flow processes with a periodic signal is provided by

$$P\left(x,y\,|\,x',y',\tau\right)=\sum_{n=0}^{n=\frac{\max lag\ time}{\left(\frac{spacing}{v_x}\right)}}\delta\left(x'-x-v_x\tau+nd,y-y'-v_y\tau+nd\right)$$

where d is the periodicity. The fitting function for cross correlation of flow processes was derived earlier. (Appendix 5). Hence by analogy, the fitting function for the cross correlation of periodic flow process is

$$G\left(\tau\right)_{f,p}=G_\infty+\frac{1}{4\left\langle C\right\rangle a^4}\times$$

$$\sum_{n=0}^{n=\frac{\max lag\ time}{\left(\frac{spacing}{v_x}\right)}}\left(\begin{array}{l}\left(\begin{array}{l}\frac{w_0}{\sqrt{\pi}}\left(e^{-\left(\frac{a-r_x+v_x\tau-nd}{w_0}\right)^2}-2e^{-\left(\frac{r_x-v_x\tau+nd}{w_0}\right)^2}+e^{-\left(\frac{a+r_x-v_x\tau+nd}{w_0}\right)^2}\right)\\ -2\left(r_x-v_x\tau+nd\right)erf\left(\frac{r_x-v_x\tau+nd}{w_0}\right)\\ +\left(a-r_x+v_x\tau-nd\right)erf\left(\frac{a-r_x+v_x\tau-nd}{w_0}\right)\\ +\left(a+r_x-v_x\tau+nd\right)erf\left(\frac{a+r_x-v_x\tau+nd}{w_0}\right)\end{array}\right)\\ \left(\begin{array}{l}\frac{w_0}{\sqrt{\pi}}\left(e^{-\left(\frac{a-r_y+v_y\tau-nd}{w_0}\right)^2}-2e^{-\left(\frac{r_y-v_y\tau+nd}{w_0}\right)^2}+e^{-\left(\frac{a+r_y-v_y\tau+nd}{w_0}\right)^2}\right)\\ -2\left(r_y-v_y\tau+nd\right)erf\left(\frac{r_y-v_y\tau+nd}{w_0}\right)\\ +\left(a-r_y+v_y\tau-nd\right)erf\left(\frac{a-r_x+v_y\tau-nd}{w_0}\right)\\ +\left(a+r_y-v_y\tau+nd\right)erf\left(\frac{a+r_y-v_y\tau+nd}{w_0}\right)\end{array}\right)\end{array}\right)$$

13. Taylor's series expansion of autocorrelation

$$p(x)=\begin{bmatrix}\frac{1}{a} & 0<x<a\\ 0 & otherwise\end{bmatrix}$$

$$E(x)=\int_{-\infty}^{\infty} xp(x)\,dx=\frac{1}{a}\int_{0}^{a} x\,dx=\frac{a}{2}$$

$$E(x^2)=\int_{-\infty}^{\infty} x^2 p(x)\,dx=\frac{1}{a}\int_{0}^{a} x^2\,dx=\frac{a^2}{3}$$

$$Var(x)=E(x^2)-(E(x))^2=\frac{a^2}{12}$$

14. Mean and variance of uniform distribution

$$p(x)=\begin{bmatrix}\frac{1}{a} & 0<x<a\\ 0 & otherwise\end{bmatrix}$$

$$E(x)=\int_{-\infty}^{\infty} xp(x)\,dx=\frac{1}{a}\int_{0}^{a} x\,dx=\frac{a}{2}$$

$$E(x^2)=\int_{-\infty}^{\infty} x^2 p(x)\,dx=\frac{1}{a}\int_{0}^{a} x^2\,dx=\frac{a^2}{3}$$

$$Var(x)=E(x^2)-(E(x))^2=\frac{a^2}{12}$$

15. Mean and variance of intensity distribution in Imaging FCS

Let the uniform distribution and normal distribution be defined as below. Note a change in the expressions. This was done in order to make sure that the expressions conform to the rules of probability density functions that the area under the curve is 1.

Uniform: $p(x)=\begin{bmatrix}\frac{1}{a} & -\frac{a}{2}<x<\frac{a}{2}\\ 0 & otherwise\end{bmatrix}$ Normal: $p(x)=\frac{1}{\sigma\sqrt{2\pi}}e^{-\frac{x^2}{2\sigma^2}}$

Property	Uniform	Normal
Probability density function	$p(x)=\frac{1}{a}$	$p(x)=\frac{1}{\sigma\sqrt{2\pi}}e^{-\frac{x^2}{2\sigma^2}}$
Range	$-\frac{a}{2}<x<\frac{a}{2}$	$-\infty<x<\infty$
Mean	0	0
Variance	$\frac{a^2}{12}$	σ^2

The probability density of the convolved distribution can be evaluated in Mathematica using the command $Convolve\left[\frac{1}{a}UnitBox\left[\frac{t}{a}\right], PDF[NormalDistribution[0,\sigma],t,t,x]\right]$.

The convolved pdf is given by the equation

$$p(x)=\frac{1}{2a}\left(erf\left(\frac{a-2x}{2\sqrt{2}\sigma}\right)+erf\left(\frac{a+2x}{2\sqrt{2}\sigma}\right)\right) \quad ;-\infty<x<\infty$$

From the properties of a PDF, we know that the area under the PDF is 1. This can be verified as

$$\frac{1}{2a}\int_{-\infty}^{\infty}\left(erf\left(\frac{a-2x}{2\sqrt{2}\sigma}\right)+erf\left(\frac{a+2x}{2\sqrt{2}\sigma}\right)\right)dx$$

From Appendix 7, we know that the value of the integral is 2a. Hence, the total probability is 1.

$$E(x)=\int_{-\infty}^{\infty}xp(x)\,dx=\frac{1}{2a}\int_{-\infty}^{\infty}x\left(erf\left(\frac{a-2x}{2\sqrt{2}\sigma}\right)+erf\left(\frac{a+2x}{2\sqrt{2}\sigma}\right)\right)dx$$

Let $\frac{x}{\sqrt{2}\sigma}=y$ and $\frac{a}{\sigma 2\sqrt{2}}=A$

$$=\frac{\sigma^2}{a}\int_{-\infty}^{\infty}y\left(erf\left(A-y\right)+erf\left(A+y\right)\right)dy=0$$

$$E\left(x^2\right)=\int_{-\infty}^{\infty}x^2p(x)\,dx=\frac{1}{2a}\int_{-\infty}^{\infty}x^2\left(erf\left(\frac{a-2x}{2\sqrt{2}\sigma}\right)+erf\left(\frac{a+2x}{2\sqrt{2}\sigma}\right)\right)dx$$

Let $\frac{x}{\sqrt{2}\sigma}=y$ and $\frac{a}{\sigma 2\sqrt{2}}=A$

$$=\frac{\sqrt{2}\sigma^3}{a}\int_{-\infty}^{\infty}y^2\left(erf\left(A-y\right)+erf\left(A+y\right)\right)dy$$

$$=\frac{2\sqrt{2}\sigma^3A}{a}\left(1+\frac{2A^2}{3}\right)=\sigma^2+\frac{a^2}{12}$$

$$Var(x)=E\left(x^2\right)-\left(E(x)\right)^2=\sigma^2+\frac{a^2}{12}$$

16. Theoretical discussion of ΔCCF distribution

The expression for the cross-correlation function for diffusion separated by r_x along the x-axis can be obtained from Appendix 6 by setting $v_x = v_y = r_y = 0$ and is an even function in r_x. ΔCCF which is defined as the differences between the forward and the backward correlation, in this case, is $G_{CCF}(r_x,\tau)$ - $G_{CCF}(-r_x,\tau)$. This expression, evaluates to zero on an average.

$$G(\tau)_{diffusion} = G_\infty + \frac{1}{2\langle C\rangle a^4}\left(\begin{array}{l}\sqrt{\frac{w_0^2+4D\tau}{\pi}}\left(e^{-\left(\frac{a}{\sqrt{w_0^2+4D\tau}}\right)^2}-1\right)\\ +aerf\left(\frac{a}{\sqrt{w_0^2+4D\tau}}\right)\end{array}\right)\times$$

$$\left(\begin{array}{l}\sqrt{\frac{w_0^2+4D\tau}{\pi}}\left(e^{-\left(\frac{a-r_x}{\sqrt{w_0^2+4D\tau}}\right)^2}-2e^{-\left(\frac{r_x}{\sqrt{w_0^2+4D\tau}}\right)^2}+e^{-\left(\frac{a+r_x}{\sqrt{w_0^2+4D\tau}}\right)^2}\right)\\ -2r_x erf\left(\frac{r_x}{\sqrt{w_0^2+4D\tau}}\right)\\ +(a-r_x)erf\left(\frac{a-r_x}{\sqrt{w_0^2+4D\tau}}\right)+(a+r_x)erf\left(\frac{a+r_x}{\sqrt{w_0^2+4D\tau}}\right)\end{array}\right)$$

This is not the case when the system exhibits flow where the function is not an even function in r_x as seen from the equation below. By setting $D = r_y = 0$, Appendix 5 is modified as

$$G(\tau)_{flow} = G_\infty + \frac{1}{2\langle C\rangle a^4}\left(\frac{w_0}{\sqrt{\pi}}\left(e^{-\left(\frac{a}{w_0}\right)^2}-1\right)+aerf\left(\frac{a}{w_0}\right)\right)\times$$

$$\left(\begin{array}{l}\frac{w_0}{\sqrt{\pi}}\left(e^{-\left(\frac{a-r_x+v_x\tau}{w_0}\right)^2}-2e^{-\left(\frac{r_x-v_x\tau}{w_0}\right)^2}+e^{-\left(\frac{a+r_x-v_x\tau}{w_0}\right)^2}\right)-2(r_x-v_x\tau)erf\left(\frac{r_x-v_x\tau}{w_0}\right)\\ +(a-r_x+v_x\tau)erf\left(\frac{a-r_x+v_x\tau}{w_0}\right)+(a+r_x-v_x\tau)erf\left(\frac{a+r_x-v_x\tau}{w_0}\right)\end{array}\right)$$

17. Materials and Methods

The plasmids of EGFR-GFP and PMT-GFP were obtained from Dr. Ichiro Maruyama's lab (OIST, Okinawa, Japan). They were recloned by Dr. Ping Liu and Ms. Ma Xiaoxiao from the lab. The sequences of the plasmids along with the construction steps can be found here[53]. Optically transparent diamond samples, fabricated diamond transistors and functional graphene samples were kind gifts from Ms. Priscilla Ang (The Graphene Research Centre, NUS). The details of the fabrication of diamond transistor are provided here[212]. Chemically processed graphene films were prepared either by spin-coating or drop-casting. Graphene grown by CVD was also employed in this study. The detailed protocols to prepare graphene samples are provided elsewhere[242-243].

18. The results have been partly published in

a) Guo, L., J. Y. Har, J. Sankaran, Y. M. Hong, B. Kannan, and T. Wohland. 2008. Molecular diffusion measurement in lipid Bilayers over wide concentration ranges: A comparative study. Chemphyschem 9:721-728.

b) Sankaran, J., M. Manna, L. Guo, R. Kraut, and T. Wohland. 2009. Diffusion, Transport, and Cell Membrane Organization Investigated by Imaging Fluorescence Cross-Correlation Spectroscopy. Biophysical Journal 97:2630-2639.

c) Wohland, T., X. Shi, J. Sankaran, and E. H. K. Stelzer. 2010. Single Plane Illumination Fluorescence Correlation Spectroscopy (SPIM-FCS) probes inhomogeneous three-dimensional environments. Opt. Express 18:10627-10641.

d) Ang, P. K., M. Jaiswal, C. H. Y. X. Lim, Y. Wang, J. Sankaran, A. Li, C. T. Lim, T. Wohland, O. z. Barbaros, and K. P. Loh. 2010. A Bioelectronic Platform Using a Graphene−Lipid Bilayer Interface. ACS Nano 4:7387-7394.

e) Sankaran, J., X. K. Shi, L. Y. Ho, E. H. K. Stelzer, and T. Wohland. 2010. ImFCS: A software for Imaging FCS data analysis and visualization. Optics Express 18:25468-25481.

f) Bag, N., J. Sankaran, A. Paul, R. S. Kraut, and T. Wohland. 2012. Calibration and Limits of Camera-Based Fluorescence Correlation Spectroscopy: A Supported Lipid Bilayer Study. Chemphyschem 21:201200032.